Title

THE LOCAL STRUCTURE OF MANGANESE IN THE PHOTOSYNTHETIC APPARATUS AND SUPEROXIDE DISMUTASE: AN X-RAY ABSORPTION STUDY

Author

Goodin, D.B.

Publication Date

1983-09-01

LBL-16901

Lawrence Berkeley Laboratory

UNIVERSITY OF CALIFORNIA

CHEMICAL BIODYNAMICS DIVISION

THE LOCAL STRUCTURE OF MANGANESE IN THE PHOTOSYNTHETIC APPARATUS AND SUPEROXIDE DISMUTASE: AN X-RAY ABSORPTION STUDY

D.B. Goodin
(Ph.D. Thesis)

September 1983

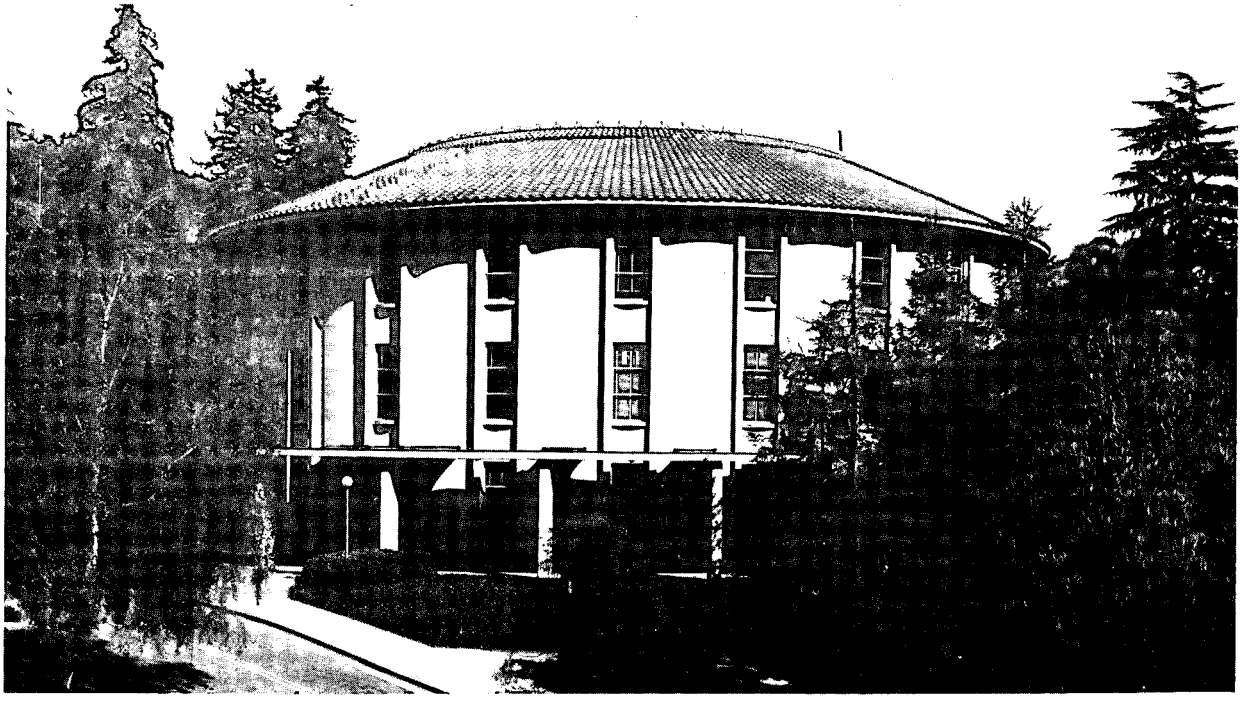

Prepared for the U.S. Department of Energy under Contract DE-AC03-76SF00098

DISCLAIMER

LBL-16901

THE LOCAL STRUCTURE OF MANGANESE IN THE PHOTOSYNTHETIC APPARATUS AND SUPEROXIDE DISMUTASE: AN X-RAY ABSORPTION STUDY

David Bruce Goodin
(Ph.D. Thesis)

Lawrence Berkeley Laboratory
University of California
Berkeley, California 94720

September 1983

This work was supported by the Office of Energy Research, Office of Health and Environmental Research, Health Effects Research Division and Office of Energy Research, Office of Basic Energy Sciences, Biological Energy Research Division of the U.S. Department of Energy under Contract No. DE-AC03-76SF00098.

ABSTRACT

The techniques of extended x-ray absorption fine structure (EXAFS), and x-ray absorption edge spectroscopy (XAES) are used to obtain specific structural information about the manganese coordination environment in synthetic inorganic complexes, and in biological redox systems.

Analysis of EXAFS data is first used to obtain a structural assignment to manganese tetraphenylporphyrin complexes capable of alkane oxidation. The data are consistent with a dimeric seven-coordinate μ-oxo-bridged structure, and implications of this structure on the resulting reactivities of the complexes are discussed.

We have applied EXAFS analysis to the manganese containing superoxide dismutases from various species to examine directly the similarities and differences in site structure between samples from distantly related organisms.

EXAFS fitting analysis for these samples using two scattering shells gave two structurally distinct and physically acceptable minima. One of these, containing 3-4 atoms of N or O at 2.00-2.04 Å and 1-2 S at 2.28-2.33 Å, was more strongly supported by the data for SOD from T. thermophilus. For eukaryotic SOD from S. cerevisiae, the other structure, consisting of 2-3 N or O atoms at 1.96-1.98 Å and 1-3 N or O atoms at 2.41-2.50 Å, was somewhat more

favorable.

Substitution of the T. thermophilus apo-enzyme with iron resulted in an inactive protein, while reconstitution with manganese yielded highly active preparations. Importantly, EXAFS analysis for the iron-substituted enzyme strongly indicates that iron enters into the same coordination environment as observed for native manganese SOD. These data are consistent with a structural model presented, in which the functional specificity of manganese and iron forms of SOD for their native metal can be explained on the basis of evolutionary relationships of their local ligand environments.

A study of the manganese involvement in photosynthetic water oxidation by higher plants was undertaken. This process proceeds as though five intermediates, S_0-S_4, operate in a cyclic fashion. A low temperature EPR signal was used as an indicator of S state composition in a manganese K-edge study of a spinach photosystem II preparation enriched in states S_1, S_2, and S_3 by illumination at -90°C. A dramatic change is observed in the edge properties between samples prepared in states S_1 and either S_2 or S_3, establishing a direct relationship between the local environment of Mn and the S state composition. Samples in S_2 and S_3 exhibit a broadening of the principal absorption peak and a shift to higher energy by as much as 2.5 eV relative to S_1 samples. The magnitude of these changes is directly related to the EPR signal intensity

induced by illumination. Models are discussed in which these data may be interpreted in terms of a conformation induced change in Mn ligation, and/or oxidation during the S_1 to S_2 transition.

Finally, the release of manganese from photosynthetic membranes by inactivating treatments was studied using low temperature EPR. This work demonstrates the existence of bound forms of manganese which contribute significantly to the population of manganese centers that have been altered by inactivation. These studies are useful in defining roles for the various pools of manganese contained in photosynthetic membranes.

Kenneth Sauer

TABLE OF CONTENTS

ACKNOWLEDGEMENTS

I have learned much in my studies at Berkeley, both professionally and personally. The following people have played a role in that growth.

I thank my research advisers, Dr. Ken Sauer and Dr. Mel Klein for their guidance and support. Both have encouraged my scientific independence, but were never too busy to help. Ken's energetic interest in photosynthesis has always been inspiring. For his patience and confidence through difficult times, I am sincerly grateful. Mel, by unselfishly showing pride in his students, is responsible for much of my enjoyment of graduate work. His wisdom and fascination with science will never be forgotten.

The x-ray absorption data could not have been collected without the considerable efforts of many people. I would like to thank Vittal Yachandra, Dave Britt, Ann McDermott, Paul Reisberg, Ron Guiles, and Sun Un for sitting bug-eyed through countless hours, listening to fan motors, and learning to look forward to Denny's at 4 AM.

Dr. Craig Hill and his students are acknowledged for the synthesis and characterization of the manganese porphyrin complexes, and Dr. James Fee for kindly providing samples of SOD for the x-ray absorption experiments.

I am grateful to the staff of LCB and SSRL for their

assistance and cooperation, and to the members of the Sauer and Klein groups for their friendship.

Drs. Jon Kirby, Alan Robertson and Al Thompson are acknowledged for introducing me to the intricacies of x-ray absorption spectroscopy, and Gary Brudvig for generating my interest in EPR.

I am indebted to my parents, Mr. and Mrs. Harry Goodin, for their love and encouragement. To Diana, who, when things seem hopeless, is able to bring out the sun.

Finally, I would like to acknowledge the countless men and women who have dedicated their lives to science. We stand on their shoulders from where a unique and beautiful view of our universe can be seen.

This work was supported by the Office of Energy Research, Office of Health and Environmental Research, Health Effects Research Division and Office of Energy Research, Office of Basic Energy Sciences, Biological Energy Research Division of the U.S. Department of Energy under Contract No. DE-AC03-76SF00098.

Synchrotron research was performed at the Stanford Synchrotron Radiation Laboratory which is supported by the Department of Energy, Office of Basic Energy Sciences, the National Science Foundation, Division of Materials Research, and the National Institutes of Health, Biotechnology Resource Program, Division of Research Resources.

ABBREVIATIONS

Chl	-	chlorophyll
DCPIP	-	2,6-dichlorophenolindophenol
DMBQ	-	2,5-dichloro-p-benzoquinone
EXAFS	-	extended x-ray absorption fine structure
HEPES	-	N-2-hydroxyethylpiperazine-N'-2-ethane sulfonic acid
MES	-	2(N-morpholino)ethane sulfonic acid
OEC	-	oxygen evolving complex
OIPh	-	iodosylbenzene
P680	-	photosystem II reaction center
PSI	-	photosystem I
PSII	-	photosystem II
TPP	-	meso-tetraphenylporphinato dianion ligand
TRIS	-	tris(hydroxymethyl)aminomethane
XAES	-	x-ray absorption edge spectroscopy

CHAPTER 1

Introduction

I. SCOPE AND PURPOSE

The reactions that make use of oxygen and its reduced counterparts are of fundamental importance in the life process. Oxygen is used as the terminal electron acceptor in the respiratory chain that provides the basic energy requirements of higher organisms. It is also the final product in the oxidative cleavage of water in the photosynthetic electron transport apparatus of higher plants. Oxygen is a potentially reactive substance. It is easily reduced, and this property is exploited by a widespread class of enzymes. Oxidases and oxygenases catalyze the oxidation of substrate by using dioxygen as an electron sink. The reactivity of oxygen and its intermediates O_2^-, $^{\cdot}OH$, and H_2O_2 also make O_2 a hazardous substance. Aerobic organisms carefully regulate the levels of these species with catalase, peroxidase, and superoxide dismutase.

As with many other enzymes involved in more general redox reactions, the great majority of those involved directly in the oxidation-reduction intermediates of dioxygen contain one or more metal atoms at the active site. It is

commonly the case that the metal atom is involved directly as an electron carrier. Much can be learned by studying and comparing the structures that nature has patiently chosen to carry out these basic reactions.

Despite a wealth of knowledge about the structure and function of iron and copper enzymes, very little is known about any biological manganese center. There are only two known examples in which manganese is used specifically as a cofactor in electron transfer reactions of dioxygen. These are the oxygen evolution complex of higher plant photosynthesis, and in a special class of superoxide dismutases.

Almost nothing is known about the structural similarities or differences in these biological manganese centers, or what structural constraints are necessary to define the specific reactivities exhibited by this class of enzymes. It is the purpose of this thesis to obtain information about the structural environment of manganese in superoxide dismutase and the oxygen evolution complex of photosynthetic membranes.

In the next section a general introduction to photosynthetic water oxidation is presented. An introduction to the properties of superoxide dismutase is deferred to chapter 4.

II. MANGANESE AND PHOTOSYNTHETIC OXYGEN EVOLUTION

The light driven reactions of photosynthesis result in the generation of reduced pyridine nucleotides and ATP used for energy metabolism in plants and ultimately the synthesis of all biological material on this planet. The generation and stabilization of charge separation in higher plants occurs in a series of membrane resident electron transfer components. Light excitation energy is transferred after absorption by pigment complexes to one of two reaction centers resulting in electron transfer to an acceptor molecule. In photosystem II, the oxidized donor is reduced by other membrane components, and the ultimate source of reducing equivalents is water, which is oxidized to dioxygen:

$$2H_2O \xrightarrow{h\nu} 4e^- + 4H^+ + O_2$$

The production of an oxygen molecule requires the removal of 4 electrons from two water molecules at an average potential in excess of 0.81 V at pH 7.

Kinetic flash yield measurements on spinach chloroplast membranes by Joliot [1] and Kok [2] provided the first mechanistic details of this process. The quantity of oxygen evolved after a series of 10 μsec flashes of saturating light is observed to depend on the flash number. Little or no oxygen is observed after the first two flashes, a maximum on the third, and from this point the quantity oscillates with a period of four. These observations have led Kok [2] to

postulate the existence of an intermediate which cycles through a series of five states, S_0-S_4, accumulating the necessary potential for water oxidation. S_0 and S_1 are stable in the dark, and in fact reach an equilibrium of 1:3 respectively. As shown in the following scheme, each photoact advances an S state by one until S_4 is produced, which results in the release of dioxygen and the return to S_0.

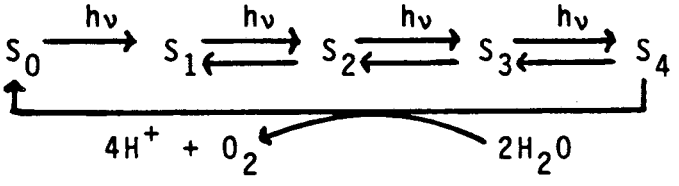

Although thermodynamic arguments have been used against a mechanism involving a series of simple one electron oxidations of water [3], proton release experiments indicate that neither is the reaction a concerted four electron process [4]. Thus, there appears to be a rather unique and complicated interaction between the S intermediate and the water acting as reaction substrate.

The identity of the S intermediate has not been established, but evidence exists that implicates a form of membrane bound manganese. Manganese deficient algae do not evolve oxygen, and this inability can be reversed without protein synthesis by addition of manganese to deficient cells [5]. Broken, washed chloroplast preparations typically contain 4-6 manganese per P_{680} reaction center, and approximately 2/3 of this quantity is released by a number of treatments such as alkaline Tris washing, mild thermal shock,

and high salt incubation that specifically inactivate oxygen evolution [6]. Blankenship and Sauer [7] observed that the manganese that is released from the membrane during Tris inactivation and observable by room temperature EPR stays with the membrane phase upon washing, but is equally distributed after sonication. It was later observed [8] that reactivation of O_2 evolution in the presence of a reducing agent was accompanied by a disappearance of the Mn^{+2} EPR signal. The accepted interpretation of these data has been that the manganese associated with O_2 evolution is released by alkaline Tris washing into the inner thylakoid envelope where it is trapped by a slow trans-membrane diffusion. Reactivation of activity, by an unknown mechanism causes this manganese to be reincorporated into the membrane.

More recent work in this area has given rise to a reevaluation of some of these ideas. Yokum et al. [9] report a chloroplast preparation from high salt buffers that contains only 4 manganese per photosynthetic unit. Tris treatment releases only one of these to an EPR detectable state and leaves another loosely bound in a form that can be removed by washing in 40 mM Ca^{+2}. Mansfield and Barber [10] have seen no difference in the amount of manganese removed by Tris in normal and inside out thylakoid membranes. In addition, this released manganese was not required to achieve a 60% reactivation of activity. Similar results have also been reported in an inside out photosystem II preparation from spinach [11].

Very little structural information is known about the active form of manganese in the oxygen evolving complex. Progress in this area has been hindered for two principal reasons. Firstly, the lability of the oxygen evolving complex has prevented its isolation in an active form. Thus, previous studies have had to be performed on preparations which are dilute and somewhat heterogeneous with respect to manganese centers. Significant advances have recently been made in that stable, active sub-chloroplast membrane preparations containing only the photosystem II light reactions are now available [12-14]. Secondly, the inability to directly observe the S intermediates has prevented their study or the development of reliable protocols for their preparation and stabilization. However, a photo-induced EPR signal rich in manganese hyperfine structure has recently been observed at low temperature in chloroplast preparations and has been interpreted as arising from reactions close to the oxygen evolution complex [15]. based on EPR simulation, these authors have proposed that the signal arises from an antiferromagnetically coupled manganese multimer. This is consistent with earlier EXAFS work indicating the presence of a metal-metal interaction at about 2.71 Å in spinach chloroplasts [16]. The oxidation state of a proposed dimeric Mn(III,IV) complex [15] giving rise to this EPR signal is also consistent with earlier X-ray absorption edge data [17] if it is assumed that the EPR signal arises from the S_2 state. This appears likely, for recent work [18] has shown

that the temperature dependence of the formation and decay of the EPR signal is similar to that expected for the S_2 state.

III. PROJECT GOALS AND THESIS FORMAT

The techniques of x-ray absorption edge and EXAFS spectroscopy were chosen as the major tools in a study to obtain specific information about the structures of the manganese sites in the photosynthetic apparatus and in manganese superoxide dismutase. X-ray absorption edge spectra can be used to extract information about the oxidation level and ligand symmetry of the metal sites, while EXAFS provides ligand identity and radial distance information. EXAFS analysis cannot give a complete structural assignment, because it does not include information about the angular distribution of ligands or their stereochemistry. If some details of a structure are known, EXAFS can be used to study specific aspects of the metal site, and can even improve upon the accuracy of information provided by x-ray crystallography. If nothing about the metal site is known, as is the case with the enzymes in this work, EXAFS will often indicate a number of possible site structures consistent with the data. Nevertheless, when no other structural tools are available, this information can provide a valuable framework for the eventual elucidation of the mechanistic details of these important enzymes.

A description of x-ray absorption spectroscopy, and data analysis methods is presented in chapter 2. The application of these methods is used in chapter 3 where an EXAFS

structural study is described on a series of novel high valent manganese tetraphenylporphyrin complexes. In chapter 4, x-ray absorption edge and EXAFS results are presented in a structural investigation of manganese superoxide dismutases. The metal site structures proposed provide a description of the structural and evolutionary relationships between these enzymes and a closely related class of iron enzymes. In chapter 5, x-ray absorption edge results on chloroplast photosystem II preparations are described under conditions in which EPR data indicate that various S state populations have been stabilized. In this way, the direct involvement of manganese with the S_2 derived EPR signal is explored in terms of specific alterations in the structural and electronic properties of manganese centers. This work is complemented in chapter 6 with a study of manganese binding to photosynthetic membranes in an attempt to better characterize the relationships between manganese content, oxygen evolution, and the appearance of EPR observable species in response to inactivating treatments.

REFERENCES

1. Joliot, P., Barbieri, G. and Chabaud, R. (1969) Photochem. Photobiol. 10, 309-329.

2. Kok, B., Forbush, B. and McGloin (1970) Photochem. Photobiol. 11, 457-475.

3. Radmer, R. and Cheniae, G. (1977) Primary Processes of Photosynthesis, (Barber, J., ed.) Elsevier, Holland 304-348.

4. Forster, V., Hong, Y.-Q. and Junge, W. (1981) Biochim. Biophys. Acta 638, 141-152.

5. Cheniae, G. (1970) Ann. Rev. Plant Physiol. 21, 467-498.

6. Cheniae, G.M. and Martin, I.F. (1970) Biochim. Biophys. Acta 197, 219-239.

7. Blankenship, R.E. and Sauer, K. (1974) Biochim. Biophys. Acta 357, 252-266.

8. Blankenship, R.E., Babcock, G.T. and Sauer, K. (1975) Biochim. Biophys. Acta 387, 165-175.

9. Yokum, C.F., Yerkes, C.T., Blankenship, R.E., Sharp, R.R. and Babcock, G.T. (1981) Proc. Natl. Acad. Sci. 78(12), 7507-7511.

10. Mansfield, R. and Barber, J. (1982) FEBS lett. 140(2), 165-168.

11. Henry, L.E.A., Lindberg Moller, B., Andersson, B. and Akerlund, H.-E. (1982) Carlsberg Res. Commun. 47, 187-198.

12. Stewart, A.C. and Bendall, D.S. (1979) FEBS lett. 107(2), 308-312.

13. Berthold, D.A., Babcock, G.T. and Yokum, C.F. (1981) FEBS lett. 134, 231-234.

14. Henry, L.E.A. and Lindberg Moller, B. (1981) Carlsberg Res. Commun. 46, 227-242.

15. Dismukes, G.C. and Siderer, Y. (1981) Proc. Natl. Acad. Sci. 78, 274-278.

16. Kirby, J.A., Robertson, A.S., Smith, J.P., Thompson, A.C., Cooper, S.R. and Klein, M.P. (1981) J. Amer. Chem. Soc. 103, 5529-5537.

17. Kirby, J.A., Goodin, D.B., Wydrzynski, T., Robertson, A.S. and Klein, M.P. (1981) J. Amer. Chem. Soc. 103, 5537-5542.

18. Brudvig, G.W., Casey, J.L. and Sauer, K. (1983) Biochim. Biophys. Acta, in press.

CHAPTER 2

The Principles and Practical Application of X-ray Absorption Spectroscopy

I. INTRODUCTION

With the development of synchrotron radiation as an extremely intense, wide bandwidth source of x-rays, a great deal of interest has been generated in the use of x-ray absorption spectroscopy as a structural probe for the study of transition metals in materials research, surface science and in dilute biological materials. An excellent and extensive review of these techniques has been provided by Lee et al. [1]. Structural information can be obtained from the details of the absorption edge itself, as well as from the small amplitude modulations (EXAFS) above the edge energy. This chapter describes the properties of the edge and EXAFS spectra, experimental techniques used for data collection, and the methods of data analysis for extraction of structural information from an x-ray absorption experiment.

II. THEORY OF X-RAY ABSORPTION SPECTROSCOPY

X-ray Absorption Edge Spectroscopy (XAES)

The absorbance in the x-ray region of common materials decreases monotonically with increasing photon energies, except for a few abrupt increases characteristic of the element under study. These absorption edges result from transitions of an electron in an inner atomic shell into unoccupied levels in or above the valence band of the element (figure 1). The edge arising from 1s electron promotion is known as the K edge. Those arising from 2s and 2p levels are called the L edges, and occur at longer wavelengths. Within an edge, a series of symmetry allowed transitions occurs to empty levels as the energy is increased, and these levels eventually converge into a continuum in which a final state photo-electron is emitted from the atom with a kinetic energy given by the difference in the photon and binding energies of the atom.

The K-edge of a particular element occurs at a characteristic wavelength which is well isolated from those of other elements. However, the exact appearance and position of an edge is determined by factors that include the effects of the core hole on the unoccupied valence states, the absorber oxidation state, and the nature and symmetry of the metal-ligand interactions. In a review by Srivastava and Nigam [2], the K-edge spectra of a large number of transition metal complexes were empirically characterized and classed according to the nature and

Figure 1. The ratio of incident to transmitted intensity in the x-ray K-edge region. Features in the edge region of an ionic complex are shown as transitions between discrete atomic energy levels.

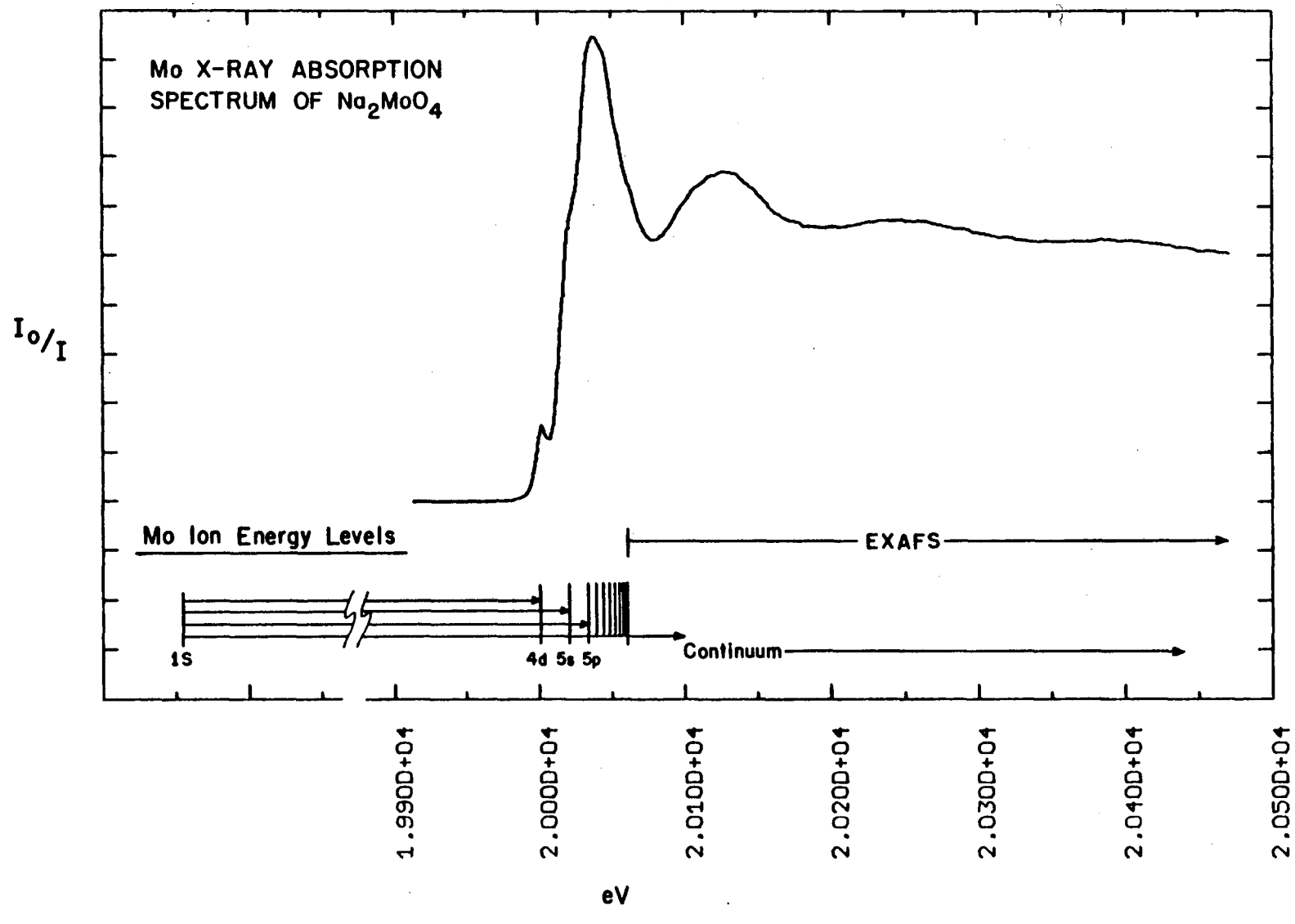
Mo X-RAY ABSORPTION
SPECTRUM OF Na_2MoO_4
I_o/I
Mo Ion Energy Levels
EXAFS
1S
4d 5s 5p
Continuum
1.990D+04
2.000D+04
2.010D+04
2.020D+04
2.030D+04
2.040D+04
2.050D+04
eV

XBL 764-5809

symmetry of the coordinating ligands.

A somewhat more quantitative treatment was later described by Shulman et al. [3] for a series of metal fluoride complexes. In this case, the extremely ionic nature of the complexes greatly simplifies the treatment, because the final state levels are well localized on the metal and can be described by atomic configurations. For example, when a transition metal undergoes the transition

$$Z(1s^2 2s^2 2p^6 3s^2 3p^6 3d^n) \longrightarrow Z(1s^1 2s^2 2p^6 3s^2 3p^6 3d^n n'l')$$

the fact that the 1s hole is close to the nucleus and well removed in energy from the valence levels allows these outer valence levels to be described by those of the Z+1 element. Thus, the energies of the transitions can be obtained from spectroscopic tables [4] by using

$$Z(1s^2 2s^2 2p^6 3s^2 3p^6 3d^n) \longrightarrow (Z+1)(1s^2 2s^2 2p^6 3s^2 3p^6 3d^n n'l')$$

as a model for the absorption process. The transitions involved are predominantly single electron processes for which the dipole selection rule holds. This means that the most strongly allowed transitions occur between the 1s and np levels, however the forbidden 1s 4s and 1s 3d transitions may be weakly allowed due to vibronic mixing with p levels [3]. This breakdown of selection rules is very sensitive to the coordination symmetry of the complex and the appearance of these features in the low energy region of the edge can thus be used as an indicator of

coordination symmetry.

For complexes that contain significant metal-ligand interactions such as is commonly found in biological materials, this simple approach is not valid and quantitative treatment requires a knowledge of the low lying unoccupied molecular orbitals of the complex. The most difficult aspect of such a treatment is the proper consideration of the effects of the partially relaxed core hole on the outer lying states. Calculations of edge properties have been carried out with fairly acceptable results [5,6] but the difficulty of performing these computations, and their inability to account for the most subtle features of the edge make the interpretation of most edge data difficult on a quantitative level.

Nevertheless, there are certain empirical features that allow a qualitative estimation of oxidation state and coordination symmetry from edge spectra. As is the case with the ionic complexes, the most strongly allowed transitions are those that occur to orbitals that transform like x, y and z under the symmetry properties of the complex. For octahedral complexes, these are the orbitals with t_{1u} symmetry, while for tetrahedral complexes the allowed transitions are to orbitals with t_2 symmetry. Thus, significant changes in the intensity of these transitions can be observed and correlated with site coordination symmetry. An example of such a case is presented in figure 2, which shows the drastic difference in the near edge

Figure 2. The ratio of incident to transmitted intensity for manganese K-edges. The absorbance is the natural logarithm of this quantity. A, Absorption edge for the tetrahedral $KMnO_4$ complex; B, absorption edge for $MnCl_2 \cdot 4H_2O$.

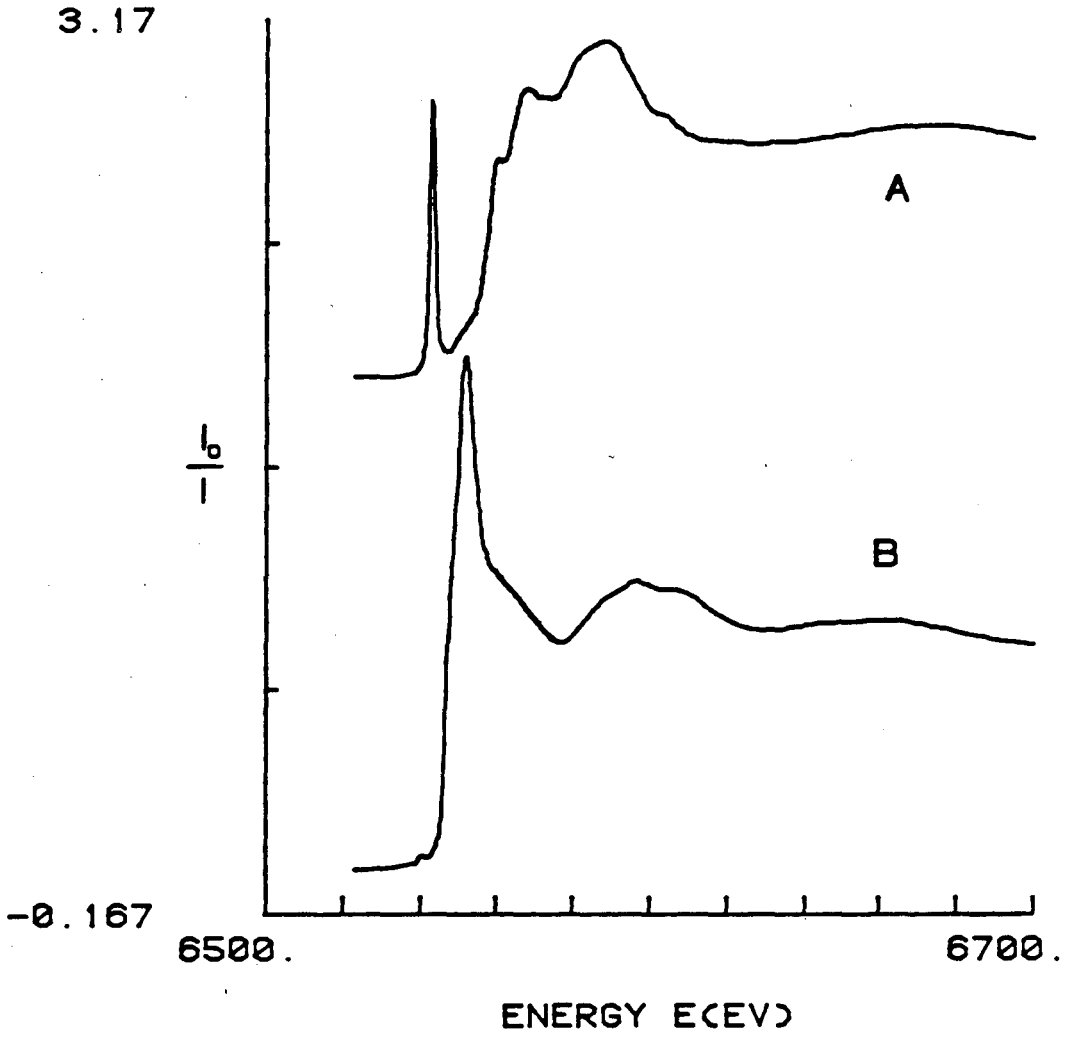
3.17
A
B
$\frac{I_0}{I}$
-0.167
6500.
6700.
ENERGY E(EV)

features of the nearly tetragonal $MnCl_2$ and tetrahedral $KMnO_4$ complexes.

Many studies have attempted to correlate properties such as the position of the principal edge peak [7], its width [8], and the position of the inflection point [9,10] with the oxidation state and coordination stoichiometry of the metal. Great care must be taken when using these properties as indicators. Changes in the intensity of pre-edge transitions for two complexes that differ in coordination symmetry may thwart attempts to use the feature as a means of obtaining metal oxidation states if they do not reflect the same transition in each case. Fairly reliable results have been obtained however, for molybdenum [9] and manganese [10] complexes using edge infection points, partly because most of these edges are quite smooth and featureless. The inflection point was observed to be a poor indicator for complexes [10] that exhibit metal-ligand π interactions or dative bonding, because the straightforward approximations of ligand covalency do not hold. Within these limitations, however, these methods have proven quite useful as qualitative indicators of metal charge and symmetry.

Extended X-ray Absorption Fine Structure (EXAFS)

EXAFS appears as an extended modulation by 5-10% of the total x-ray cross section above an edge. These modulations arise from interference effects experienced by the final state photo-electron. The first practically useful description of this effect was provided by Sayers et al.

[11] and Stern [12]. A physical interpretation of EXAFS is illustrated in figure 3. At a given energy E above an edge, the absorption process results in the creation of a photo-electron of energy $E_{PE} = E_{h\nu} - E_B$ where E_B is the binding energy of the electron in the atom. The photo-electron expands as a spherical wave with a well defined phase and a wavelength proportional to 1/k, where $k = (2m_e[E_{h\nu} - E_o])^{1/2}(h)^{-1}$ and E_o is the energy at which the electron becomes free. This wave has a probability $[F_i(k)]^2$ of scattering off the i^{th} ligand with a phase shift of $\phi_i(k)$ and thus may return to the original absorbing atom with a definite coherence. The total phase difference between the outgoing and backscattered wave is $2kR_i + \alpha_i(k)$, where R_i is the distance to the i^{th} ligand, $\alpha_i(k) = 2\delta(k) + \phi_i(k) - \pi$, $\delta(k)$ is the phase shift experienced by the photo-electron each time it encounters the central atom, and π is subtracted by convention to make EXAFS amplitudes positive. Thus the total photo-electron final state wave-function, and the absorbance itself, is modulated by the wave-vector k at a frequency proportional to R_i. The relation derived [12] for this effect is shown in equation 1,

$$\chi(k) = \sum_i \frac{N_i}{kR_i^2} |F_i(k,\pi)| e^{-\sigma_i k^2} \sin(2kR_i + \alpha_i(k)) \qquad (1)$$

where N_i is the number of atoms in the i^{th} shell and σ_i is the Debye-Waller disorder parameter describing the thermal

Figure 3. Schematic diagram of EXAFS photo-electron interference. In A) the incident photon energy is such that the back-scattered final state photo-electron arrives at the central atom in phase with the outgoing wave; in B) the photon energy is such that destructive interference ocurs.

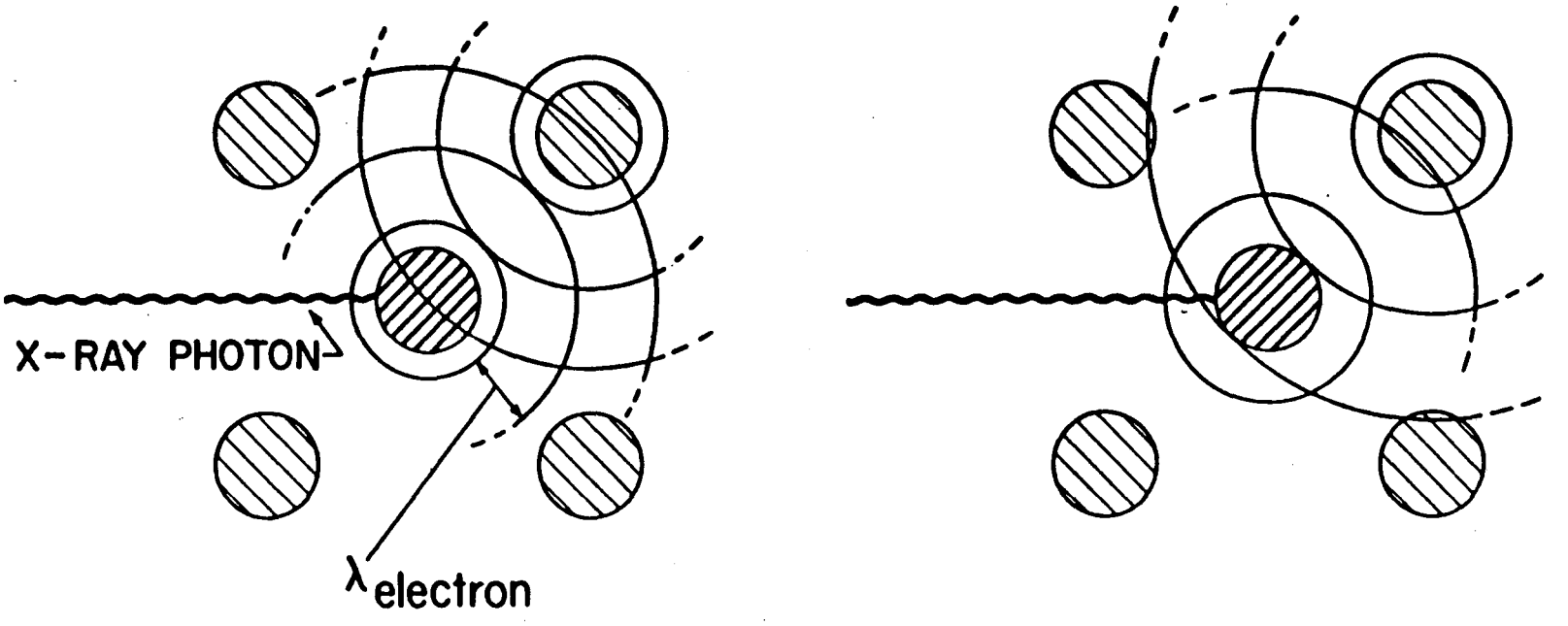

XBL 764-5808

and static displacement from the average scatterer distance.

It is apparent from equation 1 that EXAFS contains information about the number of scatterers and their distance. This information depends upon the knowledge of the scattering amplitude F(k) and phase $\alpha(k)$, which in turn depend on the type of absorbing and scattering atoms. Once known, this dependence allows the elemental identification of scattering atoms.

III. The X-ray Absorption Experiment

Basic Experimental Setup

Collection of x-ray absorption data is conceptually simple. The absorbance μx, where x is the sample thickness, is calculated as $\ln(I_0/I)$ from a measurement of I_0, the incident intensity, and I, the transmitted intensity. The total x-ray cross section is composed of two parts, $\mu = \mu_{PE} + \mu_B$, where μ_{PE} is due to the photo-electric absorption of interest, and μ_B is a background absorbance arising from scatter and the slowly varying absorption from other distant edges.

X-radiation produced as synchrotron emission from electron storage rings and synchrotrons provides an ideal source for these measurements because of its broad band nature at an intensity that is 3 to 4 orders of magnitude higher than conventional x-ray generators. This intensity reduces the time required to make the very precise measurement of absorbance necessary for EXAFS spectra. This is particularly true for samples at low concentrations where data that may take 10 hours to collect would require 1000 hours using conventional sources.

A description of the equipment and computer programs used for data collection have been described previously [13,14,15,16]. A brief summary of the major components follows.

Monochromatic x-rays are produced using a double silicon or germanium crystal diffraction monochromator. Reflections

from the hkl plane of the crystal held at angle θ from the beam direction is satisfied at the wavelengths $n\lambda = 2d_{hkl}\sin\theta$, where n is the order of diffraction and dh_{kl} is the lattice spacing for the that plane. The wavelength is changed by rotating the double crystal assembly under computer control. The presence of higher order reflection harmonics (n>1) are undesirable and can be reduced by slightly detuning one of the crystals with respect to the other so that they are no longer exactly parallel.

The measurement of intensities for absorbance spectra are typically done with gas flow ionization chambers built at the Stanford Synchrotron Radiation Laboratory (SSRL) and described by Kincaid [13]. The lengths and gas composition are optimized for ≈10% absorption for the I_0 measurement and a large absorbance for I.

Sample considerations are minimal in that EXAFS can be obtained on any phase of matter. However, sample homogeneity is an important concern. Care must be taken to avoid non-uniform samples, or those containing crystal fragments such as ice in frozen samples. The latter can easily be accomplished using glycerol glasses. The x-ray beam may have a non-uniform intensity across its dimensions. If these 'hot spots' move while scanning the energy, a 'spotty' sample will introduce artifacts. If crystals are present in the sample, diffraction peaks can be introduced in fluorescence mode data.

For most samples and especially enzymes, the possibility

of reduction or damage by solvated electrons and radicals produced by the beam must be considered. Data collection at low temperature aids in the immobilization of these species, but radiation effects can still be observed [17,18]. It is therefore of great importance that means be available to assess the integrity of samples after data collection.

Energy Registration

A number of factors make reliable energy calibration important. The energy resolution of a typical unfocussed beam line at SSRL is approximately 1-2 eV, which is comparable to the lifetime widths of most x-ray transitions. Monochromator calibration errors much larger than this can occur. Sudden shifts in energy can result from beam steering or orbit changes each time electrons are injected into the ring. Effects have also been observed [15] due to monochromator slippage as well as crystal and mirror heating. The behavior of the storage ring is often unpredictable, so it is advantageous to collect short (≈20 min) scans and average them later. For dilute samples, as many as 100 of these scans may be required. Especially for edge studies, where effects of <1 eV are often significant, it is critical to maintain an accurate calibration. For these studies we have utilized a method for simultaneous measurement of reference data [19] illustrated in the experimental setup of figure 4. A reference material, typically $KMnO_4$, with a feature slightly below the edges of other manganese compounds is placed in series with a normal

Figure 4. Experimental diagram of an x-ray absorption and fluorescence experiment. The monochromatic beam intensity is measured before and after transmission through the primary sample 1. Simultaneous measurement of absorbance for a reference sample 2 in series with the first measurement is possible if the relative edge jump of sample 1 is small.

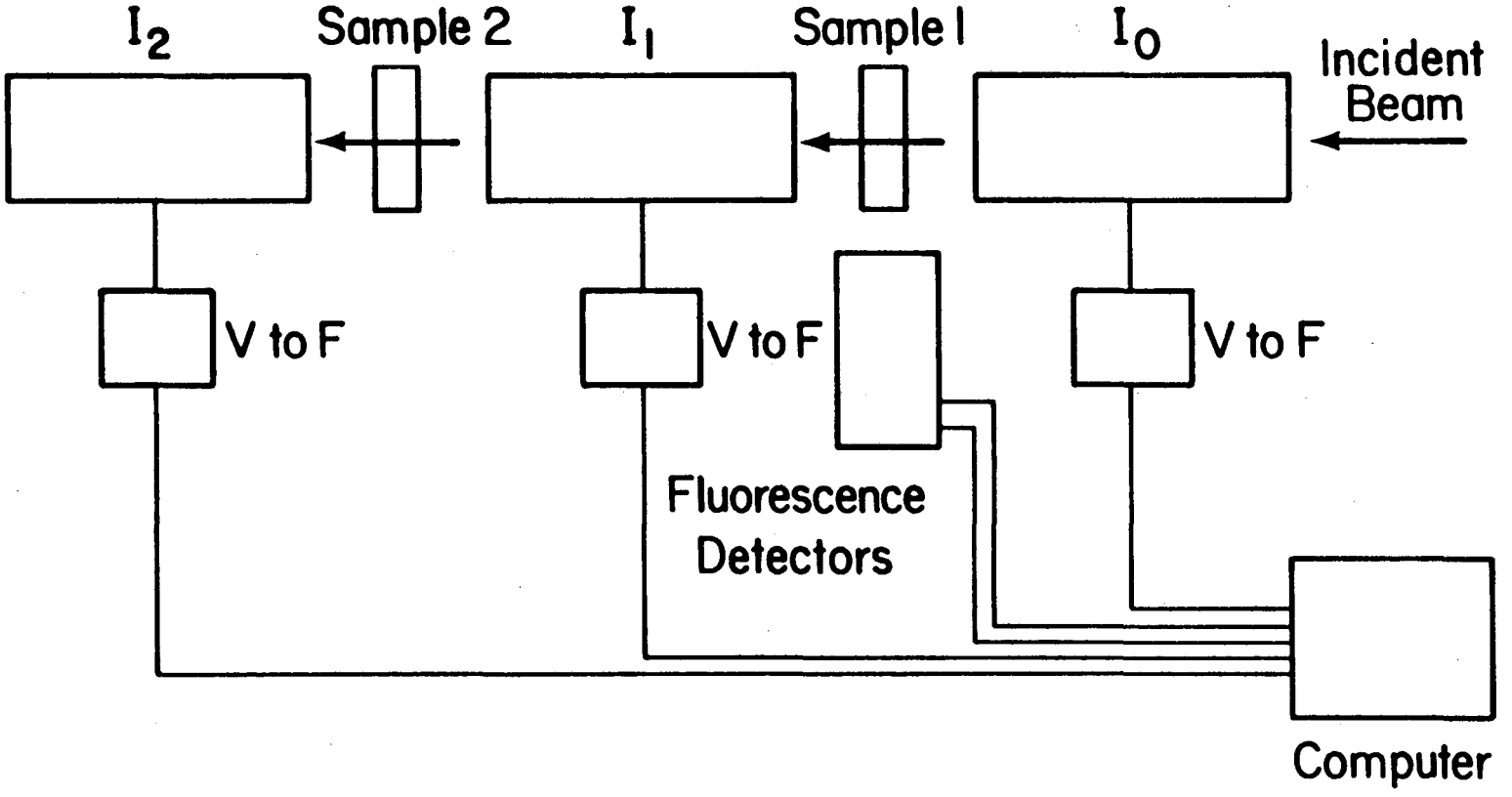

XBL 7910-5068

absorption arrangement. For dilute primary samples for which the transmitted flux does not vary drastically, it is possible to collect data for the reference feature during each scan.

Measurements at Low Concentrations

At low absorber concentrations, intrinsic difficulties are encountered in the precision of the x-ray absorbance related to the need for measurement of small differences in the very large photon fluxes. The use of K-α fluorescence detection [20] has been very successful in extending measurements to concentrations of 1 mM or less. The K-α x-ray fluorescence intensity is related to the photo-electric cross section $(\mu x)_{PE}$ by

$$F = I_0 \eta \frac{(\mu x)_{PE}}{(\mu x)_T} (1-e^{-(\mu x)_T}) \qquad (2)$$

where η is the fluorescence efficiency (approximately 20% for Mn) and $(\mu x)_T$ is the total sample absorbance [20].

Detection of K-α emission from a sample is contaminated by scattered radiation at the incident photon energy and, because this contributes to background, it becomes increasingly important to discriminate against this scatter for the concentrations typically used for biological samples. Detectors with high energy resolution such as multi-element crystal monochromators [21] and solid state detectors [20] are capable of such discrimination, but have other drawbacks. The barrel monochromators suffer from limited

acceptance solid angles and the solid state devices are subject to serious count rate limitations. Refinements in the use of fluorescence filters made of the Z-1 element in combination with collimation techniques [22] have made it practical to use high count rate, low resolution scintillation detectors into the sub-millimolar regime. With the use of multi-element detectors, these techniques were found to compare favorably with high resolution devices for scatter/fluorescence ratios >100 [23].

In this work we have used a seven element detection array similar to that described by Powers et al. [18]. Detector elements were constructed using disks of aluminized Nuclear Enterprises NE104 scintillation plastic. This material has a scintillation decay time of 2 nsec, allowing extremely high count rates. The disks were coupled to EMI 9813 eleven stage photomultiplier tubes. Two channels were created to take advantage of the increased signal-to-noise of the tube in the center of the array. The other six tubes were logically summed using a progressive 15 nsec delay line and diode adding circuit. The pulses from each channel, amplified with a x10 gain pre-amplifier (EMI VA.02), were used to trigger an Ortec 436 leading-edge discriminator, and the output NIM logic pulses were counted by a computer-interfaced hex-scaler.

Fluorescence filters were obtained by electroplating 0.35 mil chromium onto 20 mil beryllium sheets (4"x4") and fitted with an aluminum soller slit assembly [22] to reduce

detection of Cr K-α fluorescence from the filter.

IV. Data Analysis Techniques

Methods for Structure Determination

There are two distinct methods for extraction of structural parameters from an EXAFS experiment. The EXAFS effect is described by a sum of amplitude and phase modulated sine terms and can be inverted by fourier transformation to give a distribution of frequency components. The phase $\alpha(k)$ is approximately linear so that if $\alpha(k) = ak + b$, then the argument of the sine in equation 1 becomes $2k(R_i + a/2) + b$, and the magnitude of the fourier transform will show peaks at $R_i + a/2$. The shifts introduced by the phase are similar for common absorber-scatterer pairs (approximately -0.5 Å for Mn-N or O), so the transform peaks can be used to provide an indication of the number of scattering shells and their distance.

Clearly the most accurate method for structure determination is that of curve fitting analysis. For this method to work, it is necessary to have knowledge of the phase and amplitude functions for each absorber-scatterer pair. This need has given rise to two methods of curve fitting. Both assume that the phase and amplitude functions are transferable from one chemical compound to another. There is evidence that this is a good assumption for the phases but not always so with the amplitudes [1,24].

The first of these methods employs empirical determination of the functions by use of model complexes. Functional forms for the phases and amplitudes are assumed,

and the parameters that determine them obtained by fitting to model data with the known structural parameters. The parameterized phase and amplitude functions are then used to fit unknown data to the structural parameters. This method has been successfully applied for many systems, yielding distances accurate to 0.015 Å if good models are used [25].

A good model complex should have a set of equivalent scatterers at equal distance from the metal and be well resolvable from other scatterer distances. The model should also be as chemically similar to the unknown as possible to insure good phase and amplitude transferability. However, for studies on completely unknown systems, no criterion is available for determining when the model is sufficiently similar. One model becomes as good as another, and may even introduce problems, if it and the unknown are quite dissimilar. In addition, if the structure of interest contains mixed ligand types at distances that are unresolvable, it becomes impossible to obtain models that satisfy both of the properties that define a 'good' model.

The second method of fitting analysis employs ab initio calculations of the phase and amplitude functions [26]. These functions have been tested and successfully used [27-29] and they constitute the method of analysis used in this work. Representative phase and amplitude functions for manganese as absorber are shown in figure 5. It is seen that the phase shifts become progressively more positive as the scatterer atomic number increases. The net effect of

Figure 5. Theoretical EXAFS phase shifts and scattering amplitudes predicted for manganese as the absorber. A) The total phase $(2\delta(k) + \alpha(k))$ and B) the scattering amplitudes are shown for Mn-C, Mn-N, Mn-O, Mn-S and Mn-Mn pairs as a function of the photo-electron wave-vector k.

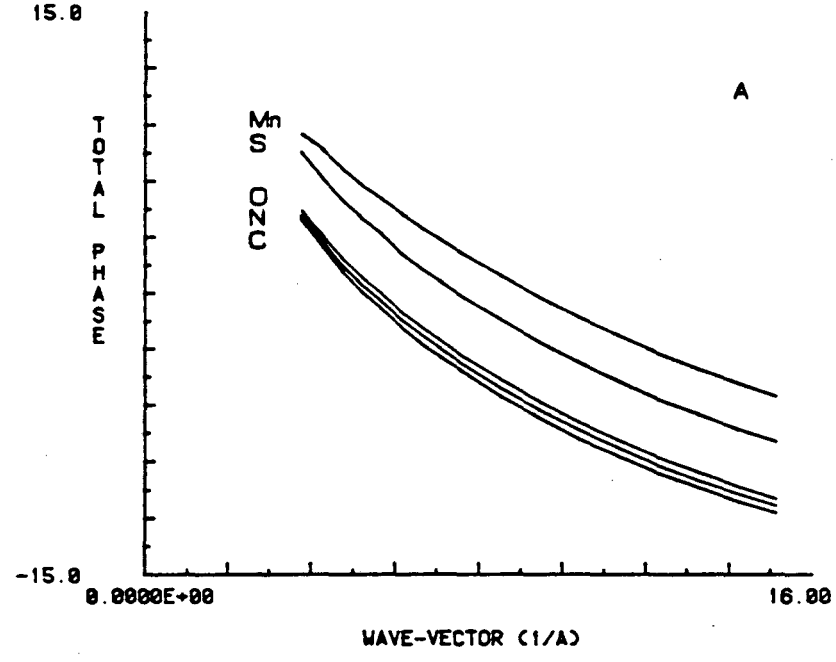
15.0
TOTAL PHASE
-15.0
A
Mn
S
O
N
C
0.0000E+00
16.00
WAVE-VECTOR (1/A)

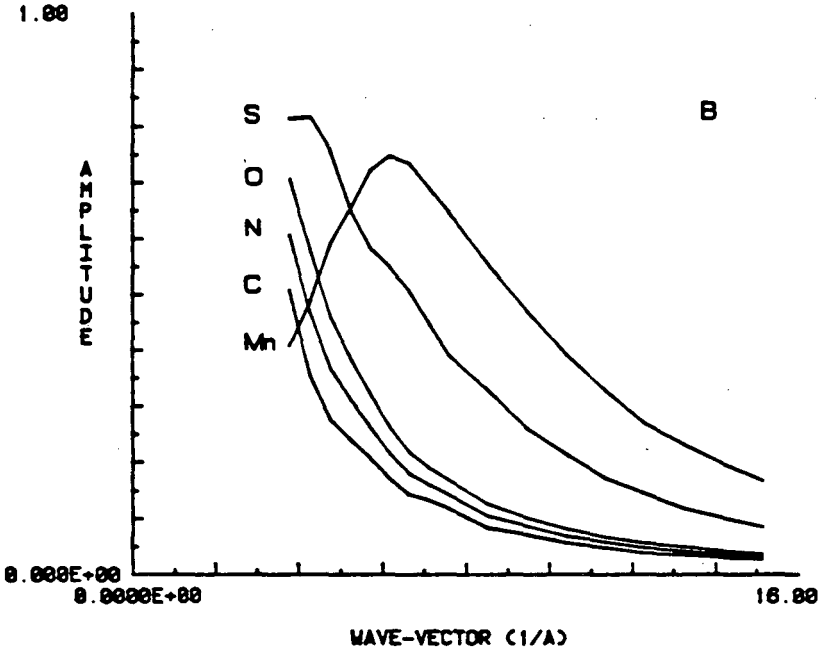
1.00
AMPLITUDE
0.000E+00
B
S
O
N
C
Mn
0.0000E+00
16.00
WAVE-VECTOR (1/A)

the phase and its curvature is to reduce the frequency in general and to slightly compress the oscillations at large values of k. As seen in figure 5, phases for carbon, nitrogen, and oxygen are very similar, which makes discrimination between C, N or O scatterers difficult at best. However the phase difference between Mn-O and Mn-S is large, making a C, N or O scatterer fairly easy to distinguish from a sulfur. The same is true for most elements that differ by at least a few in atomic number. The amplitudes shown in figure 5 also show elemental trends. The scattering amplitude increases with the scatterer atomic number and is observed to peak at higher values of k. This property also aids in elemental identification.

A number of problems have been described that make the theoretical amplitude information somewhat uncertain. Eisenberger has shown [24] that in some cases the amplitude is chemically sensitive, affecting its transferability. Observed reductions of experimental amplitudes by about a factor of 2 relative to theoretical values have been attributed partly to many-body effects [30] and partly to experimental origin [27]. For this reason amplitude correction factors have been applied in the data analysis using theoretical amplitude functions [28,29], and it is understood that the number of scattering atoms predicted by this method is somewhat uncertain.

It is not possible to exactly determine the position of E_o from EXAFS spectra, and discrepancies between the

experimental and calculated values make it necessary to use E_0 as a variable parameter. The value of E_0 is usually chosen at or a few eV above the edge maximum, and later optimized during the fitting analysis. E_0 and the distance R are slightly correlated [15]; however, an error of 1 eV in E_0 corresponds to a change of approximately 0.003 Å in the fitted distance, so the effect is minimal for errors in E_0 of a few eV. Changes in E_0 produce changes in $\chi(k)$ which decrease as $1/k$, whereas changes in the distance cause changes in $\chi(k)$ that are linear with k. For this reason it is not possible to obtain a good fit to a completely wrong distance by adjusting E_0. In addition, it has been noted that errors in the transferability of phase information as a result of chemical differences have similar effects on $\chi(k)$ as do errors in E_0 [1]. It is therefore possible by adjusting E_0 to effectively absorb many of the deficiencies in the approximations used in the calculation of phase information.

Ideally, when dealing with systems in which nothing is known about the site structure, it is best to proceed initially with analysis using calculated phase and amplitude information. In this way, unbiased formulations of the structural environment about the metal can be obtained, and many possibilities tested without the need for synthesis and characterization of complex model systems. As these ideas are refined, it becomes favorable to obtain and use model complexes with chemical and structural properties that

satisfy the criteria outline above. The two methods may be used in a complementary way, retaining the highest probability of making a correct structural identification on one hand, and later obtaining the most sensitive and accurate structural parameters possible.

Methods of Data Analysis

After data collection at SSRL, all data were processed and analyzed on the LCB VAX 11/780. Programs were written or adapted for use on the VAX and are briefly described in appendix A.

Pre-processing

Program REFORM was used to read SSRL data files, check for errors and output the ratio of I_0/I or F/I_0 in a format compatable with the remaining programs. Program HYPERPLOT was used to plot large quantities of data for the visual survey of useful data scans.

Adding

When large amounts of data needed to be averaged, this was performed using program EXADD. Each data file, weighted by the number of seconds per point used for collection, is displayed over the averaged file before being added to it, allowing close visual inspection. The most critical aspect of averaging data is to maintain energy calibration of the individual scans. When simultaneous reference measurement techniques [19] are used, this information is present with each data file, and program EXADD is capable of performing this task automatically. If desired, the program checks the

reference data for each scan, finds the position of the reference feature using derivative techniques, and uses linear interpolation to shift the data to match the reference feature to that in the first data file.

Preparation for Fitting

Considerable data analysis is required to normalize and remove the background from the EXAFS components. Much of the strategy for this analysis has been described by Robertson [15] and Kirby [14]. The interactive program EXAFS was written by adapting and extending previously existing software, and is capable of performing all analysis procedures described in this section.

Conversion to energy - The data are collected as a function of monochromator angle. Conversion to photon energy is performed first by using the monochromator position at the copper edge as a reference and the monochrometor crystal parameters.

Pre-edge removal - The slowly varying background absorbance (or scatter for fluorescence mode) is subtracted from the data. The background function used is usually a first- or second-order polynomial fit of the form $B(E) = a_0 + a_1 \ln(E) + a_2[\ln(E)]^2$ and was chosen for its ability to follow the curvature of the pre-edge region of most data [14]. This function is fit to the data from about 300-500 eV below the edge to about 20-50 eV below the edge, and the fitted function then extrapolated over the entire data set. The exact range and order of fit is determined by

its behavior above the edge. An appropriate example is shown in figure 6A.

Edge normalization - Two types of edge normalization are required. The absorption cross section per atom is obtained by a simple normalization of the edge rise to unity. This is performed by doing a quadratic polynomial fit to the data beyond the edge and extrapolating this fit to a point at the edge rise. The data are then normalized by dividing by this value. The second normalization is to the free-atom absorbance. EXAFS spectra are desired as relative modulations of the absorption cross section, but this cross section in the absence of EXAFS is not constant. The normalized free-atom cross sections are constructed from the McMaster tablulated fits [14] and used for normalization. Data at this point appear as shown in figure 6b.

Background removal - The removal of the slowly varying background above the edge was performed in at least two stages. In the first, a single low-order (always < 4) polynomial fit to the entire EXAFS region was subtracted from the data. This removed most of the slope and monotonic curvature. The second stage involves subtraction of smoothed data from the unsmoothed data to remove low frequency curvature. In a typical case, a triple smooth is performed in which for each point the data for a fixed region around that point is averaged. This smoothed data is then smoothed twice more. The amount of curvature removed is adjusted by varying the smoothing window. Each time this is

Figure 6. Creation of normalized EXAFS spectra for α-MnS. In A) pre-edge background removal is performed by fitting the pre-edge region to a logarithmic quadratic polynomial. In B) the normalized spectrum with unit edge jump is shown.

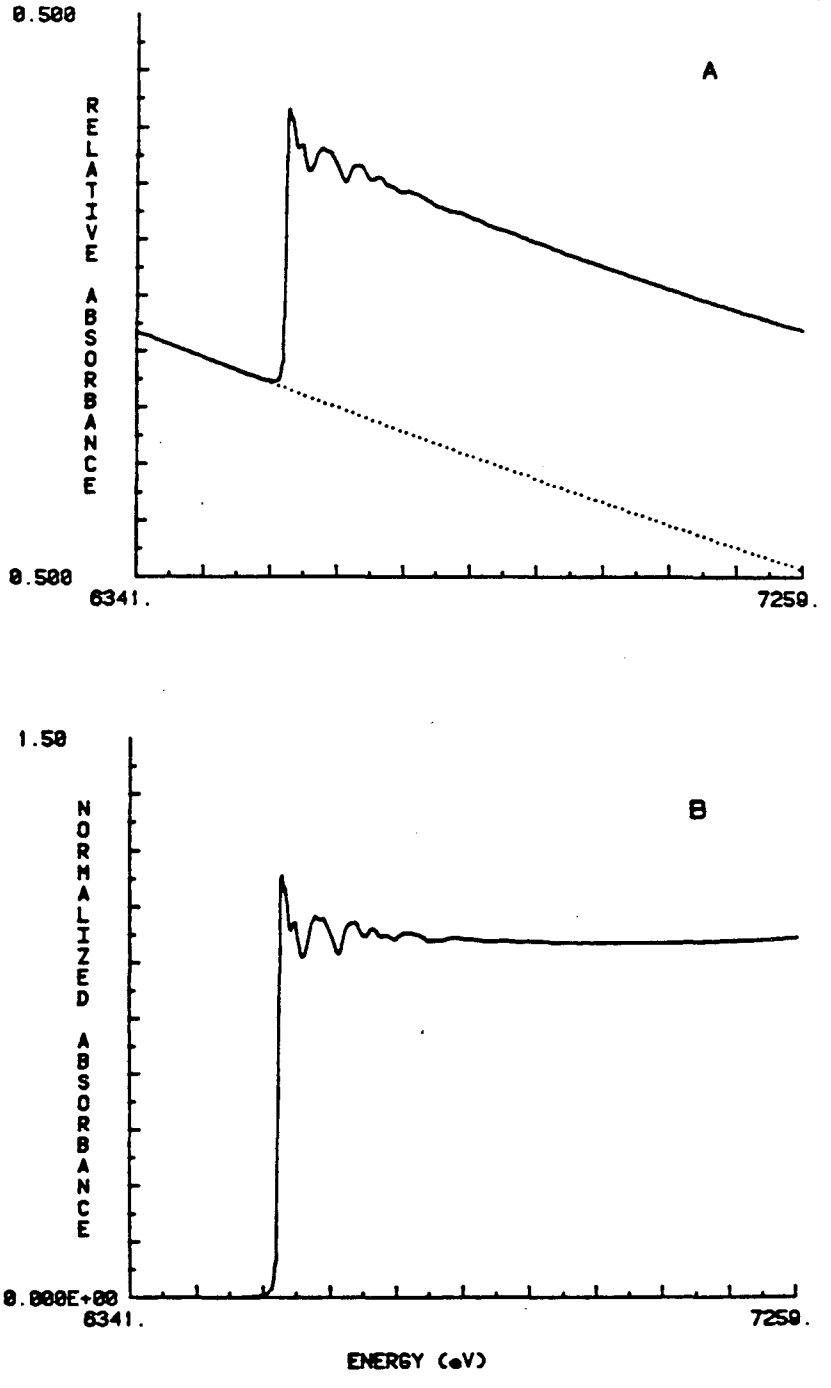
0.500
A
RELATIVE ABSORBANCE
0.500
6341.
7259.
1.50
B
NORMALIZED ABSORBANCE
0.000E+00
6341.
7259.
ENERGY (eV)

changed, the background is removed and the data fourier transform is examined. The smoothing window is adjusted to reduce fourier transform peaks below R_{eff} = 1 Å but none of the principal peaks are allowed to change by more than a few percent. This insures that frequency components corresponding to the EXAFS are unaffected. This procedure is sometimes employed before conversion from energy to photo-electron wave-vector space and is always employed after conversion. An example of a satisfactory smoothed background is shown in figure 7 along with the fourier transform of data before and after this background removal.

Care must be taken when using this technique for data in energy space. In this case, the EXAFS modulations are non-linear and decrease in frequency with increasing energy values, and smoothed functions may begin to follow these components at the high energy end of the data. It is often desirable to retain the background removed so that its fourier transform may be examined.

Fourier transformation and filtering - After conversion to k-space and linearization of the point density, fourier transforms can be taken. The transform computed is

$$\phi(R) = \int_{k_1}^{k_2} k^n \, W(k) \, \chi(k) \, e^{i2kR} \, dk \qquad (3)$$

where the data used extend from k_1 to k_2. Multiplication by an apodization window W(k) causes the data do go smoothly to zero at its endpoints and is done to reduce truncation

Figure 7. Background removal for α-MnS EXAFS. In A) a triply smoothed background (dotted line) was removed from the data (solid) after conversion to wave-vector space. The background function was created by successively using a sliding average of 2.4 Å^{-1} width. The fourier transform modulus B) is shown before and after background removal and demonstrates the removal of only frequency components below R_{eff} = 1 Å.

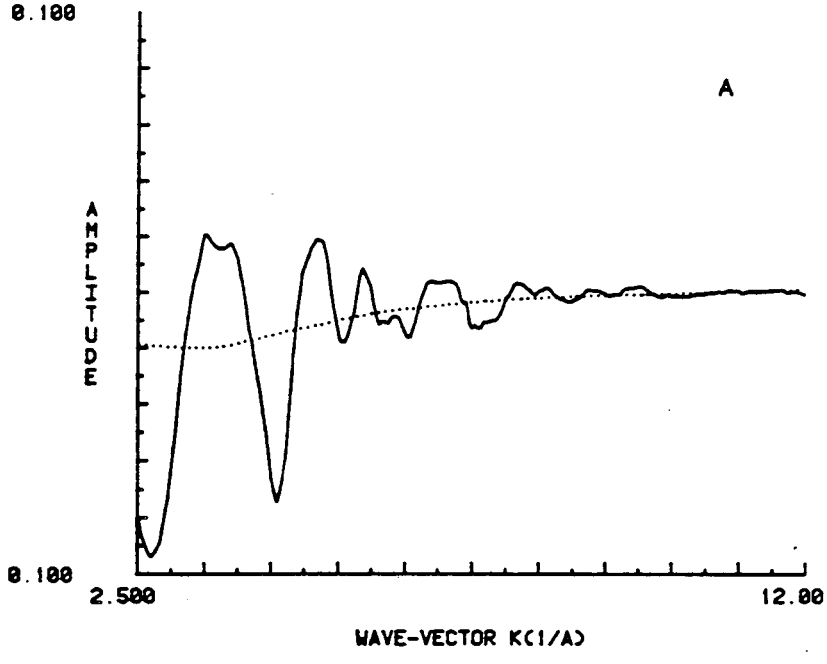
0.100
A
AMPLITUDE
0.100
2.500
12.00
WAVE-VECTOR K(1/A)

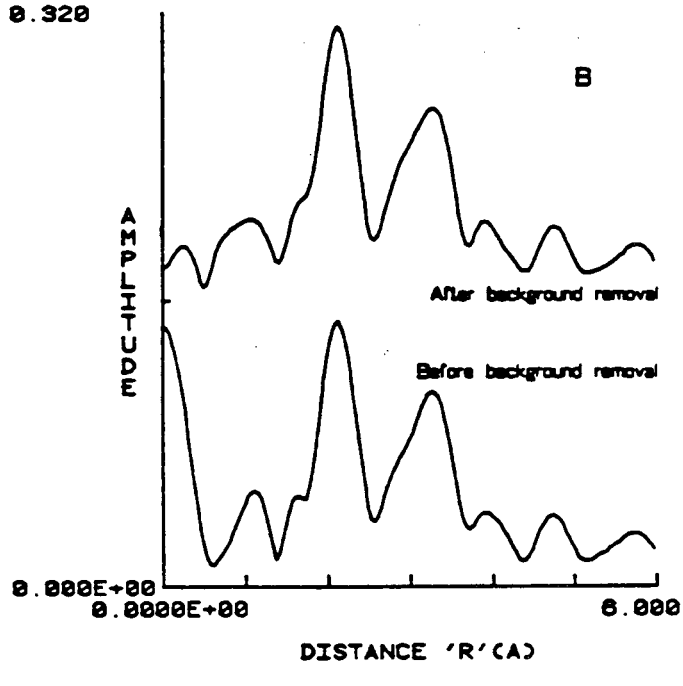
0.320
B
After background removal
Before background removal
AMPLITUDE
0.000E+00
0.0000E+00
6.000
DISTANCE 'R'(A)

sidelobes in the transform [15]. The k^n weighting, where n is typically 0-3, is used to reduce the damping of EXAFS modulations at high k values. This sometimes has desirable effects on the fourier transform. The R-space resolution is increased at the expense of signal-to-noise, because of the more constant EXAFS signal over the entire data range. This also prevents low k EXAFS components from dominating the spectrum. Errors in the phase as a result of uncertainty in the value of E_0 are greatest at low k values, and this weighting reduces their effects.

Isolation of specific scattering components is often necessary to reduce the complexity and inter-parameter dependence during fitting. This is accomplished by fourier filtering. Fourier transform peaks that are well resolved from other scattering contributions are isolated by applying a modified Hamming window function [14]. The resultant isolated fourier peak is transformed back into wave-vector space and used for fitting. If possible, the fourier transform of the data is taken without application of the Kaiser apodization window. If this were not done, the convolution of the window function with the data in R space would be difficult to remove after filtering and back transformation. It is usually possible to do this without introducing large truncation sidelobes by adjusting the limits of the data transformed so that they are near zero.

Fitting Analysis - In this method, non-linear least squares minimization of

$$F(R,N,\sigma,E_0) = \sum_i [(y_i - \chi(k_i))\ k_i{}^n]^2 \qquad (4)$$

is employed with respect to the structural parameters where y_i are the data values at point i and $\chi(k_i)$ the computed EXAFS amplitude from equation 1. Weighting by k^n is done for reasons described for fourier transform analysis. Program EXFIT was written for EXAFS single- and multi-shell fitting utilizing the minimization package MINUIT described earlier [14]. For each scattering shell included in the fit, four parameters, R, N, σ, and ΔE_0 can be allowed to vary, although any combination of them can be fixed at any point in the analysis.

Data below 3.5 to 4.0 Å^{-1} should not be used for analysis because approximations used in deriving the EXAFS relation are not good below these values [31].

The following general strategy is useful during fitting analysis. Fourier transform information is used to generate a chemically plausible structure. Fourier filtering is then used if possible to isolate the individual scattering peaks. This proposed structure is tested by fitting to these isolated peaks. For each peak, fits to a single shell of scatterers is attempted first. Other types of scattering atoms are also attempted. If a fit is found acceptable, it is refined, and a search is made for other minima. If no single shell fit is acceptable, a second shell of scattering atoms is introduced.

Each of the 'fits' mentioned above is composed of a series of steps. In a typical fit, the atom types and initial values of parameters are selected. For each new trial, a series of minimization stages are initiated by releasing a few parameters at a time. R and N are usually allowed to vary first in order to achieve a rough overall phase and amplitude match. The remaining parameters are then released and minimization continued. The Debye-Waller factor, σ, is set initially to -0.005 and allowed to vary between 0.0 and -0.02. Values of ΔE_0 are allowed to vary during fitting by 20 eV in either direction. In addition, fits to two scattering shells with ΔE_0 corrections that differ by 17 eV or more are considered unacceptable. This value was chosen on the basis of our experience with fitting model complexes and similar studies by others [17].

There are limitations to curve fitting analysis that should always be in mind. Rarely are parameters completely independent. However, parameter correlation is not so serious for EXAFS as it is for techniques that involve fitting to exponentials. This is because sine functions are more orthogonal than most other functions. Nevertheless, severe problems are sometimes encountered especially when parameters of two scattering shells are similar. The presence of strongly coupled parameters can be evaluated by examination of the covariance matrix provided by program EXFIT.

Addition of another scattering shell to a given fit will

nearly always improve its quality, and it is sometimes difficult to decide if its addition is justified. The best criterion is to require that significant improvement is obtained and that the parameters are sufficiently different from those of other shells. One should always be concerned that the features uniquely described by the additional shell are supported by the quality of the data.

Finally, as is common with most fitting procedures, local false minima may exist in addition to the true minimum. The best approach to avoid this problem is to use many different parameter starting values. A convenient optional feature of program EXADD utilizes a Monte-Carlo parameter search for finding global minima. It is helpful to realize that fitting to a sine wave, as to any periodic function, will exhibit a regular series of local minima. For typical EXAFS spectra these local minima occur at about 0.4 Å to either side of the true minimum [32], and can easily be checked.

REFERENCES

1. Lee, P.A., Citrin, P.H., Eisenberger, P. and Kincaid, B.M. (1981) Rev. Mod. Phys. 53(4), 769-806.

2. Srivastava, U.C. and Nigam, H.L. (1972) Coordination Chem. Rev. 9, 275-310.

3. Shulman, R.G., Yafet, Y., Eisenberger, P. and Blumberg, W.E. (1976) Proc. Natl. Acad. Sci. 73(5), 1384-1388.

4. Moore, C.E. (1952) Atomic Energy Levels, Natl. Bur. Stand. Cir. 467, vol. II.

5. Kutzler, F.W., Natoli, C.R., Misemer, D.K., Doniach, S. and Hodgson, K.O. (1980) J. Chem. Phys. 73(7), 3274-3288.

6. Natoli, C.R., Misemer, D.K., Doniach, S. and Kutzler, F.W. (1980) Phys. Rev. A 22(3), 1104-1108.

7. Vainshtein, E., Ourutskaya, R., Kotlyar, B. and Linde, U.R. (1964) Soviet Physics: Solid State 5, 2150-2153.

8. Nigam, H.L. and Srivastava, U.C. (1971) Chem. Commun. 14, 761-763.

9. Cramer, S., Eccles, T., Kutzler, F., Hodgson, K. and Mortenson, L. (1976) J. Amer. Chem. Soc. 98, 1286-1287.

10. Kirby, J.A., Goodin, D.B., Wydrzynski, T., Robertson, A.S. and Klein, M.P. (1981) J. Amer. Chem. Soc. 103, 5537-5542.

11. Sayers, D.E., Stern, E.A. and Lytle, F.W. (1971) Phys. Rev. lett. 27, 1204-1207.

12. Stern, E.A. (1971) Phys. Rev. B 10(8), 3027-3037.

13. Kincaid, B.M. (1975) Ph.D. Thesis, Stanford University.

14. Kirby, J.A. (1981) Ph.D. Thesis, University of California, Berkeley.

15. Robertson, A.S. (1979) Ph.D. Thesis, University of California, Berkeley.

16. Pianetta, P. and Lindau, I. (1977) J. Electron. Spectroscopy and Related Phenomena 11, 13-38.

17. Peisach, J., Powers, L., Blumberg, W.E. and Chance, B. (1982) Biophys. J. 38, 277-285.

18. Powers, L., Chance, B., Ching, Y. and Angiolillo, P. (1981) Biophys. J. 34, 465-498.

19. Goodin, D.B., Falk, K.-E., Wydrzynski, T. and Klein, M.P. (1979) 6th Annual Stanford Synchrotron Radiation Laboratory Users Group Meeting 10-11.

20. Jaklevic, J., Kirby, J.A., Klein, M.P., Robertson, A.S., Brown, G.S. and Eisenberger, P. (1977) Solid State Commun. 23, 679-682.

21. Hastings, J.B., Eisenberger, P., Lengeler, B. and Perlman, M.L. (1979) Phys. Rev. lett. 43, 1807-1810.

22. Stern, E.A. and Heald, S.M. (1979) Rev. Sci. Instrum. 50(12), 1579-1582.

23. Cramer, S.P. and Scott, R.A. (1981) Rev. Sci. Instrum. 52(3), 395-399.

24. Cramer, S.P. and Hodgson, K.O. (1979) Prog. Inorg. Chem. 25, 1-39.

25. Teo, B.-K. and Lee, P.A. (1979) J. Amer. Chem. Soc. 101, 2815-2832.

26. Stern, E.A., Heald, S.M. and Bunker, B. (1979) Phys. Rev. lett. 42(20), 1372-1375.

27. Antonio, M.R., Teo, B.-K., Clelend, W.E. and Averill, B.A. (1983) J. Amer. Chem. Soc. 105, 3477-3484.

28. Kirby, J.A., Robertson, A.S., Smith, J.P., Thompson, A.C. Cooper, S.R. and Klein, M.P. (1981) J. Amer. Chem. Soc. 103, 5529-5537.

29. Eisenberger, P. and Lengeler, B. (1980) Phys. Rev. B 22, 3551-3562.

30. Rehr, J.J., Stern, E.A., Martin, R.L. and Davidson, E.R. (1978) Phys. Rev. B 17(2), 560-565.

31. Stern, E.A., Sayers, D.E. and Lytle, F.W. (1975) Phys. Rev. B 11(12) 4836-4846.

32. Cramer, S.P. (1979) Synchrotron Radiation Applied to Biophysical and Biochemical Research (Castellani, A. and Quercia, I.F. eds.) 291-322.

CHAPTER 3

X-Ray Absorption Studies of High Valent Manganese Iodosylbenzene Tetraphenylporphyrin Complexes.

I. INTRODUCTION

Synthetic high valent metallo-porphyrins have been actively studied because of the ability of many to catalyze the oxidation of organic substrates [1]. A novel manganese tetraphenylporphyrin complex with the stoichiometry $[XMn(TPP)(OIPh)]_2O$, X = Cl (I) or Br (II) has been isolated from a system capable of catalyzing the oxidation of alkanes [2]. The spectral properties of these complexes have indicated structural similarities with well characterized dimeric μ-oxo bridged complexes isolated from the same system when $X = N_3^-$ or OCN^- [3]. Comparison of NMR ring current chemical shifts for the TPP phenyl protons in I and II with those for the dimeric $[Mn(IV)TPP(N_3)]_2O$ complex strongly indicates the presence of a cofacial μ-oxo dimeric structure. This is supported by observed similarities of optical spectra, and by the magnetic susceptibility of the complexes which indicates anti-ferromagnetic coupling.

The nature of the interaction of the iodosylphenyl moiety with the metal has been indicated only indirectly

[2]. Infared band shifts observed upon labeling with ^{18}O-iodosylbenzene have indicated, but do not demonstrate direct ligation of this group to the metal. Proton NMR shows a strong perturbation of the OIPh phenyl proton chemical shifts by the porphyrin ring that are consistent with placing the OIPh group directly above the porphyrin plane with a Mn-O-I distance between 2.5 and 3.5 Å.

The ambiguity remaining in the structural assignment of complexes I and II is represented in figure 1 by two proposed structures [2] that are consistent with observed properties, in which the role of the iodosylphenyl group is obscure. This is unfortunate, because it is this interaction which probably plays an important role in determining the unique reactive properties exhibited by these complexes.

A mechanism proposed for the activation of alkanes by these μ-oxo complexes has implicated an intermediate monomeric Mn(IV) oxo complex involved in hydrogen abstraction to produce free alkyl radicals [4]. This is followed by abstraction of axial ligand groups on the porphyrin by the radical species to produce the observed mixture of oxidation products. However, because of the uncertainty of ligation of the X or OIPh moieties, the role of these groups in the activation or product forming reactions remains unclear. Substitution on the iodosylbenzene group is observed to affect product distributions in some cases but not in others [4]. In addition, direct attack on the metal by the alkyl radical was

Figure 1. Two proposed structures [2] for the complexes $[ClMn(TPP)(OIPh)]_2O$ (I) and $[BrMn(TPP)(OIPh)]_2O$ (II).

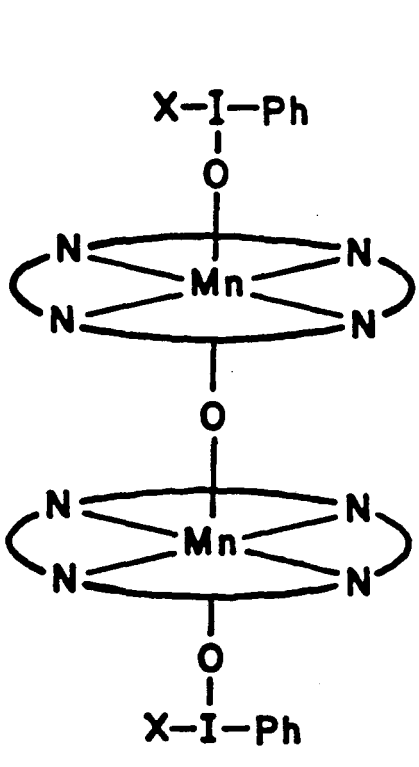

A

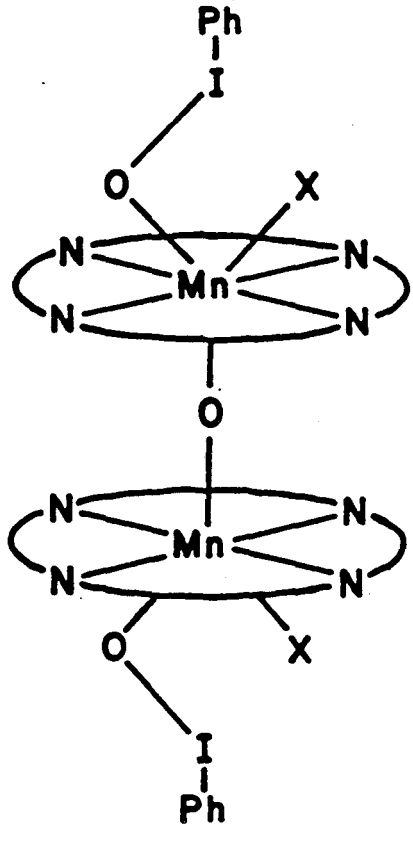

B

X = Cl (I) or Br (II)

considered unlikely on the basis of steric accessibility of the resulting seven-coordinate metal structure. Certainly, the structural assignment from among the possibilities presented in figure 1 would have important implications on this issue.

One of the goals of our studies has been to further the understanding of the role of biological metal centers in oxidative electron transfer reactions and the obvious extensions of this knowledge to systems capable of homogeneous catalysis. Thus we have undertaken a direct structural investigation of complexes I and II by X-ray Absorption Edge (XAES) and Extended X-ray Absorption Fine Structure (EXAFS) techniques. These techniques are ideal for determination of the ligation environment of the metal. In particular, the availability of two homologous structures differing only in the halide constituent provides a definitive structural assignment for the complexes.

II. Materials and Methods

Sample Preparation

Samples of $[ClMn(TPP)(OIPh)]_2O$ (I), $[BrMn(TPP)(OIPh)]_2O$ (II), $Mn(III)(TPP)(N_3)HOCH_3$ (III), $Mn(IV)(TPP)(OCH_3)_2$ (IV) and $[Mn(IV)(TPP)(N_3)]_2O$ (V) were prepared in the laboratory of C.L. Hill by published methods [2,3] and stored at 77°K until use. X-ray absorption samples were prepared by suspension in a powdered teflon matrix at concentrations sufficient to produce an absorbance of 2.3 at a photon energy above the K absorption edge. Samples were held in a Kynar* cell jacketted in a N_2 gas stream at -70° to -90°C for data collection to prevent decomposition. Sample integrity was verified after EXAFS data collection by optical spectroscopy, and less than 5% decomposition was observed for all reported data.

Data Collection and Analysis

X-ray absorption spectra were collected at the Stanford Synchrotron Radiation Laboratory utilizing beam lines IV-3 and II-3. Data were obtained in the absorption mode using nitrogen gas ionization chambers to measure the incident and transmitted intensity. Accurate relative energy registration for edge data was maintained using a double absorption method [5].

After energy calibration, individual scans were coadded and monochromator-induced glitches removed. A low-order (1 or 2) polynomial pre-edge background was removed and the edge height normalized to unity. Reported edge positions

were determined as the major inflection point on the edge. This was obtained from the zero-crossing of the second derivative of a sliding quadratic fit to 1.7 eV width across the data. Preparation of EXAFS data for analysis and fitting methods are described in chapter 2.

III. Results and Discussion

Edge Spectra

The x-ray absorption spectra in the K-edge region for complexes I and II and for three Mn tetraphenylporphyrin complexes of known structure are shown in figure 2. The edge for $Mn(III)(TPP)(N_3)HOCH_3$ shows a splitting of the principal edge peak attributed to 1s-np transitions. Splittings of this transition have been observed in the spectra of complexes having lower than cubic symmetry [6] in which the p-derived states are not degenerate. As expected for high-spin Mn(III) complexes, this one exhibits a large tetragonal distortion. A somewhat different edge structure is observed for the Mn(IV) complexes, which are all very similar. The nearly identical edges of the μ-oxo dimeric $[Mn(IV)(TPP)(N_3)]_2O$ and complexes I and II is evidence for structural isomorphism. All three exhibit a peculiar splitting of 2-2.5 eV in the weak 1s-3d transition below the edge onset. This splitting is either absent or unresolved in the monomeric $Mn(IV)(TPP)(OCH_3)_2$ complex of figure 2.

Two explanations have been provided for similar structures observed in iron and cobalt fluoride complexes [7]. The splitting may arise from transitions to different d multiplet states. The transitions that are expected for Mn^{+4} ($3d^3$) between the 1s and 3d levels are obtained from the atomic levels of the $[Fe^{+4}$ (core)$]3d^4$ configuration which exhibit a change in total spin multiplicity of ±1/2 from the initial state [7]. There are a number of these [8],

Figure 2. Absorption K-edge spectra of manganese tetraphenylporphyrin complexes. I) $[ClMn(TPP)(OIPh)]_2O$, II) $[BrMn(TPP)(OIPh)]_2O$, III) $Mn(III)(TPP)(N_3)HOCH_3$, IV) $Mn(IV)(TPP)(OCH_3)_2$ and V) $[Mn(IV)(TPP)(N_3)]_2O$.

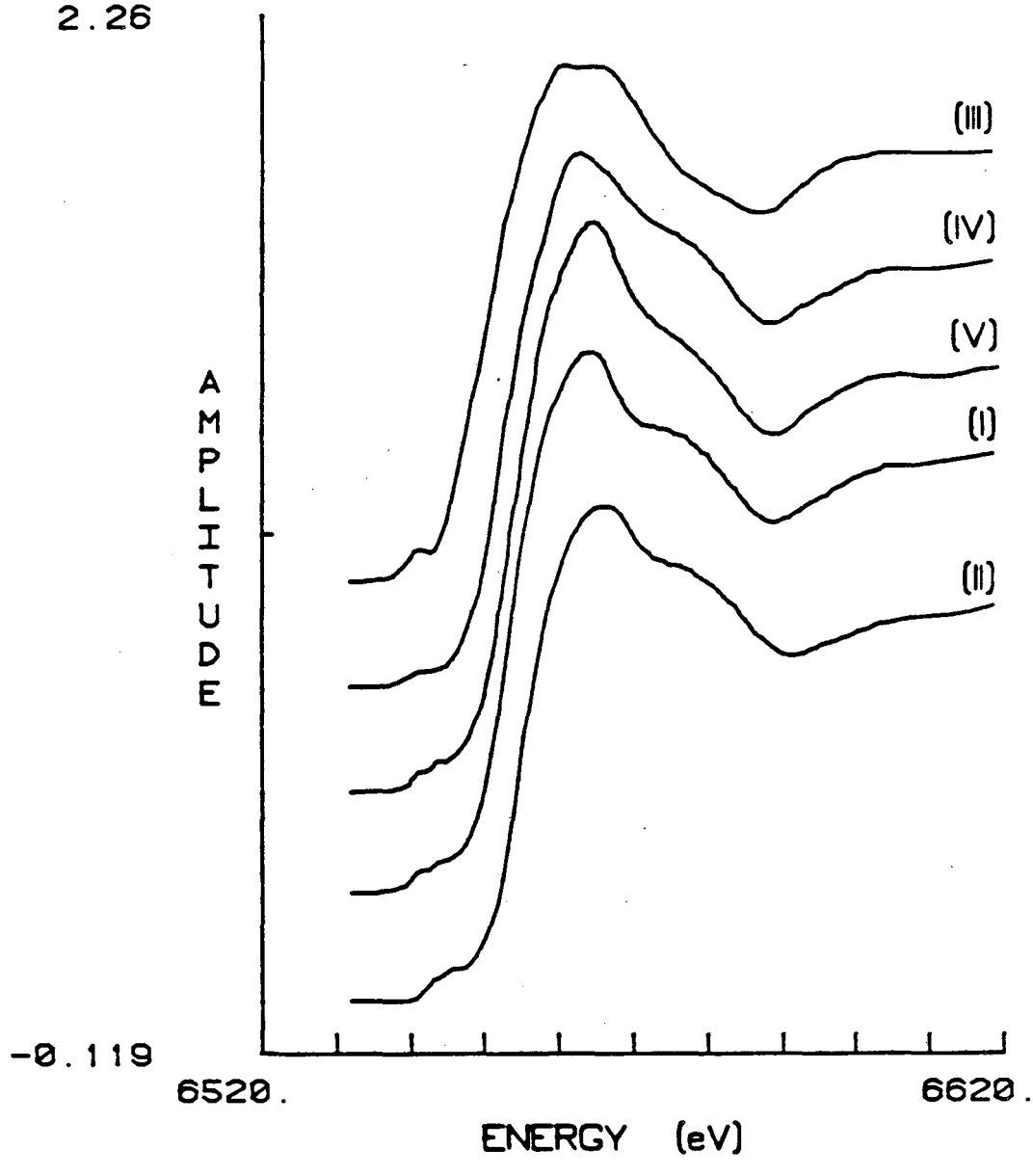
2.26
(III)
(IV)
(V)
(I)
(II)
AMPLITUDE
-0.119
6520.
6620.
ENERGY (eV)

including the ^5D ground state and a series of spin triplet term states at 3.0 to 3.5 eV above the ^5D level. The predicted splitting is therefore somewhat larger than observed in the 1s-3d transition. This treatment is valid, however, only for very ionic complexes where the localized atomic levels provide a good description of the transition final state. This is obviously not the case for these porphyrin complexes which contain significant ligand orbital interaction.

It is also possible that the observed splitting arises from crystal field effects. For such a splitting to occur in a d^3 complex containing empty $d_{x^2-y^2}$ and d_{z^2} orbitals implies a large tetragonal distortion. The absence of such structure in the Mn(III)(TPP) complex is expected because only one spin-allowed transition to the empty d_{z^2} based orbital exists.

The inflection point positions for these edges are presented in Table 1. Errors stated in the positions are standard deviations of independent measurements. Although correlations of edge inflection points have been used for a variety of manganese complexes to obtain oxidation state information, this method cannot be reliably used for cases in which significant delocalization of charge onto the ligands occurs [9]. However, comparison of edges within the porphyrin series is still informative. Table 1 shows that the two well characterized Mn(IV) complexes exhibit edge positions that are significantly different. The higher

Table 1. Edge Inflection Points for Manganese Tetraphenylporphyrin Complexes

Complex	Edge inflection ± sd (eV)	Shift
$Mn(III)TPP(N_3)HOCH_3$	6551.83 ± 0.10	
$[Mn(IV)TPP(N_3)]_2O$	6553.35	1.52
$Mn(IV)TPP(OCH_3)2$	6552.81 ± 0.12	0.98
$[ClMn(IV)TPP(OIPh)]_2O$	6553.75 ± 0.1	1.92
$[BrMn(IV)TPP(OIPh)]_2O$	6553.37 ± 0.1	1.54

energy inflection for the dimeric species is possibly due to the presence of the bridging oxo ligand which is expected to be more electropositive than the methoxy ligands in the monomeric species. The inflection positions of complexes I and II are very similar to the μ-oxo dimeric structure, providing additional support not only for the Mn(IV) oxidation state assignment, but also for the presence of a dimeric structure. There is, in addition, a difference in the inflections between the supposedly isomorphous complexes I and II that is larger than the estimated uncertainty. This observable perturbation of the metal environment by the halide ion is in the correct direction to be explained as a difference in ligand covalency, with Br^- forming a more covalent ligation than Cl^-, and provides evidence that the halide is involved in direct metal coordination.

EXAFS Spectra

EXAFS analysis was performed to determine the direct structural ligation of these complexes. In order to test the accuracy of structural information obtained and to evaluate the transferability of theoretical scattering phase and amplitude functions [10] in the tetraphenylporphyrin system, EXAFS data for the complexes Mn(III)(TPP)(N_3)$HOCH_3$ (III) and Mn(IV)(TPP)$(OCH_3)_2$ (IV) were analyzed. Unfortunately, the instability of the μ-oxo dimeric complex (V) prevented collection of EXAFS data of analyzable quality. As will be seen, the behavior of these structurally characterized [11,12] complexes during analysis can also be

used to aid in the analysis and interpretation of the data for complexes I and II.

Fitting analysis (chapter 2) was used on specific scattering components obtained by fourier filtering EXAFS data after background removal. The normalized absorption edge was converted to photo-electron wave-vector (k) space by choosing E_o = 6562 eV which is near the edge maximum. These data, after background removal and multiplication by k^3, are presented for complexes III and IV in figure 3.

A representative fourier transform power spectrum for complex (III) is shown in figure 4. Fourier isolation of the major scattering component occuring at R_{eff} = 1.6 Å was accomplished by back transformation after application of an isolation window over the region denoted. This region contains contributions of all scattering atoms within the first shell of manganese.

No acceptable fits to a single shell of atomic scatterers were obtained for these data. This reflects the presence of two sets of distances in the complexes: the porphyrin nitrogens and the axial ligands, which are unresolved in the single fourier filtered peak. The best two-shell fits to this fourier transform peak for complexes III and IV are shown in figure 5 and the fit parameters are included in table 2. Although nitrogen scattering functions were used for the first shell and oxygen functions for the second, this specificity is not meaningful, because adjacent elements contribute very similar behavior. Thus,

Figure 3. EXAFS spectra weighted by k^3 after background removal. A) Mn(III)(TPP)(N_3)$HOCH_3$ (complex III) and B) Mn(IV)(TPP)(OCH_3)$_2$ (complex IV).

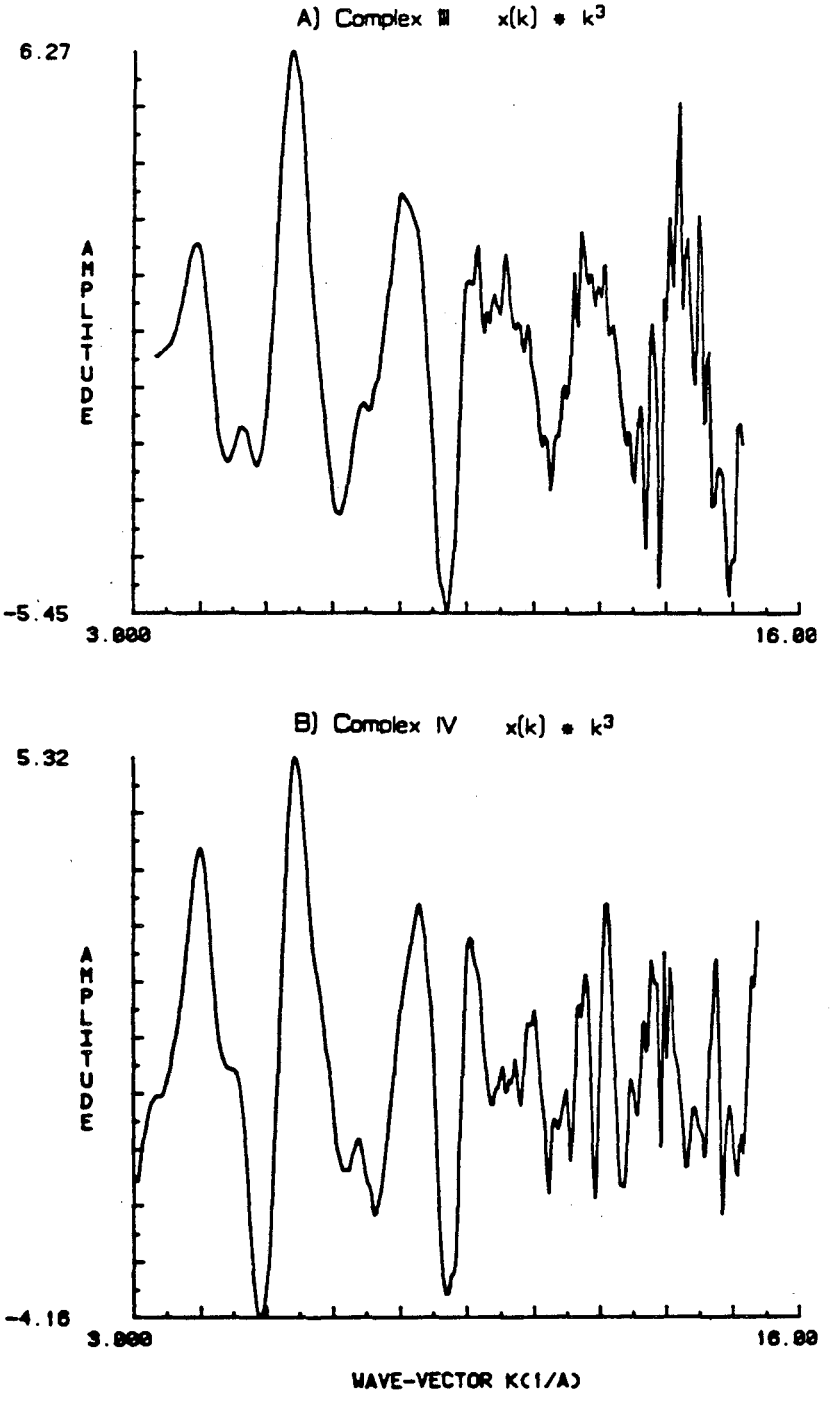
A) Complex III x(k) * k3
6.27
AMPLITUDE
-5.45
3.000
16.00
B) Complex IV x(k) * k3
5.32
AMPLITUDE
-4.16
3.000
16.00
WAVE-VECTOR K(1/A)

Figure 4. Magnitude of the fourier transform of the EXAFS for $Mn(III)(TPP)(N_3)HOCH_3$ (complex III). The k^3 weighted data between k = 2.5 and 15.0 $Å^{-1}$ were used for transformation after application of a Kaiser = 2 apodization window (appendix A). Fourier isolation of the major scattering component was accomplished by applying a Hamming window function to the R-space data between the indicated arrows before back-transformation.

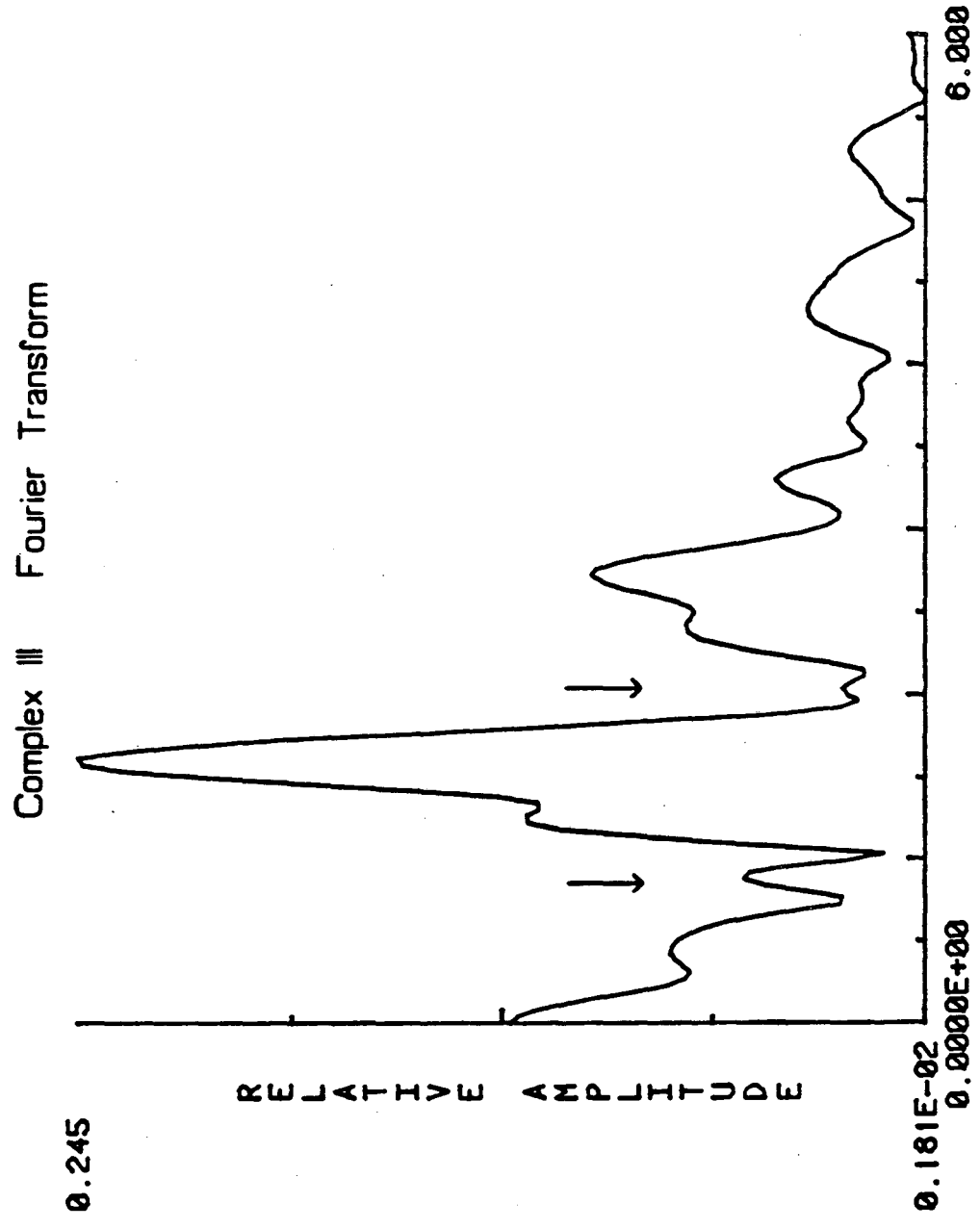
Complex III Fourier Transform
0.245
RELATIVE AMPLITUDE
0.181E-02
0.0000E+00
6.000
DISTANCE (A)

Figure 5. Two-shell fits to the k^3-weighted fourier-filtered components of the first fourier transform peak for A) Mn(III)(TPP)(N_3)$HOCH_3$ and B) Mn(IV)(TPP)(OCH_3)$_2$. Filtered data (solid line) and fitted EXAFS (dotted line) from k = 3.5 to 15. $Å^{-1}$ were used in the fit.

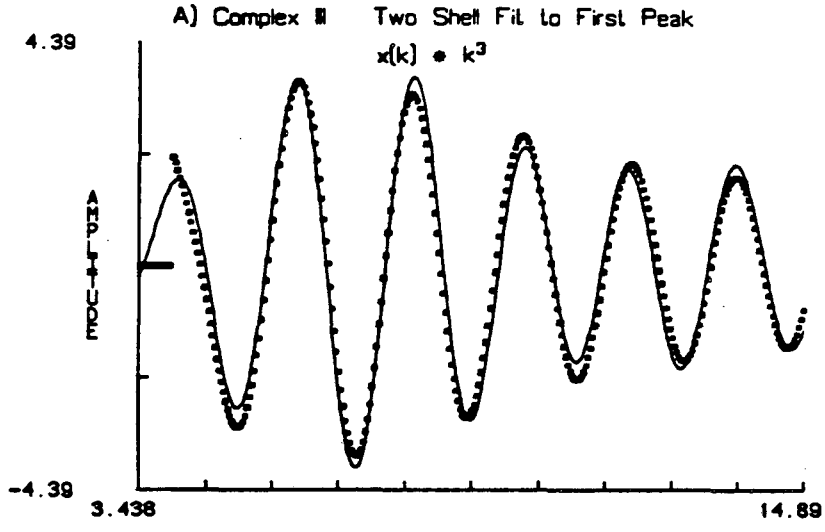

FCN =	38.4219	
R =	2.0039520	2.3596361
N =	1.0047500	0.9233894
SIG=	-0.0034575	-0.0181562
DE0=	0.1352482	-0.9020100
ATOM =	N	O

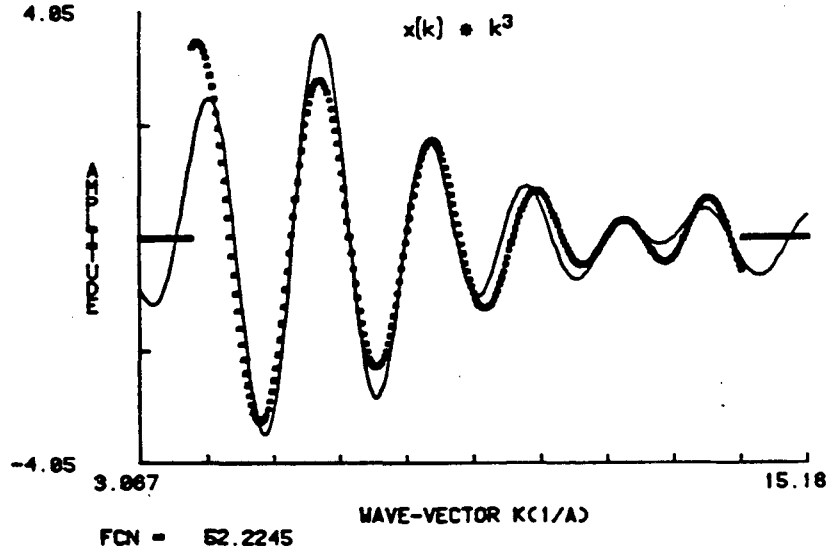

FCN =	52.2245	
R =	2.0168560	1.0888041
N =	1.3775240	0.6856973
SIG=	-0.0010360	-0.0014364
DE0=	-1.9383926	11.0832207
ATOM =	N	O

Table 2. EXAFS and Crystal Structure Parameters for Mn(III)TPP(N_3)$HOCH_3$ (III) and Mn(IV)TPP(OCH_3)$_2$ (IV).

EXAFS Parameters					Crystal structure		
Complex	Atom	N[a]	R (Å)	σ	Atom	N	R (Å)
Complex III	N	3.8	2.004	-.003	N	4	2.031 ± .012[b]
	O	1.8	2.360	-.018	O	1	2.329
					N	1	2.176
Complex IV	N	2.8	2.017	-.001	N	4	2.012 ± .022[b]
	O	1.8	1.889	-.001	O	2	1.839

a) Corrected amplitudes (see text).

b) Standard deviation of average distance for porphyrin distances.

similar quality fits to nearly identical parameters could be achieved with any combination of these elements.

Comparison of the fitted structural parameters to those obtained from crystal structures in table 2 shows that agreement is in general quite good. In all cases the fitted ligand distances fall within 0.05 Å of the crystal structure values. As discussed in chapter 2, the number of atoms obtained from the theoretical amplitude functions is subject to systematic errors. Of a factor of two discrepancy in the observed and theoretical amplitude functions, most has been attributed to many-body effects [13] and the remainder to experimental origin [14]. We have usually observed a reduction in the fitted amplitudes by a factor of about two, but this factor is expected to be somewhat dependent on the data range and on the scatterer atom type [13].

Thus, the number of atoms predicted in table 2 after this correction agree fairly well with the known values. Nevertheless, the number of scatterers determined by EXAFS are subject to experimental errors, and the values observed for these complexes suggest about a 20% uncertainty in their determination.

Complex III presents a particularly interesting example of the limitations of EXAFS analysis for compounds containing very heterogeneous ligand distances. In this case, in addition to 4 porphyrin nitrogen ligands at 2.03 Å, the complex contains an axial methoxy oxygen ligand at 2.33 Å and an azide nitrogen at 2.18 Å. All three of these

ligands contribute to the unresolved major fourier transform peak. However, meaningful three-shell fits to this peak are impossible due to the large number of degrees of freedom in the fit. The fit to two shells shown in table 2 shows that compensation for this extra ligand occurs. Approximately two atoms are obtained in the second shell, and the Debye-Waller term is about an order of magnitude larger than for the first shell. Thus the interpretation for this result is that 2 ligands exist, but with a large disorder in their distance.

The EXAFS spectra for the $[ClMn(IV)(TPP)(OIPh)]_2O$ (I) and $[BrMn(IV)(TPP)(OIPh)]_2O$ (II) complexes, weighted by k^2, are shown in figure 6. In this case the k^2 weighting was a compromise to maintain a roughly constant EXAFS modulation for both complexes. From these spectra it is clear that a significant difference is observed between the two complexes. This immediately indicates that either the two are structurally unrelated, or that the halide substitution is contributing to the observed scattering. Bromine is a much stronger scatterer than chlorine and its scattering amplitude envelope peaks at a higher photo-electron wave-vector (k) value. This difference is reflected in the overall larger EXAFS envelope for the Br complex.

Shown in figures 7 and 8 are fourier transforms for these complexes after weighting the data by k^0, k^1 and k^3. The purpose of examination of these different weightings is inherent in the behavior of the scattering amplitude for

Figure 6. EXAFS spectra weighted by k^2 after background removal for A) $[ClMn(TPP)(OIPh)]_2O$ (complex I) and for B) $[BrMn(TPP)(OIPh)]_2O$ (complex II). Both spectra are plotted using the same scale and k range for comparison.

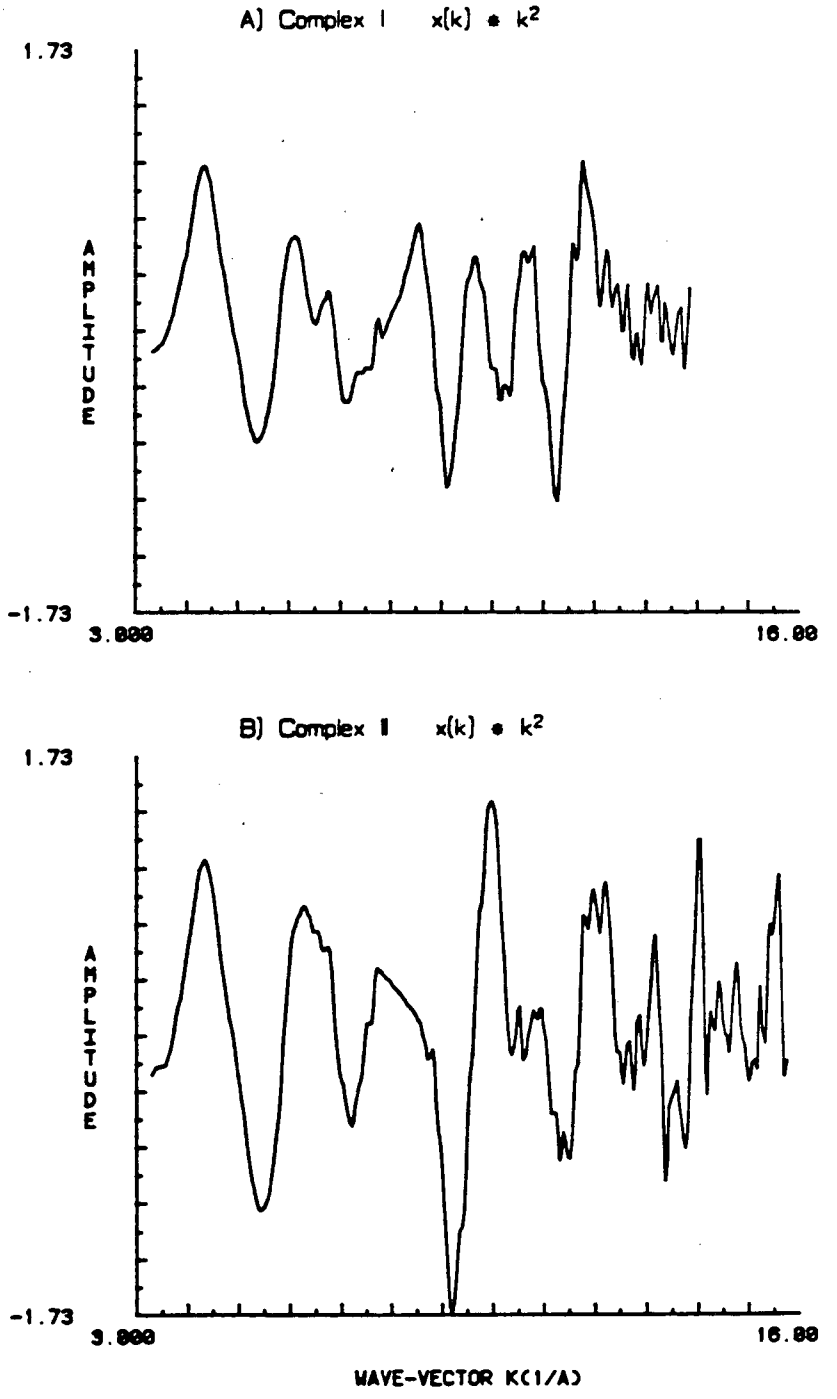
A) Complex I x(k) * k²
1.73
AMPLITUDE
-1.73
3.000
16.00
B) Complex II x(k) * k²
1.73
AMPLITUDE
-1.73
3.000
16.00
WAVE-VECTOR K(1/A)

Figure 7. Fourier transform magnitudes of EXAFS data for $[ClMn(TPP)(OIPh)]_2O$. Shown are transforms for data weighted by k^0, k^1 and k^3. Transformed data extend from k = 2.5 to 15. $Å^{-1}$.

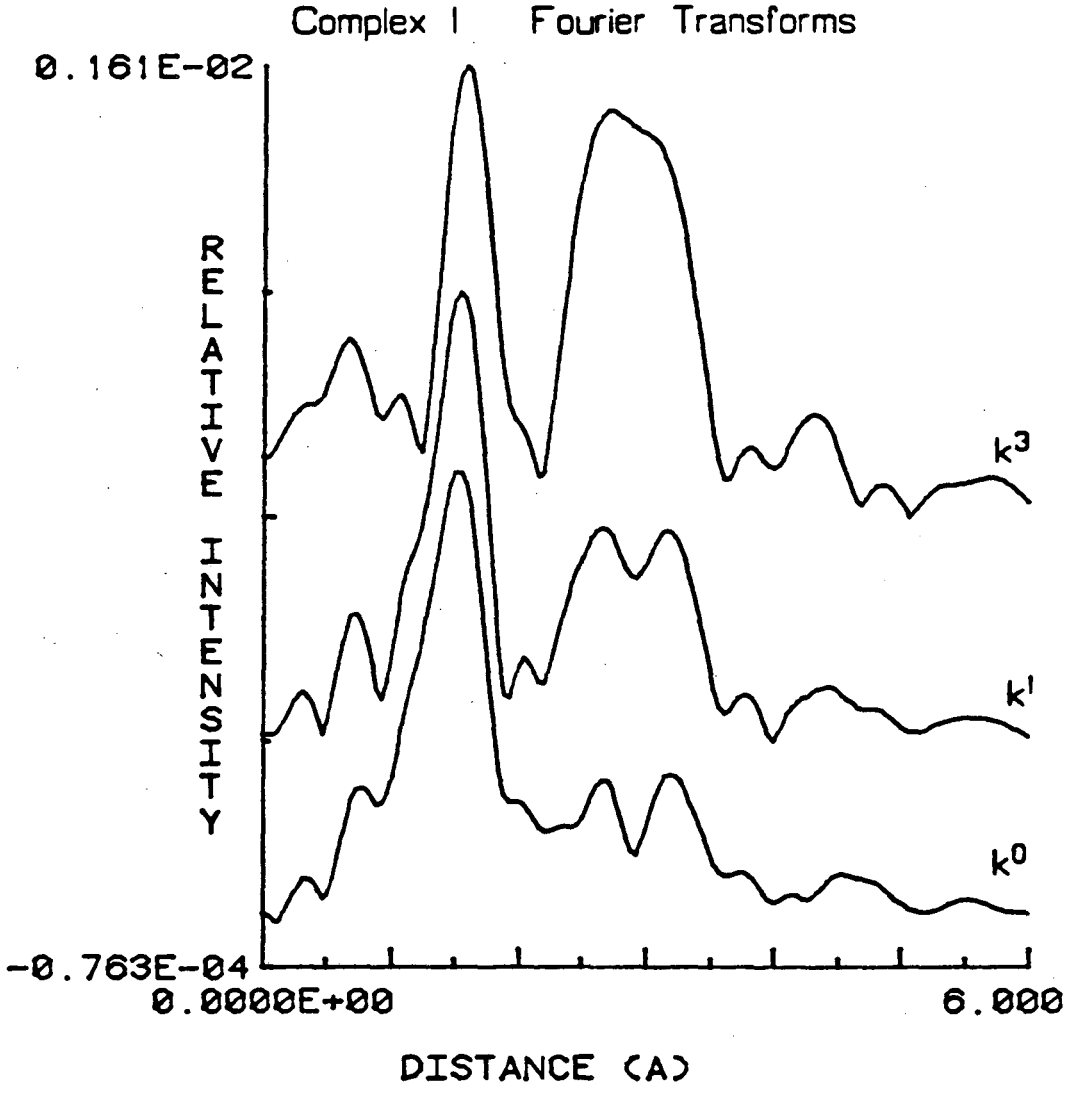
Complex I Fourier Transforms
0.161E-02
RELATIVE INTENSITY
k3
k1
k0
-0.763E-04
0.0000E+00
6.000
DISTANCE (A)

Figure 8. Fourier transform magnitudes of EXAFS data for $[BrMn(TPP)(OIPh)]_2O$. Shown are transforms for data weighted by k^0, k^1 and k^3. Transformed data extend from k = 2.5 to 16. $Å^{-1}$.

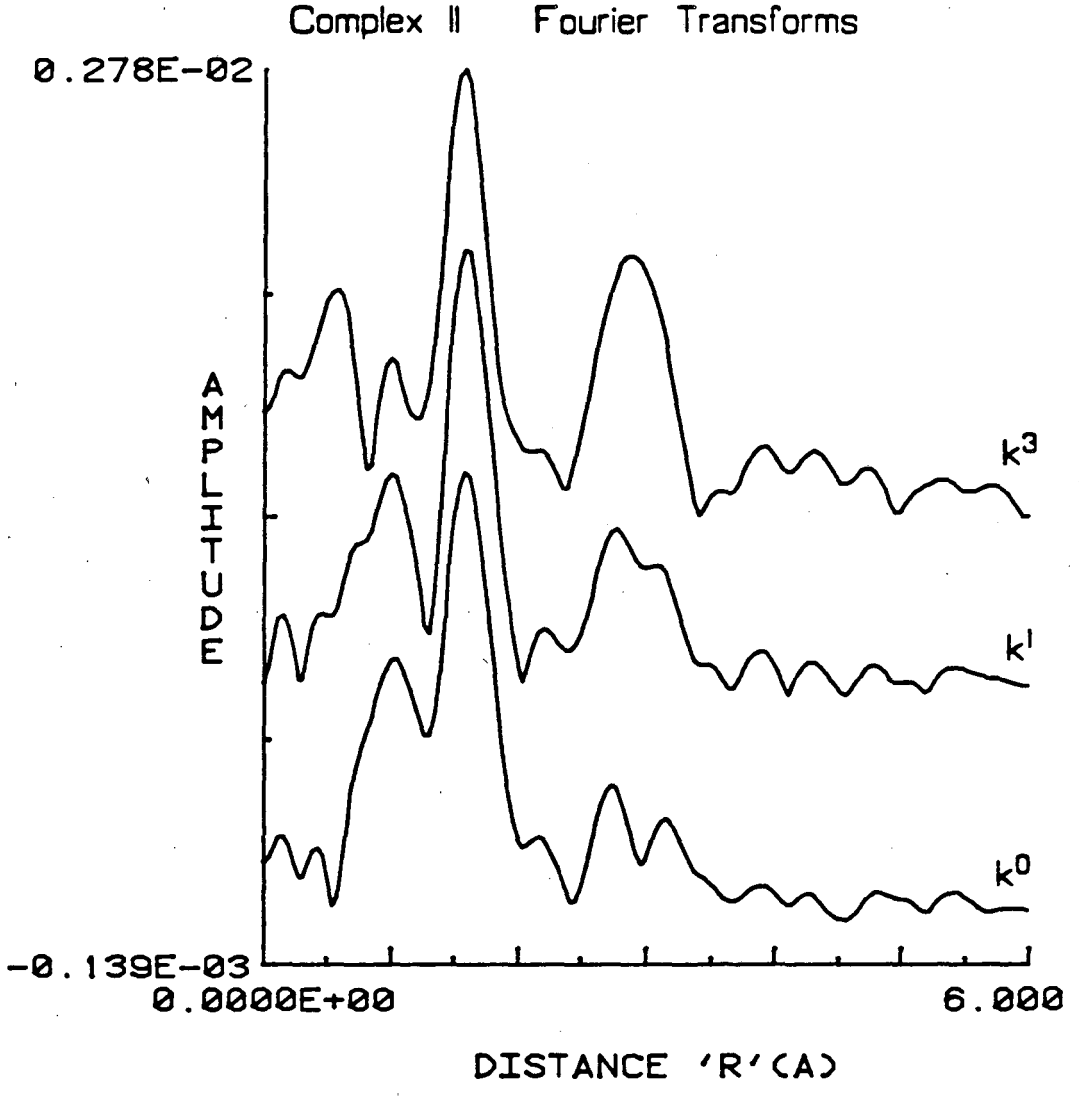
Complex II Fourier Transforms
0.278E-02
-0.139E-03
AMPLITUDE
k3
k1
k0
0.0000E+00
6.000
DISTANCE 'R'(A)

different elements. As indicated above, the amplitude contributed by lighter elements will peak at lower K values than for heavier elements. Thus, if the data are weighted by a larger power of k, the contribution from heavier elements is enhanced. The transforms shown in figures 7 and 8 both show evidence for three scattering contributions at R_{eff} = 1.5, 2.6 and 3.1 Å. Of these, both of the peaks at higher R_{eff} grow dramatically as the k weighting is increased. This indicates the presence of two heavier atoms in the coordination outer-sphere, and is consistent with the proposed structures in figure 1 containing manganese and iodine at these longer distances. This effect is greater for the Cl containing complex, and from this it may be surmised either that the second and third peaks of complex I are heavier than for complex II, or that the first peak of complex I contains an atomic composition that is relatively lighter than for the Br containing complex.

To see this effect more clearly, the fourier-filtered, k^3-weighted components of the first peak for these complexes is presented in figure 9 and for the two higher R peaks weighted by k^1 in figure 10. Although slight differences between the two complexes are observed in the EXAFS contributions from the second and third peaks (figure 10), a large difference in the amplitude envelope is seen in the filtered first peak components (figure 9). This observation firmly establishes the presence of the halide in the inner coordination sphere of the complexes.

Figure 9. Fourier-filtered EXAFS components comprising the first scattering peak for k^3-weighted data of A) $[ClMn(TPP)(OIPh)]_2O$ and B) $[BrMn(TPP)(OIPh)]_2O$. In each case, a fourier transform without applied apodization window was used for isolation before back-transformation.

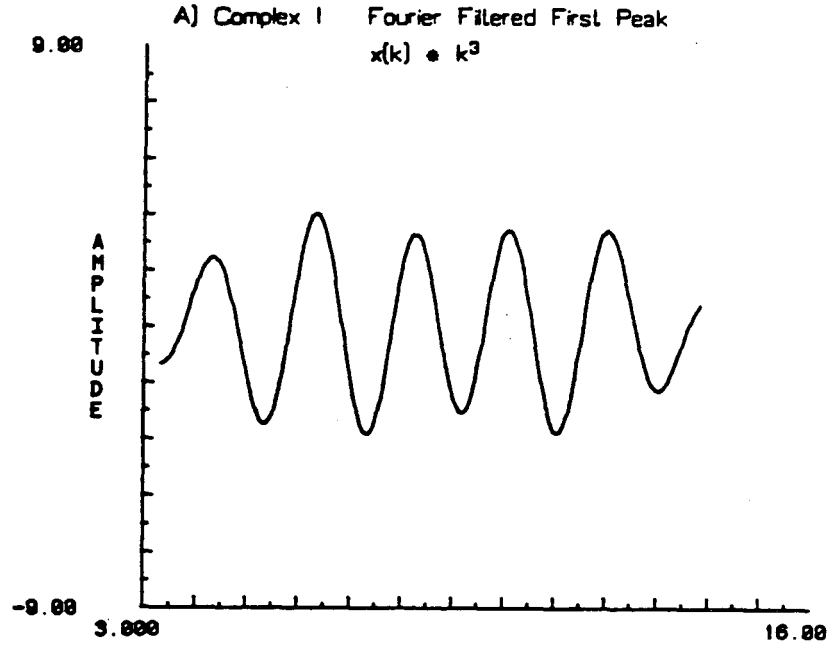
A) Complex I Fourier Filtered First Peak
x(k) * k3
9.00
AMPLITUDE
-9.00
3.000
16.00

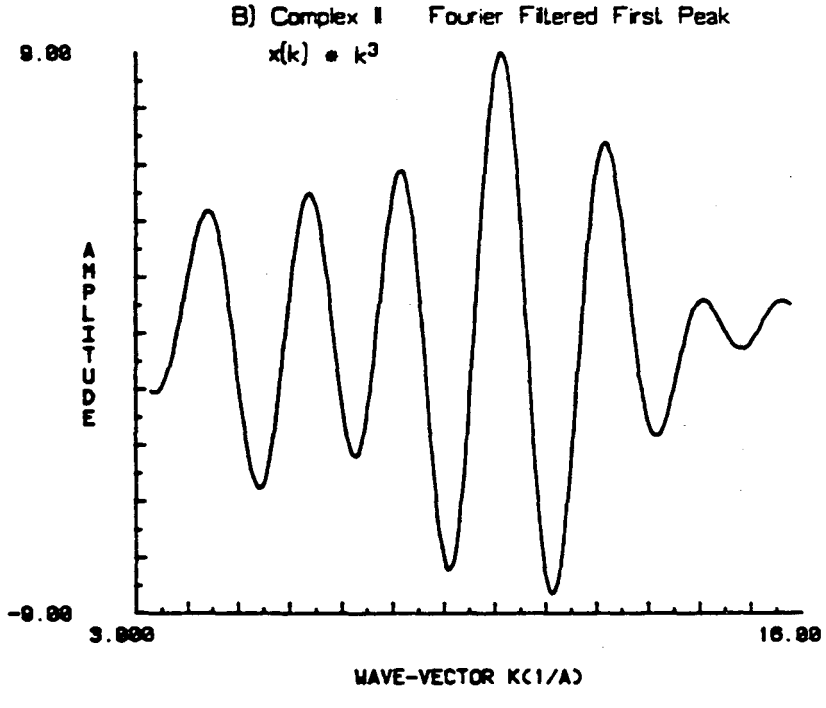
B) Complex II Fourier Filtered First Peak
x(k) * k3
9.00
AMPLITUDE
-9.00
3.000
16.00
WAVE-VECTOR K(1/A)

Figure 10. EXAFS components comprising the scattering peaks between R_{eff} = 2.2 and 3.7 Å for k^1-weighted data of A) $[ClMn(TPP)(OIPh)]_2O$ and B) $[BrMn(TPP)(OIPh)]_2O$.

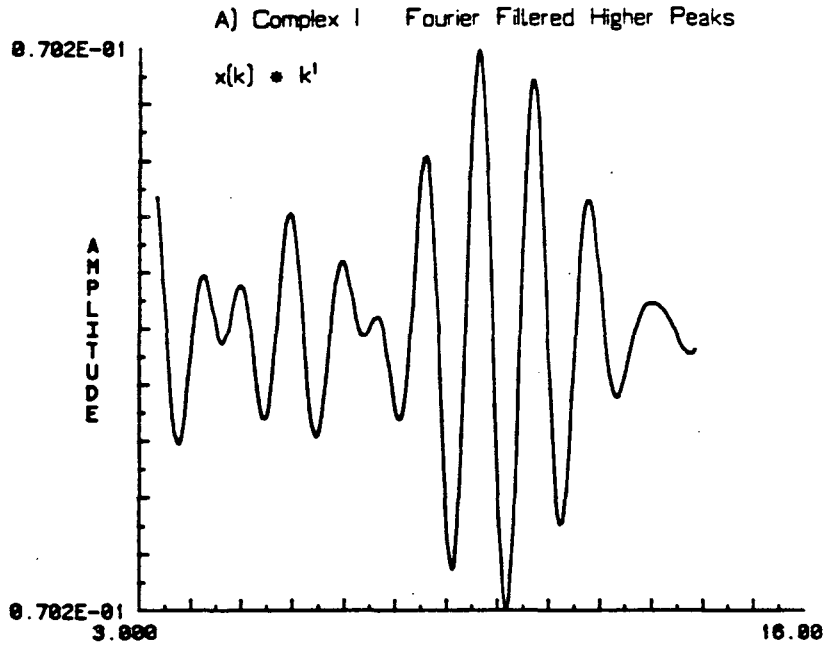
A) Complex I Fourier Filtered Higher Peaks
x(k) * k'
0.702E-01
AMPLITUDE
0.702E-01
3.000
16.00

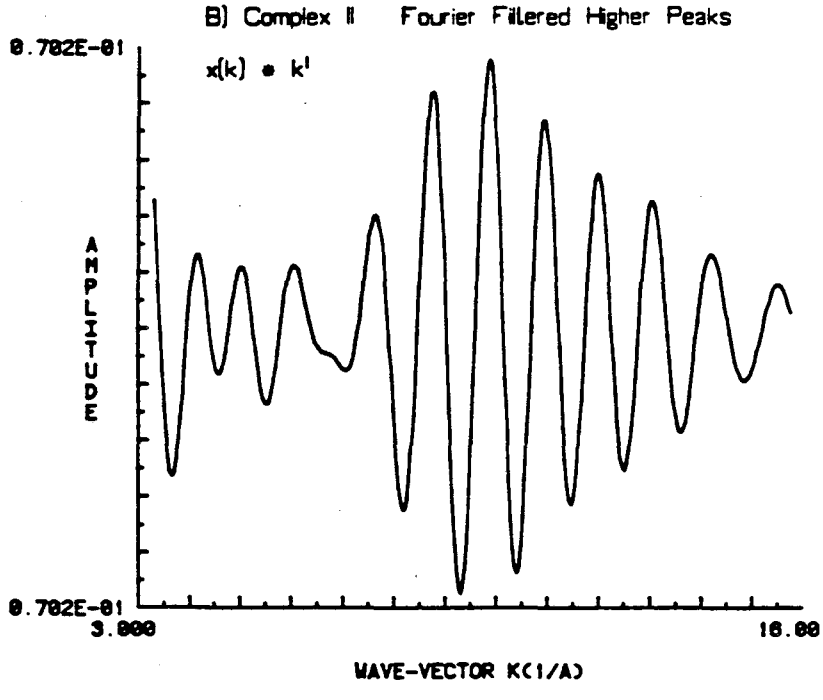
B) Complex II Fourier Filtered Higher Peaks
x(k) * k'
0.702E-01
AMPLITUDE
0.702E-01
3.000
16.00
WAVE-VECTOR K(1/A)

The above indications that structure B shown in figure 1 is correct make EXAFS fitting analysis particularly difficult. This is because this structure contains a first coordination sphere that is very heterogeneous in nature. It contains 4 unique sets of ligands at similar distances, and it is unreasonable to attempt to fit to this number of shells. There is little resolution of these components in the first fourier transform peak, because the data do not continue through enough oscillations for a beat to be observed.

The EXAFS analysis of the $Mn(IV)(TPP)(OCH_3)_2$ complex discussed earlier can be used to aid in the analysis of complexes I and II. Shown in figure 11 are two fits to the filtered first peak for complex I. In these fits, the first shell parameters, corresponding to the porphyrin nitrogens have been fixed to the values obtained in the best fit to the same shell of complex IV. The parameters for a second shell of ligands was then minimized. Even with this strategy, it was not possible to obtain meaningful minima by fitting to more than one of these additional shells. Thus a single additional shell is expected to reflect the contribution from the dominant scattering ligands other than the porphyrin nitrogens. If proposed structure B of figure 1 is correct, this will be the halide atom, and if structure A is correct, this will be the two oxygen atoms. From figure 11 it is seen that both of these possibilities give acceptable quality fits to the data for complex I. However,

Figure 11. Fits to two scattering shells of the k^3-weighted fourier-filtered components of the first transform peak of $[ClMn(TPP)(OIPh)]_2O$. The fitting range extends from k = 3.5 to 14. $Å^{-1}$. The solid line is filtered data and the dotted line the fitted EXAFS function.

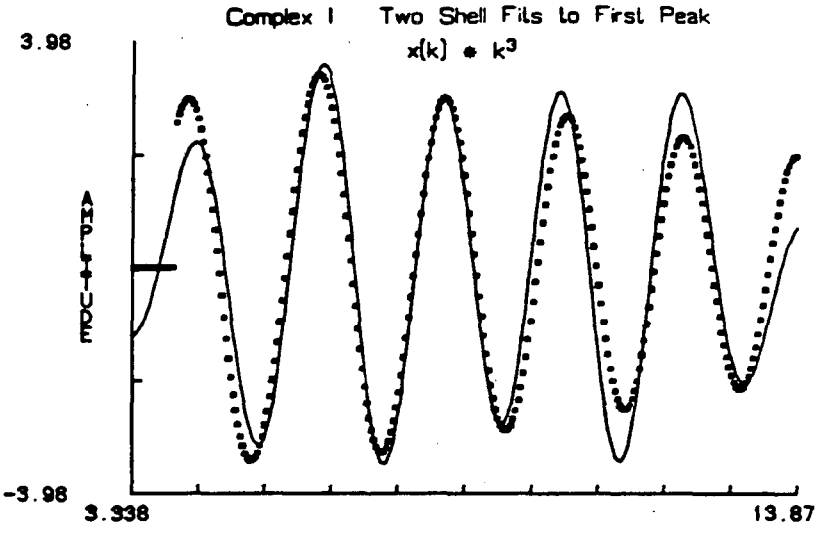

FCN =	109.721	
R =	2.0168560	1.9541247
N =	1.3775240	0.7734481
SIG=	-0.0010360	0.0000000
DE0=	-1.9383926	20.0000000
ATOM =	N	O

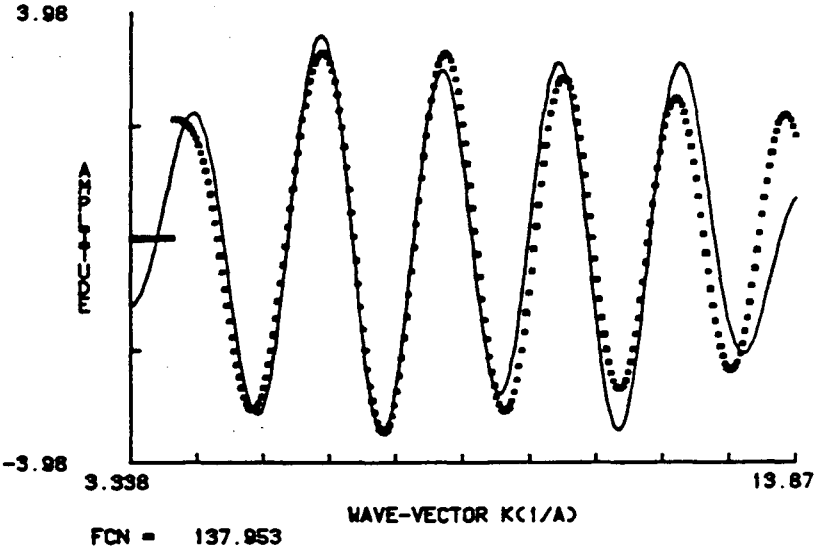

FCN =	137.953	
R =	2.0168560	2.0487583
N =	1.3775240	0.8266227
SIG=	-0.0010360	-0.0090485
DE0=	-1.9383926	-4.6717091
ATOM =	N	CL

the values of the Debye-Waller parameter and the variable E_o parameter obtained for the oxygen trial fit exceed physically acceptable limits and thus make the fit to Cl preferred. In this case, approximately 1.6 Cl atoms are indicated at a distance of 2.05 Å from manganese.

In a similar manner, fits to the first peak of the Br-containing complex II are presented in figure 12. In this case, the fit quality using bromine as the second scattering shell is considerably better than for oxygen. In addition, the same unacceptable behavior of the parameters for the oxygen shell occurs, making the bromine-containing fit preferred. For this case, 1.2 Br atoms are predicted at 1.90 Å from manganese.

Fits to the fourier-filtered second and third peaks for complexes I and II were performed. The quality of fits to two atomic shells, using manganese and iodine scattering functions were not exceptional. This is due to the 8 second-shell porphyrin carbon atoms that are also contributing to these components. In this case it was possible to obtain well behaved minima using three scattering shells by adding one shell at a time to the fit, starting with the most dominant scatterer. These fits for complexes I and II are presented in figure 13. It is seen from data that the large number of oscillations at this higher frequency and the appearance of multiple beats provides the information content that allows three-shell fitting.

Figure 12. Fits to two scattering shells of the k^3-weighted fourier-filtered first peak of $[BrMn(TPP)(OIPh)]_2O$. The fitting range was the same as for figure 11.

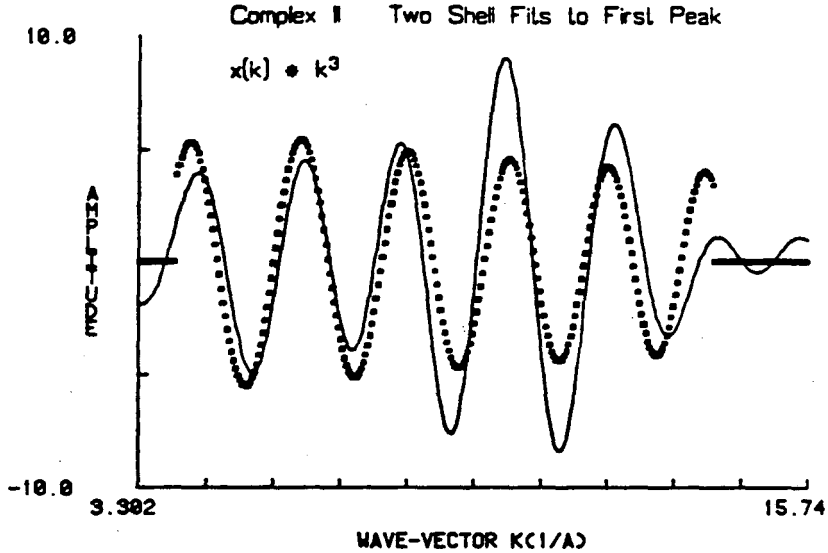

FCN =	1467.41	
R =	2.0168560	1.9817860
N =	1.3775240	1.3338152
SIG=	-0.0010360	0.0000000
DE0=	-1.9383926	20.0000000
ATOM =	N	O

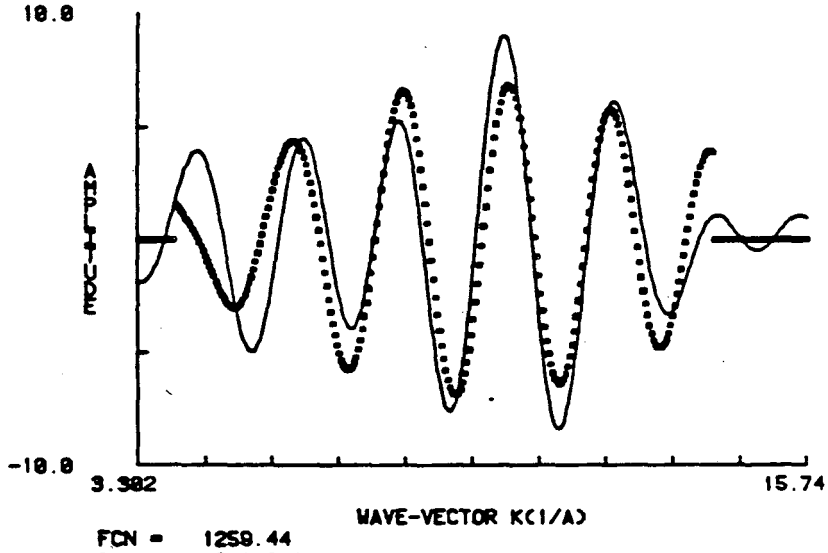

FCN =	1259.44	
R =	2.0168560	1.9836323
N =	1.3775240	0.6053158
SIG=	-0.0010360	-0.0056718
DE0=	-1.9383926	-1.1266441
ATOM =	N	BR

Figure 13. Three shell fits to the k^1-weighted fourier-filtered components from R_{eff} = 2.2 to 3.7 Å for complexes A) $[ClMn(TPP)(OIPh)]_2O$ and B) $[BrMn(TPP)(OIPh)]_2O$. The fitting range was from 3.5 to 14. $Å^{-1}$ in both spectra.

Three Shell Fits to Higher Fourier Peaks

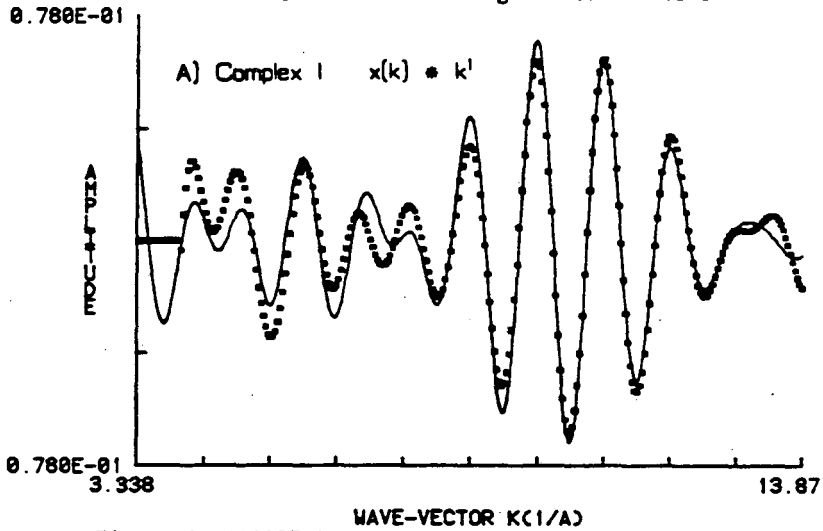

FCN =	0.122602E-01		
R =	2.8516550	3.6433799	3.4210291
N =	0.9273483	1.1461312	4.4733610
SIG=	-0.0065236	-0.0056147	-0.0023425
DE0=	-3.7589207	-6.1003656	2.3876572
ATOM =	I	MN	C

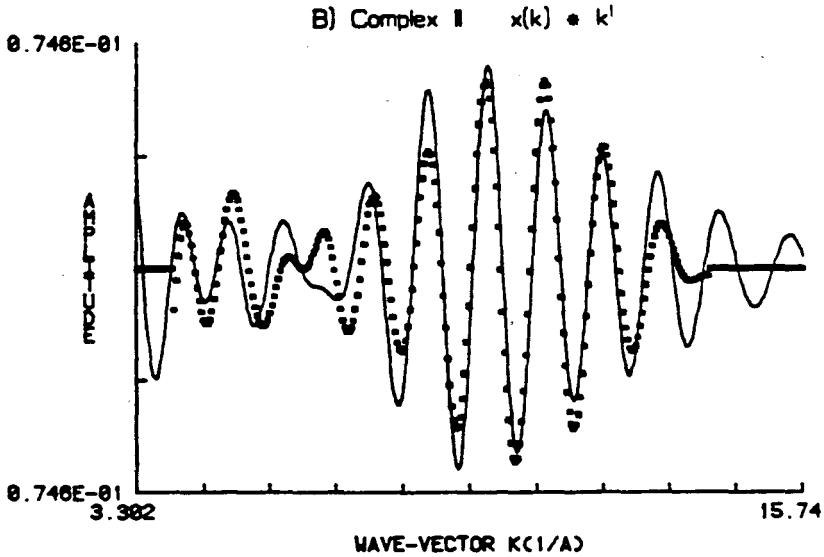

FCN =	0.484118E-01		
R =	2.8256950	3.5975909	3.3384550
N =	1.8257620	0.8317973	4.4695091
SIG=	-0.0078121	-0.0068523	-0.0003254
DE0=	1.6266315	-5.0946054	2.1402378
ATOM =	I	MN	C

IV. Conclusions

The predicted structural parameters for all shells are presented in table 3 and the relevant distances included in the assigned structure of figure 14. This structure contains a Mn-O-Mn distance of 3.60-3.64 Å which is similar to, but approximately 0.1 Å longer than observed in the crystal structure of the similar $[Mn(IV)(TPP)(N_3)]_2O$ [3]. In the latter structure, the manganese atoms were observed to lie approximately 0.1 Å out of the porphyrin plane toward the bridging oxygen. In the case of complexes I and II, the unusual ligation on the anterior axial face of the porphyrin may force an in-plane metal coordination, with the resulting longer Mn-O-Mn distance.

The number of atoms predicted for the manganese and iodine shells is somewhat larger than expected. Although this may be artifactual, in that it may result from chemical effects on the amplitude transferablity, it could also be the result of a well characterized anomalous enhancement due to the focusing of photo-electrons by intervening atoms [15]. This is expected for manganese in which the linear bridging oxo ligand is directly in line with the two manganese atoms. This cannot be the case for iodine, however. The observed Mn-I distance is 2.83-2.85 Å which requires a bent Mn-O-I structure. Assuming reasonable Mn-O and O-I distances of ≈1.85-1.95 and 1.9-2.0 Å respectively, the observed Mn-I distance gives an Mn-O-I angle of ≈95°.

This μ-oxo bridged, seven-coordinate, bifacially ligated

Table 3. EXAFS Parameters for $[ClMn(IV)TPP(OIPh)]_2O$ (I) and $[BrMn(IV)TPP(OIPh)]_2O$ (II).

	Atom Type	# atoms[a]	Distance (Å)	σ	ΔE_o (eV)
Complex I	N[b]	-	-	-	-
	Cl	1.6	2.05	-.009	-4.7
	I	1.8	2.85	-.007	-3.8
	Mn	2.2	3.64	-.006	-6.1.
	C	8.9	3.42	-.002	2.4
Complex II	N[b]	-	-	-	-
	Br	1.2	1.90	-.006	-1.1
	I	2.0	2.83	-.008	1.8
	Mn	1.6	3.60	-.007	-5.1
	C	8.9	3.34	-.0003	2.1

a) Amplitudes corrected (see text).

b) Porphyrin nitrogen shell parameters fixed to values determined for complex IV.

Figure 14. Assigned structures for $[ClMn(TPP)(OIPh)]_2O$ (complex I) and $[BrMn(TPP)(OIPh)]_2O$ (complex II).

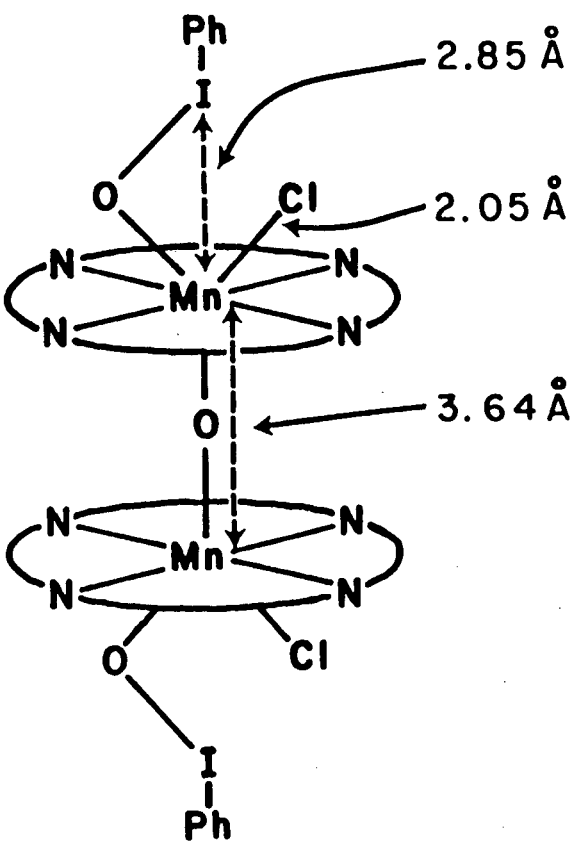
Ph
I
2.85 Å
O
Cl
2.05 Å
N
N
Mn
N
N
O
3.64 Å
N
N
Mn
N
N
O
Cl
I
Ph

(I)

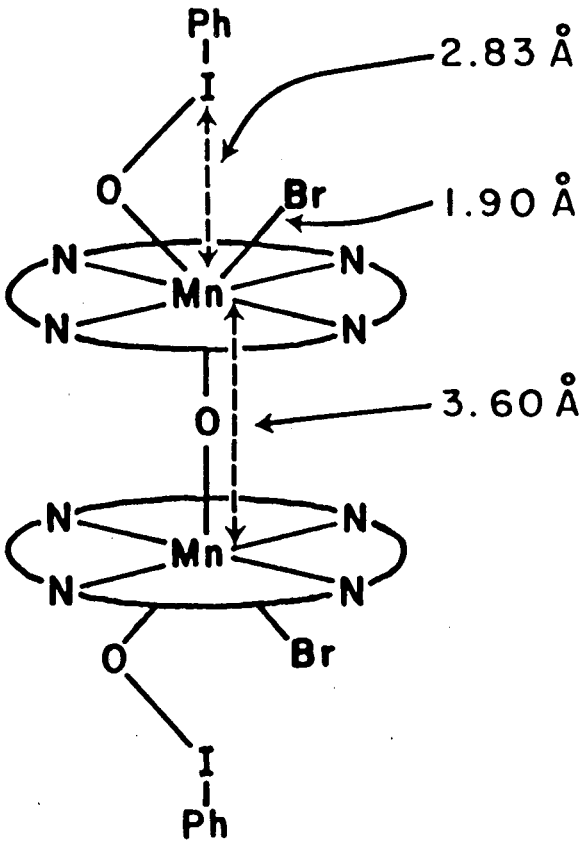
Ph
I
2.83 Å
O
Br
1.90 Å
N
N
Mn
N
N
O
3.60 Å
N
N
Mn
N
N
O
Br
I
Ph

(II)

complex is, in the least, a uniquely interesting model for oxidative catalysis, and its structural characterization will provide an important framework for the detailed elucidation of the mechanism of its important properties.

REFERENCES

1. Groves, J.T. (1980) Metal Ion Activation of Dioxygen, (Spiro, T.G. ed.) Chapter 3.

2. Smegal, J.A., Schardt, B.C. and Hill, C.L. (1983) J. Amer. Chem. Soc. 105, 3510-3515.

3. Schardt, B.C., Hollander, F.J. and Hill, C.L. (1982) J. Amer. Chem. Soc. 104, 3964-3972.

4. Smegal, J.A. and Hill, C.L. (1983) J. Amer. Chem. Soc. 105, 3515-3521.

5. Goodin, D.B., Falk, K.-E., Wydrzynski, T. and Klein, M.P. (1979) 6th Annual Stanford Synchrotron Radiation Laboratory Users Group Meeting, 10-11.

6. Blumberg, W.E., Peisach, J., Eisenberger, P. and Fee, J.A. (1978) Biochem. 17(10), 1842-1846.

7. Shulman, R.G., Yafet, Y., Eisenberger, P. and Blumberg, W.E. (1976) Proc. Natl. Acad. Sci. 73(5), 1384-1388.

8. Moore, C.E. (1952) Atomic Energy Levels, Nat. Bur. Stand. Cir. 467, vol. II.

9. Kirby, J.A., Goodin, D.B., Wydrzynski, T., Robertson, A.S. and Klein, M.P. (1981) J. Amer. Chem. Soc. 103, 5537-5542.

10. Teo, B.-K. and Lee, P.A. (1979) J. Amer. Chem. Soc. 101, 2815-2832.

11. Camenzind, M.J., Hollander, F.J. and Hill, C.L., J. Amer. Chem. Soc., submitted.

12. Day, V.W., Stolts, B.R., Tasset, E.L., Day, R.O. and Marianelli, R.S. (1974) J. Amer. Chem. Soc. 96, 2650-2652.

13. Rehr, J.J., Stern, E.A., Martin, R.L. and Davidson, E.R. (1978) Phys. Rev. B 17(2), 560-565.

14. Stern, E.A., Heald, S.M. and Bunker, B. (1979) Phys. Rev. lett. 42(20), 1372-1375.

15. Teo, B.-K. (1981) J. Amer. Chem. Soc. 103, 3990-4001.

CHAPTER 4

Studies of the Metal Site Structure of Manganese Superoxide Dismutase by X-ray Absorption Spectroscopy

I. INTRODUCTION

Superoxide dismutases are metallo-enzymes which catalyze the dismutation of the superoxide radical to H_2O_2 and O_2 (equation 1). Superoxide is produced in low levels as a side product of oxidative catabolism and aerobic respiration, and its cytotoxicity has been proposed as the driving force behind the evolution of the dismutases [1]. This has not been conclusively demonstrated, however, and it has also been proposed that they have some other unknown primary function [2].

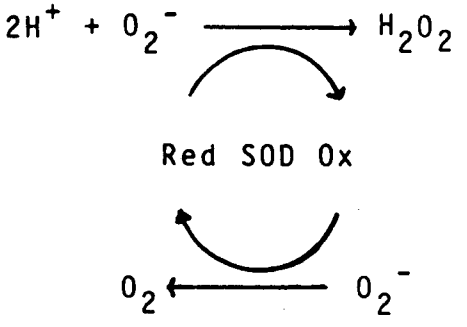

(5)

Superoxide dismutases exist in nearly all organisms capable of aerobic respiration and are even observed in a few

photosynthetic obligate anaerobes [3].

Three structurally distinct types of superoxide dismutase have been found. The more thoroughly studied form is dimeric, contains one atom of copper and zinc per subunit, and is found predominantly in the cytoplasm and between the outer and inner mitochondrial membranes of eukaryotic cells. It is believed that the enzyme functions by alternating between two redox states, and x-ray absorption edge studies have shown that only copper is involved in this redox cycle [4]. This copper is coordinated by 4 histidine ligands in a slightly distorted square planar geometry [5], and evidence exists for water coordination at an axial position accessible by an external protein crevice [6].

The other two forms of the enzyme contain either manganese or iron, and appear to be closely related. The iron form is found in prokaryotic organisms as a dimer of ≈20 Kd subunits containing one atom of iron per subunit. The manganese enzyme is also found in a few prokaryotes where it exhibits similar subunit structure, but is most commonly found in the mitochondrial matrix and associated with chloroplast thylakoid membranes of eukaryotic organisms, where it is isolated in tetrameric form [7].

Although the Cu/Zn enzymes bear very little resemblance to the manganese or iron forms on the basis of amino acid sequence or inhibitor sensitivity, the manganese and iron enzymes have very similar properties indicating a close

evolutionary relationship to each other. The manganese and iron forms are insensitive to cyanide, a potent inhibitor of the Cu/Zn SOD [8]. The superoxide dismutases containing manganese or iron have similar amino acid compositions and a high degree of sequence homology, but little similarity in this regard is observed between any of these enzymes and those of the Cu/Zn family [9]. Roughly 67% homology in the N-terminal sequences of 15 manganese and iron superoxide dismutases is observed, including at least 5 complete conservations within the first 50 residues. It has been noted that this sequence similarity is so strong that it is not possible to distinguish between the manganese and iron forms on the basis of regional or overall amino acid sequence or composition [3].

Despite these similarities, the incorporation of metal ions into most Mn or Fe enzymes appears to be element specific. As mentioned above, there is a definite preference for a given organism to produce one or the other of the enzyme types. E. coli contains both Fe and Mn SOD, but the amino acid sequences are slightly different, and only the manganese enzyme is inducible by increasing the oxygen tension [10]. In addition, many metal replacement studies [11-15] have indicated a requirement of a given enzyme for the metal it originally contained. In each case the substitution was accomplished by unfolding the peptide followed by renaturation in the presence of the appropriate metal. Chromatographic and spectral properties of the

native enzymes were recovered and metal ions were observed to bind in roughly stoichiometric amounts [14,15] indicating a return to native conformation. However, reconstitution of manganese SOD from B. stearothermophilus with Mn^{+2}, Fe^{+2}, Co^{+2}, Ni^{+2} and Cu^{+2} resulted in a manganese enzyme that was completely active. No activity was detected for any of the other metals [11,13,14]. Exactly the converse was observed in studies of the Fe enzyme from P. ovalis reconstituted with Fe^{+2}, Mn^{+2}, Cd^{+2} and Cr^{+2} [12,15], indicating a definite functional preference for iron. Therefore, whatever the structural or functional difference between the Mn and Fe forms of SOD, it is very likely that it is due to a very specific and subtle interaction between the metal and its ligation site.

Relatively few structural or mechanistic details about manganese and iron superoxide dismutases are known. Effects on the water proton spin relaxation rates have indicated the presence of 2 protons in the inner coordination sphere of native Mn SOD and 1 in the iron protein [16], consistent with a proposed direct water and hydroxyl coordination respectively. This is supported by the recently observed pH dependence of midpoint potential [17], inhibitor association, and kinetics [18] for iron SOD. On the basis of the temperature dependence of the magnetic susceptibility [19] the native state of Mn SOD appears to contain Mn^{+3}, which can be reduced by dithionite to Mn^{+2}. This evidence is supported by the concurrent bleaching of a weak absorption

band at 480 nm and the appearance of a complex EPR signal at g=6 upon reduction.

We have undertaken an x-ray absorption edge and EXAFS study of manganese SOD isolated from prokaryotic and eukaryotic sources. We have examined the oxidation state of Mn in resting native and reduced states, in order to establish the degree of localization of charge on the metal and thus the extent to which the center can be considered a functional part of the catalytic mechanism. Results of a simulation of the low temperature EPR signal in reduced SOD are also presented giving support to oxidation state assignments and information about the symmetry of the zero-field splitting tensor. Analysis of EXAFS data was performed that suggests a set of ligand groupings and distances. These methods are applied to manganese protein from E. coli, T. thermophilus, and S. cerevisia and for T. thermophilus SOD in which manganese is replaced with iron at the active site. In this way it was possible to examine directly the similarities and differences in site structure between SOD from distantly related organisms. The data are consistent with a structural model in which the functional specificity of the manganese enzyme for manganese over other metals can be explained on the basis of local ligand environment.

II. MATERIALS AND METHODS

Spectroscopic Measurements

X-ray absorption spectra were collected at the Stanford Synchrotron Radiation Laboratory, Stanford, CA. Data in the edge region were obtained on wiggler beam line IV-2 during parasitic operation (2.1 GeV electron energy, 50 ma stored electron current) and beam line VII-3 during dedicated operation (3.0 GeV, 80 ma). EXAFS data were obtained on the focused beam line II-3 during dedicated operation (3.0 GeV, 60-80 ma). Monochromatic x-rays were produced using a Si<111> double crystal monochromator. All data were collected by measurement of the K-α x-ray fluorescence excitation function [20]. Single photon counting was employed using a segmented multi-wire proportional chamber [21] or an array of plastic scintillation detectors [22] fitted with an x-ray filter/Soller slit assembly [23]. Critical energy registration was maintained for each scan by simultaneous measurement of the pre-edge transition of $KMnO_4$ [24]. Protein samples were frozen into lucite backed sample cells held in a jacketted stream of liquid nitrogen boil-off maintained at -75° to -110° C during data collection.

Analysis of edge and EXAFS data was done according to methods described in chapter 2.

EPR spectra were collected at 10°-15° K on a Varian E-9 or E-4 spectrometer equipped with an Air Products liquid helium flow cryostat. Instrumental conditions are described with the figures. Simulation of EPR powder spectra were

done using the methods and programs described in chapter 6.

Protein metal analysis was performed by atomic absorption on aqueous samples of protein digested in HNO_3

Protein Samples

SOD activity was obtained by measurement of the cyanide-insensitive ability of the enzyme to inhibit the auto-oxidation of pyrogallol at pH 8.2 [25]. This was monitored by the absorbance at 420 nm for a solution containing 0.2 mM pyrogallol, 50 mM Tris-HCl (pH 8.2), 1 mM EDTA and 1 mM KCN in the presence and absence of protein. One unit of activity was defined as an amount of enzyme necessary to decrease the maximal auto-oxidation rate of 1 ml by 50%.

Samples of manganese SOD from E. coli and T. thermophilus were prepared in the laboratory of J.A. Fee by established methods [26].

Purification of SOD from S. cerevisiae was accomplished by a method similar to that used by Ditlow and Johansen [27]. Dried bakers yeast (1 Kg) was suspended in 4 l H_2O for 2 hrs at 37°C followed by centrifugation at 4000xg for 5 min. The pellet was resuspended in 500 ml 50 mM Tris (pH 7.4) and the cells ruptured in a Gaulin type homogenizer 4 times at 450 $Kg(cm)^{-1}$ with cooling to <30°C. After centrifugation at 8000xg for 20 min the milky supernatant was rapidly (≈2 min) heated to 70°C by immersion in a steam jet. This temperature was maintained for 2 min before cooling to 40°C with crushed ice. Centrifugation at 4500xg for 45 min afforded ≈3 l of an opalescent yellow-brown

supernatant which was dialyzed against 3 changes of 15 l of 10 mM Tris (pH 7.9) (hereafter called T10/7.9) for 16 hrs until pH equilibrium was attained. This was applied onto a 6x15 cm Celex D column equilibrated with T10/7.9, washed with 500 ml buffer and eluted with a 0-200 mM NaCl gradient. Active fractions were pooled, dialyzed against T10/7.9 and concentrated to ≈150 ml by ultrafiltration over an Amicon PM10 membrane. Dilution/reconcentration was continued until the NaCl concentration was less than 50 mM (measured by conductance). This material was loaded onto a 2x35 cm DEAE Biogel A 100-200 mesh anion exchange column and washed with T10/7.9. Active fractions from a 0-200 mM NaCl gradient were pooled and dialyzed in T10/7.9 for 15 hrs, lyophilized and redissolved in ≈40 ml T10/7.9. This material was loaded onto a 2.5x20 cm cellulose CM cation exchange column equilibrated with H_2O and eluted with 100 mM Tris (pH 7.4). A light pink band containing approximately 250,000 units (≈30 mg protein) was collected and concentrated to ≈0.5 ml. This material showed a single major band by polyacrylamide gel electrophoresis and a characteristic weak absorption maximum at 477 nm.

Metal Substitution

Removal and replacement of manganese in SOD from T. thermophilus with manganese or iron was accomplished by a modification of a proceedure for B. stearothermophilus SOD by Brock et al. [13], and is outlined in figure 1. A solution of approximately 10 mg of T. thermophilus Mn SOD in

Figure 1. A shematic diagram of the proceedure used for metal substitution in manganese SOD from T. thermophilus.

T. THERMOPHILUS METAL SUBSTITUTION

DIALYZE –

8 M UREA pH 3.7

↓

8 M UREA, 50 mM TRIS pH 7.6
+ Mn^{+2} or Fe^{+2} (10 mM)

↓

50 mM TRIS pH 7.6, 20% GLYCEROL
+ Mn^{+2} or Fe^{+2} (1mM)

↓

50 mM TRIS pH 7.6, 20 – 0% GLYCEROL

↓

50 mM TRIS pH 7.6, 10 mM EDTA, 48 hrs.

↓

50 mM TRIS pH 7.6, 24 hrs.

REPLACEMENT	RELATIVE ACTIVITY	METAL CONTENT
Mn	14100 units/umole (100%)	0.74 Mn/subunit
Fe	< 360 units/umole (<3%)	0/53 Fe/subunit

2 ml was denatured by dialysis against ≈100 ml of 8 M urea, (pH 3.7) (acetic acid) for 8 hrs at 4°C. During this time the characteristic purple color was lost. Dialysis buffer was changed to 8 M urea, 50 mM Tris/HCl (pH 7.5) (hereafter called T50/7.5) for 12 hrs. The protein solution was split into 2 bags and dialyzed against 100 ml 8 M urea (pH 3.7, acetic acid) and 10 mM $MnCl_2$ (sample 1) or $FeCl_2$ (sample 2) for 4 hrs. No color was evident at this stage. This was followed by dialysis for 4 hrs against 100 ml 8 M urea, T100/7.6 and 10 mM $MnCl_2$ or $FeCl_2$. Dialysis was continued in T100/7.6 and 20% glycerol (necessary to prevent protein precipitation) and 1 mM $MnCl_2$ (or $FeCl_2$) for 12 hrs. During this period, the Fe^{+2} dialysis solution turned green and the Mn^{+2} solution became pink. Dialysis of the protein was continued against 2 changes of T100/7.6, 15% glycerol and 10 mM EDTA for 3.5 hrs. Samples were loaded into fresh dialysis bags at this point and the glycerol concentration carefully lowered from 15% to 0% in T25/7.6 in a series of four 2 hr dialysis steps. Final dialysis was done against many changes of T25/7.6, 10 mM EDTA for 48 hrs and then for 24 hrs in the absence of EDTA. The resulting yellow-brown iron and red-purple manganese reconstituted samples were contentrated over an Amicon YM10 ultrafiltration membrane for EXAFS, metal analysis, and activity measurements.

III. RESULTS

Radiation effects

The production of hydrated electrons by high intensity x-rays and their effects on biological samples is of valid concern [28]. In general, x-ray absorption spectra should be collected at low temperature to immobilize solvated radicals from diffusion, and successful data collection can usually be obtained in this manner. However, careful monitoring of samples for radiation damage is important. We have observed no effect of irradiation for protein solutions in 10 mM phosphate or Tris buffers at -75°C or below, conditions under which edge data were collected. No change in protein activity, color, EPR spectra or edge spectra as a function of time were noted.

For the native form of T. thermophilus Mn SOD, EXAFS spectra were attempted in 50% glycerol solutions at -75°C. The glycerol glass was used to avoid background fluctuations in the EXAFS region caused by diffraction from micro-crystals in the sample. Under these conditions, however, bleaching of protein color was observed. EPR spectra after irradiation showed evidence of Mn^{+2} release from the protein by the appearance of the characteristic $Mn^{+2}(H_2O)_6$ signal. These effects were also easily observed as time dependent changes in the EXAFS spectra (figure 2). None of these changes was observed for the reduced SOD from T. thermophilus under these conditions.

Data could be successfully collected on the native

Figure 2. Time dependent changes in the EXAFS spectra of native manganese SOD from T. thermophilus in a 50% glycerol glass at -75°C. Shown are data averaged over different times during data collection ; a) the first third of the data set; b) the second third; and c) the last third.

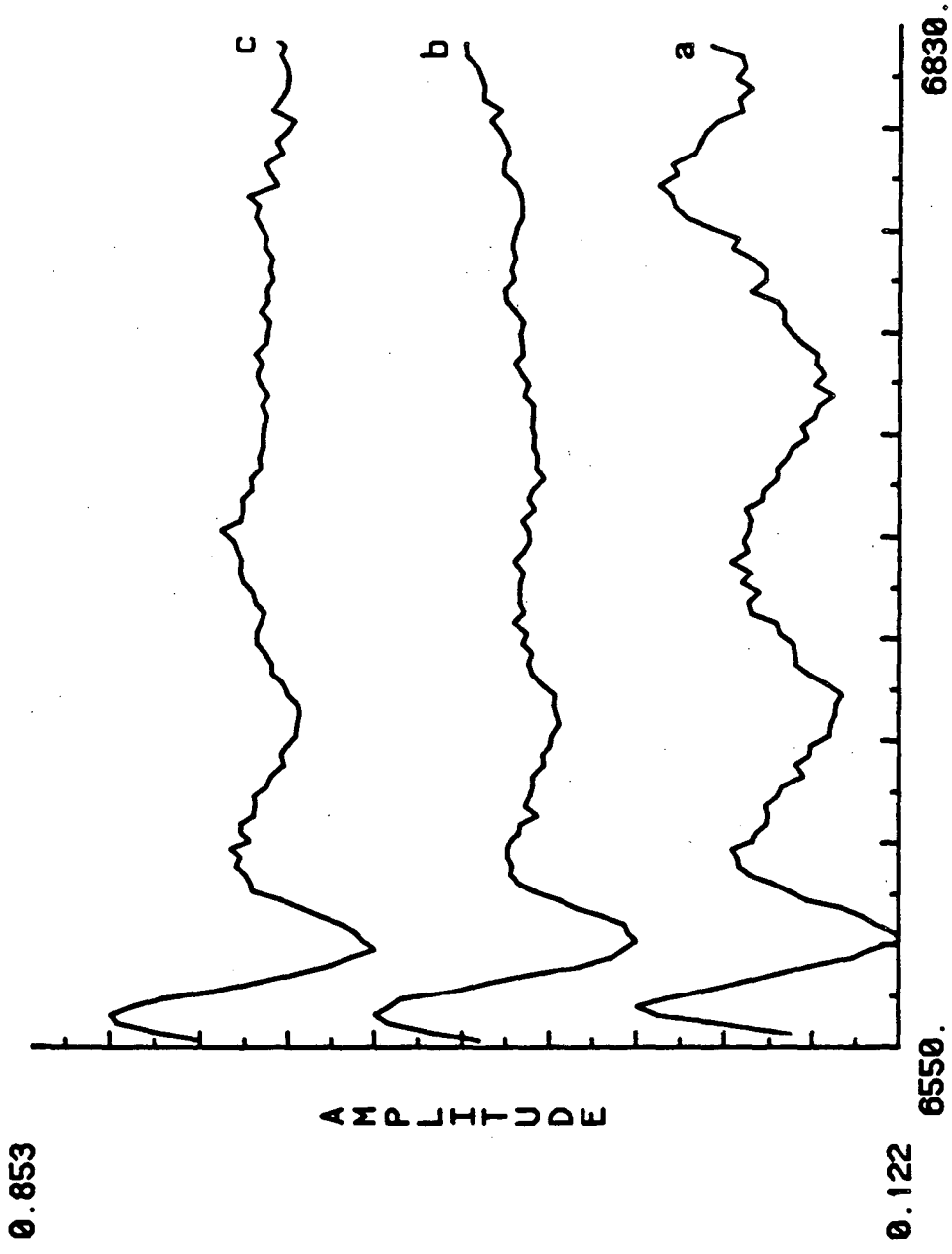
c
b
a
0.853
0.122
AMPLITUDE
6550.
6830.
ENERGY E(EV)

enzyme without any observed effects for samples prepared from an NH_4SO_4 precipitated protein slurry in the absence of glycerol.

All forms of the yeast Mn SOD were free from observed irradiation effects even though collected in 50% glycerol glass solutions. This may in part be due to careful maintenence of sample temperatures at -90°C or below.

Edge Spectra

Fluorescence detected K-edge spectra for native and reduced E. Coli Mn SOD are presented in figure 3. The major difference between them is the marked shift in position of the reduced sample to lower energy. The difference in inflection point energies shown in table 1 is 1.47 eV. From previous correlations of Mn edge inflection points with coordination charge [29], this would be the average shift expected for a 0.7 electron reduction. The absolute positions observed are consistent with Mn^{+3} and Mn^{+2} for native and reduced SOD, respectively. Aside from a slightly steeper slope observed for the edge rise of the reduced sample, the overall shapes of the two edges are very similar. This is considered to be evidence for the absence of a significant change of ligand symmetry upon reduction. A noteworthy feature exhibited by both spectra of figure 3 is the small pre-edge transition occuring at about 9 eV below the major inflection. Transitions in this region, assigned to final states derived from metal 3d orbitals, are normally forbidden, but can become weakly allowed for complexes with

Figure 3. X-ray absorption K-edge spectra of manganese SOD from E. coli. On the same scale are plotted the native enzyme (solid line) and a dithionite reduced sample (dotted line).

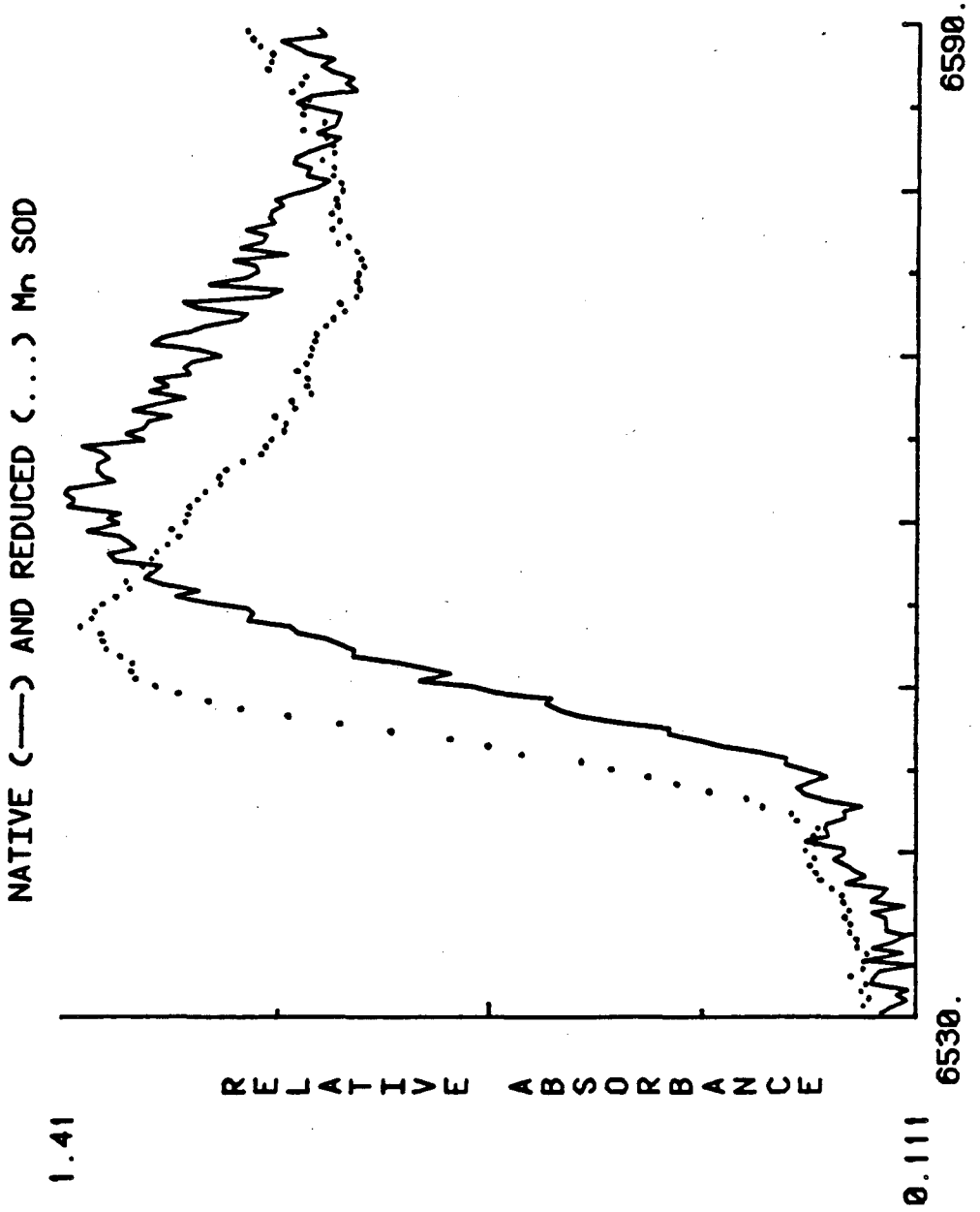
NATIVE (——) AND REDUCED (. . .) Mn SOD
RELATIVE ABSORBANCE
1.41
0.111
6530.
6590.
ENERGY E(eV)

Table I.
SOD EDGE INFLECTIONS

E. Coli

NATIVE	6548.35 eV	Δ = 1.47
REDUCED	6546.88 eV	

S. Cerevisiae

NATIVE	6548.92 eV	Δ = 0.
20 mM AZIDE	6548.04 eV	Δ = 0.88
3 mM H_2O_2	6547.65 eV	Δ = 1.27

unfilled 3d sublevels and ligand configurations which lack inversion symmetry [30]. The lowered symmetry causes breakdown of the dipole selection rules by allowing significant 3d-4p vibronic mixing.

Edge data for yeast Mn SOD of somewhat higher quality are shown in figure 4. Also shown are spectra for samples in the presence of 3 mM H_2O_2 and 20 mM NaN_3. Addition of H_2O_2 to the protein resulted in immediate bleaching of its color as is observed upon reduction. It has been demonstrated that H_2O_2 at these concentrations inactivates only the Fe SOD, leaving the Mn enzyme fully active [31]. Azide also induced loss of protein color, and is known to be a weak inhibitor of Mn SOD with a 50% loss of activity observed at this concentration [31]. As was the case for native and reduced prokaryotic enzyme, no major change of principal edge features is observed for these treatments other than a shift of inflection point (table 1). The shift of 1.27 eV for the H_2O_2 treated sample is comparable with that observed for reduction of E. coli enzyme, while N_3^- induced a somewhat smaller shift. In addition, the '1s-3d' transition, which is present in native and peroxide treated enzyme, is absent for the azide sample, suggesting a direct interaction of N_3^- with the metal center that may result in a change in coordination symmetry. The inflection position of the native yeast SOD edge is 0.57 eV higher than that for the prokaryotic enzyme which, if significant, may indicate a slightly more covalent coordination by the prokaryotic form.

Figure 4. Normalized K-edge spectra for manganese SOD from S. cerevisiae. Shown are a) the edge for native enzyme; b) native enzyme in the presence of 3 mM H_2O_2; and for c) in the presence of 20 mM NaN_3. Protein concentrations were approximately 1.5 mM.

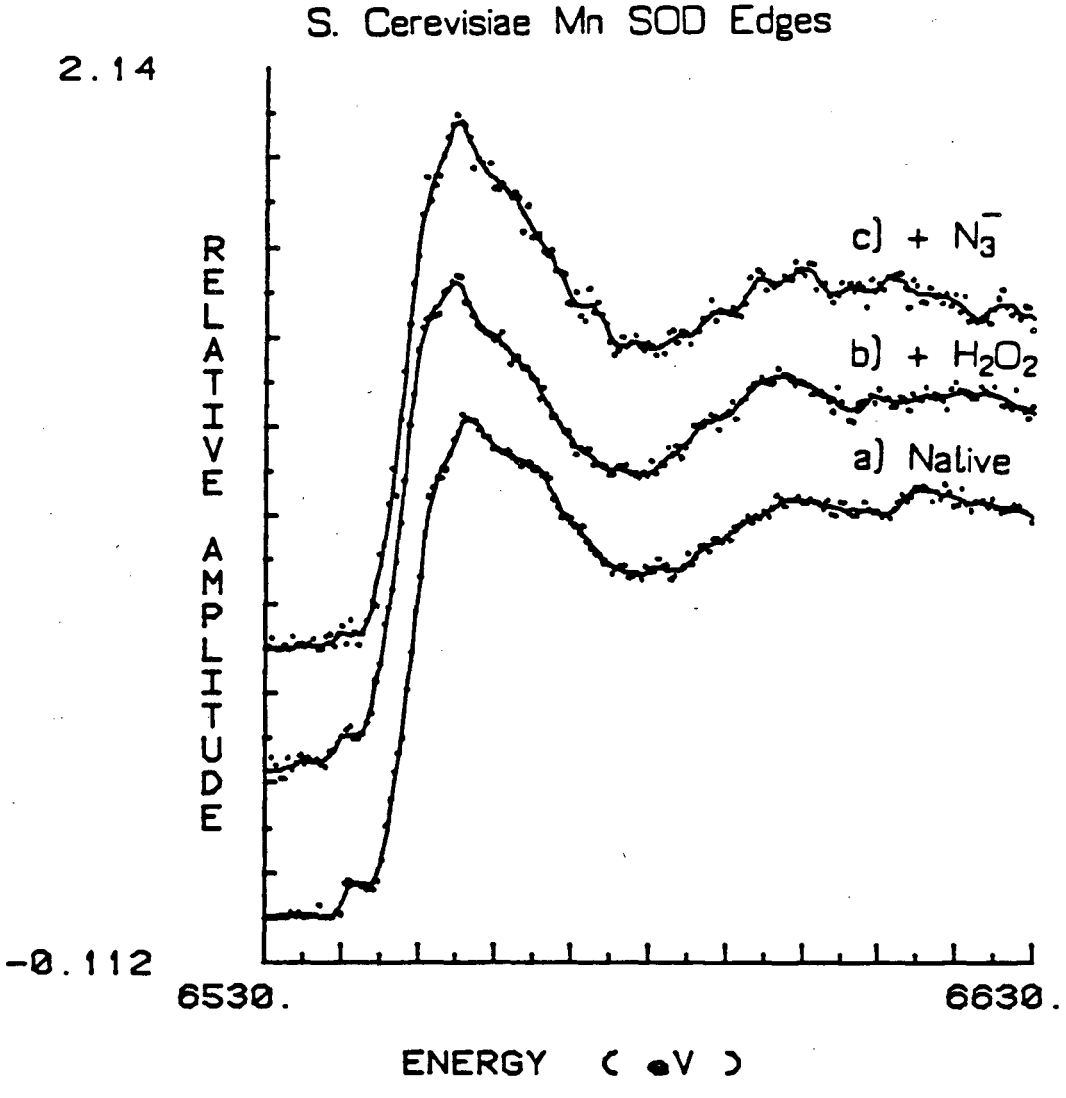
S. Cerevisiae Mn SOD Edges
2.14
-0.112
RELATIVE AMPLITUDE
c) + N_3^-
b) + H_2O_2
a) Native
6530.
6630.
ENERGY (eV)

Additional resolution of features for the yeast data are observed as a result of the improved statistics. The principal absorption maximum is flanked on either side by features that appear as shoulders. Similar appearance of edge spectra has been attributed to a three-fold splitting of the 4p states [4]. Such a splitting is absent for purely octahedral and tetrahedral geometries and is maximal for square planar complexes. If this assignment is correct for the SOD spectra, it would indicate that the absence of inversion symmetry implied above is not due to a purely tetrahedral site.

EPR simulation of Reduced SOD

The reduced Mn SOD exhibits an EPR spectrum at low temperature centered around g=6 [19]. This is consistent with the +2 oxidation state assignment for this form. A more quantitative description of this signal is provided by computer simulation. The method used was that described in appendix B. It involves diagonalization of the hamiltonian matrix at a number of magnetic field values for each of many angles with respect to the applied field. Transition probabilities were calculated at each interpolated resonance field and used to generate the spectral intensity. The hamiltonian used is

$$H = \beta_e H \cdot g_e \cdot S + \beta_n H \cdot g_n \cdot I + S \cdot A \cdot I + D(S_z^2 - 1/3S(S+1)) + E(S_x^2 - S_y^2) \quad (6)$$

which includes electron and nuclear Zeeman terms, the nuclear

hyperfine term and the spin-orbit dipolar interaction which describes the anisotropic zero-field splitting. As shown in figure 5 the observed spectrum can be adequately described using an $S = 5/2$ (high spin Mn^{+2}) spin manifold, an isotropic hyperfine interaction of $-.0075\ cm^{-1}$, and an axial zero-field splitting tensor with $E/D = 0.027$. The quality of the simulation is very sensitive to this ratio, as is demonstrated by changing E/D from 0.027 to 0.034 in figure 5.

EXAFS spectra

More specific and detailed information about metal coordination was provided by fitting analysis of the EXAFS region of the absorption edge. EXAFS spectra were prepared for fitting by fourier isolation of particular scattering components. Figure 6 shows a representative example for reduced T. thermophilus SOD of the fourier transform magnitude and applied isolation filter.

Least squares fits to fourier-filtered data were performed using methods described in chapter 2. Values for E_o were chosen during analysis at or near the principal edge peak, and were 6560. eV for Mn SOD samples and 7140. eV for the Fe data.

1. Native SOD from T. thermophilus

As mentioned earlier, successful data collection was possible for the native prokaryotic enzyme only in a precipitated protein slurry. However, data for the reduced enzyme, which was stable in both solution and precipitated

Figure 5. Simulation of EPR spectra observed for the reduced Mn SOD from T. thermophilus. In a) is shown the observed EPR signal at 10°K, 10 mW microwave power at 9.18 GHz and using a 100 KHz field modulation of 4 G. In b) and c) are simulations obtained using methods described in the text. The parameters employed in the simulation include an isotropic g value of 2.0023 and an isotropic nuclear hyperfine interaction of -0.0075 cm^{-1}. For each of approximately 2200 angles randomly chosen over 1/8 of the sphere, the hamiltonian was diagonalized at 10 field values between 400 and 2000 Gauss. The transition probabilities obtained for the observed resonances were convoluted with gaussians of linewidths r_x = 25 G, and $r_y = r_z$ = 45 G during spectral averaging. For b) D = 1.0 cm^{-1} and E = 0.027 cm^{-1} and for c) D = 1. cm^{-1} and E = 0.034 cm^{-1}.

Reduced Mn SOD EPR Spectrum and Simulation

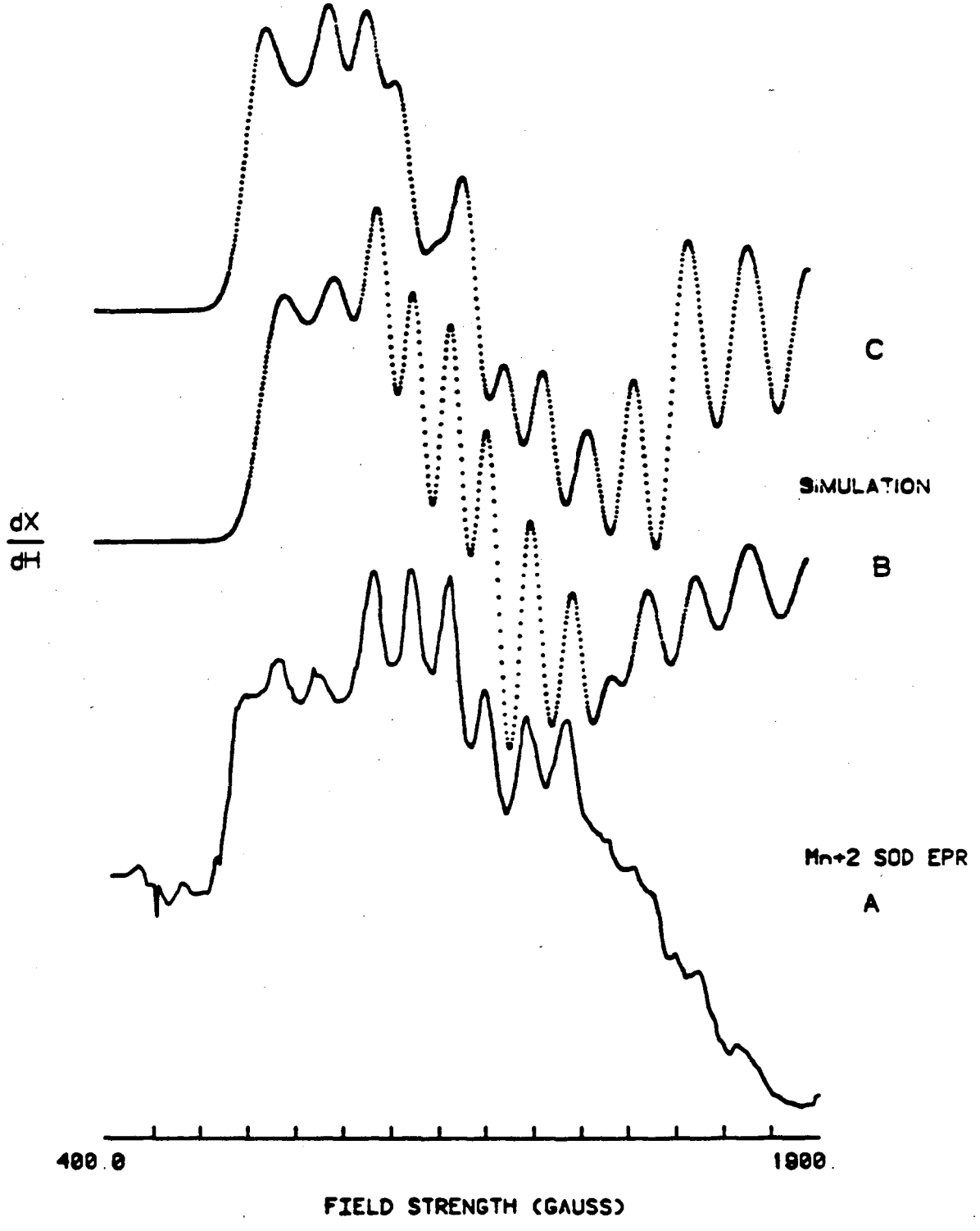

Figure 6. Fourier transform magnitude of data weighted by k^2 between k = 2.5 and 11. $Å^{-1}$ for reduced manganese SOD from T. thermophilus. Isolation of the major scattering components was accomplished by application of an isolation window before back transformation. The modulus of the filtered components used for the isolation are also shown (dotted line).

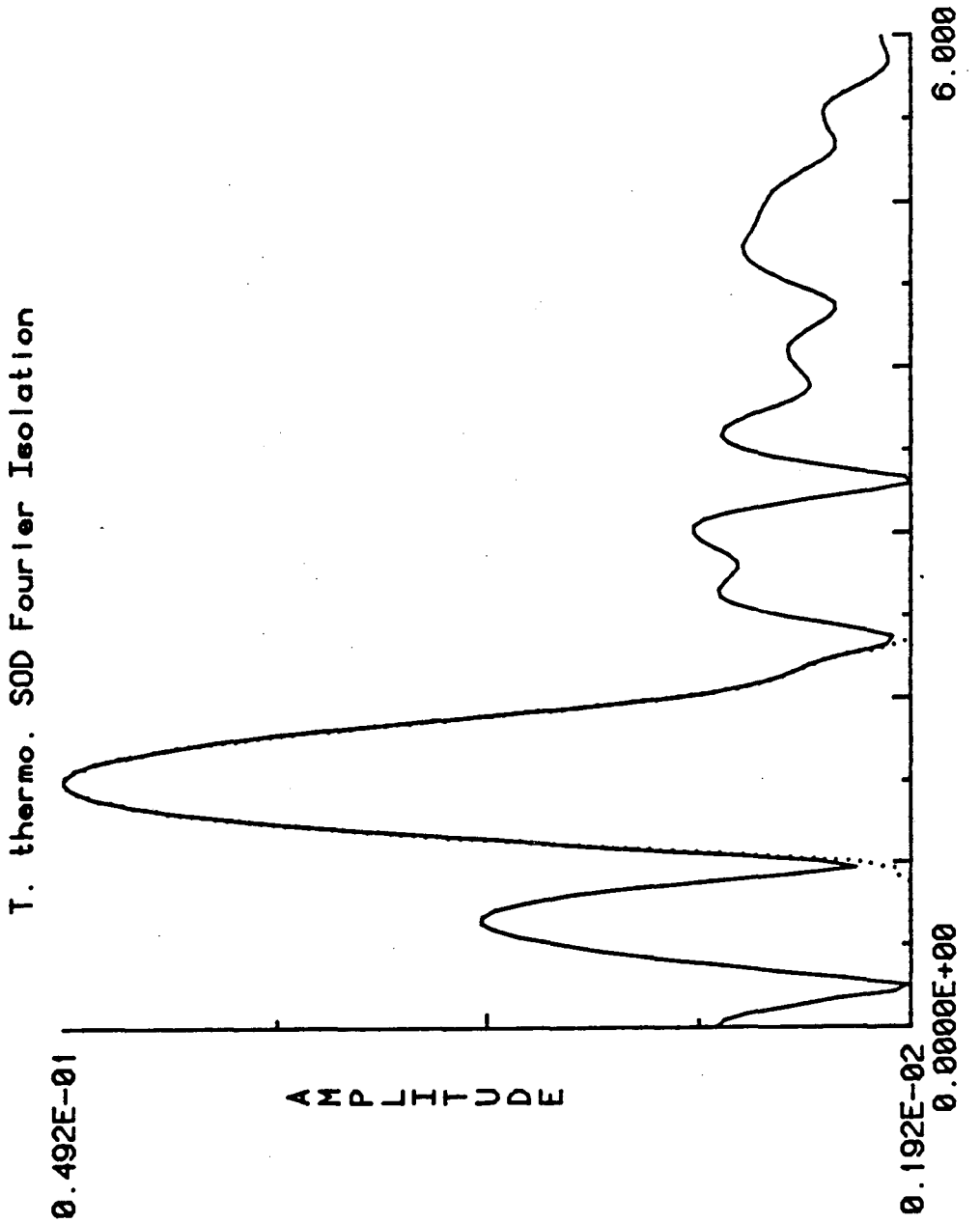
T. thermo. SOD Fourier Isolation
0.492E-01
AMPLHTUDE
0.192E-02
0.0000E+00
6.000
DISTANCE (A)

form, are presented in figure 7. These spectra show evidence for change in metal environment upon precipitation. For this reason, structural information obtained from data on the precipitated enzymes are considered of questionable meaning and are not presented.

2. Reduced SOD from T. thermophilus

The k^2 weighted EXAFS data and fourier isolate for reduced Mn SOD from T. thermophilus is presented in figure 8. The best single shell fit was obtained with nitrogen backscattering functions and is shown in figure 9. It is evident from the poor quality of this fit that more than one incompletely resolved shell of scatterers is contributing to the EXAFS components of the major fourier transform peak, and that a second set of scattering atoms must be introduced.

Fitting two shells of atoms to data that exhibit incompletely resolved fourier transform peaks is complicated. Parameters describing the two shells become correlated. As a result, minima become shallow and ranges of parameter values must be considered. In addition, false minima appear as a result of the increased number of degrees of freedom. If more than one minimum exists with physically acceptable parameter values, unambiguous structural assignment may be difficult or impossible.

By using a large number of trial two-shell fits and initial parameter values, three minima of good quality were found for the reduced prokaryotic SOD. These minima,

Figure 7. The k^2-weighted EXAFS spectra for reduced Mn SOD from T. thermophilus, a) in a 50% glycerol glass and b) as an NH_4SO_4 precipitated slurry.

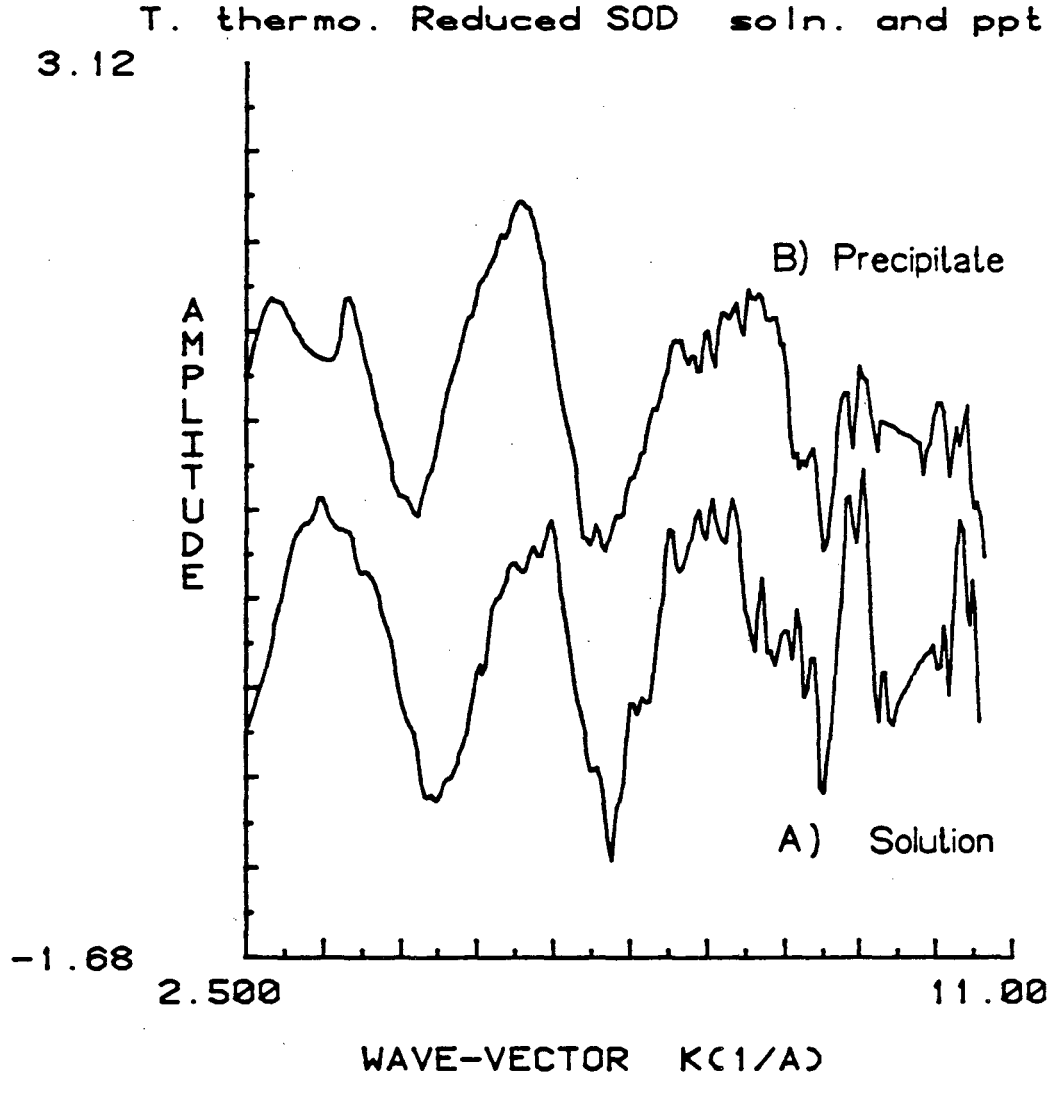
T. thermo. Reduced SOD soln. and ppt.
3.12
-1.68
AMPLITUDE
B) Precipitate
A) Solution
2.500
11.00
WAVE-VECTOR K(1/A)

Figure 8. EXAFS data weighted by k^3 for reduced Mn SOD from T. thermophilus (solid line) and the fourier-filtered major scattering components (dotted line).

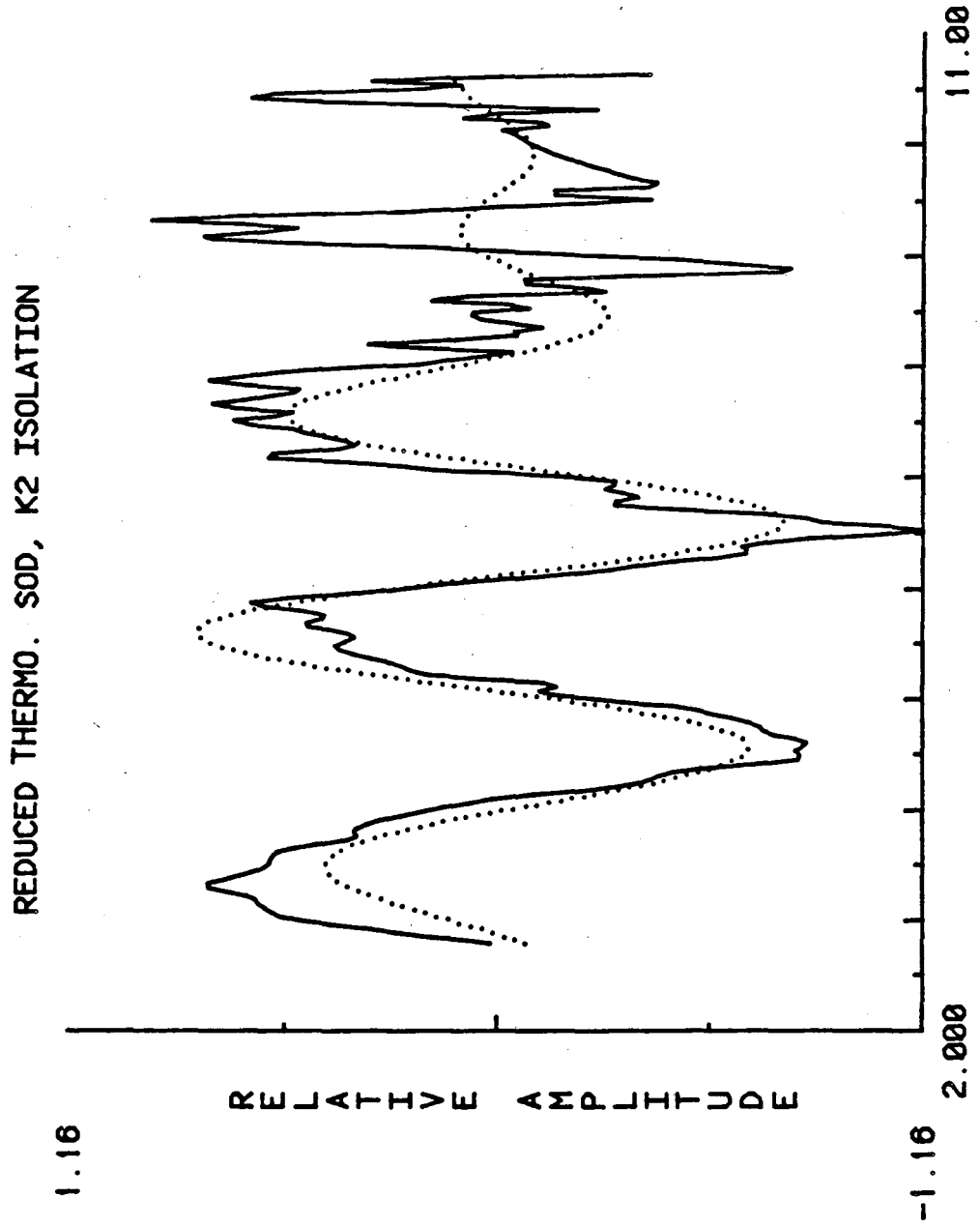
REDUCED THERMO. SOD, K2 ISOLATION
1.16
-1.16
RELATIVE AMPLITUDE
2.000
11.00
WAVE-VECTOR (1 / A)

Figure 9. One-shell fit to the filtered data of figure 8 for reduced Mn SOD from T. thermophilus using nitrogen scattering functions. Data from 3.5 to 11 $Å^{-1}$ were used in the fit. FCN is the sum of the squares of the fitting residual, R the fitted distance in Å, N the uncorrected amplitude, SIG the Debye-Waller parameter, and DEO is the correction in the choice of E_o at 6560.0 eV.

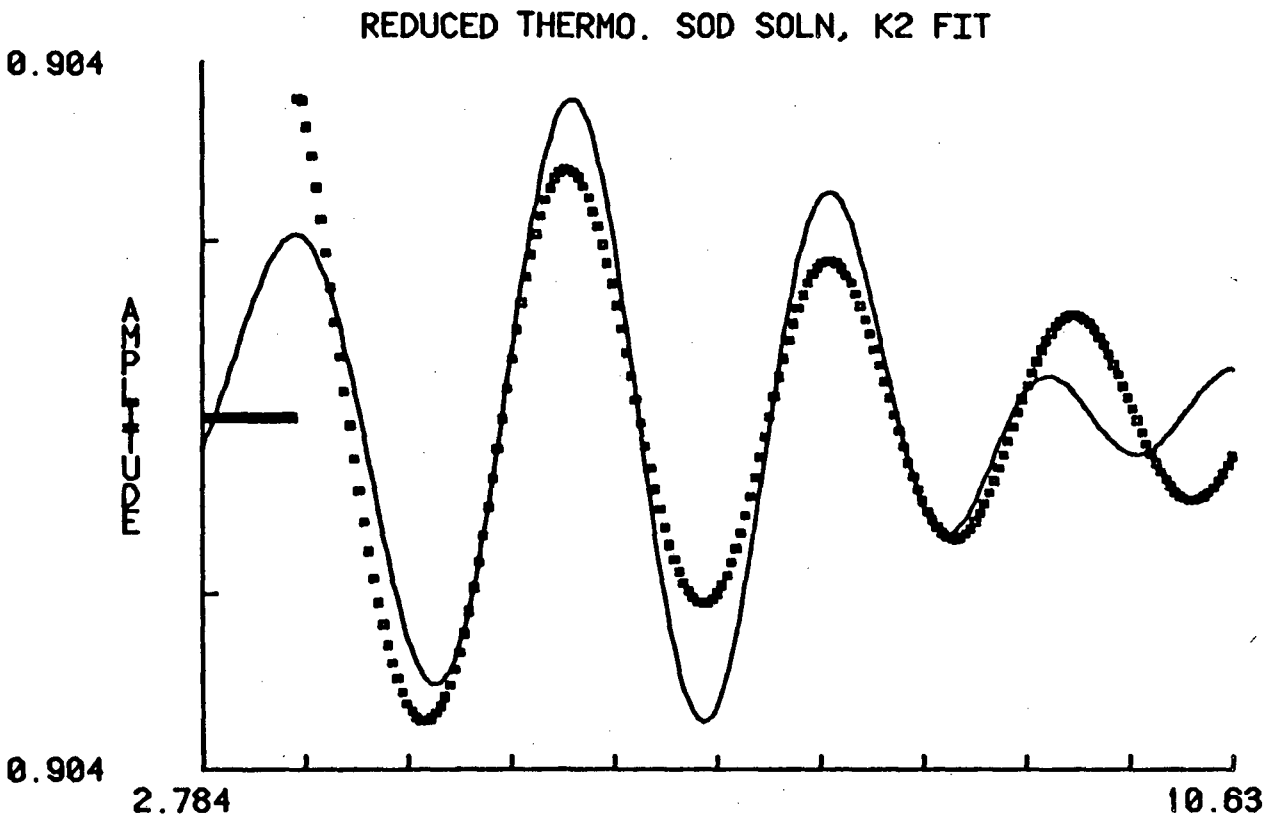

FCN = 4.86419
R = 2.1028781
N = 2.2857599
SIG= -0.0050091
DE0= -4.9578495
ATOM = N

Figure 10. Two-shell fits to the fourier filtered EXAFS of reduced Mn SOD from T. thermophilus.

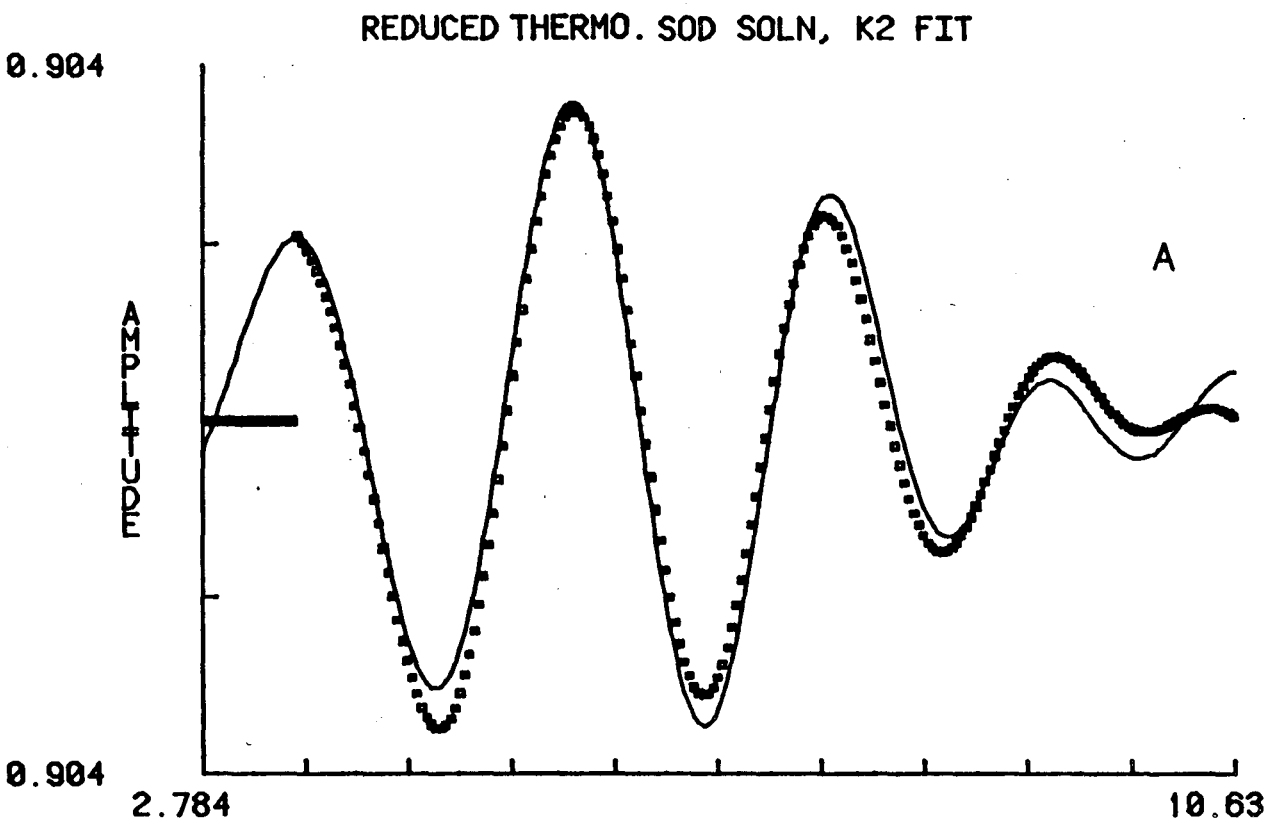

FCN =	0.820896	
R =	2.0121665	2.3247967
N =	1.4784515	0.6196386
SIG=	-0.0000023	-0.0000012
DE0=	-19.9999676	-6.1208620
ATOM =	N	S

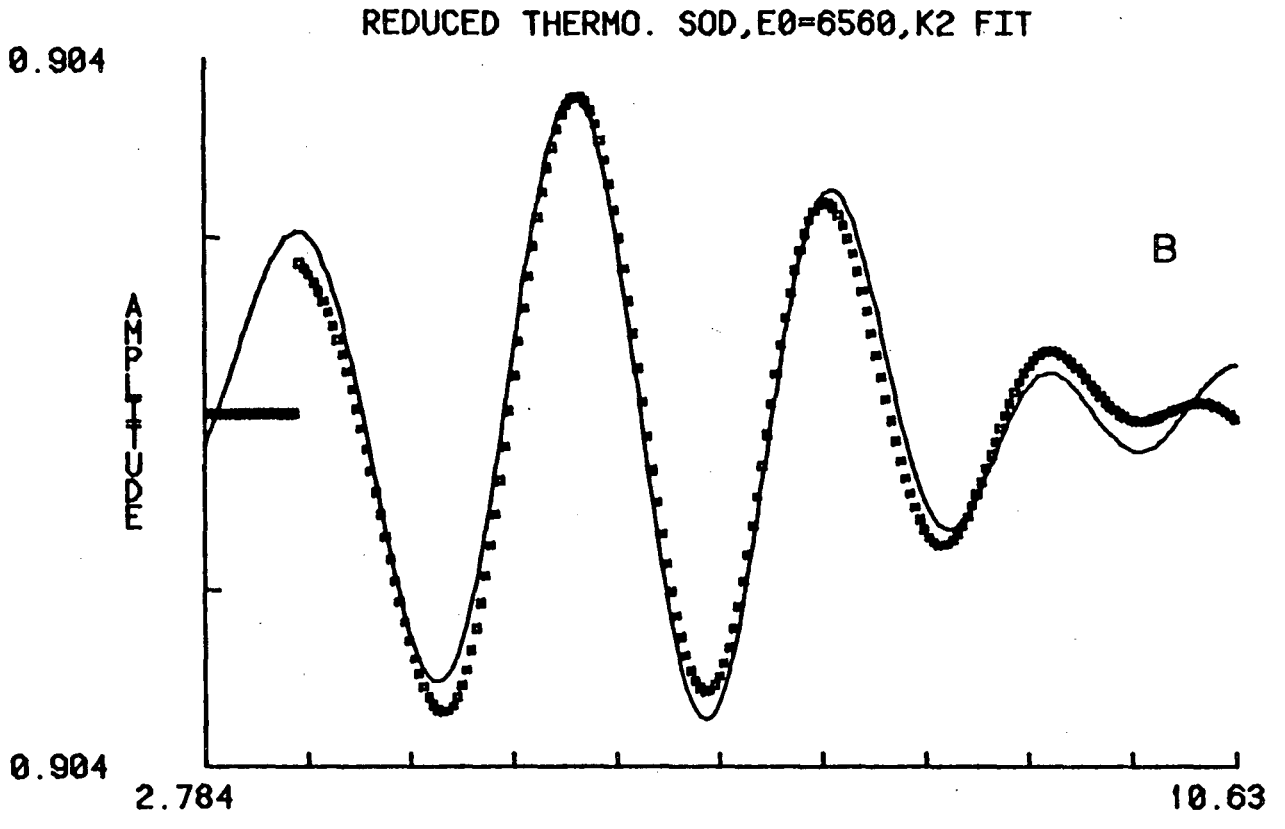

FCN =	0.886581	
R =	2.0286989	2.4618719
N =	2.2171743	1.4628494
SIG=	-0.0058629	0.0000000
DE0=	-20.0000000	-20.0000000
ATOM =	N	O

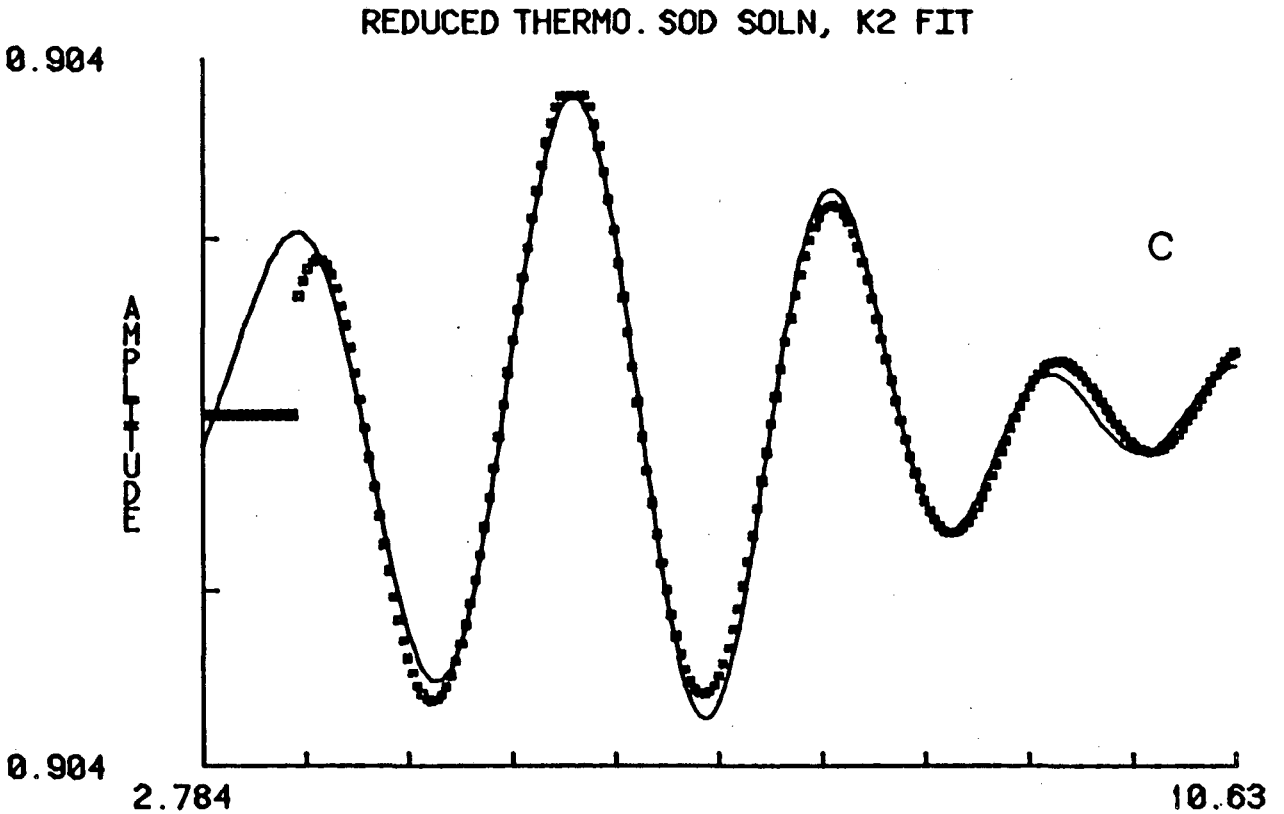

FCN =	0.253435	
R =	2.2007480	1.7203388
N =	1.4889721	0.5703804
SIG=	-0.0000016	-0.0000030
DE0=	14.0956116	19.2630310
ATOM =	N	N

labeled A, B and C are shown in figure 10. Each represents a somewhat different ligand environment around the manganese. Although most of the scattering ligands are best fit to nitrogen, oxygen cannot be excluded. Fit A contains a shell of N or O atoms at 2.01 Å and a contribution from sulfur at 2.32 Å. Fit B indicates a shell of N or O atoms at 2.03 Å and another N or O shell at 2.46 Å. The third possibility, C, contains N or O atoms at 2.20 Å and another shell of N or O at 1.72Å.

Attempts were made to identify the false minima within this set, or to at least establish a preferred minimum. All three of the minima are of comparable quality, so that discrimination among them is not possible on that basis. For these minima, some parameter values are near or at limits considered physically acceptable. However, elimination of a fit on this basis could be in error, because for these cases, the fit quality often remains quite acceptable after forcing the parameter back inside its limit. This behavior is characteristic of the observed shallow nature of the minima.

A conservative evaluation method has been described to aid in the analysis of EXAFS data that exhibit problems associated with unresolved shells [32]. The number of scatterers in each of the two shells is fixed, and a fit to the data performed by minimizing with respect to all of the other parameters. An array is then constructed by fixing the number of atoms at other values, and contours of the minima

are constructed. A locus of points can then be identified by designating regions for which all parameter values remain within acceptable values. Well behaved data will exhibit minima within such a locus, and thus false minima can sometimes be identified. In addition, the relative depth of the minima can be observed and used along with locus boundaries to assign ranges to parameter values.

Plots of loci for the three minima of reduced T. thermophilus SOD are shown in figure 11. For minimum A, (figure 11a) the minimum lies between an overall coordination of 4 and 5 atoms, and is contained in a fairly well-defined locus of acceptable parameter values. A range of 3 to 4 atoms of N or O are defined by the locus boundaries, and 1 to 2 atoms of sulfur are contained by a locus boundary and the steeply rising wall of the minimum. Minimum B (figure 11b) is more shallow and lies at a total coordination of 6-7 atoms. It lies on the edge of a parameter locus boundary in a way that excludes any fit to less than 7 atoms. A range of 3 to 6 atoms of N or O in the first shell and 3 or more atoms of O or N for the second are indicated, making this minimum very indeterminate as to its composition. Minimum C (figure 11c) is well contained in a locus of acceptable parameter values, and is centered between a 4 and 5 coordinate structure, although anywhere between 3 and 5 atoms in the first shell and 1 to 3 atoms in the second give acceptable fits within the locus.

An estimate of the precision in the ligand distances

Figure 11. Fitting contours for the three minima (A-C) of figure 10 for reduced Mn SOD from T. thermophilus. On each axis are the corrected number of atoms in the two shells of the fits used to construct the contours. The numbers within the graph are the FCN values obtained for each fit with the corresponding number of atoms fixed. Thus, the diagonal lines represent exact coordination by 4, 5, and 6 total atoms. The areas inside the heavy lines (shaded areas) are the loci of fits for which all fitted parameter values remained within acceptable limits. These limits were; $-0.03<\sigma<0.0$, $-20.0<\Delta E_o<20.0$ and $-17.0<(\Delta E_o{}^a - \Delta E_o{}^b)<17.0$.

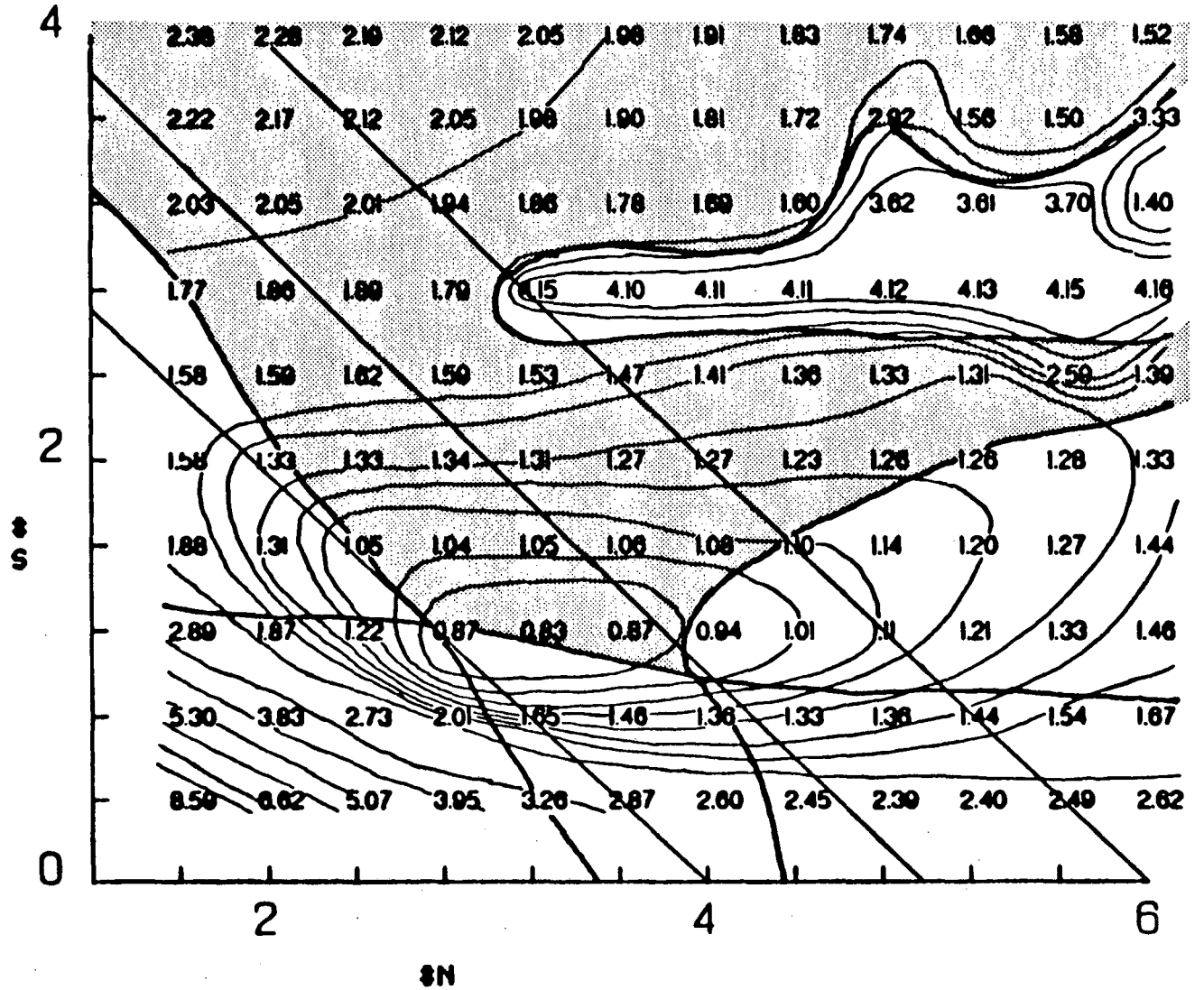
4
2
0
2
4
6
$S
$N
A

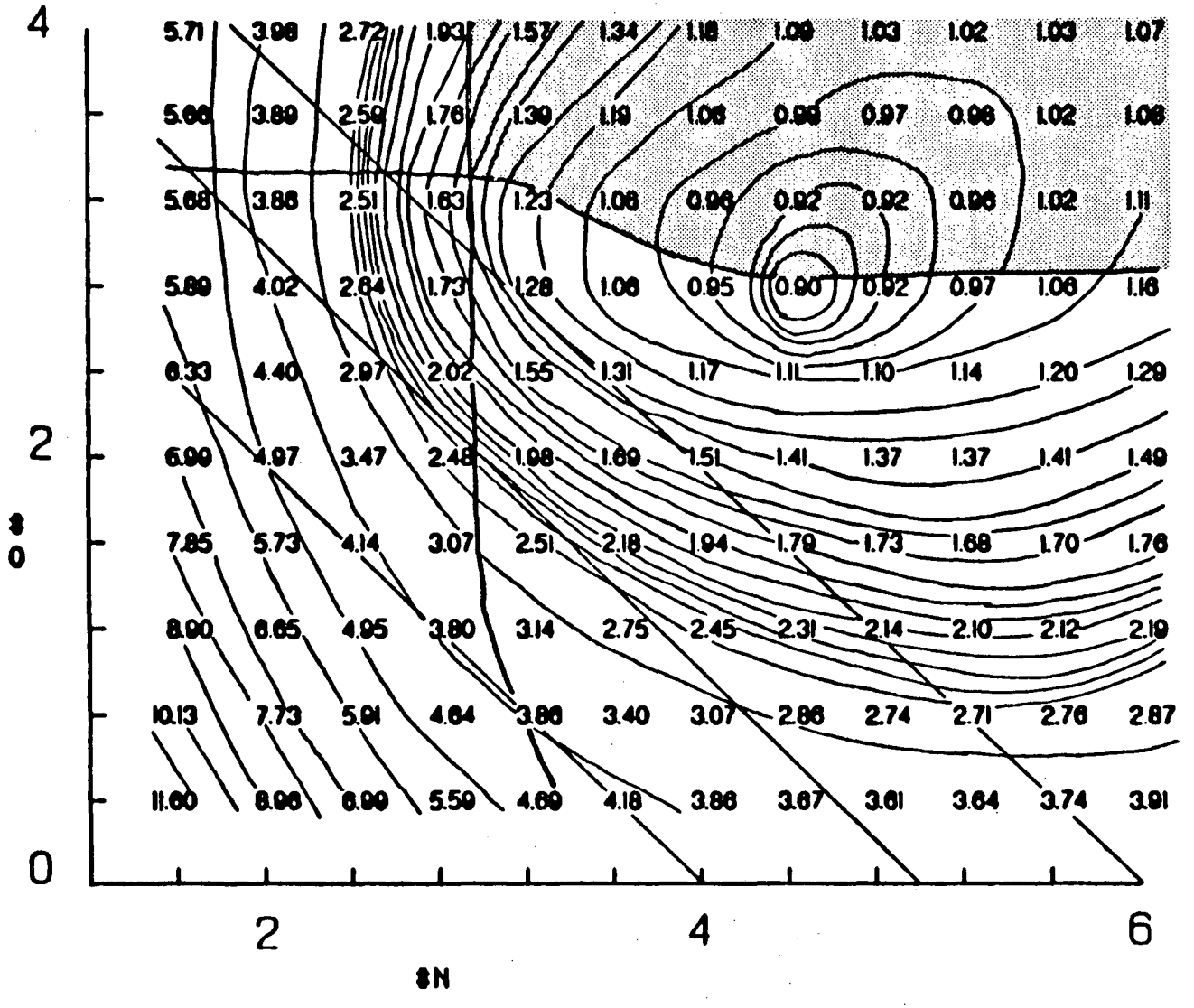
4
2
0
2
4
6
$N
5.71 3.98 2.72 1.93 1.57 1.34 1.18 1.09 1.03 1.02 1.03 1.07
5.66 3.89 2.59 1.76 1.39 1.19 1.06 0.98 0.97 0.98 1.02 1.08
5.68 3.86 2.51 1.63 1.23 1.06 0.96 0.92 0.92 0.96 1.02 1.11
5.89 4.02 2.64 1.73 1.28 1.06 0.95 0.90 0.92 0.97 1.06 1.16
6.33 4.40 2.97 2.02 1.55 1.31 1.17 1.11 1.10 1.14 1.20 1.29
6.99 4.97 3.47 2.48 1.98 1.69 1.51 1.41 1.37 1.37 1.41 1.49
7.85 5.73 4.14 3.07 2.51 2.18 1.94 1.79 1.73 1.68 1.70 1.76
8.90 6.65 4.95 3.80 3.14 2.75 2.45 2.31 2.14 2.10 2.12 2.19
10.13 7.73 5.91 4.64 3.86 3.40 3.07 2.86 2.74 2.71 2.76 2.87
11.60 8.96 6.99 5.59 4.69 4.18 3.86 3.67 3.61 3.64 3.74 3.91

B

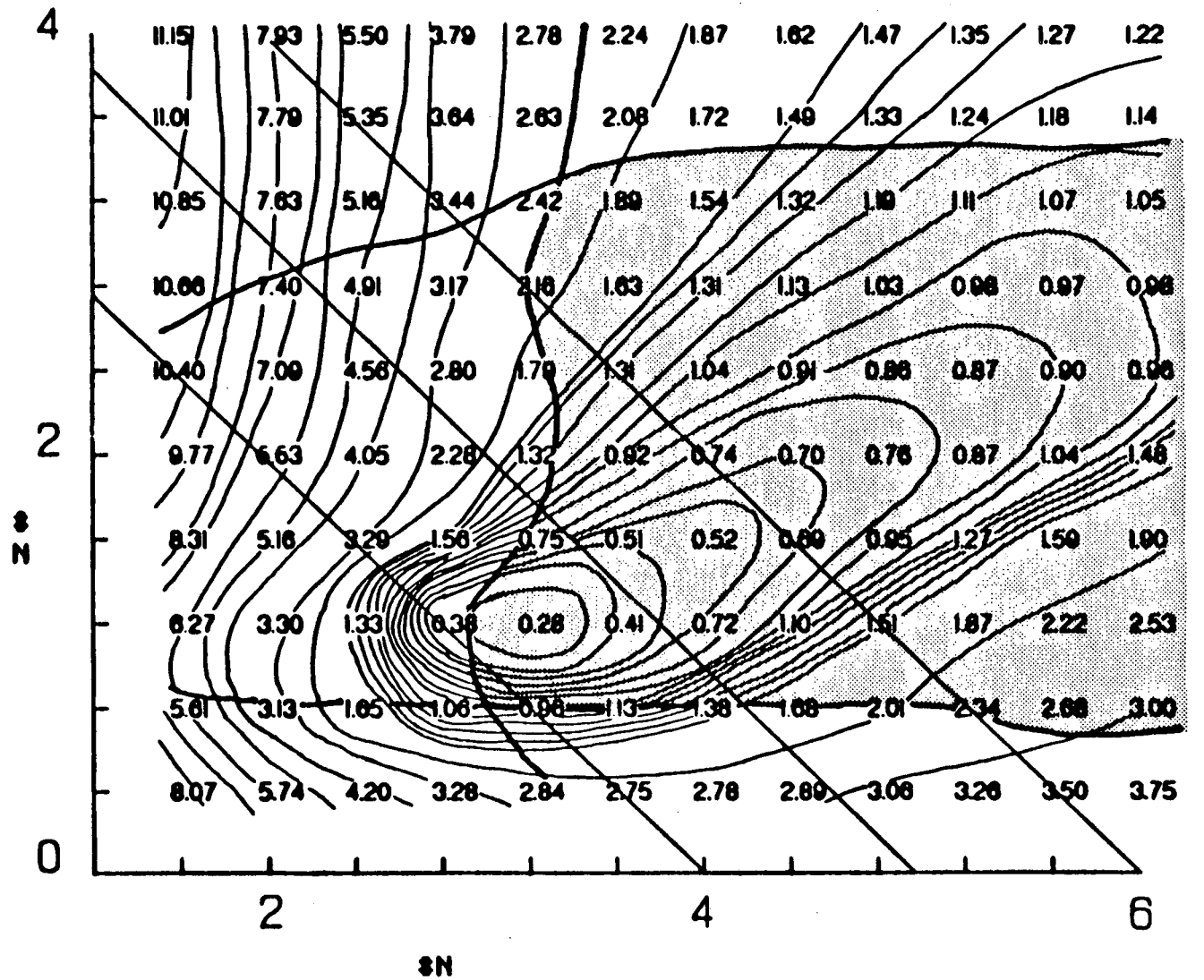
4
2
0
2
4
6
$N
$N
11.15 7.93 5.50 3.79 2.78 2.24 1.87 1.62 1.47 1.35 1.27 1.22
11.01 7.79 5.35 3.64 2.63 2.08 1.72 1.49 1.33 1.24 1.18 1.14
10.85 7.63 5.18 3.44 2.42 1.89 1.54 1.32 1.19 1.11 1.07 1.05
10.66 7.40 4.91 3.17 2.18 1.63 1.31 1.13 1.03 0.98 0.97 0.98
10.40 7.09 4.56 2.80 1.79 1.31 1.04 0.91 0.86 0.87 0.90 0.96
9.77 6.63 4.05 2.28 1.32 0.92 0.74 0.70 0.76 0.87 1.04 1.48
8.31 5.16 3.29 1.56 0.75 0.51 0.52 0.69 0.95 1.27 1.59 1.90
6.27 3.30 1.33 0.38 0.28 0.41 0.72 1.10 1.51 1.87 2.22 2.53
5.61 3.13 1.65 1.06 0.98 1.13 1.38 1.68 2.01 2.34 2.68 3.00
8.07 5.74 4.20 3.28 2.84 2.75 2.78 2.89 3.08 3.26 3.50 3.75

C

observed at a given minimum can be provided by stating the range of values observed for all of the fits within the locus. The parameter values at the minima and their estimated ranges aregiven in table 2.

3. Iron Substituted SOD from T. thermophilus

In view of the similarities in physical properties and amino acid sequences between Mn and Fe superoxide dismutases, it would be of great importance to discover what differences, if any, exist in metal coordination between the forms. Of related importance is the requirement for the 'natural' metal observed in most SODs for which metal replacement has been successful. We have obtained EXAFS data for T. thermophilus SOD in which manganese was replaced by Fe in order to determine whether it goes into the native manganese site.

Successful metal replacements in many superoxide dismutases have not been possible. We were unable to use established methods for metal replacement using the T. thermophilus enzyme without precipitation upon reduction of the urea concentration, but were successful in using a modification in the refolding procedure employing a slow dialysis out of glycerol solution. Reconstitution of the apo-enzyme with Mn gave a protein containing 0.74 Mn/subunit. This enzyme regained the purple color and spectral properties characteristic of native SOD and showed a high specific activity. As expected, the Fe-reconstituted enzyme, containing 0.53 Fe/subunit and no detectable Mn, was

Table 2. EXAFS Structural parameters for manganese SOD and iron substituted manganese SOD. Parameters were obtained from two shell fits to the first Fourier-filtered scattering peak. Parameter ranges were obtained from the boundaries of fit loci (see text).

			Shell 1					Shell 2					#Shell 1
Sample	Fit	Total coord.	Atom type	#	range	R_1	range	type	#	range	R_2	range	#Shell 2
T. thermophilus (Reduced)	A	4-5	N	3.0	3-4	2.01	2.00-2.04	S	1.2	1-2	2.32	2.28-2.33	2.5
	B	7-8	N	4.4	3-6	2.03	2.03-2.04	O	2.9	3-?	2.46	2.45-2.47	1.5
	C	4-5	N	3.0	3-5	2.20	2.14-2.21	N	1.1	1-3	1.72	1.65-1.76	2.7
T. thermophilus Fe substituted	A	3.5	N	2.1		1.89		S	1.4		2.21		1.5
	B	7.7	N	3.8		1.91		O	3.9		2.35		1.0
	C	4.0	N	3.3		2.07		N	0.7		1.61		4.7
S. cerevisiae (Native)	A	2-3	N	1.5	1-2	1.95	1.95-1.97	S	0.7	1-2	2.32	2.29-2.37	2.1
	B	4-5	N	2.1	2-3	1.97	1.96-1.98	O	1.8	1-3	2.46	2.41-2.50	1.2
	C	3-5	N	2.3	2-4	2.13	2.06-2.13	N	0.6	1	1.67	1.62-1.71	3.8

pale yellow-brown in color and showed an activity of less than 3% of the Mn reconstituted control. The low temperature EPR spectrum of the Fe substituted protein is shown in figure 12. A large symmetric signal is seen at g = 4.3 in addition to weaker components at g = 5.28, 4.93, 3.88, and 3.59. The g values of the weaker signals are quite similar to those reported for active Fe SOD [33], while the principal g = 4.3 signal is very similar to that observed for Fe SOD inactivated with H_2O_2 [34].

The k^3 weighted EXAFS data and fourier isolate of the major fourier transform peak for Fe substituted SOD is presented in figure 13. The best single-shell fit to these data was with N or O atoms and, like the case for the Mn enzyme, was inadequate. Two-shell fits were performed, and three minima of good quality were found which correspond very closely with those obtained for the Mn form. These fits are presented in figure 14, and distances and numbers of atoms are included in table 2. Examination of table 2 shows that the only significant differences between the corresponding fits to the Mn and Fe substututed SOD is a consistent 0.1 Å shorter distance for the Fe sample. This is entirely consistent with the expected contraction of ligand distance if the enzymes contained Fe^{+3} and Mn^{+2} centers respectively.

4. Manganese SOD from S. cerevisiae

In order to examine the coordination site of SOD from distantly related organisms, we have collected EXAFS spectra

Figure 12. X-band EPR spectrum for Fe-substituted manganese SOD from T. thermophilus. The protein concentration was approximately 0.5 mM.

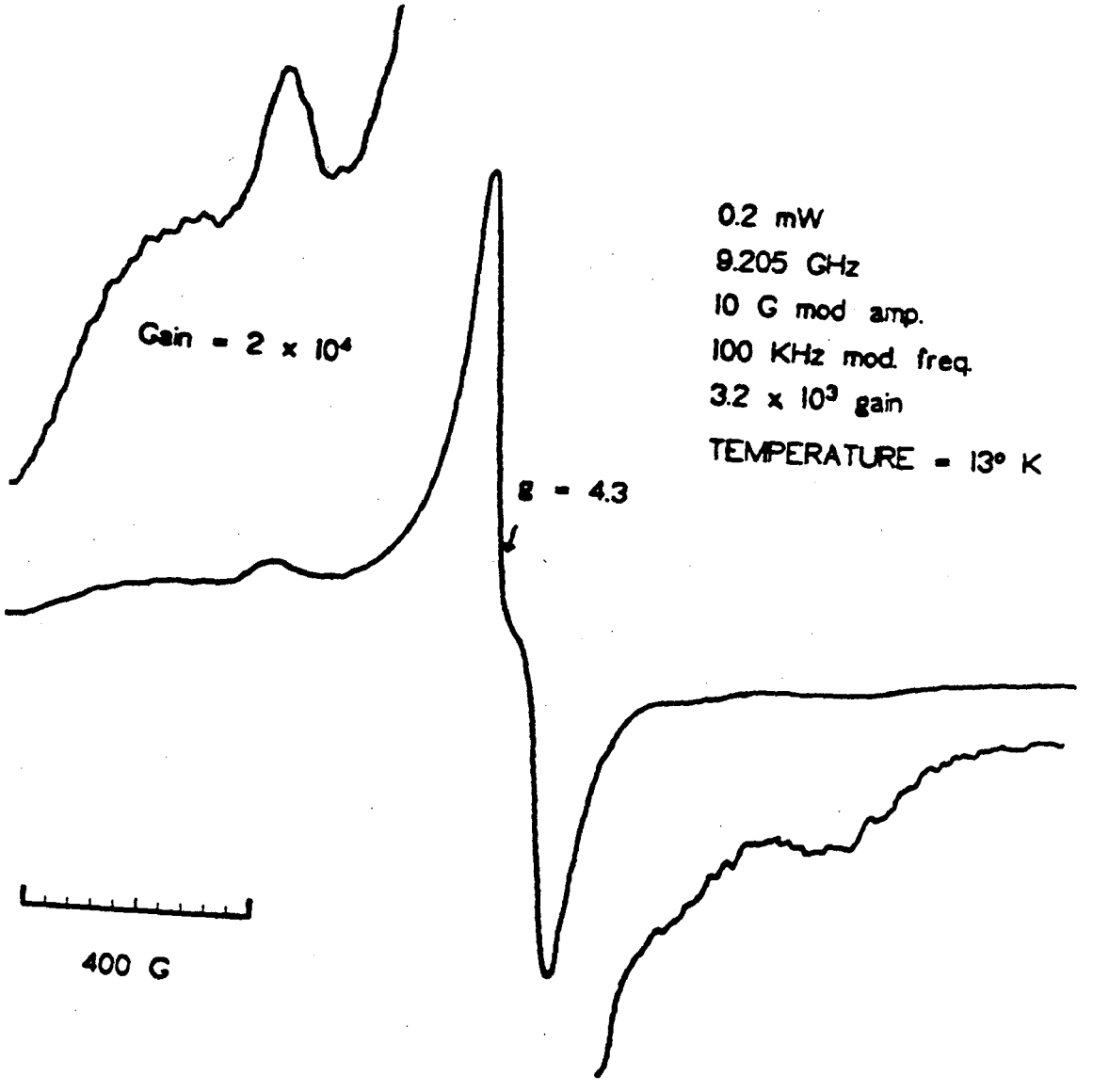
Gain = 2 x 10⁴
g = 4.3
0.2 mW
9.205 GHz
10 G mod amp.
100 KHz mod. freq.
3.2 x 10³ gain
TEMPERATURE = 13° K
400 G

Figure 13. K^3-weighted EXAFS (solid line) and fourier-isolated major scattering components (dotted line) for Fe substituted manganese SOD from T. thermophilus.

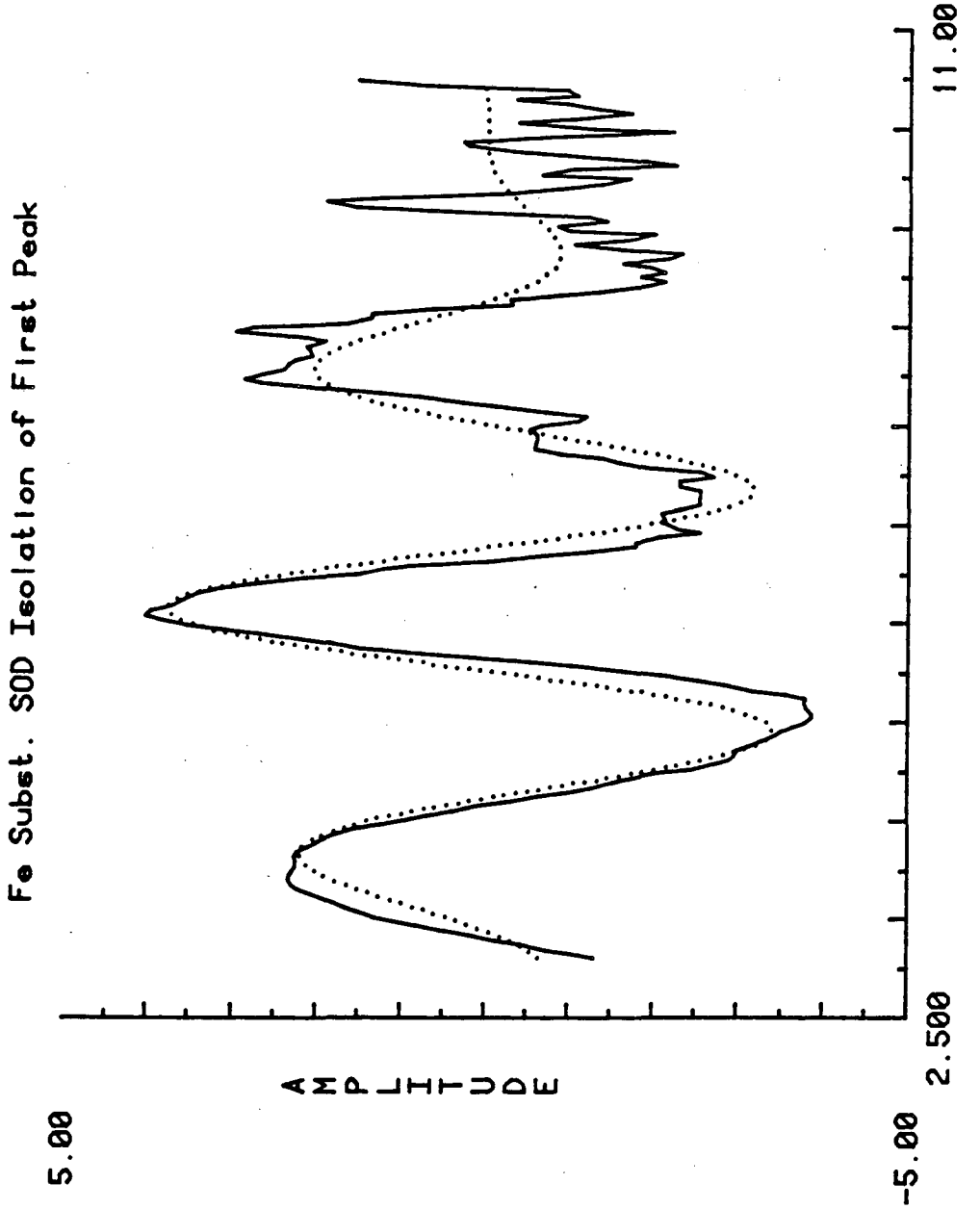
Fe Subst. SOD Isolation of First Peak
AMPLITUDE
5.00
-5.00
2.500
11.00
WAVE-VECTOR K(1/A)

Figure 14. The three best two-shell fits to the k^3-weighted fourier-filtered EXAFS of Fe substituted SOD from T. thermophilus. Fits were performed on data between k = 3.5 and 11.0 $Å^{-1}$.

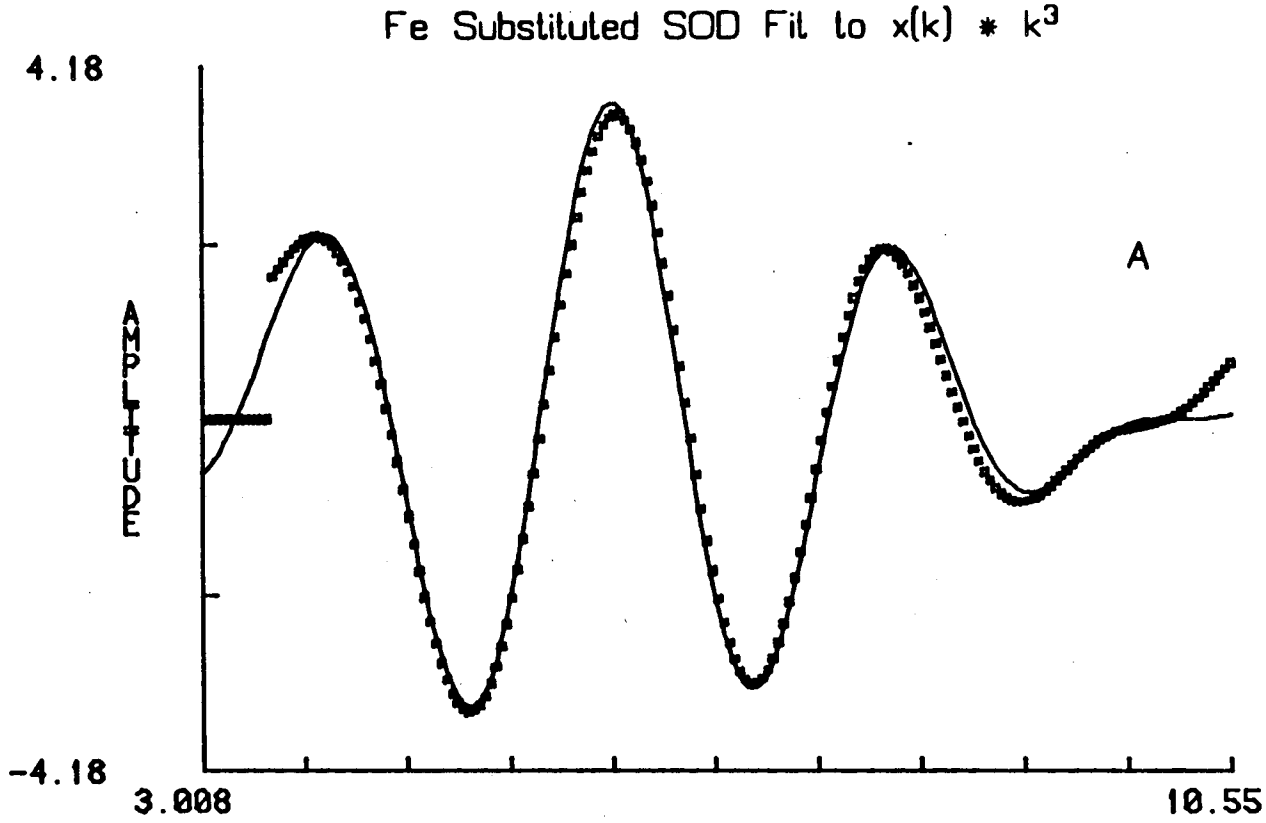

FCN =	6.41300	
R =	1.8900397	2.2112851
N =	1.0677395	0.6931724
SIG=	-0.0023563	-0.0097066
DE0=	-19.9999313	-5.2614841
ATOM =	N	S

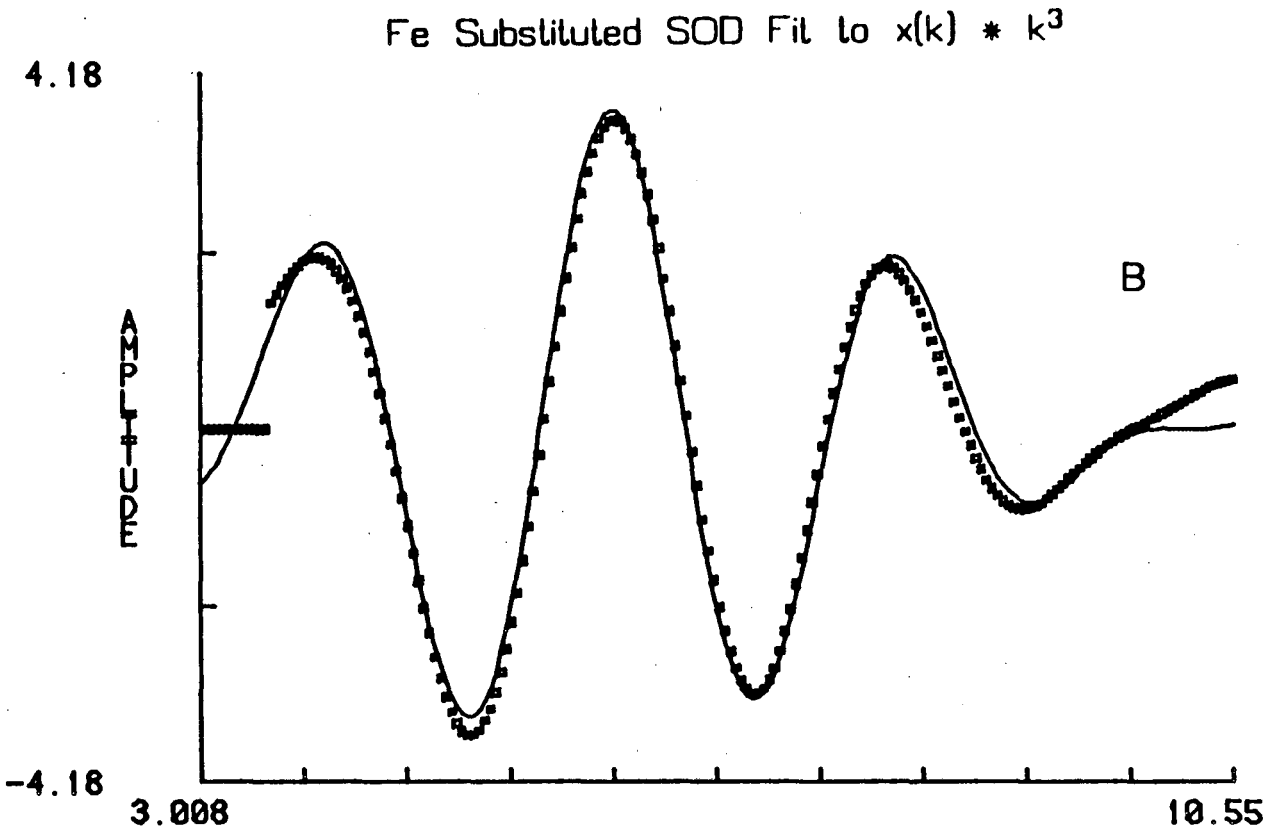

FCN =	7.64790	
R =	1.9100649	2.3516655
N =	1.8868142	1.9549192
SIG=	-0.0111877	-0.0143037
DE0=	-19.9998970	-19.9983711
ATOM =	N	O

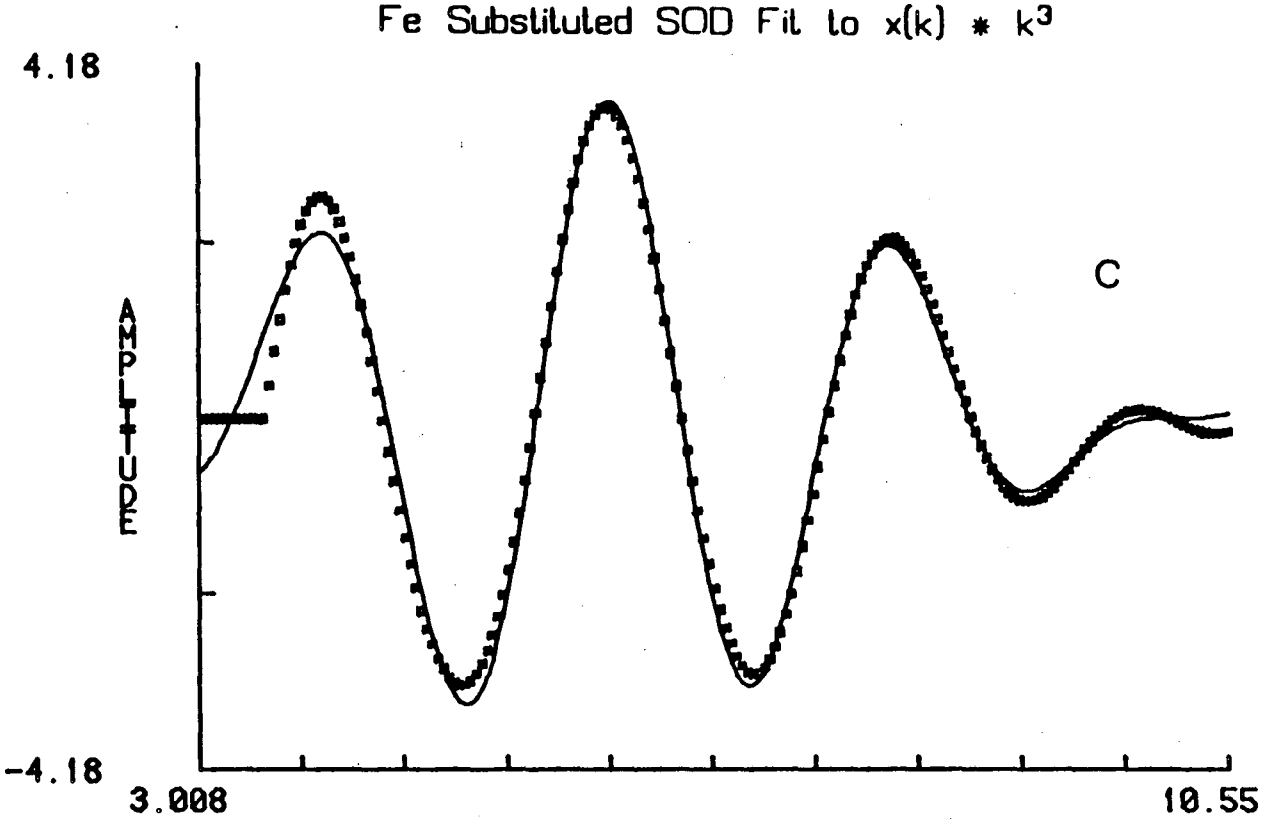

FCN =	5.76047	
R =	2.0685437	1.6058414
N =	1.6301355	0.3335793
SIG=	-0.0122071	-0.0014365
DE0=	13.9900322	19.9984665
ATOM =	N	N

for Mn SOD isolated from S. cerevisiae. The K^2 weighted EXAFS data and fourier isolate are presented in figure 15 for native (oxidized) yeast SOD. Data were also collected for yeast enzyme in the presence of 20 mM N_3^- and are presented in figure 16. Only a limited data set for this form was obtained. Comparison of these two data sets indicates that differences in the EXAFS amplitude envelope may exist, but not in the phase. However, the N_3^- data do not extend far enough for meaningful fitting analysis.

The best single shell-fit to native yeast SOD data is shown in figure 17, demonstrating again the inadequate nature of a single-shell description. Three two-shell minima were found for yeast, roughly corresponding to minima A, B and C for the other two forms investigated. These fits are presented in figure 18. Examination of the parameters given with these fits indicate that significant differences exist in the number of coordinating atoms between these minima and those given previously.

To examine the significance of these differences in the yeast EXAFS, fit loci were constructed. These are presented in figure 19 for the minima labeled A, B and C. Unlike the case for the prokaryotic enzyme, the locus for minimum A (figure 19a) is nearly non-existent. The minimum itself is centered at a total coordination number between 2 and 3, and only a narrow sliver of this region represents fits to acceptable parameter values. A range of only 1 to 2 atoms of N or O in the 1st shell are indicated and 2 or fewer

Figure 15. K^2-weighted EXAFS (solid) and fourier-filtered major scattering peak (dotted) for manganese SOD from S. cerevisiae.

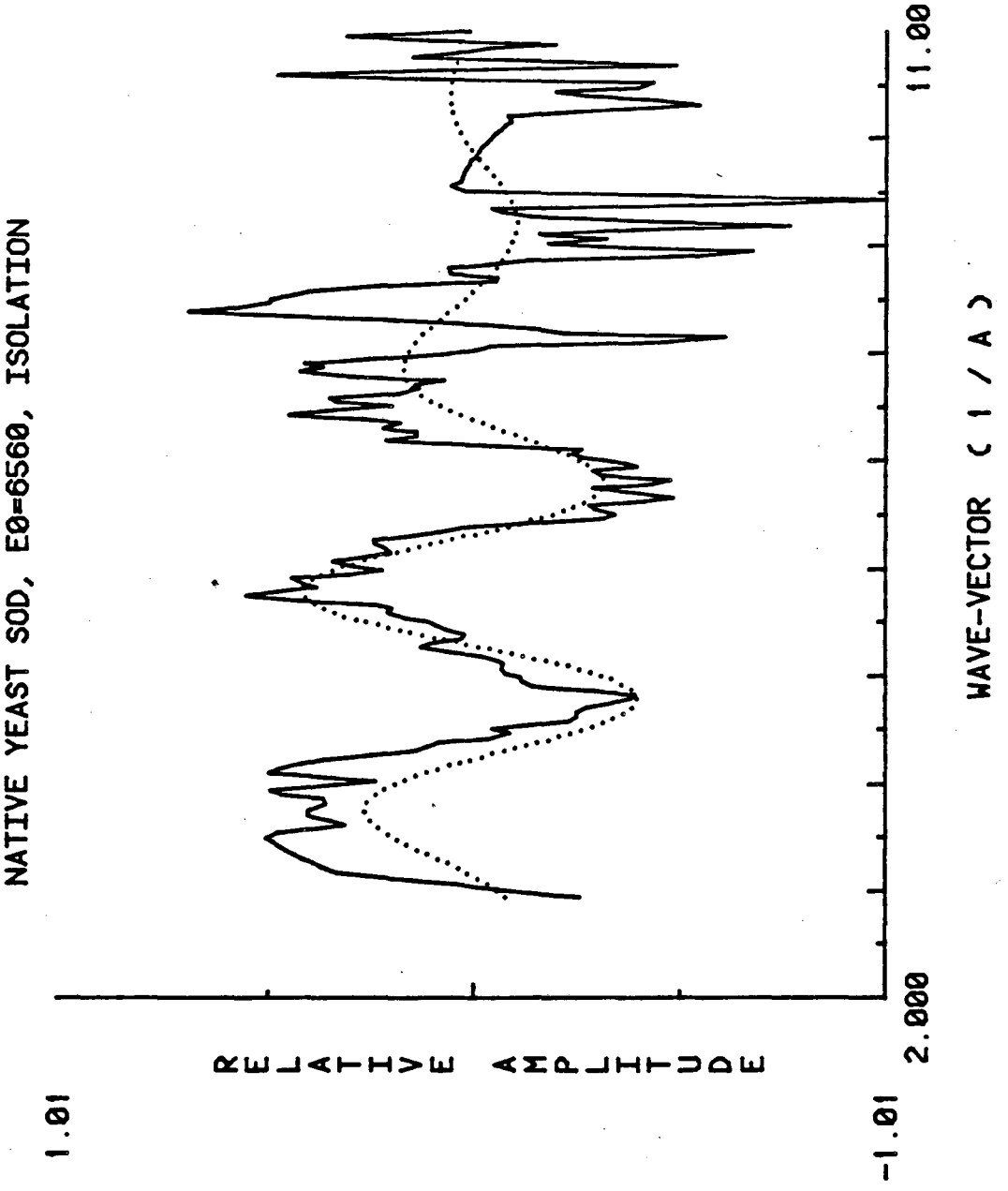
NATIVE YEAST SOD, E0=6560, ISOLATION
RELATIVE AMPLITUDE
1.01
-1.01
2.000
11.00
WAVE-VECTOR (1 / A)

Figure 16. K^2-weighted EXAFS (solid) and fourier-filtered major scattering peak (dotted) for manganese SOD from S. cerevisiae in the presence of 20 mM NaN_3.

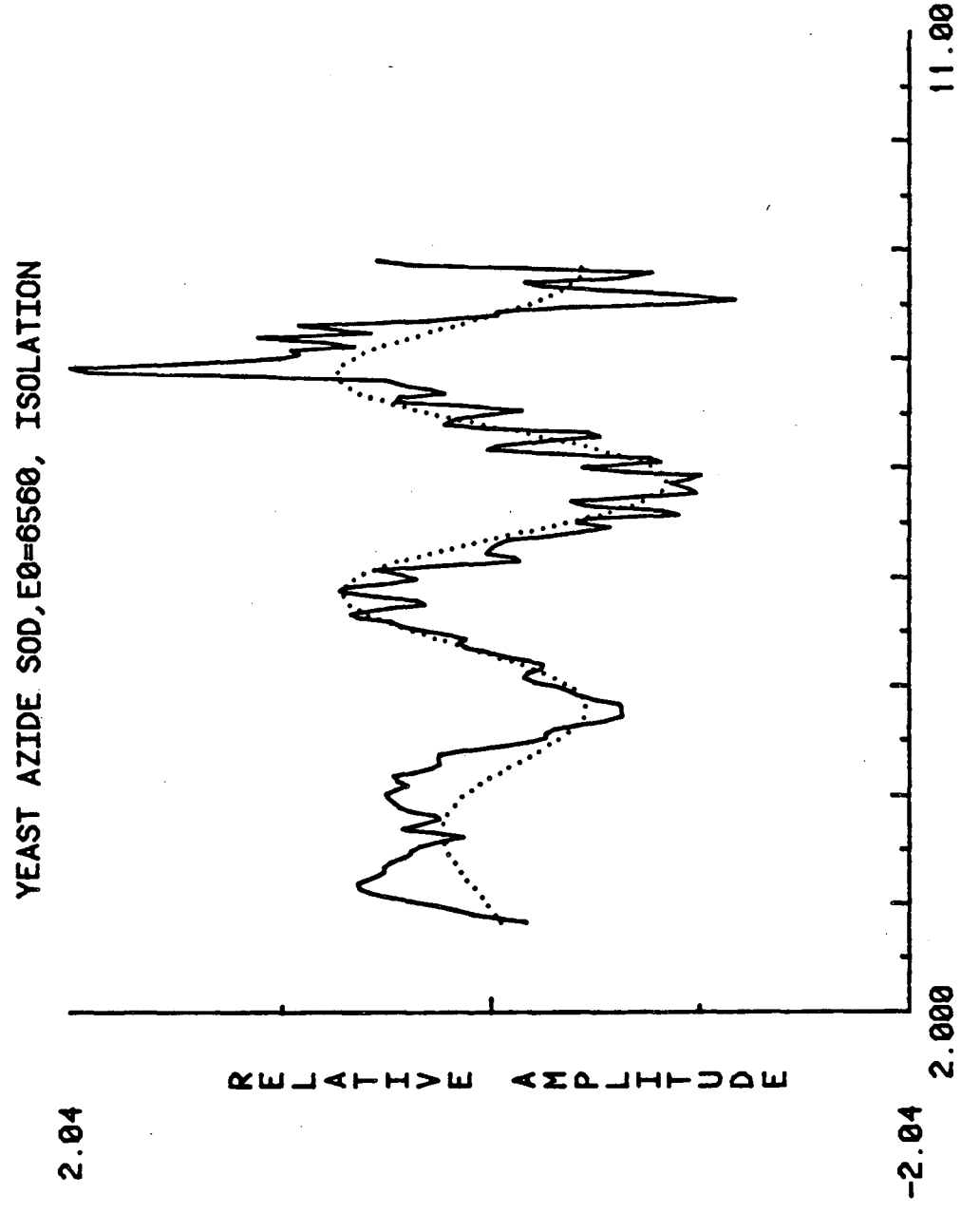
YEAST AZIDE SOD,E0=6560, ISOLATION
RELATIVE AMPLITUDE
2.04
-2.04
2.000
11.00
WAVE-VECTOR (1 / A)

Figure 17. One-shell fit to the k^2-weighted fourier-filtered data between k = 3.5 and 12.0 $Å^{-1}$ for native manganese SOD from S. cerevisiae.

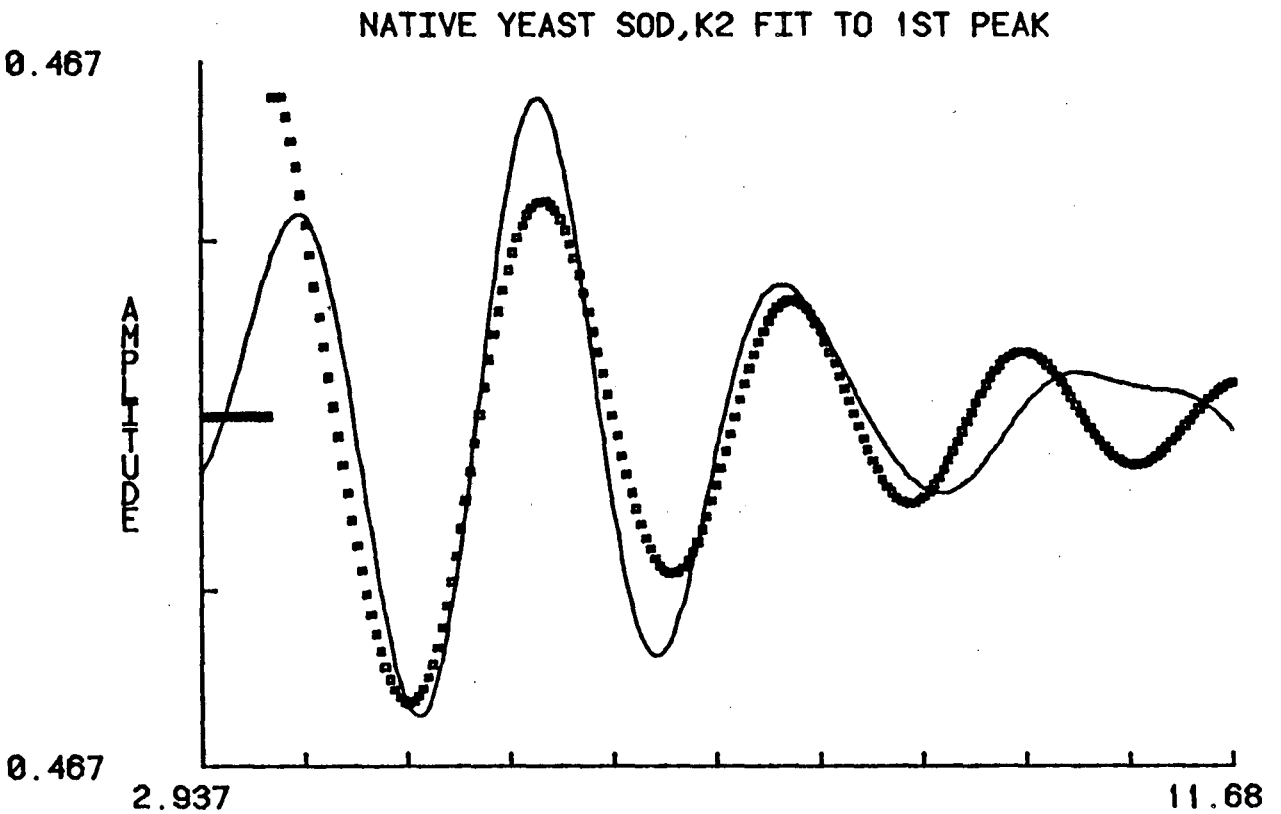

FCN = 1.31815
R = 2.0060124
N = 1.2982446
SIG= -0.0098734
DE0= -10.1660957
ATOM = N

Figure 18. Three two-shell fits to the fourier-filtered k^2 data for native manganese SOD from S. cerevisiae.

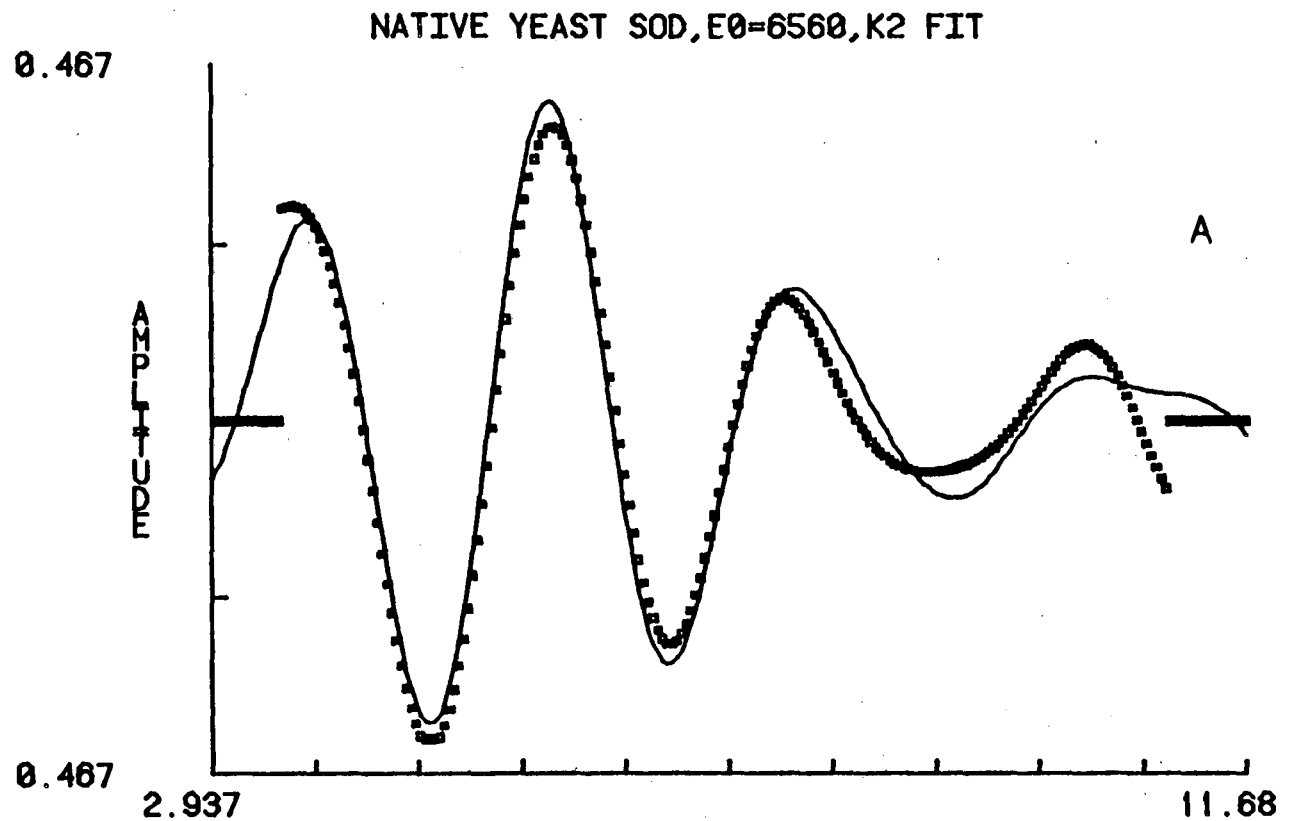

FCN =	0.238237	
R =	1.9544718	2.3183610
N =	0.7634699	0.3618856
SIG=	-0.0002126	-0.0084936
DE0=	-20.0000000	-0.1393585
ATOM =	N	S

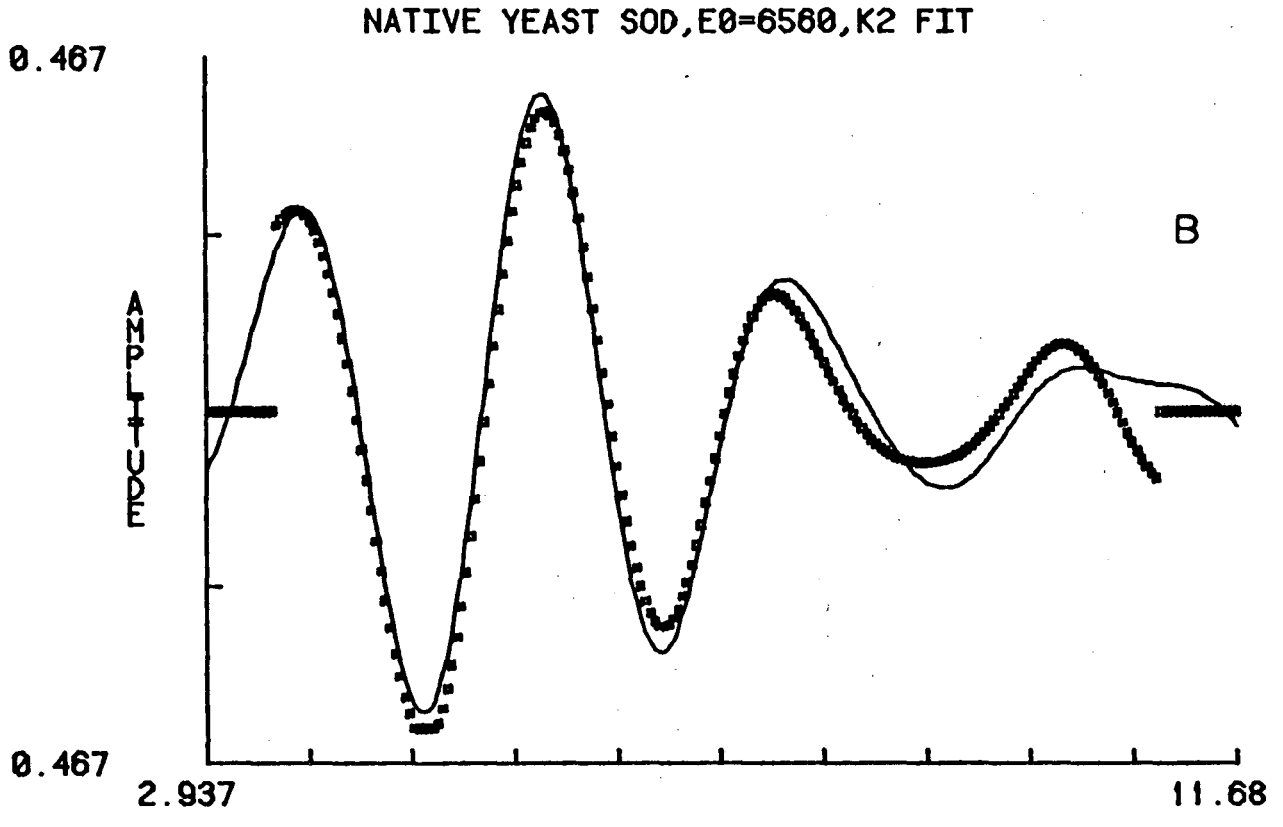

FCN =	0.262819	
R =	1.9651309	2.4631605
N =	1.0731816	0.9112579
SIG=	-0.0059721	-0.0101144
DE0=	-19.9999981	-14.9773073
ATOM =	N	O

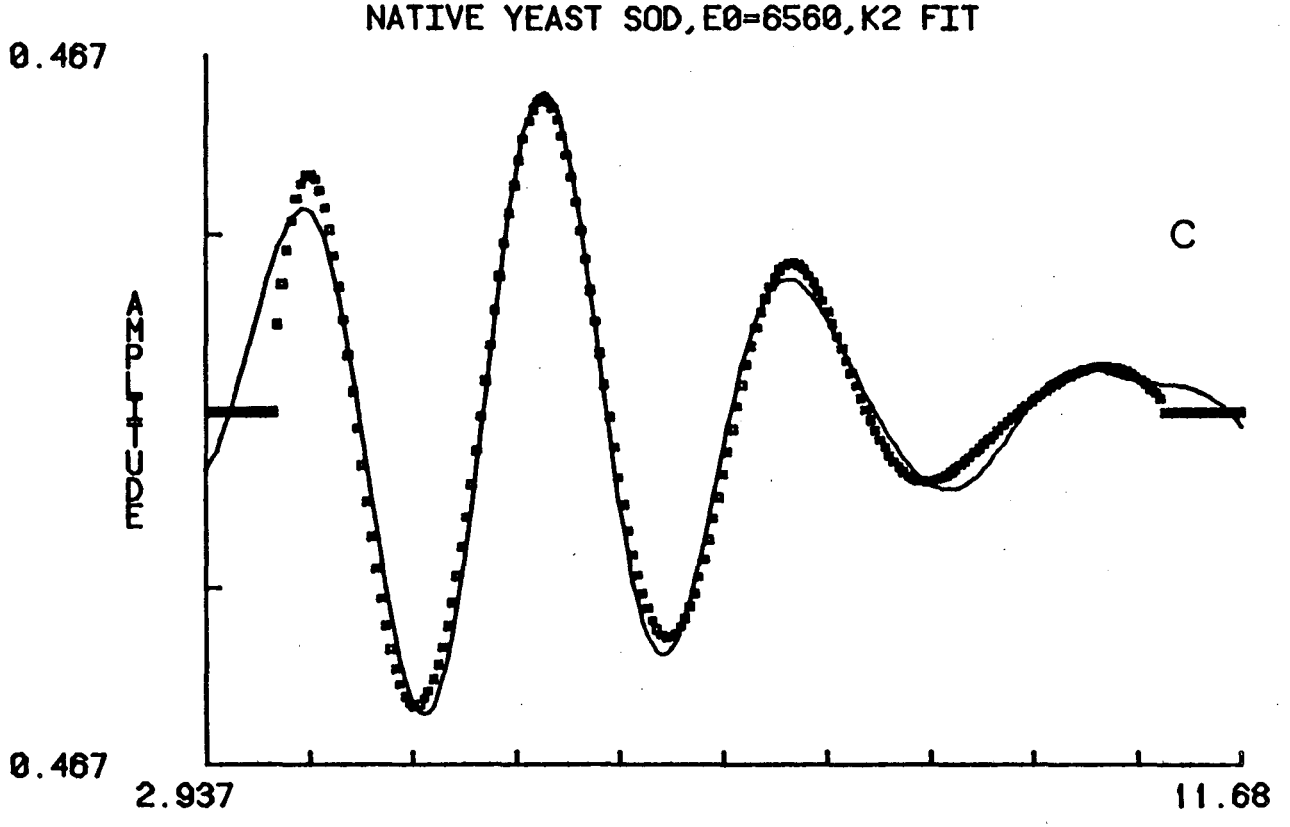

FCN =	0.114146	
R =	2.1323261	1.6747633
N =	1.1520544	0.3074044
SIG=	-0.0191926	0.0000000
DE0=	14.4347305	19.9950905
ATOM =	N	N

Figure 19. Loci of minima (A-C) constructed from fitting contours for the three minima of figure 18 for S. cerevisiae Mn SOD. For a description of the contours, see figure 11.

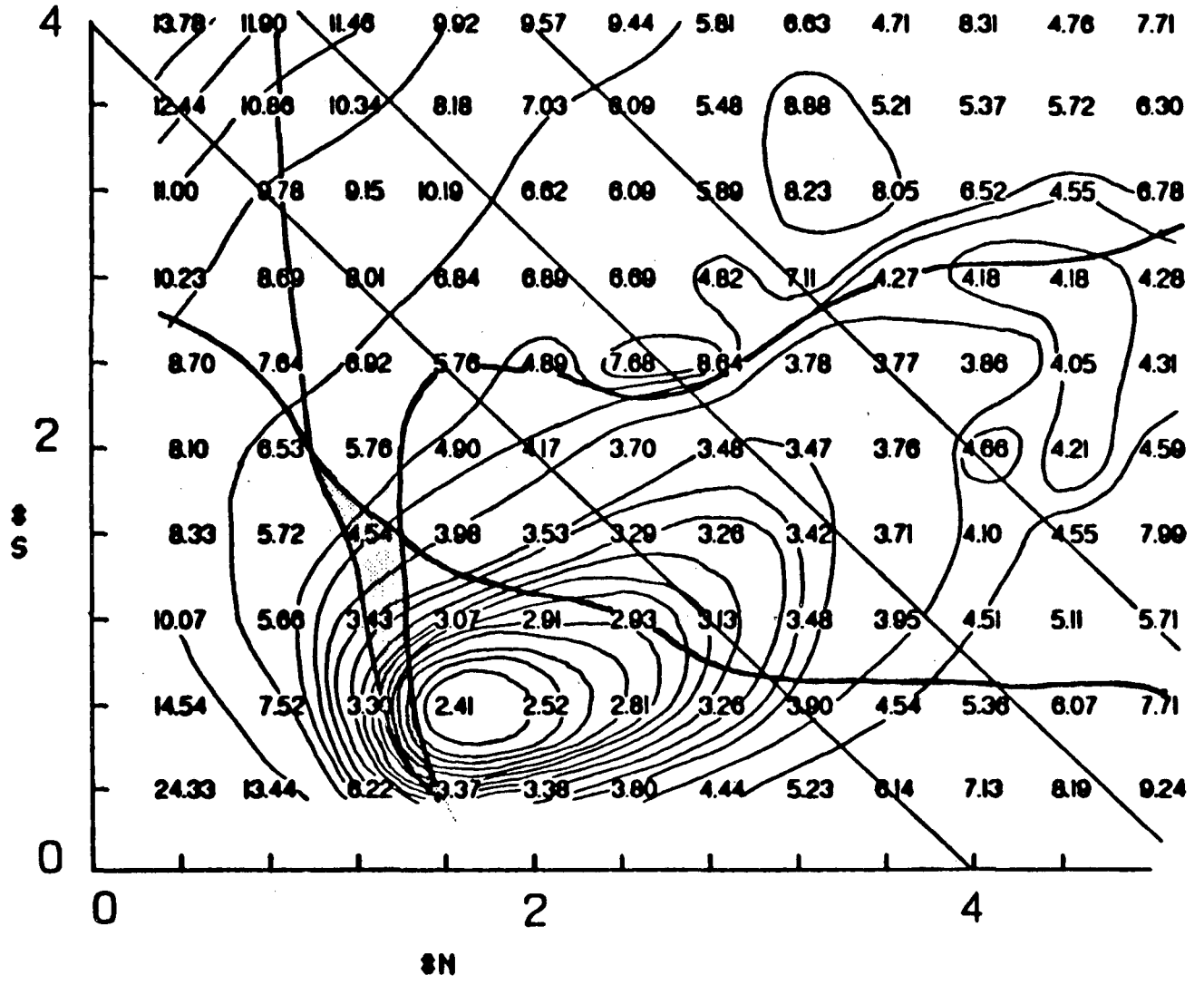
4
2
0
0
2
4
$S
$N
13.78 11.90 11.46 9.92 9.57 9.44 5.81 6.63 4.71 8.31 4.76 7.71
12.44 10.86 10.34 8.18 7.03 6.09 5.48 8.88 5.21 5.37 5.72 6.30
11.00 9.78 9.15 10.19 6.62 6.09 5.89 8.23 8.05 6.52 4.55 6.78
10.23 8.69 8.01 6.84 6.89 6.69 4.82 7.11 4.27 4.18 4.18 4.28
8.70 7.64 6.92 5.76 4.89 7.68 8.64 3.78 3.77 3.86 4.05 4.31
8.10 6.53 5.76 4.90 4.17 3.70 3.48 3.47 3.76 4.66 4.21 4.59
8.33 5.72 4.54 3.98 3.53 3.29 3.26 3.42 3.71 4.10 4.55 7.99
10.07 5.66 3.43 3.07 2.91 2.93 3.13 3.48 3.95 4.51 5.11 5.71
14.54 7.52 3.30 2.41 2.52 2.81 3.26 3.90 4.54 5.36 6.07 7.71
24.33 13.44 6.22 3.37 3.38 3.80 4.44 5.23 6.14 7.13 8.19 9.24

A

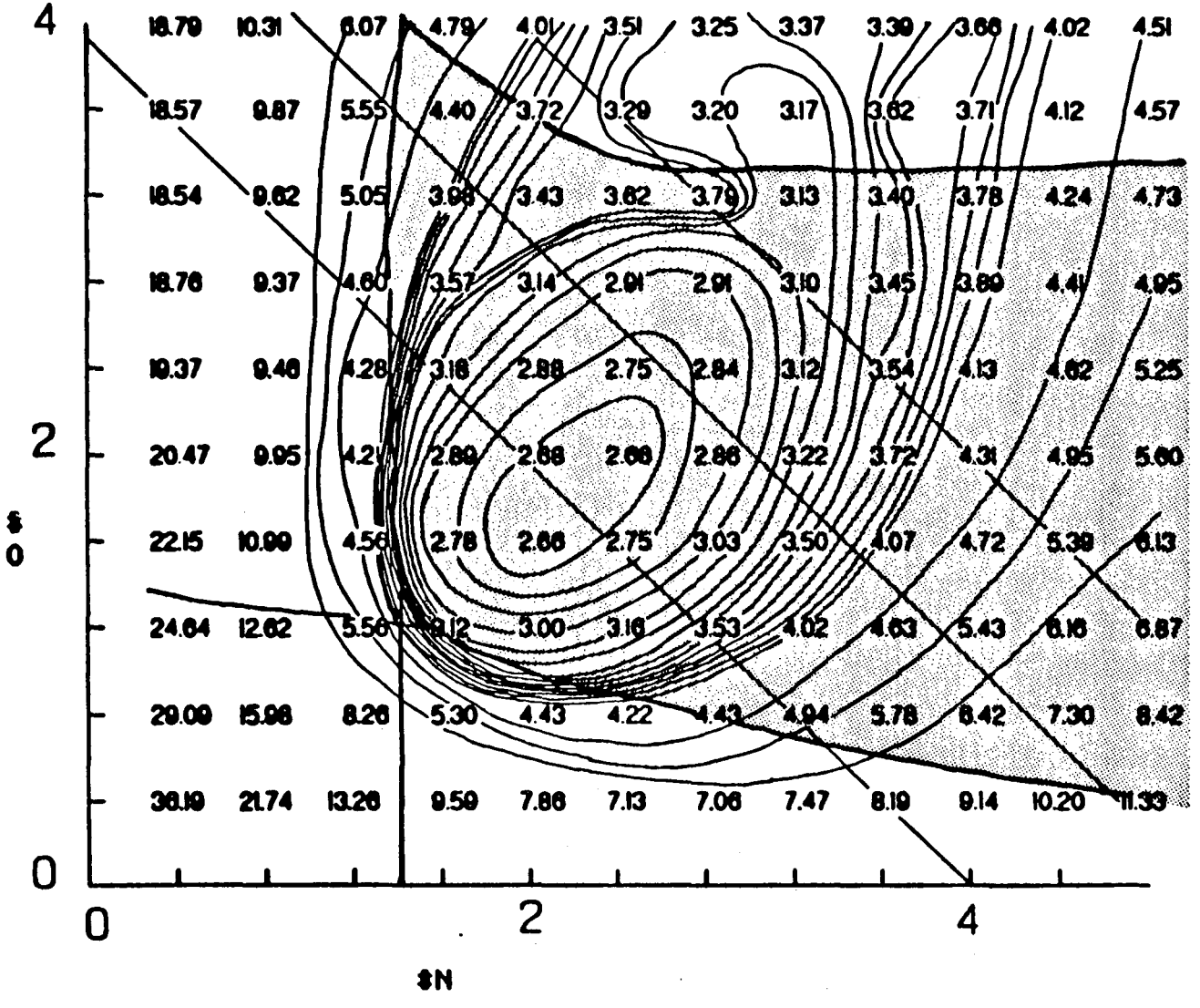
4
2
0
$
0
0
2
4
$N
18.79 10.31 6.07 4.79 4.01 3.51 3.25 3.37 3.39 3.66 4.02 4.51
18.57 9.87 5.55 4.40 3.72 3.29 3.20 3.17 3.62 3.71 4.12 4.57
18.54 9.62 5.05 3.98 3.43 3.62 3.79 3.13 3.40 3.78 4.24 4.73
18.76 9.37 4.60 3.57 3.14 2.91 2.91 3.10 3.45 3.89 4.41 4.95
19.37 9.46 4.28 3.16 2.88 2.75 2.84 3.12 3.54 4.13 4.62 5.25
20.47 9.95 4.21 2.89 2.68 2.66 2.86 3.22 3.72 4.31 4.95 5.60
22.15 10.99 4.56 2.78 2.66 2.75 3.03 3.50 4.07 4.72 5.39 6.13
24.64 12.62 5.56 3.12 3.00 3.16 3.53 4.02 4.63 5.43 6.18 6.87
29.09 15.98 8.26 5.30 4.43 4.22 4.43 4.94 5.78 6.42 7.30 8.42
36.19 21.74 13.26 9.59 7.86 7.13 7.06 7.47 8.19 9.14 10.20 11.33

B

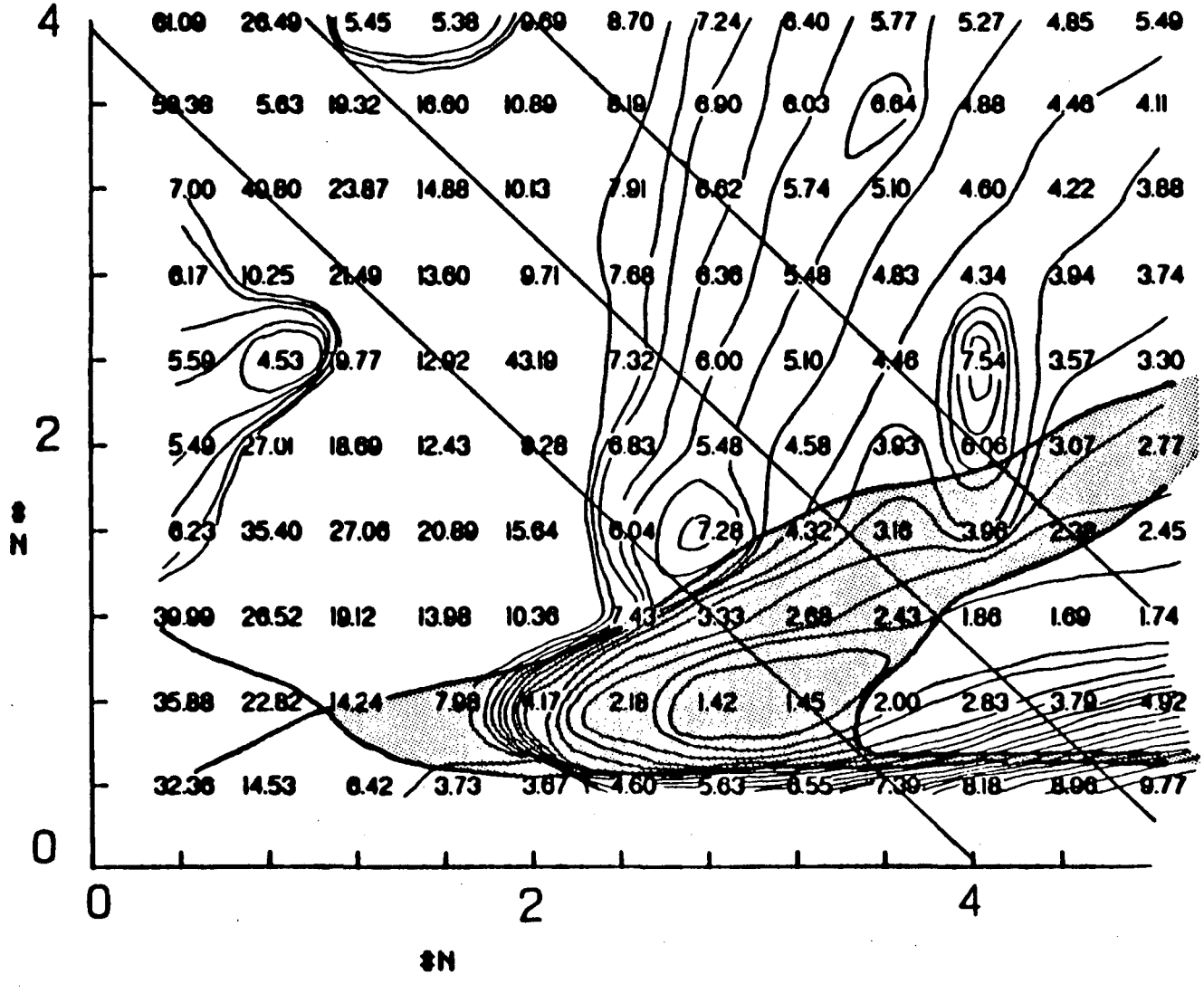
4
2
0
0
2
4
$N
$N
61.09 26.49 15.45 5.38 9.69 8.70 7.24 6.40 5.77 5.27 4.85 5.49
58.38 5.63 19.32 16.60 10.89 8.19 6.90 6.03 6.64 4.88 4.46 4.11
7.00 40.80 23.87 14.88 10.13 7.91 6.62 5.74 5.10 4.60 4.22 3.88
6.17 10.25 21.49 13.60 9.71 7.68 6.36 5.48 4.83 4.34 3.94 3.74
5.59 4.53 19.77 12.92 43.19 7.32 6.00 5.10 4.46 7.54 3.57 3.30
5.49 27.01 18.69 12.43 8.28 6.83 5.48 4.58 3.93 6.06 3.07 2.77
6.23 35.40 27.06 20.89 15.64 6.04 7.28 4.32 3.16 3.96 2.38 2.45
39.99 26.52 19.12 13.98 10.36 7.43 3.33 2.68 2.43 1.86 1.69 1.74
35.88 22.82 14.24 7.98 4.17 2.18 1.42 1.45 2.00 2.83 3.79 4.92
32.36 14.53 6.42 3.73 3.67 4.60 5.63 6.55 7.39 8.18 8.96 9.77

C

atoms of S in the second. No fit to more than 3 total atoms is possible within established limits of the parameters. In particular, the region at the global minimum is characterized by fits in which values of ΔE_0 for the two scattering shells are different by 20 eV or more. Also at variance with the prokaryotic enzyme, minimum B (figure 19b) contains a broad well-defined minimum centered around a 4 or 5 coordinate structure within a large region of acceptable fits. A range of approximately 2-3 N or O atoms in the 1st shell and 1-3 atoms of O or N in the second is indicated. Minimum C in figure 19c is centered about a 4-coordinate fit and inside a long narrow locus, so that the first shell may be composed of 2-4 atoms of N or O and 1 atom of N or O in the second. These results are summarized in table 2.

5. Verification of Sulfur Transferability for a Model Complex

The question of phase and amplitude transferability discussed in chapter 2 should be considered whenever possible. This issue is most acute when using theoretically derived functions or for empirically derived values in which the model complexes are chemically distinct from the structure under study. The existence of nitrogen, oxygen and/or sulfur ligands has been implicated in superoxide dismutase. Adequate fitting results have been obtained by our methods for Mn^{+2} and Mn^{+3} complexs containing nitrogen and oxygen ligands in common chemical forms [35] (see also chapter 3). A protein environment can be expected to

contribute either a thiolate or thio-ether sulfur coordination. Although thioether manganese complexes suitable for EXAFS transferability tests are not available, we have examined a Mn^{+2} thiophenylate complex for this purpose. The complex $Mn^{+2}(S\text{-}Ph)_4^{-2}$ provided by D. Coucouvanis contains 4 sulfur atoms in a tetrahedral geometry with an average Mn-S distance of 2.442 Å and an rms spread of 0.015 Å [36], and is therefore an ideal EXAFS model complex for sulfur phase and amplitude information.

The best single shell fit to the k^3 weighted EXAFS data for this complex is presented in figure 20. It is a fit to sulfur and is considerably better than any fit obtained with other elements. In addition, the predicted Mn-S distance of 2.43 Å is in excellent agreement with the crystal structure value, and requires a factor of 1.96 amplitude correction to give the correct coordination number. Most importantly, the phase and amplitude match to the data is exceptional, indicating that the theoretical functions used for sulfur are completely transferable for this complex.

Figure 20. One-shell fit to the k^3-weighted EXAFS data for the $Mn(S\text{-}C_6H_5)_4(P(C_6H_5)_4)_2$ complex. Data from k = 3.5 to 11.0 $Å^{-1}$ were used in the fit.

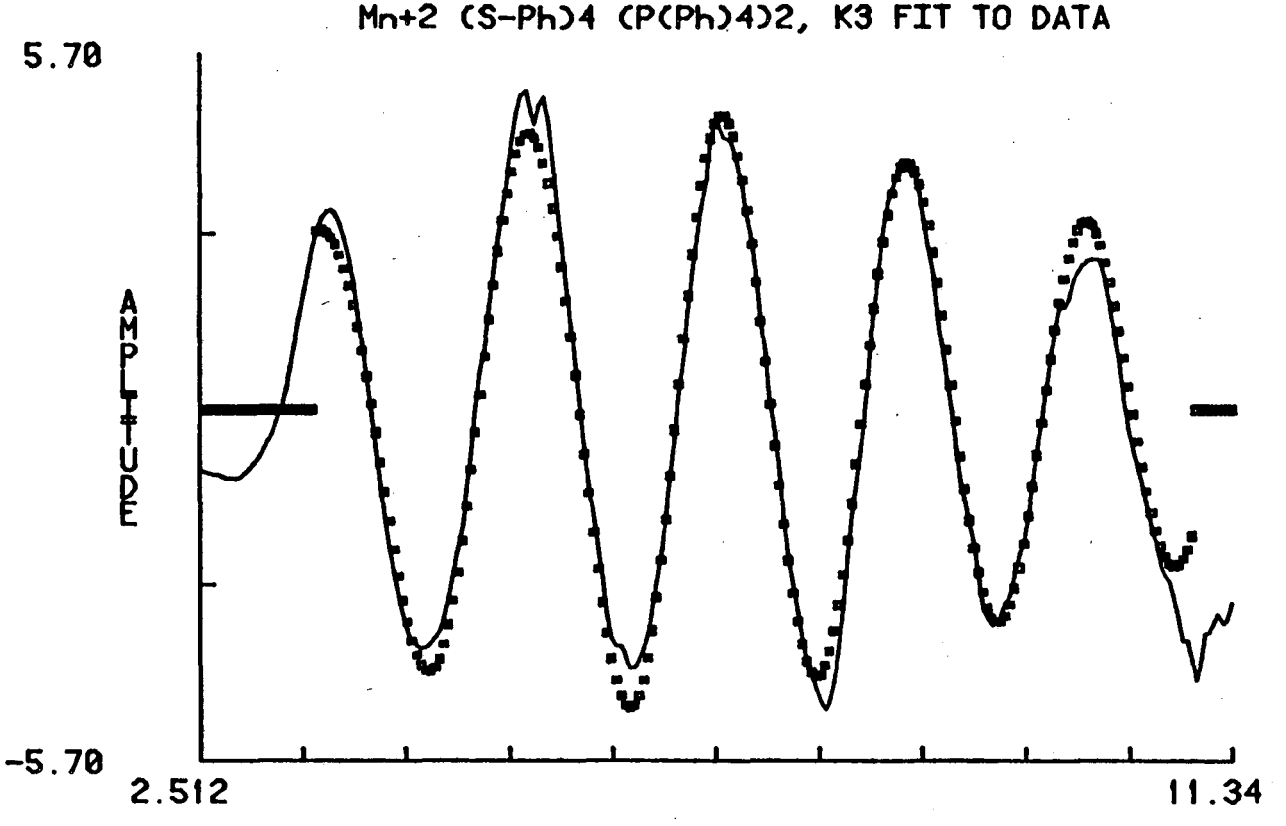

FCN = 34.6303
R = 2.4307513
N = 2.0387480
SIG= -0.0093014
DE0= -4.8451920
ATOM = S

IV. DISCUSSION

The x-ray K-edge data have provided valuable information concerning the metal sites of Mn superoxide dismutase. The inflection positions and magnitude of edge shifts reported for enzymes isolated from both prokaryotic and eukaryotic organisms firmly establish metal oxidation states of +2 and +3 for the reduced and native forms, respectively. This assignment is supported by the ability to simulate the low temperature EPR signal of the reduced enzyme with an electron spin of 5/2 and a nearly axial zero-field splitting tensor.

The absence of a change in the shape of the edge upon reduction indicates that very little structural changes occur during cycling of the enzyme. It may be that the only important structural factors imposed by the enzyme are those that define a needed redox potential. Potentials have been determined for a number of Mn and Fe dismutases and are all found to be very close to +260 mV [17]. This value is optimally placed, because it is roughly midway between the potentials for superoxide oxidation to O_2 and reduction to H_2O_2.

The presence of a weak '1s-3d' transition for native and reduced forms strongly implicate a distorted structure that lacks inversion symmetry. This feature is not observed for completely symmetric Mn^{+2} complexes. Treatment of the yeast enzyme with H_2O_2 does not alter this feature and thus appears simply to result in metal reduction. This is

consistent with the fact that H_2O_2 does not inactivate Mn SOD [31]. On the other hand, the presence of the weak inhibitor N_3^- affects the disappearance of this feature, indicating an alteration in metal coordination. This is not inconsistent with observational differences in the EXAFS data.

EXAFS analysis provides three solutions for the Mn SOD site structure. One of these, minimum C, contains 3 to 5 atoms of nitrogen (or oxygen) at 2.20 Å and 1 to 3 nitrogens (or oxygens) at 1.72 Å for the reduced prokaryotic sample, and predicts for the native eukaryotic enzyme 2 to 4 nitrogen (or O) ligands at 2.13 Å and 1 atom of nitrogen (or oxygen) at 1.67 Å. From a chemical standpoint, this structure is highly unusual because of the 1.7 Å distance, which is shorter than most Mn-N and Mn-O bond lengths by at least 0.2 Å. Proton spin relaxation data [16] have implicated a water molecule in the inner sphere coordination of Mn SOD from E. coli. It is possible that the ligand indicated at 1.7 A represents direct water coordination at a shorter than normal distance.

It is assumed, however, that this 1.7 Å distance is unreasonably short, and a situation arises in which different structures seem to be indicated for the two Mn enzymes studied. For the T. thermophilus enzyme, structure A, containing 3 to 4 N or O atoms at 2.01 Å and 1 to 2 sulfur ligands at 2.32 Å is favored over structure B containing 3-6 N or O ligands at 2.03 Å and 3 or more O or N atoms at 2.46

Å. Even though minimum B exhibits a large spread of possible coordination number, it cannot be reduced to less the 7 atoms without exceeding parameter limits. The yeast EXAFS data implicate two similar structures, one (A) with 1 to 2 N or O scatterers at 1.95 Å and 1 to 2 S atoms at 2.32 Å, and the other (B) with 2 to 3 N or O at 1.97 Å and 1 to 3 O or N atoms at 2.46 Å. However, it is the latter that is more strongly supported by these data, because there is no well-defined locus of acceptable fits for minimum A. In fact, no matter which of the minima are taken, the total number of coordinating ligands predicted for that solution is considerable smaller for the yeast enzyme.

Although different structures may be indicated for SOD in T. thermophilus and S. cerevisiae, a number of factors lead one to treat this with some reserve. The physical properties of the two proteins are somewhat different due to the fact that the prokaryotic dismutases are dimeric while those from eukaryotes are tetrameric, but their spectroscopic properties are very similar. Secondly, the observed EXAFS minima for the two enzymes are quite similar in nature, excluding differences in the number of atoms predicted. The only difference in distances predicted for minima A or B between the two enzymes is the 0.05 Å shorter distance in the first shell for the yeast form, a difference that may be expected from the change in oxidation state.

Examination of the amplitude ratios for scattering shells within a given fit (table 2), demonstrates additional

similarities between corresponding fits of different proteins. For example, minimum A of the prokaryotic enzyme has a shell 1 to shell 2 amplitude ratio of 2.5, and this ratio for minimum A of the yeast enzyme is 2.1. Thus, if the two enzymes have different sites, their effect on the EXAFS must be small, so that similar sets of minima describe both sites. It would then be surprising that the false minimum for one enzyme so closely resembles the correct minimum for the other.

Finally, comparisons of edge spectra should be considered, where evidence both for and against a structural difference can be found. The general edge features are quite similar. The weak '1s-3d' transition is observed for both enzymes and the splitting of the '1s-4p' transition at the edge peak which is clearly seen in the yeast data, is also evident in the reduced T. thermophilus sample. However, it should be noted that the edge positions for the prokaryotic samples occur to lower energy than for yeast by 0.57 and 0.77 eV in native and reduced forms respectively. This shift is deemed significant and is in fact consistent with the differing structures proposed by EXAFS, should they be real. The change in coordination charge between a structure containing 4 nitrogen ligands and one containing 3 nitrogens and 1 sulfur would result in a predicted edge shift of 0.59 eV [29], very close to that observed. Thus the edge data could accommodate such a ligand substitution if the site geometry were not greatly altered.

The EXAFS data for iron substituted T. thermophilus SOD strongly indicate that the iron enters into a coordination that is very similar if not identical to that in the natural Mn form. The only significant difference observed is a 0.1 A contraction of distances expected for the Fe^{+3} versus Mn^{+2}. This is most intriguing in view of the fact that the Fe-substituted protein is inactive, unlike the Mn reconstituted form. Thus the EXAFS results, coupled with the fact that the iron-substituted enzyme exhibits an EPR spectrum that is distinct from natural Fe dismutases, suggests that the metal site for active natural Fe SOD differs in some way from that in Mn SOD. It is proposed either that the Fe SOD requires a different set of ligands contributed by the protein, or that the geometrical placement of the ligands is different. This alteration may be necessary to finely tune the redox potential of each metal for optimum dismutase activity.

Recently, reports have appeared of two Fe dismutases that are unique in that they can be successfully reconstituted with Mn [37,38]. Both the Fe- and Mn-reconstituted enzymes exhibit the spectroscopic features and inhibitor sensitivities characteristic of the respective natural forms. It will be interesting to learn whether this ability exhibited by these enzymes is the result of a specific flexibility at the metal-peptide site which allows different ligating groups or metal-ligand geometry to occur.

Biochemical Implications

Any common peptide is capable of providing nitrogen and oxygen ligands to metals. It is significant, however, that amino acid analysis of manganese SOD from B. stearothermophilus contains no cysteine, but 2 methionine residues [9]. Thus, if the proposed model for the Mn SOD site containing sulfur is correct, it must contain a methionine ligand. Metal-methinonine coordination is known to occur in some enzymes, e.g. cytochrome c and the blue copper centers, although the 2.32 Å distance proposed for SOD is somewhat shorter than observed for these examples. Partial N-terminal amino acid sequences are known for 14 manganese and iron dismutases, and a portion of these sequences is reproduced in table 3. There are a number of complete or nearly complete conservations in this region, in particular His 26, His 30 and His 31. In addition, this region of the sequence is strongly predicted to be α-helical [3]. This would bring all three of these histidine residues to roughly the same face of the helix and may well provide a metal ligation site. Most importantly, a methionine residue at position 23 (E. coli numbering) is present in all Mn SOD sequences except S. cerevisiae. This methionine would also project from the same side of the proposed α-helix, and may thus be a candidate for metal coordination.

Very recently, the crystal structure at 3.1 Å resolution for iron SOD from E. coli has been reported [39]. In this structure, residues 21-40 are indeed observed in a

Table 3.

Organism	type	amino acid sequence (10)
R. Sphaeroides	Mn	A H D A L A A L G M M K E T M E Y H H D I H H D A
T. aquaticus	Mn	P Y E A L E P H I - D A R T M E I H H Q K H H G A
E. coli	Mn	A Y D A L E P H F - D K Q T M E I H H T K H H Q T
B. stearo.	Mn	P Y D A L E P H I - D K E T M N I H H T K H H N T
chicken liver mito.	Mn	D Y G A L E P H I - S A E I M Q L H X X K
human liver mito.	Mn	D Y G A L E P H I - N A Q I M Q L H X S K
S. cerevisiae	Mn	D F G A L E P Y I - S G Q I N E L H Y T
C. vinosum	Fe	E K N A L E P V I - S A E T I E Y H Y G X X H Q T
C. thiosulphato.	Fe	A B B A L Z P H I - X A Z T I G F H Y G K H H A A
P. ovalis	Fe	A H D A L Q P H I - S K E T L E Y H H B K H H N T
E. coli	Fe	A K D A L A P H I - S A E X I E Y H Y G K
P. leiognathi	Fe	A M N A L E P H I - S Q E T L Z Y G Y G K H H B T
D. desulphuricans	Fe	A K D A L X P K I - S A K T F D F X X G K
S. platensis	Fe	D Q D A L E S S K M S A N T L S Y H H G K H H A A

from J. I. Harris et al., Eur. J. Biochem.(1980)106,297-303.

α-helical conformation, and the histidine at position 26 is a ligand to iron. At least 3 additional ligands are present and are contributed by other regions of the peptide.

Although the substitution of asparagine for methionine in S. cerevisiae Mn SOD would appear to argue against the involvement of this position in metal binding, the same could be said of the known histidine ligand at position 26 which is replaced with glycine in the Fe SOD from P. leiognathi. In fact this methionine substitution would be in perfect accord with EXAFS indications that a sulfur coordination at 2.32 Å in the prokaryotic enzyme is replaced with nitrogen or oxygen ligand(s) at 2.45 Å in the dismutase from S. cerevisiae. The ligand replacing sulfur may be contributed by asparagine or a nearby residue. Closer examination of the sequence data shows that in every iron SOD, this methionine is replaced with either leucine or isoleucine. Whether a ligand or not, it appears that the residue at position 23 plays a significant role in the determination of metal specificity. The absence of a potential ligand at this position may indeed serve this role, and provide the proposed difference in metal coordination by Mn and Fe dismutases. It is believed that iron SOD is the more ancient of the two forms. Thus a single point mutation in the leu or isoleu codon to produce methionine may have served as the diverging point in the evolution of these closely related classes of enzymes.

REFERENCES

1. McCord, J.M., Keele, Jr, B.B. and Fridovich, I. (1971) Proc. Natl. Acad. Sci. 68, 1024-1027.

2. Fee, J.A. (1981) Oxygen and Oxy-Radicals in Chemistry and Biochemistry, (Rodgers, M.A.J. and Powers E.L., eds.) Acad. Press, New York, 205-221.

3. Harris, J.I., Auffret, A.D., Northrop, F.D. and Walker J.E. (1980) Eur. J. Biochem. 106, 297-303.

4. Blumberg, W.E., Peisach, J., Eisenberger, P. and Fee, J.A. (1978) Biochem. 17(10), 1842-1846.

5. Richardson, J.J., Thomas, K.A., Rubin, B.H and Richardson D.C. (1975) Proc. Natl. Acad. Sci. 72, 1349-1353.

6. Gaber, B.P., Brown, R.D., Koenig, S.H. and Fee, J.A. (1972) Biochim. Biophys. Acta 271, 1-5.

7. Asada, K., Kanematsu, S., Okaka, S. and Hayakawa, T. (1980) Chemical and Biochemical Aspects of Superoxide and Superoxide Dismutase (Bannister, J.V. and Hill, H.A.O., eds.) Elsevier (Holland), 136-153.

8. Weisiger, R.A. and Fridovich I. (1973) J. Biol. Chem. 248, 3582-3592.

9. Brock, C.J. and Walker, J.E. (1980) Biochem. 19, 2873-2882.

10. Gregory, P.M., Yost, F.J. and Frodovich I. (1973) J. Bacteriol. 115, 987-991.

11. Ose, D.E. and Fridovich, I. (1979) Arch. Biochem. Biophys. 194(2), 360-364.

12. Yamakura, F. and Suzuki, K. (1976) Biochem. Biophys. Res. Commun. 72(3), 1108-1115.

13. Brock, C.J., Harris, J.I. and Sato, S. (1976) J. Mol. Biol. 107, 175-178.

14. Brock, C.J, and Walker, J.E. (1980) Chemical and Biochemical Aspects of Superoxide and Superoxide Dismutase (Bannister, J.V. and Hill, H.A.O., eds.) Elsevier (Holland), 237-241.

15. Yamakura, F., Suzuki, K., Petsko, G.A. and Tsernoglou, D. (1980) ibid., 242-253.

16. Villafranca, J.J., Yost, F.J. Jr, and Fridovich, I. (1974) J. Biol. Chem. 249(11), 3532-3536.

17. Barrette, W.C. Jr, Sawyer, D.T., Fee, J.A. and Asada, K. (1983) Biochem. 22(3), 624-627.

18. Fee, J.A., McClune, G.J., Lees, A.C., Zidovetzki, R. and Pecht, I. (1981) Isr. J. Chem. 21, 54-57.

19. Fee, J.A., Shapiro, E.R. and Moss, T.H. (1976) J. Biol. Chem. 251, 6157-6159.

20. Jaklevic, J., Kirby, J.A., Klein, M.P., Robertson, A.S., Brown, G.S. and Eisenberger, P. (1977) Solid State Commun. 23, 679-682.

21. Thompson, A., Goodin, D., Jaklevic, J., Klein, M.P. and Perez-Mendez V. (1980) 7th Annual SSRL Users Group Meeting, 62.

22. Powers, L., Chance, B., Ching, Y. and Angiolillo, P. (1981) Biophys. J. 34, 465-498.

23. Stern, E.A. and Heald S.M. (1979) Rev. Sci. Instrum. 50(12) 1579-1582.

24. Goodin, D.B., Falk, K.-E., Wydrzynski, T. and Klein, M.P. (1979) 6th Annual SSRL Users Group Meeting, 10-11.

25. Marklund, S. and Marklund, G. (1974) Eur. J. Biochem. 47, 469-474.

26. Keele, Jr, B.B., McCord, J.M. and Fridovich, I. (1970) J. Biol. Chem. 245(22), 6176-6181.

27. Ditlow, C. and Johansen, J.J. (1982) Carlsberg Res. Commun. 47, 71-79.

28. Chance, B., Angiolillo, P., Yang, E.K. and Powers, L. (1980) FEBS lett. 112, 178-182.

29. Kirby, J.A., Goodin, D.B., Wydrzynski, T., Robertson, A.S. and Klein, M.P. (1981) J. Amer. Chem. Soc. 103, 5537-5542.

30. Shulman, R.G., Yafet, Y., Eisenberger, P. and Blumberg, W.E. (1976) Proc. Natl. Acad. Sci. 73(5), 1384-1388.

31. McEuen, A.R., Hill, H.A.O., Dring, G.J. and Ingnam, G.S. (1980) Chemical and Biochemical Aspects of Superoxide and Superoxide Dismutase (Bannister, J.V. and Hill, H.A.O., eds.) Elsevier (Holland), 272-283.

32. Peisach, J., Powers, L., Blumberg, W.E., and Chance, B. (1982) Biophys. J. 38, 277-285.

33. Slykhouse, T.O. and Fee, J.A. (1976) J. Biol. Chem. 251, 5472-5477.

34. Twilfer, H., Gersonde, K., Meier, B. and Schwartz, A.C. (1980) Chemical and Biochemical Aspects of Superoxide and Superoxide Dismutase (Bannister, J.V. and Hill, H.A.O., eds.) Elsevier (Holland), 168-175.

35. Kirby, J.A. (1981) Ph.D. Thesis, University of California, Berkeley.

36. Swenson, D., Baenziger, N.C. and Coucouvanis, D. (1978) J. Amer. Chem. Soc. 100, 1932-1934.

37. Gregory, E.M. and Dapper C.H. (1983) Arch. Biochem. Biophys. 220(1), 293-300.

38. Meier, B., Barra, D., Bossa, F., Calabrese, L. and Rotilio, G. (1982) J. Biol. Chem. 257(23), 13977-13980.

39. Stallings, W.C., Powers, T.B., Pattridge, K.A., Fee, J.A. and Ludwig, M.L. (1983) Proc. Natl. Acad. Sci. 80, 3884-3888.

CHAPTER 5

The Nature and Localization of the Multi-line EPR Signal in Photosynthetic Membranes

I. INTRODUCTION

Oxygen evolution by algae and green plants is one of the most intricate yet least understood of the light driven, electron transfer reactions of photosynthesis. Kinetic studies have established the existence on at least a functional level of five states, S_0-S_4, involved in the stabilization and storage of oxidizing equivalents generated at the photosystem II reaction center [1]. It is also widely held that membrane-bound manganese plays a role in this process [2]. Of the 4 - 6 manganese per photosynthetic unit contained in isolated chloroplast membranes, approximately two-thirds has been observed to be converted to an EPR visible form during inactivation of the oxygen evolution complex (OEC) by a number of methods including alkaline Tris washing [3]. It has been proposed that this manganese is released into the aqueous medium of the inner thylakoid space, and that its disappearance upon reactivation of oxygen evolution is due to reincorporation of the manganese

into the membrane [4,5].

More recent studies, however, have justified a rexamination of the structure and composition of the oxygen evolution complex. Some experiments appear to contradict earlier work on manganese content, release and requirements in the water splitting reactions. A study of right-side out and inside out spinach thylakoids indicates that manganese release by Tris inactivation is not specifically to the inside of the enclosed membrane [6]. Both of these preparations contained 6-7 Mn per reaction center, and 50-60% of this was removed from the membrane by washing after inactivation. This removed manganese was not required for reactivation to 60% of original activity. Similar results have also been reported for photosystem II preparations from spinach prepared by phase-partition methods [7]. Other work has shown the specific release of peptides by high salt washing [8] and treatment with alkaline Tris buffer [7,9,10] that are associated with the functional stability of the OEC. Although reconstitution with one of the released peptides has been shown to restore oxygen evolution in depleted membranes [8], none of these peptides appears to contain manganese as isolated.

On the other hand, more evidence for the direct involvement of manganese has been provided with the discovery of a light-induced EPR signal observed at low temperature in spinach chloroplasts [11]. This signal, containing 19 or more lines, was assigned to a manganese

species on the basis of its hyperfine splittings. Simulation of the hyperfine structure is consistent with a weakly exchange-coupled Mn(III,IV) binuclear or Mn(III,III,III,IV) tetra-nuclear manganese center [12]. The simulations of the latter more closely resemble the observed spectra. The temperature dependence for the light-induced formation and subsequent decay of this signal indicates that the signal is correlated with the presence of the S_2 state of the OEC [13]. Studies on whole chloroplasts have shown that treatments that effect oxygen evolution, including alkaline Tris washing, cause the disappearance of this signal [14]. It was concluded that the signal arises from the OEC because restoration of PSII electron flow using artificial donors could be accomplished without the return of the signal.

It is not known, however, whether the signal can be generated in inactivated preparations in which water oxidation has been restored. Even though the nature of the Tris releasable fraction of manganese is again controversial, it would be of great interest to determine whether the EPR signal species resides with this fraction, or that which remains bound to the membrane after extraction. We have investigated the behavior of this signal during Tris inactivation and reactivation procedures to determine whether it correlates with oxygen evolution capacity, manganese content or both. Such experiments could be important in deciding whether the signal species is a direct participant in electron transfer or serves in another ancilliary role.

The physical nature of the EPR signal species and the structural factors that determine its appearance are also not clear. The signal may arise from photo-oxidation of a manganese complex. It could also arise by oxidation of a nearby species, causing an uncoupling of spin states, changes in spin relaxation properties, or simply a geometrical perturbation of the manganese environment. We have addressed these questions by examination of the X-ray K-edge fluorescence excitation spectra of photosynthetic membranes under conditions that exhibit this EPR signal. This technique can be used to characterize changes in manganese ligand geometry and electronic structure [15,16] that accompany S state conversion.

II. MATERIALS AND METHODS

Broken chloroplasts were prepared from destemmed market spinach by grinding in a Waring blender for 10-15 s at 4°C in a buffer containing 0.4 M NaCl, 20 mM Tricine (pH 8.0), 2 mM $MgCl_2$ and 5 mM EDTA. The homogenate was strained through 8 layers of cheesecloth and centrifuged at 4°C for 10 min. at 6000xg. The pellet was resuspended in 0.15 M NaCl, 20 mM Tricine (pH 8.0), and 5 mM $MgCl_2$ and spun at 500xg for 30s. The supernatant was decanted through a Kimwipe and centrifuged at 6000xg for 10 min. The pellet was washed in the resuspension buffer and pelleted as above. This chloroplast pellet was suspended in the appropriate measuring or treatment buffers for use.

Preparation of oxygen-evolving PSII sub-chloroplast membranes was done by one of two published methods [17,10], with the exception that all buffers used were based on 50 mM MES (pH 6.0), 15 mM NaCl and 5 mM $MgCl_2$.

Tris inactivation of chloroplast or PSII preparations was accomplished by suspending chloroplasts in 200 mM Tris (pH 8.5) and 1 μM gramicidin D. The mixture was incubated in ambient light at 4°C, while O_2 evolution activity measurements of aliquots were performed. When the activity had declined to 20% of control rates (approximately 40 min.) the inactivation was quenched by adding 0.1 M HCl to achieve pH = 7.6. Membranes were recovered by centrifugation at 6000xg for 10 min., and washed in 0.4 M sucrose, 50 mM HEPES (pH 7.6), and 10 mM NaCl for chloroplast samples and in 50 mM

MES (pH 6.0), 15 mM NaCl and 5 mM $MgCl_2$ for PSII preparations. Reactivation of O_2 evolution activity was accomplished by suspension in the above buffers containing 0.3 mM DCPIP and 2 mM ascorbate, followed by incubation in ambient light. After recovered O_2 activity had reached a plateau (approximately 40-60 min.), the membranes were collected by centrifugation.

Rates of oxygen evolution were measured using a Clark-type oxygen electrode biased at -0.6 V vs. Ag|AgCl. Illumination was with a 200 W quartz lamp filtered with Corning 3-68 and 1-56 glass filters. Samples were suspended to 20-30 µg Chl/ml in 50 mM HEPES (pH 7.6), 20 mM NaCl, 5 mM $MgCl_2$, 1 µM gramicidin D, and 2 mM $K_3Fe(CN)_6/K_4Fe(CN)_6$ for chloroplasts, and in 20 mM MES (pH 6.0), 20 mM NaCl, 5 mM $MgCl_2$, 500 µM DMBQ and 2 mM $K_3Fe(CN)_6/K_4Fe(CN)_6$ for PSII membranes. Chlorophyll concentration was determined by the method of Arnon [18].

EPR measurements were performed on a Varian E-109 spectrometer equipped with a model E102 microwave bridge. Samples were run at 10 - 12°K in an Air Products liquid helium cryostat at a microwave frequency of 9.12 GHz and using 100 KHz field modulation. Other instrument settings are provided with figure legends. Manganese analysis by low temperature EPR was determined by measurement of the amplitude of the lowest field hyperfine transition of $Mn^{+2}(H_2O)_6$ in samples diluted 1:1 with 0.1 M HCl and calibrated against controls in the same buffer containing

Mn^{+2} as an internal standard. This is important because the signal amplitudes are somewhat sensitive to the type and concentration of buffers used. As will be discussed in chapter 6, we have observed that not all forms of Mn^{+2} in photosynthetic membranes exhibit the g=2 EPR signal. Another signal occurring at low magnetic fields is observed at low temperature (<77°K) and is attributed to Mn^{+2} bound to membrane protein components. None of the acid digested samples reported exhibited this EPR signal. Measurements of the multi-line EPR signal were made by suspending samples at 2-5 mg Chl/ml in buffer containing 50% glycerol. Samples were incubated at 4°C for specified times in complete darkness before equilibration at -90°C in a Varian V 6040 NMR temperature controller and illuminated with a 400 W tungsten lamp through a 5 cm water filter. After illumination, samples were immediately frozen and stored at 77°K. All signal intensities were corrected for EPR tube volume.

X-ray absorption edge spectra were collected at the Stanford Synchrotron Radiation Laboratory, Stanford, CA. on wiggler beam line VII-3 during dedicated operation (3.0 GeV electron beam energy, 60-80 ma current) and using a Si<111> double crystal monochromator. The ratio of the fluorescence and incident intensities were measured using an NE104 plastic scintillation array similar to that described by Powers et al. [19], and equipped with Cr fluorescence filters and soller slit assembly [20]. Energy calibration was maintained by simultaneous measurement of the reference pre-edge feature

of $KMnO_4$ at 6543.3 eV [21].

X-ray absorption samples were prepared by layering pellets of spinach PSII membranes in 50% glycerol, 50 mM MES (pH 6.0), 15 mM NaCl and 5 mM $MgCl_2$ at approximately 8 mg chl/ml (100-200 μM Mn) into narrow lucite sample cells with an open cavity of dimensions 5x30x2 mm. Dark adaptation, illumination and EPR measurements were carried out directly in these sample cells. The exact incubation and illumination protocols are described with the results. During X-ray measurements, samples were suspended in a jacketted N_2 boil-off jet maintained at -80 to -100°C in semi-darkness. After pre-edge background subtraction, the x-ray edge position was taken as the inflection point of the edge. This was calculated by fitting a quadratic polynomial to each point in the spectrum over a fixed 8 eV energy region evenly spaced about the point. The derivative of the fitted polynomial was taken as an approximation to the true first derivative at that point.

III. RESULTS

Multi-line EPR signal in PSII preparations

The assignment of the multi-line EPR signal to a species involved in water oxidation effectively requires that it be observable in active PSII preparations lacking PSI. Such a signal has been observed for PSII particles of P. laminosum, although its presence was not entirely reproducible [22]. Under intense continuous illumination for 30 s at -90°C and in the presence of buffer containing 50% glycerol we easily observe this signal for the Triton X-100 PSII preparations from spinach. This is shown as part of figure 1. It is interesting that the generation of this signal is completely reproducible provided that dark adaptation times in excess of 30 min. at 0°C are given prior to illumination. It has been reported that the S_3 relaxation time for this PSII preparation is approximately 400 s at 23°C, and that deactivation of S_2 is also exceedingly slow [23]. If this is correct, dark adaptation for 5-10 min at 0°C, which is the normal protocol for spinach chloroplasts, would be insufficient. This may explain the unusually long dark adaptation times necessary for the consistent generation of the signal in this material and the difficulties experienced in other preparations.

Effects of Tris Inactivation and Reactivation on the State of Manganese

Chloroplast membranes isolated in high salt and uncoupled with 1μM gramicidin were Tris washed under mild

conditions [7] allowing the process to be monitored. The inactivation was quenched by reducing the pH to 7.0 when the activity had dropped to 20% of that observed initially. The course of the reactivation of oxygen evolution in the presence and absence of 10 mM Mn^{+2} was also monitored. Quantities of Mn^{+2} observed by EPR after acid digestion and oxygen evolution rates for these samples are presented in table 1. In agreement with recent studies [6,7], we observe a loss of 58% of membrane bound manganese to a value of 2.8 Mn/400 Chl associated with 75-80% inactivation. Reactivation to 60% of the original activity can be accomplished with reduced DCPIP in the absence of added manganese. During this process the observed quantity of Mn^{+2} falls further to 21% of the original, leaving only 1.4 Mn/400 Chl. Also noteworthy is the observation that the presence of Mn^{+2} in the reactivating medium causes a variable but significant stimulation of reactivation. Because of a large amount of unspecifically bound Mn that could not be washed free for these reactivated membranes without significant loss of activity, it was not possible to obtain a meaningful Mn content. After 30 s of continuous illumination at -90°C, the multi-line EPR spectrum was observed for control samples, but no trace of this signal was seen in the Tris-treated or reactivated samples.

Similar results were observed with the PSII preparation. Even partial inactivation to 35% of control rates completely abolished the EPR spectrum. For this sample virtually 100%

Table 1. Tris inactivation/reactivation of spinach chloroplasts. O_2 evolution rates and quantities of Mn^{+2} observed by EPR after acid digestion are shown for active and Tris-washed chloroplast membranes. Also shown are Tris-washed membranes reactivated in the presence and absence of 10 mM $MnCl_2$. Conditions for Tris inactivation and reactivation are descrived in Materials and Methods. The multi-line EPR signal was observed only for the active control samples.

Sample	O_2 rate (μmoles O_2/mg Chl hr)		Mn^{+2} observed by EPR by acid digestion. (per 400 Chl)	Multi-line EPR + observed,-not	
	Expt 1	Expt 2	Expt 1	Expt 1	Expt 2
active chloroplasts	240 (100%)	106 (100%)	6.7 (100%)	+	+
Tris treated "	60 (25%)	20 (19%)	2.8 (42%)	-	-
Reactivated -Mn^{+2}	139 (58%)	60 (57%)	1.4 (21%)	-	-
Reactivated +Mn^{+2}	211 (88%)	67 (63%)	-		

reactivation was achieved after a 45 min. incubation in ambient light and in the presence of 0.3 mM DCPIP and 2 mM ascorbate, yet the multi-line EPR signal was not observed (figure 1).

X-ray Absorption Experiments

We have measured the x-ray absorption k-edge for spinach PSII preparations for dark adapted and for illuminated samples exhibiting the multi-line EPR signal. The samples used had high rates of oxygen evolution (526 μmoles of $O_2 mg^{-1}{}_{chl}{}^{-1}hr^{-1}$ at pH 6.3 with DMBQ as acceptor) and a manganese content of 0.0143 Mn/chl. This corresponds to 3.6 Mn per reaction center assuming a photosynthetic unit of 250 Chl [24]. Sample A was prepared in state S_1 by illumination for 60 s at -90°C followed by dark adaptation for 1 hr at 0°C. This pre-illumination was given in order to reduce the S_0 concentration which would otherwise be present in about 25% of the OEC centers. Samples B and C were prepared in state S_2 by first generating S_1 according to the above procedure followed by 60 s illumination at -90°C. For sample D, an attempt to generate S_3 was made in which S_2 was prepared as above, followed by warming the sample in the dark for 5-10 s to 0°C. This was then illuminated for 60 s at -90°C. All samples were immediately frozen and stored at 77°K.

The S_3 protocol was based on the assumption that only one equivalent is transferred at -90°C because reoxidation of Q^- is blocked. Any additional excitation reaching the reaction center would result in rapid charge recombination

Figure 1. Multi-line EPR spectra observed for spinach Triton-X100 PSII preparations. Treated and untreated membrane samples were suspended to 4 mg chl/ml in 50 mM MES (pH 6.0), 15 mM NaCl, 5 mM $MgCl_2$ and 50% glycerol. Dark adaptation and illumination protocols are described in materials and methods. EPR specta were recorded at 9.19 GHz, 100 mW microwave power, and using a 100 KHz field modulation of 32 G. Sample temperature was 12°K, and the receiver gain (4×10^3) was the same for all spectra. The trace for dark adapted PSII membranes is shown in A, and for the same membranes after 30 s continuous illumination at -90°C in B. Tris inactivated PSII membranes (giving 35% of control O_2 evolution rate) are shown in C, and after reactivation to 100% of control activity in D. For both C and D, the samples were dark adapted and then illuminated exactly as described for sample B.

Spinach PSII Multi-line EPR Signals

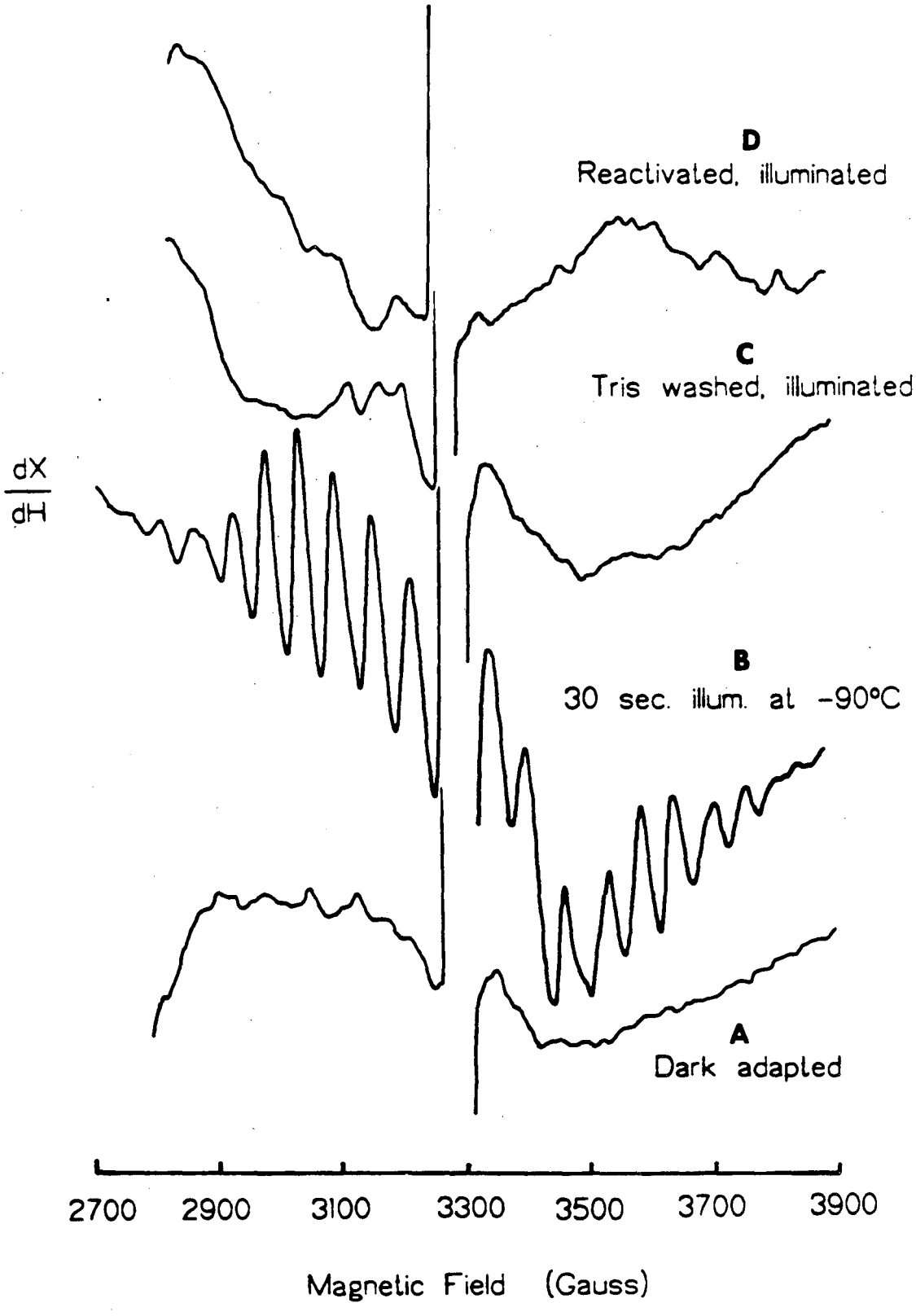

between $P680^+$ and I^-. At 0°C the reoxidation of Q^- is faster than S_2 relaxation, so that brief warming to this temperature may prepare the reaction center for another one-equivalent transfer.

EPR spectra were recorded for samples A-D prior to x-ray absorption measurements. Figure 2 shows the absence of the multi-line signal in the S_1 sample, its presence in the two S_2 samples and a significant reduction of the amplitude for the S_3 sample. The amplitudes of the EPR signals measured before and after x-ray data collection are presented in table 2. Only sample B showed a significant change in signal amplitude. No effects on the signal amplitude after repeated cycling between the storage temperature of 77°K and the measurement temperature of 175°K was observed for control samples.

It is difficult to prepare x-ray absorption samples of photosynthetic membranes that have been uniformly illuminated with saturating light because of the large difference in the sample absorbance at visible and x-ray wavelengths. The minimum manganese concentration required for an edge experiment ($\approx 200\mu M$) requires chlorophyl concentrations of about 10 mM. At this concentration, approximately 90% of an incident actinic illumination at 500 nm is absorbed in the first 0.1 mm of the sample. Three crucial factors were necessary in order to perform these experiments sucessfully. The use of membrane preparations lacking PSI is of aid in that the photosynthetic unit size

Figure 2. Multi-line EPR spectra observed for x-ray absorption edge samples of spinach PSII sub-chloroplast membranes. Samples were pellets (approximately 8 mg chl/ml) centrifuged out of the buffer of figure 1. EPR spectra were recorded at 14°K, using 100 mW microwave power at 9.22 GHz anda 100 KHz field modulation of 32 G. Illumination protocols for the various S states are described in the text. The samples are; sample A, S_1; sample B, S_2; sample C, a second S_2; sample D, S_3.

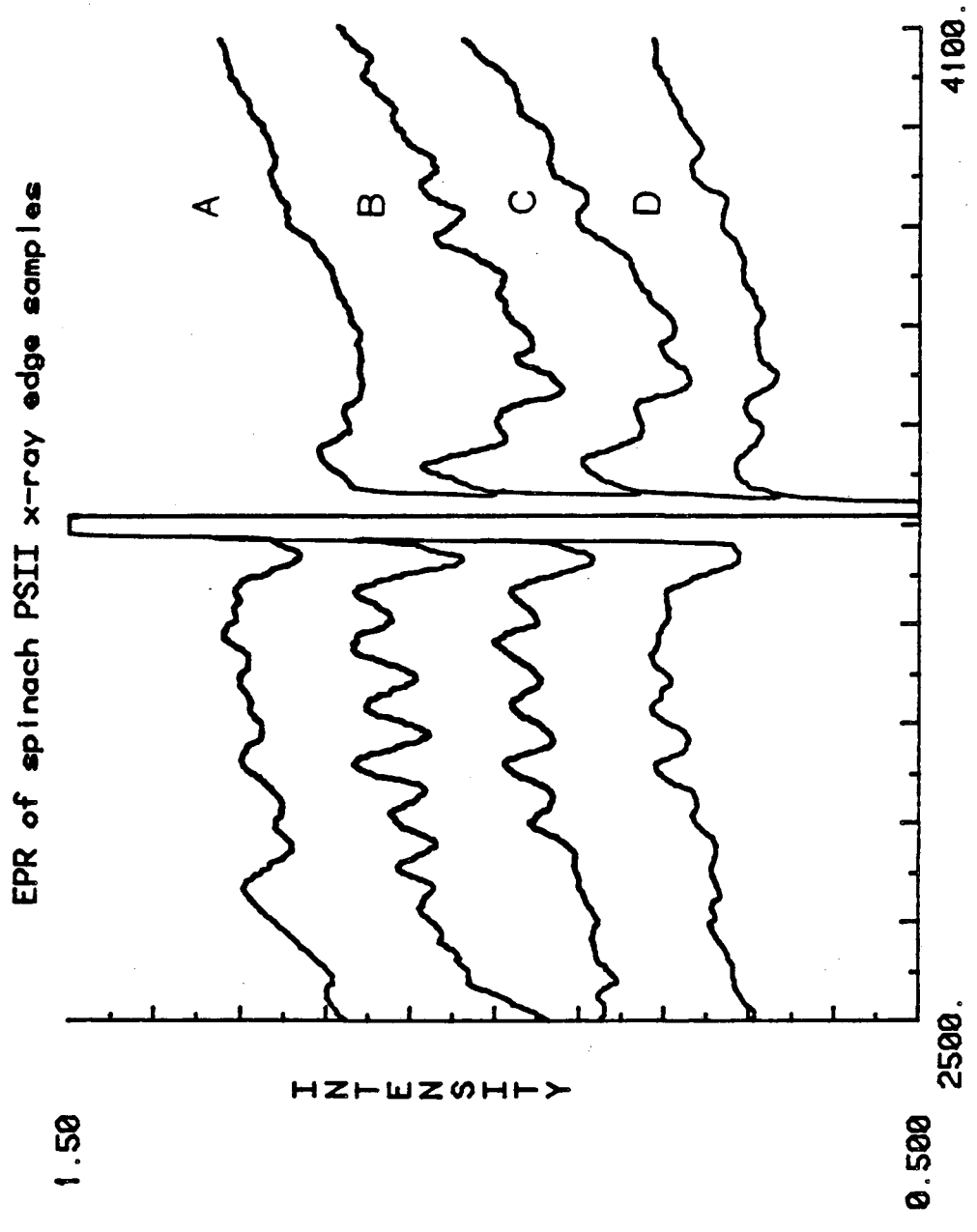
EPR of spinach PSII x-ray edge samples
A
B
C
D
1.50
0.500
INTENSITY
2500.
4100.
FIELD STRENGTH (GAUSS)

Table 2. Multi-line EPR amplitude for X-ray edge samples of spinach PSII membranes. EPR amplitudes before and after XAS were calibrated with an S_2 sample that was not exposed to the X-ray beam.

Sample	MLS amplitude (arbitrary units)	
	Before XAS	After XAS
A (S_1)	1.5	1.7
B (S_2)	5.5	2.9
C (second S_2)	4.0	0.0 *
D (S_3)	2.0	2.3

* This is Sample E (Relaxed to S_1).

is smaller, and therefore a greater fraction of the incident illumination is channeled into PSII. Secondly, in addition to providing increased signal-to-noise, fluorescence detection techniques are more surface sensitive because of strong self absorption. 90% of the fluorescence signal arises in the first 0.5 mm of a water containing sample at 6.5 KeV. Finally, and most importantly, is the ability to block electron transfer by illumination at low temperature so that S_2 will not advance after it is formed, allowing its accumulation by continuous illumination. Using sample thicknesses of approximately 0.5 mm and illumination from both sides, it was found that no increase in the multi-line EPR signal was observed for illumination periods greater that 60 s. Nevertheless, it must be noted that the intensity of actinic light was far from uniform across the sample depth.

The x-ray K-edge spectra for these samples are presented in figure 3. The S_2 sample (B) shows a significantly broader principal absorption maximum and (possibly as a result) a shift to higher energy relative to the S_1 sample (A). The second S_2 sample (C) edge is consistent with the first and a 1 hr dark adaptation of this sample (labeled E) regenerates the edge observed for S_1. The K-edge for S_3 (D) is quite similar to those observed for S_2. The small difference in shape that is observed may not be meaningful because differences of a similar magnitude are also observed for the two S_2 samples. This probably reflects small differences in the S state composition from sample to sample.

Figure 3. X-ray absorption edge spectra for spinach PSII preparations. Data were collected at -80° to -100°C as described in Materials and Methods. Each edge is the sum of approximately 20-30 individual 20 min. scans. The samples are; sample A, S_1; sample B, S_2; sample C, a second S_2; sample D, S_3; and sample E, S_1 prepared from sample C after its edge was recorded by dark adaption for 1 hr at 0°C in total darkness. A smoothed curve (solid line) is drawn through the data points to aid in the visualization of statistically significant features.

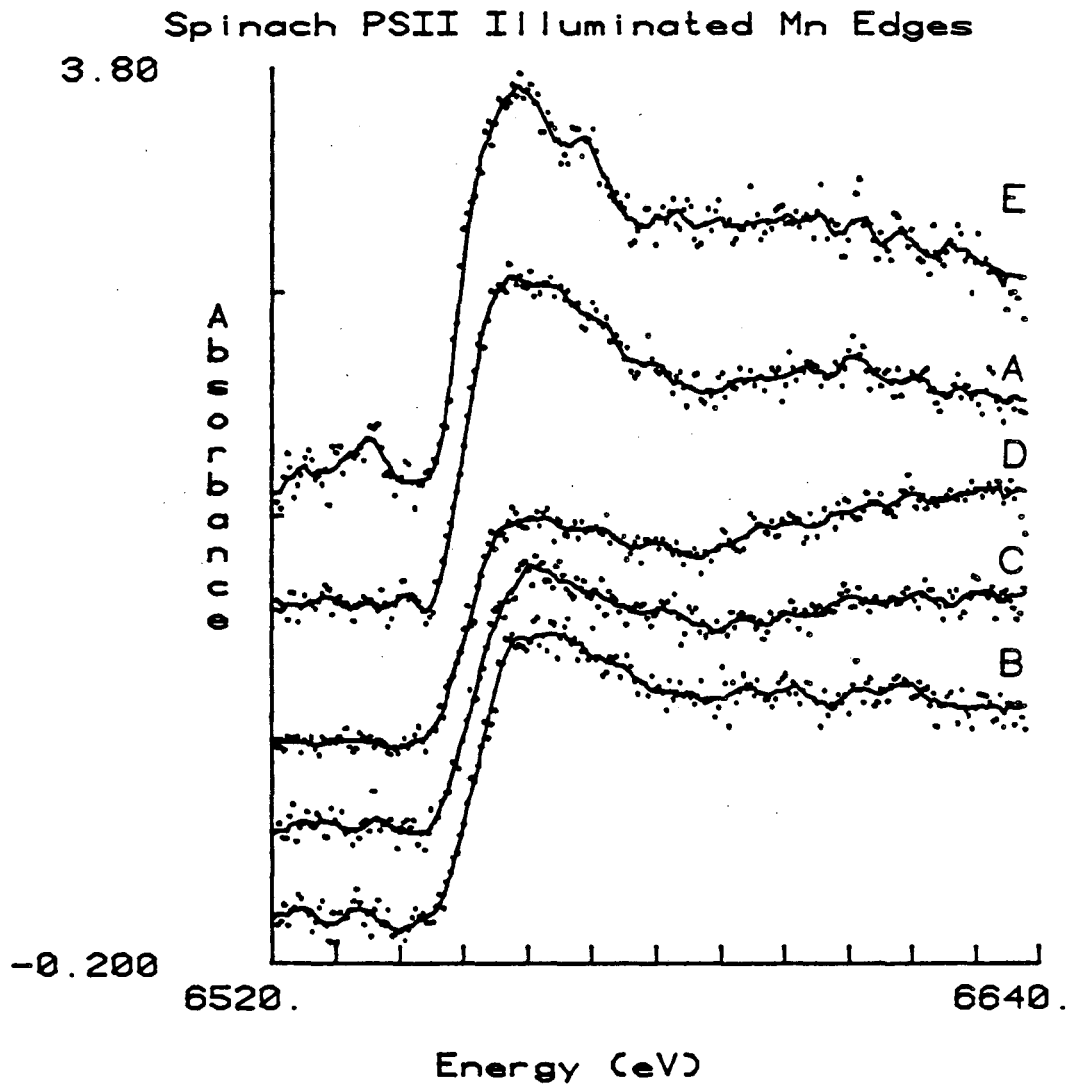
Spinach PSII Illuminated Mn Edges
3.80
-0.200
Absorbance
E
A
D
C
B
6520.
6640.
Energy (eV)

The edge inflection point positions for these spectra are shown in table 3, and show a distribution of values. Each of the positions differ by much more than the estimated uncertainty of 0.2 eV indicating again a slightly different S state composition for each sample. Evidence for this is shown in figure 4 which shows that the edge inflection points for S_1 and S_2 samples are in fact well correlated with the observed multi-line EPR signal intensities.

The lowest edge inflection is observed for the freshly dark-adapted S_1 sample, and the highest inflection for one of the S_2 samples. The difference between these is 2.51 eV. The average edge shift observed between the S_1 and S_2 samples is 1.78 eV. For comparison, the edge positions reported previously [15] for selected manganese samples are presented in table 4. It is seen that the average S_1 inflection point is similar to and slightly higher than that reported for dark adapted whole chloroplasts, and the S_2 samples give an average edge shift that is very similar to that observed in a Mn(IV,IV) μ-dioxo dimeric complex.

Table 3. K-edge inflection point energies for spinach PSII samples. Derivatives were obtained from a 25 point sliding fit to a 2nd order polynomial (3 eV per fit).

Sample	K-edge inflection (eV)	
A (S_1)	6549.88	
		Avg. S_1 = 6549.53
E (S_2 relaxed to S_1)	6549.17	
B (S_2)	6551.68	
		Avg. S_2 = 6551.31
C (Second S_2)	6550.93	
D (S_3)	6550.19	

Table 4. K-edge inflections obtained from Kirby et al. [15].

Sample	K-edge inflection (eV)
Dark adapted whole chloroplasts	6549.1
Tris washed chloroplasts	6547.9
Mn(III) $(acac)_3$	6550.7
$[Mn\ (IV,IV)\ (Phen)_2]_2\ O_2$	6551.0

Figure 4. A plot of the amplitudes of the multi-line EPR signal for illuminated Spinach PSII membrane samples versus the K-edge inflection point energies.

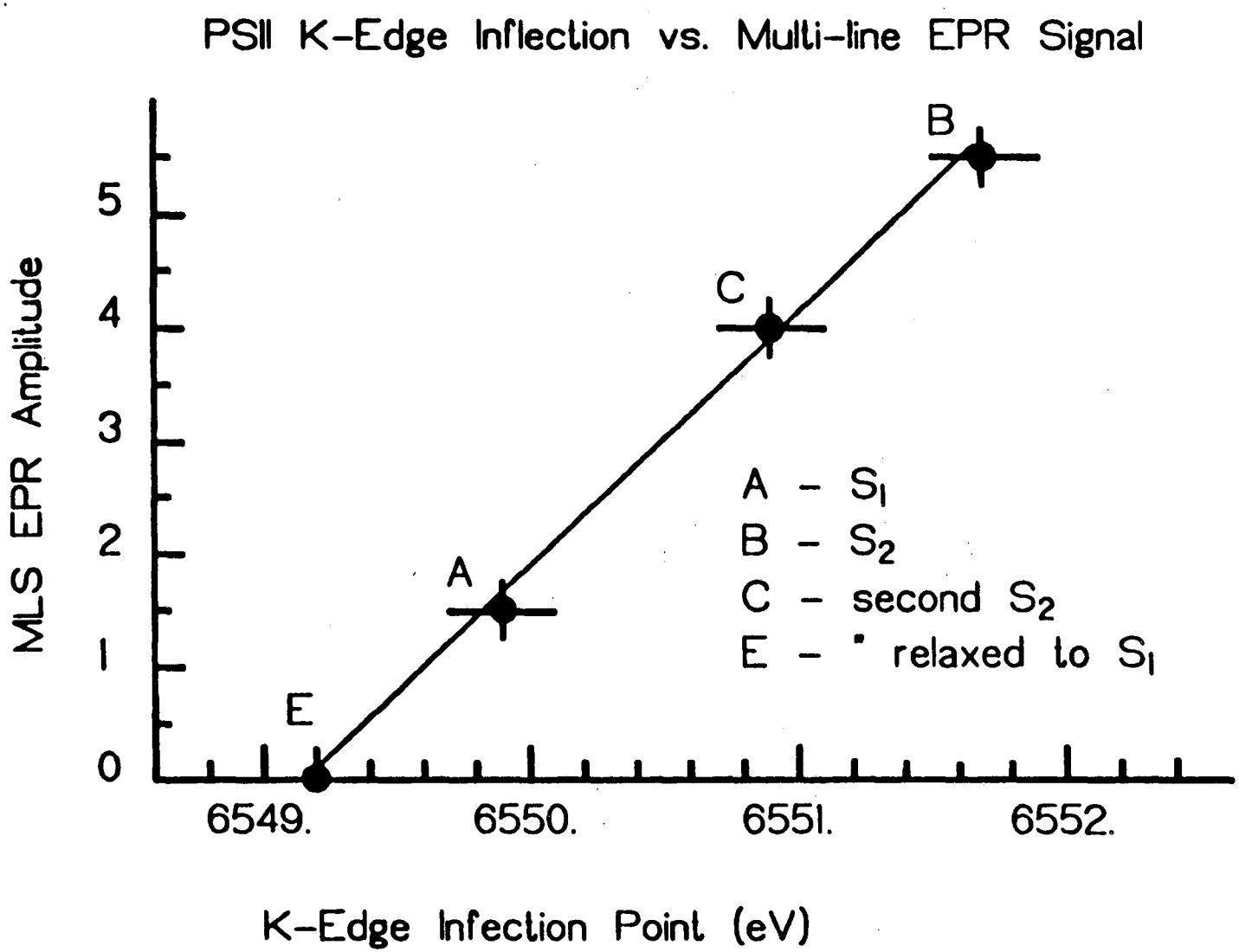
PSII K-Edge Inflection vs. Multi-line EPR Signal
MLS EPR Amplitude
0
1
2
3
4
5
6549.
6550.
6551.
6552.
K-Edge Infection Point (eV)
A
B
C
E
A - S1
B - S2
C - second S2
E - * relaxed to S1

IV. DISCUSSION

The rates of oxygen evolution and the quantities of Mn^{+2} observed by EPR for Tris-inactivated chloroplasts and subsequently reactivated samples are similar to those recently reported [6,7]. In those studies, it was concluded that the Tris-releasable fraction of manganese was not required for oxygen evolution. However, it is possible that the quantities determined by these methods do not represent all of the chloroplast manganese and may thus be systematically low. In chapter 6 it will be shown that some complexed forms of Mn^{+2} give rise to EPR signals at very low magnetic fields, and that these signals can be induced simply by the presence of high chloride concentration. Acid digestion of chloroplast samples reported in this work were done at low HCl concentrations (≈0.05 M) and no resulting signals occurring at low fields were observed. However, it is possible that other forms of manganese present in the samples exhibit neither the g=2 or the low field EPR signals and may therefore escape detection.

Considering only the relative amounts of manganese determined for these samples, it is seen that Tris-inactivated chloroplasts can be reactivated to 60% of control rates without added Mn^{+2} to give samples which contain only ≈20% of the original manganese pool. These results appear to support the conclusion that at least a portion of the manganese removed by Tris in these samples is not required for significant restoration of oxygen

evolution. However, the fact that reactivation is stimulated by added manganese indicates that some of the manganese lost from the membranes upon inactivation is serving in a functional role. This stimulation of restored activity by added manganese was variable and always less that 90%, possibly reflecting some irreversible destruction or removal of other components in or near the oxygen evolution comlex upon inactivation. On of the candidates for this component is a 32 Kd peptide which has been observed to be released from PSII preparations upon Tris-inactivation [7].

We have observed that reactivated membranes are somewhat labile with respect to oxygen evolution. Initial rates of evolution drop to 20% or less within 1 min of saturating illumination. Samples that have been reactivated in the presence of manganese exhibit both stimulated initial rates and prolonged activity. Thus, alternative explanations for the effects of added manganese may involve its role in a stabilizing interaction to PSII components or as an electron donor in a fashion similar to the reduced donors (ie. DCPIP) required for reactivation of the OEC [25]. It is clear that additional studies will be necessary to discriminate between these alternatives.

We have made reliable observations of the light-induced manganese multi-line EPR signal in PSII preparations from spinach chloroplasts. This observation provides support for the proposed connection of the species giving rise to this signal with the components of photosystem II reactions.

However, for reasons that are not completely understood, no signal has been observed for chloroplast or PSII preparations inactivated by Tris washing or subsequently reactivated. Two conclusions can be drawn from this observation. The first is that Tris treatment has removed from the membrane the signal species or a component necessary for its generation. However, this species must not be required for restored PSII electron transport from the OEC to Q. Alternatively, the conditions necessary for the generation or observation of the signal may have been altered but not destroyed by Tris. For example, this could occur if an alteration has taken place that effectively relaxes the EPR in the treatd samples by exposure of coupling to a paramagnetic center. We feel that this is more likely, because the EPR signal is completely absent in samples that have been only partially inactivated. In addition, we have observed that Tris interferes with two other low temperature manganese EPR signals observed at g=2 and at low fields (discussed in Chapter 6). These signals also cannot be generated in Tris treated samples, and only reappear after extensive washing of the membrane. Un-protonated Tris may bind or interact with the signal species without always inactivating oxygen evolution. Support for this notion comes from additional observations that the multi-line signal cannot be generated in PSII samples in the presence of 50 mM NH_3 at pH 7.8, but can be observed at pH 6.0. Un-protonated NH_3, like Tris, is known to interact with the OEC in states S_2 and S_3.

A large reproducible change is observed in the manganese x-ray K-edge absorption spectra of PSII samples prepared in states S_1 and S_2. Changes of the nature observed are classic behavior for loss of ligand symmetry caused by metal oxidation and/or forced ligand geometry distortion. However, it is probable that only a subset of the total pool of manganese would be expected to contribute to the observed change. The effect of a shift of one of the components with respect to the other is to broaden the principal absorption maximum in a manner similar to that observed. Simulations constructed by adding the S_1 edge to a second edge that has been shifted shows that the magnitude of the shift necessary to induce the observed broadening is approximately 10 eV. This is larger than can be expected for a change in oxidation state alone, and demonstrates that a significant change in the intrinsic line shape of a portion of the manganese edge has occurred.

This fact must be considered in the interpretation of the change(s) experienced at the manganese site. Changes in edge shape of this nature are commonly observed between complexes of Mn^{+2} and those of higher oxidation states, often because of distortions arising from Jahn-Teller effects. Therefore the observed change in edge line shape may be the result of metal oxidation, but it may also be induced by other factors such as protein conformation change. In either case, it may be said that a significant perturbation of the inner coordination symmetry or ligation

has occured upon illumination.

The magnitude of the changes observed are unexpectedly large. From previous correlations of manganese edge inflection point positions [15], we expect an edge shift of approximately 2.3 eV per unit coordination charge difference. The simplest interpretation of the multi-line EPR signal associated with S_2 is that only one charge equivalent per P_{680} has been transferred. Thus, the observed S_1 to S_2 average K-edge shift of 1.78 eV is larger than one would expect if only one electron equivalent were removed from a total pool of 3.6 manganese atoms.

There are a number of explanations for this observation. The first is that the photosynthetic unit size of the preparation is much smaller than reported [24], which would result in fewer manganese per PSII than indicated. Alternatively, the geometry of more than one manganese center could be altered if it were involved in a structural role between two components on the donor side of photosystem II. Oxidation of one component may cause a change in its conformation or association with its neighboring component, distorting the environment of the bound manganese in the process. It is somewhat unusual, however, that this would occur at the illumination temperature of -90°C. Finally, it is possible that more than one charge equivalent is transferred from the OEC under the illumination conditions used. This could occur if, for example, one oxidizing equivalent is stored on a PSII donor other than manganese in

S_1. Transition to state S_2 could then cause the accumulation of both oxidizing equivalents onto the manganese center.

In regard to proposed oxidation states of manganese sites in these centers, the combination of the x-ray edge data with the fact that the S_2 state exhibits a paramagnetic species is of great utility. The edge positions of PSII samples in state S_1 are similar to and slightly higher in energy than observed in a previous study on whole chloroplasts [15]. In that study, we proposed that the average manganese oxidation state in dark adapted membranes lies between +2 and +3. Thus for the dark adapted PSII preparation, which contains a lower and presumably more homogeneous manganese content, the edge position also lies between observed Mn^{+2} and Mn^{+3} complexes, but is somewhat more in the direction of Mn^{+3}. The average inflection position observed for samples prepared in S_2 by low temperature illumination strongly suggests a Mn+4 oxidation level.

These values represent the average state of all of the manganese present in the samples. The manganese site in the OEC may be monomeric, and would therefore be a minor constituent of the total manganese pool. If this were the case, it would be difficult to predict the oxidation level of this center without accurate information about the environment of the remaining pool. In fact, the large magnitude of the change observed in the edge upon illumination may be used as an argument that a significant

fraction of the 3.6 Mn per PSII are contributing to this change.

There is evidence that the OEC consists of exchange coupled metal centers [12,26], and a number of models for the site have included dimeric manganese species [2,27]. Based on the observation that state S_2 is paramagnetic, Dismukes et al. [12] have proposed that it contains a Mn(III,IV) complex, and the edge properties observed in this work support this assignment. The presence of a definite edge absorption maximum for the S_1 samples is characteristic of many Mn+2 complexes. If it is true that two oxidizing equivalents are removed from the manganese center in the S_1 to S_2 transition as discussed above, these observations would be consistent with the presence of a Mn(II,III) complex in S_1. However, a Mn(III,III) complex which ungoes a large change in ligation in the S_1 to S_2 transition might also give rise to the observed properties.

An attractive model for the oxygen evolution complex has been proposed by Renger [27], which involves the formation of the dioxygen bond at the level of peroxide in a binuclearly complexed manganese center. The presence of species with high reduction potentials that may be difficult to stabilize was avoided by allowing charge transfer to occur onto partially oxidized oxygen intermediates in a series of 1 electron removal steps. One of the features of this model is an additional donor other than the manganese center that is oxidized in the S_0 to S_1 transition. This was

proposed in order that both states S_0 and S_1 would have the properties of being stable in the dark. In addition, this oxidation was not coupled to a deprotonation step in order to explain data [28] indicating a proton release pattern of 0,1,1,2. This is as yet somewhat controversial, in that other work [29] indicates that this pattern is 1,0,1,2.

This model was later modified and expanded to incorporate results of manganese release studies by Wydrzynski and Sauer [30]. It employs the 1,0,1,2 proton release pattern of Fowler [29] and an oxidation of the manganese center in the S_0 to S_1 transition instead of the alternate donor of Renger. Most notably, the oxidation levels of the manganese in state S_3 were proposed to be lower than for S_2 in accordance with quantities of Mn^{+2} released by heat treatment of flash pre-illuminated chloroplast samples. However, the recent assignment of a paramagnetic manganese center to S_2 [12] is not easily accounted for by the Mn(III,III) oxidation level of S_2 in this model.

It is possible to incorporate the S state oxidation levels indicated in this work into a speculative but consistent model of the OEC that is similar in nature to the ones described above. This is shown in figure 5. In this scheme, the OEC contains two closely coupled manganese centers and two species labeled D, possibly serving as ligands to the metal which are themselves capable of electron donation.

Figure 5. A proposed scheme for the changes in manganese oxidation associated with S state cycling.

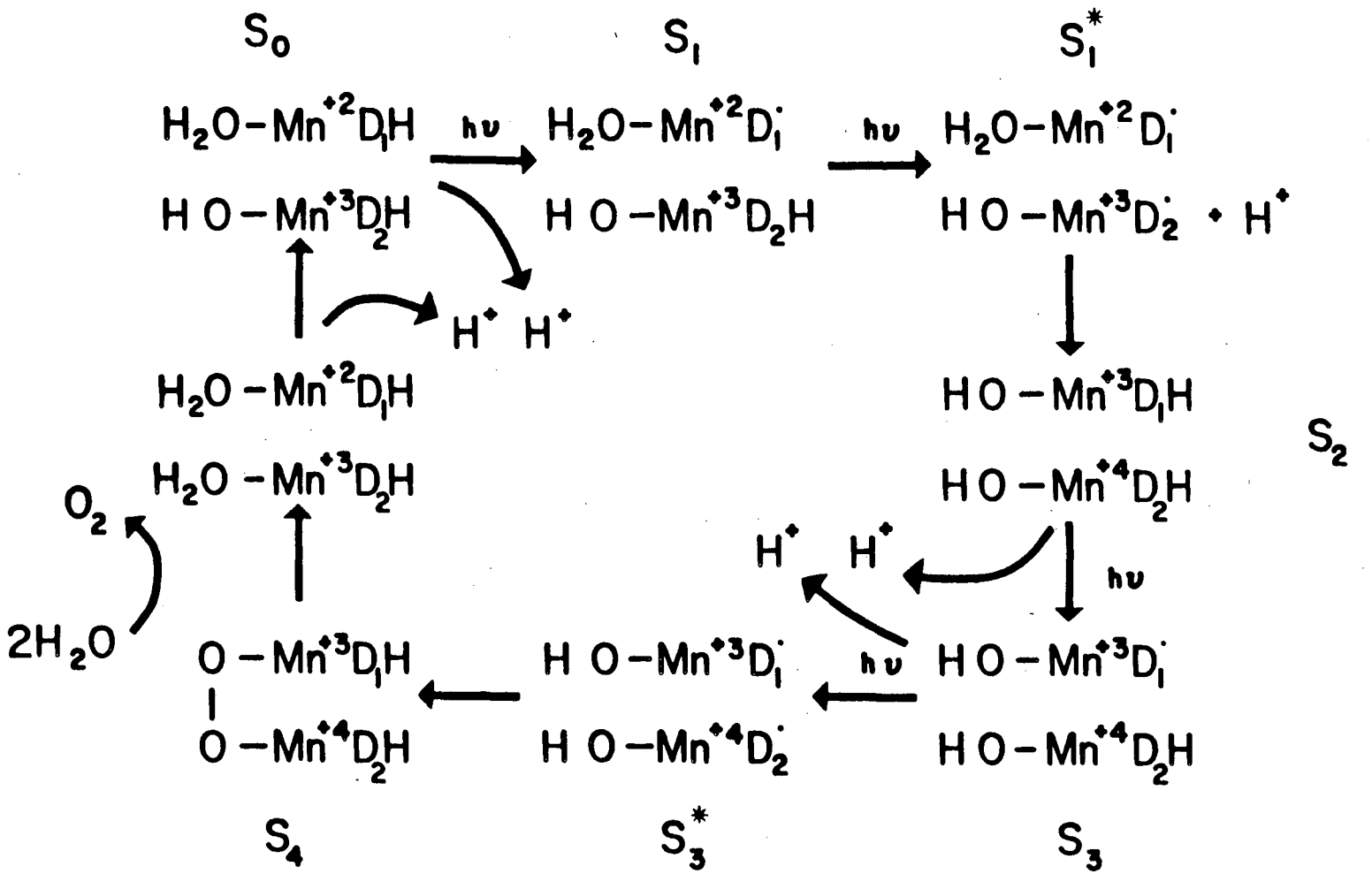
S0
S1
S1*
H2O-Mn+2D1H
hυ
H2O-Mn+2D1·
hυ
H2O-Mn+2D1·
H O-Mn+3D2H
H O-Mn+3D2H
H O-Mn+3D2·
• H+
H+ H+
H2O-Mn+2D1H
HO-Mn+3D1H
S2
H2O-Mn+3D2H
HO-Mn+4D2H
O2
H+ H+
hυ
2H2O
O-Mn+3D1H
H O-Mn+3D1·
hυ
HO-Mn+3D1·
O-Mn+4D2H
H O-Mn+4D2·
HO-Mn+4D2H
S4
S3*
S3

One of the unique features of this model is that charge is transferred onto the metal centers only after the ligated donor species (D) have been oxidized by one equivalent each. This mode of transfer, in which oxidation of a ligand occurs prior to the transfer of charge onto the metal species, provides a convenient means by which oxidizing equivalents may be moved from the outer to the inner coordination sphere of the metal. In contrast to many electron-transfer proteins, in which the metal is directly oxidized or reduced, this kind of process is thought to be kinetically slower and may result in longer lived oxidized intermediates. This is because a change in oxidation level necessarily involves a perturbation or rearrangement of the ligand species. These arguments have been used in favor of this type of mechanism for electron-storage as opposed to electron-transfer enzymes [12].

In order to properly account for the 1,0,1,2 proton release pattern observed by Fowler [29], it is necessary to propose that oxidation of this donor is coupled to a deprotonation step. This is indicated by showing the reduced and oxidized forms as DH and D$^{\cdot}$ respectively.

In state S_0, the metal centers are shown in the Mn(II,III) oxidation state, and are complexed to the reduced forms of the donor ligands. In addition, two complexed water molecules are shown, one of which as a deprotonated hydroxyl ion bound to the Mn^{+3} atom. Transition from state S_0 to S_1 occurs simply by the oxidation of one of the donor

species with the release of a proton. The following transition occurs first by oxidation of the second donor species to give the hypothetical unstable intermediate labeled S_1^*. This state relaxes to S_2 after two charge equivalents are transferred from the oxidized donor species to manganese giving a Mn(III,IV) complex. A second water deprotonation step is shown, so that after proton uptake by the newly reduced donors, no net proton release has occured in the S_1 to S_2 transition. Transition from S_2 to S_3 results from oxidation of a donor molecule in a process analagous to the S_0 to S_1 step. The final light induced stage proceeds as before with the formation of an unstable intermediate S_3^* containing a Mn(III,IV) complex and two oxidized donors. There are a number of ways in which this intermediate could proceed to release oxygen. For example, the hydroxyl ligands could be oxidized to give a binuclear peroxo-bridged species and a Mn(III,IV) complex containing the reduced donors shown as S_4. A water ligand exchange raction very similar to that proposed by Renger [27] may then accompany the release of dioxygen, regenerating state S_0 after water deprotonation. In this last photochemical step, two protons are shown to be released, one before and one after release of dioxygen.

The transition from S_3 to S_0 may be viewed as involving a concerted two electron oxidation of the hydroxyl ligands rapidly followed in the dark by a second concerted two electron process as the oxygen group leaves the OEC. In

this way, it is not necessary to propose stabilized forms of the highly reactive hydroxyl radical, peroxo- or superoxo-intermediates.

Like the model proposed by Renger [27], this scheme involves a significant smearing out of charge from the manganese center onto ligands, avoiding the use of highly oxidized manganese species. In fact, this scheme employs only two formal oxidation levels for the manganese center; Mn(II,III) and Mn(III,IV). However, unlike the additional donor proposed by Renger, the oxidized forms of D• are not held throughout the S state cycle, but are instead proposed to play an intricate role in the redox reactions. The scheme of figure 5 is fairly consistent with that proposed by Wydrzynski and Sauer [30] in that S_1 contains a Mn(II,III) species, and S_3 contains manganese with an oxidation level that is similar to that in S_2.

Other than accounting for the large change in manganese oxidation level between S_1 and S_2 indicated by this work, there are a number of attractive features of this scheme. It is indicated from the model that the oxidation level of the manganese site may not be significantly altered in the transition from S_2 to S_3, where oxidation of D_1H is instead possible. Behavioral similarity of S_2 and S_3 is often observed. For example, both states appear to be the sites of Tris or NH_3 inactivation. An explanation for the dark relaxation of S_2 and S_3 may also be inherent in such a model, if only the states consisting of an oxidized

manganese center undergo relaxation. This is also entirely consistent with the observation that our attempt to generate S_3 caused most of the multi-line EPR signal to disappear, but shows an absorption edge that is not very different from the S_2 samples. It is proposed that charge is not transferred directly to Mn during S_2 to S_3, but that interaction of the Mn spin system with D$^{\cdot}$ alters its relaxation properties. This brings up the question of whether the Mn(II,III) complex in state S_1 might be expected to exhibit EPR signals. The additional spin on the D$^{\cdot}$ ligand could be expected to greatly alter the relaxation properties of such a signal in a manner analogous to that proposed for the state S_3. If the spins were strongly coupled, an integral spin state might result, exhibiting no EPR properties at all. Recently a report was made of an unusual signal attributed to manganese containing many lines over a broad field range for photosynthetic membranes in state S_1 [31]. This signal could only be observed at temperatures below 8°K and at very high power levels indicating an unusually efficient relaxation mechanism. The signal has not been verified, however, and is poorly characterized at this time.

Of course the identity of the ligand species D is unknown, but it would make sense to propose a quinone species. Extraction studies have implicated quinones as components on the donor side of photosystem II [32]. Multimeric manganese semiquinone complexes have been reported, and some of these complexes indeed exhibit two-

electron metal-ligand transfer equilibria similar to that suggested in the model [33]. If this were the case, additional properties of the donor side of PSII could be easily interpreted. The reduced form of DH may represent the fully reduced form of the complexed quinone, and D$^{\cdot}$ would represent the semiquinone form. As mentioned above, the EPR signals from the species in state S_1 may be difficult or impossible to observe. However, transition of S_1 to S_2 would proceed by way of the transient intermediate shown, consisting of a Mn(II,III) and two semiquinone radicals in an overall half integral spin complex. If the unpaired spin density were localized primarily on the quinone species, this transient state may be associated with the signal II_{vf} transient. The decay of this transient state would occur as the semiquinone ligands are reduced by the metal center and should therefore parallel the rise of the multi-line EPR signal. A similar, but predictably slower transient would accompany transition from S_3 to S_0 as is observed experimentally [34]. It is not easy to predict from this model, however, the fact that the flash yield observed for signal II_{vf} on the second flash is large and has decay kinetics intermediate between that on the first and third flash [34]. Instead, this model would predict two kinetic components oscillating with a flash pattern characterized by: fast, mixture, slow, mixture, etc. It may thus be necessary to propose that the state shown for S_3 in the model relaxes to give a Mn(IV,IV) complex with the decay of the

signal II species.

REFERENCES

1. Forbush, B., Kok, B. and McGloin, B. (1971) Photochem. Photobiol. 14, 307-321.

2. Sauer, K. (1980) Accts. Chem. Res. 13, 249-256.

3. Cheniae, G.M. and Martin, I.F. (1970) Biochim. Biophys. Acta 197, 219-239.

4. Blankenship, R.E. and Sauer, K. (1974) Biochim. Biophys. Acta 357, 252-266.

5. Blankenship, R.E., Babcock, G.T. and Sauer, K. (1975) Biochim. Biophys. Acta 387, 165-175.

6. Mansfield, R. and Barber, J. (1982) FEBS Lett. 140, 165-168.

7. Henry, L.E.A., Lindberg Moller, B., Andersson, B. and Akerlund, H.-E. (1982) Carlsberg Res. Commun. 47, 187-198.

8. Akerlund, H.-E., Jansson, C. and Andersson, B. (1982) Biochim. Biophys. Acta 681, 1-10.

9. Yamamoto, Y., Doi, M., Tamura, N. and Nishimura, M. (1981) FEBS Lett. 133, 256-268.

10. Kuwabara, T. and Murata, N. (1982) Plant Cell Physiol. 23, 533-539.

11. Dismukes, G.C. and Siderer, Y. (1981) Proc. Natl. Acad. Sci. 78, 274-278.

12. Dismukes, G.C., Ferris, K. and Watnick, P. (1982) Photobiochem. Photobiophys. 3, 243-256.

13. Brudvig, G.W., Casey, J.L. and Sauer, K. (1983) Biochim. Biophys. Acta, in press.

14. Hansson, O. and Andreasson, L.-E. (1982) Biochim. Biophys. Acta 679, 261-268.

15. Kirby, J.A., Goodin, D.B., Wydrzynski, T., Robertson, A.S. and Klein, M.P. (1981) J. Amer. Chem. Soc. 103, 5537-5542.

16. Shulman, R.G., Yafet, Y., Eisenberger, P. and Blumberg, W.E. (1976) Proc. Natl. Acad. Sci. 73(5), 1384-1388.

17. Berthold, D.A., Babcock, G.T. and Yokum, C.F. (1981)

FEBS lett. 134, 231-234.

18. Arnon, D.I. (1949) Plant Physiol. 24, 1-15.

19. Powers, L., Chance, B., Ching, Y. and Angiolillo, P. (1981) Biophys. J. 34, 465-498.

20. Stern, E.A. and Heald, S.M. (1979) Rev. Sci. Instrum. 50, 1579-1582.

21. Goodin, D.B., Falk, K.-E., Wydrzynski, T. and Klein, M.P. (1979) 6th Annual Stanford Synchrotron Radiation Laboratory Users Group Meeting 10-11.

22. Ke, B., Inoue, H., Babcock, G.T., Fang Z.-X. and Dolan, E. (1982) Biochim. Biophys. Acta 682, 297-306.

23. Lavorel, J. and Seibert, M. (1982) FEBS Lett. 144, 101-103.

24. Babcock, G.T., Ghanotakis, D.F., Ke, B. and Diner, B.A. (1983) Biochim. Biophys. Acta 723, 276-286.

25. Hauska, G. (1979) Encyclo. Plant Physiol., vol. 5, Photosynthesis I, (Trebst, A. and Avron, M., eds.) 253-265.

26. Kirby, J.A., Robertson, A.S., Smith, J.P., Thompson, A.C., Cooper, S.R. and Klein, M.P. (1981) J. Amer. Chem. Soc. 103, 5529-5537.

27. Renger, G. (1978) Photosynthetic Water Oxidation (Metzner, H., ed.) Academic Press, London, 229-248.

28. Junge, W., Renger, G. and Auslander, W. (1977) FEBS Lett. 79, 155-159.

29. Fowler, C.F. (1977) Biochim. Biophys. Acta 462,414-421.

30. Wydrzynski, T. and Sauer, K. (1980) Biochim. Biophys. Acta 589, 56-70.

31. Dismukes, G.C., Abramowicz, D.A., Ferris, K.F., Mathur, P., Siderer, Y., Upadrashta, B. and Watnick, P. (1983) Proceedings of the International Symposium on Photosynthetic Oxygen Evolution and Photosystem II Photochemistry, in press.

32. Kohl, D.H. and Wood, P.M. (1969) Plant Physiol. 44, 1439-1445.

33. Lynch, M.W., Valentine, M. and Hendrickson, D.N. (1982) J. Amer. Chem. Soc. 104, 6982-6989.

34. Babcock, G.T., Blankenship, R.E. and Sauer, K. (1976) FEBS Lett. 61, 286-289.

CHAPTER 6

A Study of Manganese Release from Chloroplast Thylakoid Membranes by Low Temperature EPR Spectroscopy

I. INTRODUCTION

The effects of agents such as NH_2OH, mild heating or alkaline Tris washing that simultaneously inactivate photosynthetic water oxidation and release significant amounts of chloroplast manganese are well known [1]. However, there are a number of aspects concerning the fate of manganese altered by these treatments that remain unclear. Earlier studies [2] based on the observation of Mn^{+2} by EPR at room temperature have shown that during Tris inactivation most of the manganese is not lost from chloroplast membranes, but merely altered in environment. This reflects the observation that inactivation accompanies the appearance of a g = 2 EPR signal from aqueous Mn^{+2}, and that this signal follows the pellet rather than the supernatant fraction. The loss of manganese from this pellet into the supernatant occurs slowly with a $t_{1/2}$ = 2.5 hrs. It was proposed that the manganese altered by Tris treatment is released to the inside of the enclosed thylakoid vesicle

where it is trapped by a slow trans-membrane diffusion.

Recent work [3] has shown, however, little difference in the amount of manganese removed by Tris inactivation from normal versus inside out thylakoid vesicles. It was concluded from this work that manganese is not specifically released into the inner thylakoid space. Other results on the kinetics of manganese equilibria in chloroplast thylakoids are somewhat inconlcusive [4], but show no evidence for slow equilibration across the chloroplast membrane. Yokum et al. [5] have done a careful study of the stoichiometry of manganese release by these treatments which provides a number of relevant observations. Chloroplast membranes isolated in sucrose buffer contained approximately 2 manganese in a form that could be displaced by 40 mM Ca^{+2} without decrease of water-splitting activity. Tris inactivation of these membranes caused 3 manganese/400 chl to be released into the EPR observable form. However, if isolated in a high salt medium, active membranes contained only 4-5 Mn/400 chl, and very little of this was displaced by calcium. When these membranes were inactivated by NH_2OH or Tris treatment, less than one manganese was observed as the aquated ion. In the presence of 40 mM Ca^{+2}, a total of 2 Mn/400 chl was observed after Tris and 3 Mn/400 chl after NH_2OH inactivation. It was proposed that the Ca^{+2} releasable manganese represents a loosely bound form, and that inactivation results in the population of these bound forms.

It is therefore apparent that membrane bound sites play a significant role in the fate of the fraction of manganese that is altered by these inactivating treatments. This chapter describes results of experiments using low temperature EPR spectroscopy to investigate membrane bound forms of manganese present in spinach chloroplast thylakoids before and after inactivating treatments.

II. MATERIALS AND METHODS

Procedures used for preparing chloroplast membranes, performing O_2 evolution measurements and EPR spectroscopy are described in chapter 5 and will not be repeated here.

Hydroxylamine-treated chloroplasts were prepared by suspending untreated chloroplasts to a concentration of 1 mg/ml chl in the presence of 1.0 mM NH_2OH in a buffer containing 0.2 M sucrose, 10 mM HEPES (pH 7.5), and 5 mM $MgCl_2$. After incubation for 3 min. on ice in the dark, the chloroplasts were collected by centrifugation at 6000xg for 5 min. TPB^- and NH_3 treatments were accomplished in a similar way by suspending chloroplasts in the above buffer which was made 10 μM and 30 mM in sodium tetraphenylboron and NH_4Cl, respectively. H_2O_2-treated chloroplasts were prepared as described by Velthuys et al. [6], except that 0.5 mM NaN_3 was present during treatment as a catalase inhibitor. Heat treatments were carried out in the dark at 50-52°C for two minutes and the samples were immediately frozen in liquid nitrogen unless otherwise noted.

Bovine serum albumin (Sigma No. A-4378) was dialyzed against 50 mM HEPES (pH 7.5), and 1 mM EDTA and then against buffer without EDTA to remove extraneous metal ions. Mn^{+2} additions were from a standardized solution of Mn^{+2} obtained by dissolving metallic manganese in nitric plus perchloric acids (4:1) and determined by atomic absorption.

Samples of treated chloroplasts were prepared for EPR by suspending membrane pellets in the above sucrose-HEPES

buffer to a concentration of about 4 mg/ml chl and frozen slowly to 77°K in 4 mm O.D. quartz EPR tubes.

III. RESULTS

Shown in figure 1 are the EPR spectra observed for chloroplasts before and after heat treatment. Upon heating, the g = 2 EPR signal from $Mn^{+2}(H_2O)_6$ is observed, but less than one Mn^{+2}/400 chl is accounted for by this signal. Also shown in figure 1 is an additional EPR signal between 0 and 300 G which is induced by heat treatment. This very low field (VLF) signal is assigned to a form of Mn^{+2} bound to the thylakoid membrane, because we have observed an identical signal in samples of Mn^{+2} added to bovine serum albumin (figure 2). A significant amount of manganese in the presence of BSA remains as the g = 2 hyperfine sextet characteristic of the hexaquo complex, but two additional signals are observed at low fields. One of these occurs at 0 to 300 G and appears to be identical to that observed in inactivated chloroplasts. A second signal is observed for Mn^{+2}-BSA at 400 to 900 G.

We have attempted to characterize the origin of these signals by comparing Mn^{+2}-BSA binding studies with those that have been reported. Mildvan and Cohn [7] have observed two classes of binding sites to BSA at room temperature, a single site with $K_1 = 3.7 \times 10^{-5}$ M and approximately five weaker binding sites with $K_2 = 3.0 \times 10^{-4}$ M. We have measured the binding of Mn^{+2} to BSA by quantitating the depletion of the g = 2 manganese EPR signal observed at 10°K by added BSA for samples of constant total manganese concentration. We observe 0.74 binding sites with

Figure 1. EPR spectra of dark adapted spinach chloroplasts before (top) and after (bottom) heat treatment. The spectra were recorded at 12°K at a microwave frequency of 9.13 GHz using 100 KHz field modulation. The microwave power was 0.2 mW and 20 mW, and the modulation amplitude was 4 G and 40 G for the g=2 and low field regions respectively.

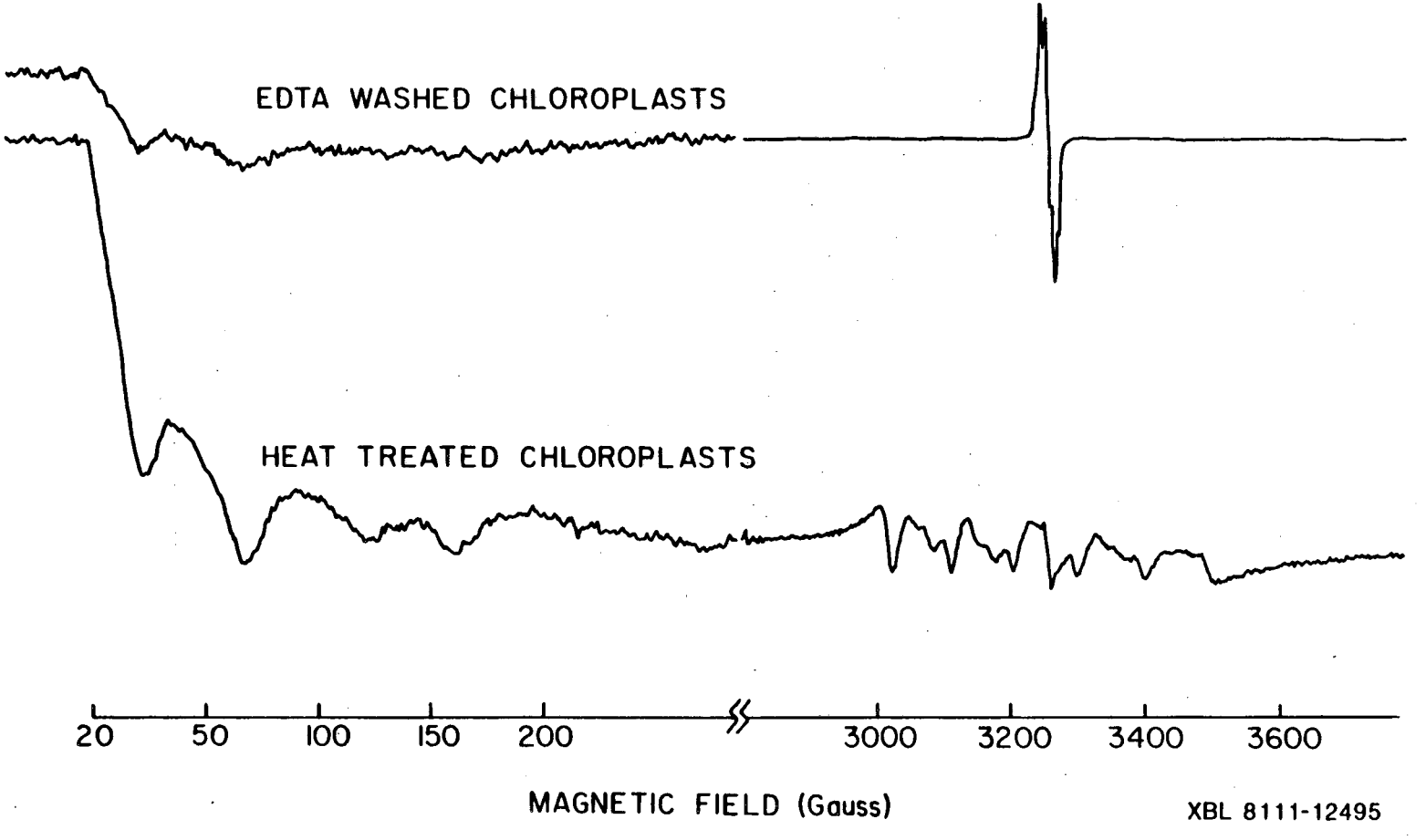
EDTA WASHED CHLOROPLASTS
HEAT TREATED CHLOROPLASTS
20
50
100
150
200
3000
3200
3400
3600
MAGNETIC FIELD (Gauss)
XBL 8111-12495

Figure 2. EPR spectra observed for 0.3 mM Mn^{+2} in the presence of 0.44 mM BSA. Instrumental conditions are described with figure 1.

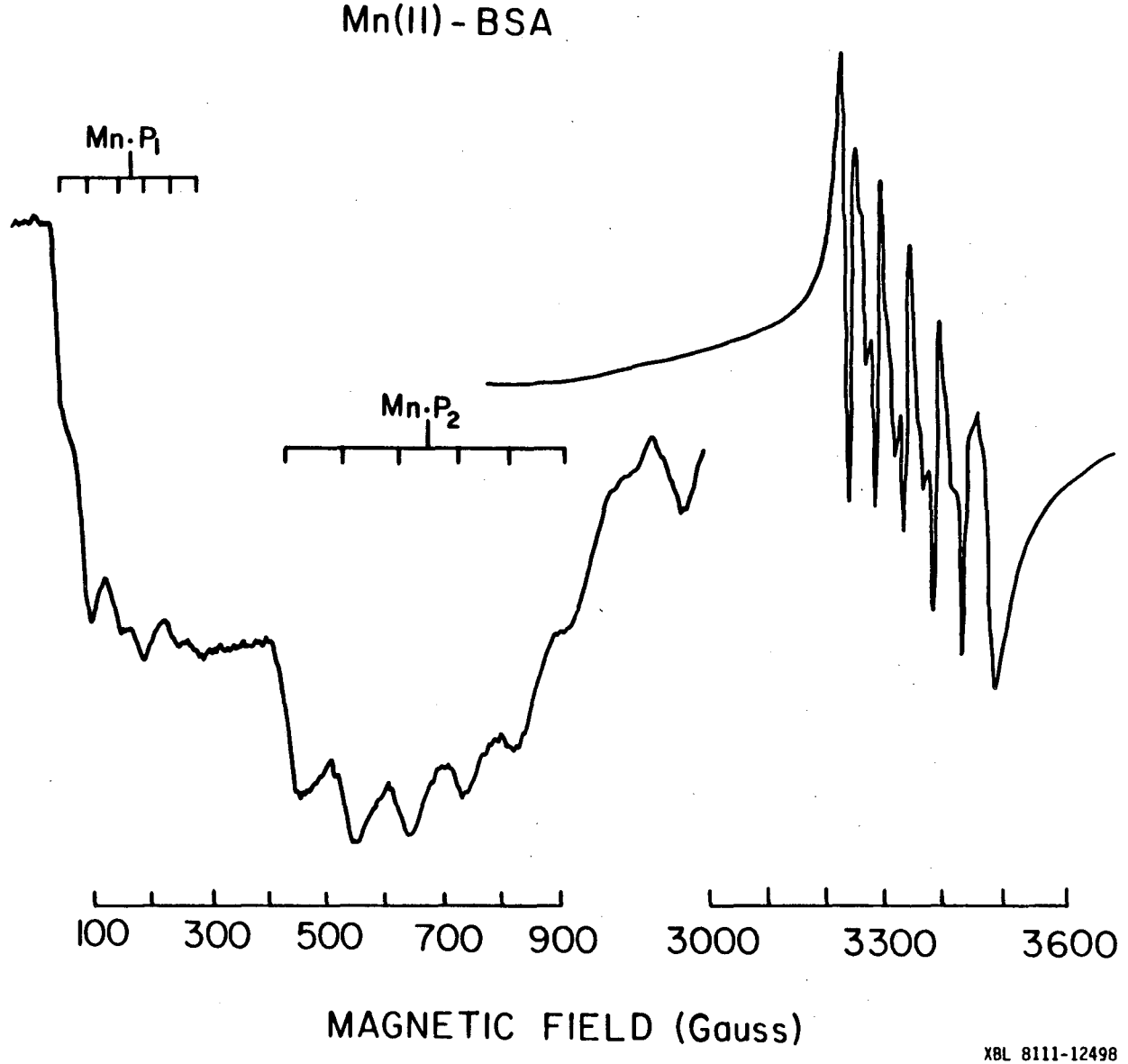

XBL 8111-12498

$K_1 = 1.75 \times 10^{-6}$ M and 2.4 sites with $K_2 = 8.2 \times 10^{-5}$ M. These correspond roughly to the tight and weak sites previously obtained. The differences observed in these binding constants and those previously obtained [7] are probably due to the fact that this study was performed on frozen solutions and thus represents the binding equilibria at the freezing point of the solution, not at room temperature.

It is desirable to relate this information to binding studies using the VLF signals in order to characterize their origin. Without knowledge of the absolute magnitude of the VLF EPR signals, it is not easy to determine the number of sites from a binding curve, but it is possible to obtain the binding constants. A double reciprocal plot of the induction of the two VLF signals is shown in figure 3. A binding constant of 1.2×10^{-4} M is obtained for the signal occurring at 0 to 300 G and provides an assignment as one of the 'weak' sites observed for BSA under these conditions. This suggests that the presence of the signal in inactivated chloroplast membranes arises from non-specific binding of manganese to membrane protein components. The other signal observed at 400 to 900 G appears to represent an extremely weak binding site to BSA. This signal was not observed for chloroplast samples under any of the conditions of these experiments.

We have used the association of this EPR signal with the weak binding site of BSA to calibrate its amplitude and thus

Figure 3. Binding curves for Mn^{+2}-BSA displayed as a double reciprocal plot of the relative amplitudes of the two VLF EPR signals versus the Mn^{+2} concentration for a constant BSA concentration of 0.44 mM. Mn-P_1 represents the VLF signal observed at 0-300 G and Mn-P_2 represents the 400-900 G signal.

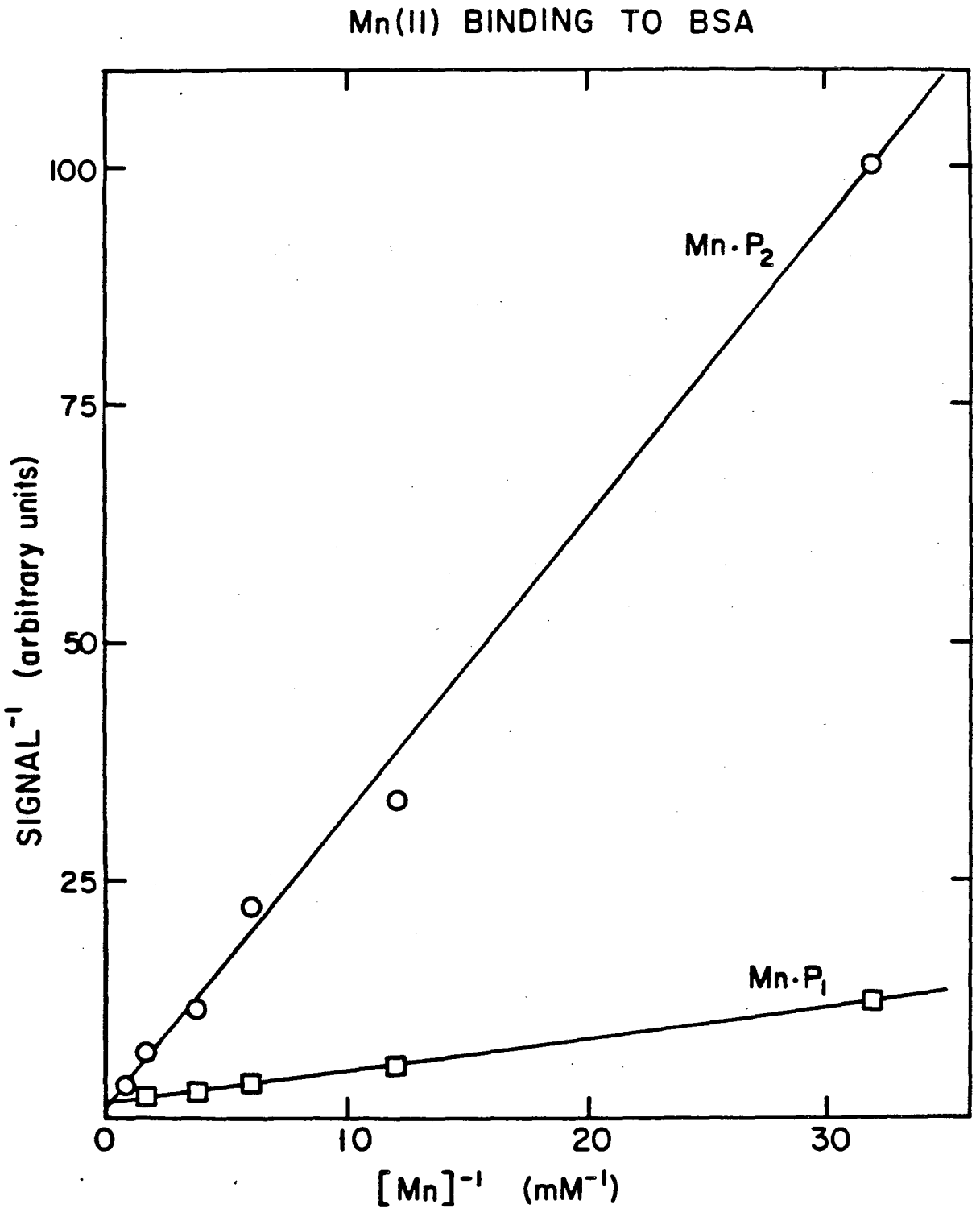
Mn(II) BINDING TO BSA
100
75
50
25
0
10
20
30
SIGNAL^{-1} (arbitrary units)
[Mn]$^{-1}$ (mM^{-1})
Mn·P$_2$
Mn·P$_1$

obtain an approximate number of manganese contributing to the signal for inactivated chloroplast samples. These quantities are presented in table 1. Untreated chloroplast preparations containing approximately 6 total Mn per PSII reaction center exhibit between 1 and 2 Mn in this VLF signal. This quantity is somewhat variable. Preparations containing less than 6 total atoms of Mn exhibit the smallest VLF amplitude.

Heat inactivation of membranes releases less than one manganese to a form observed as the g = 2 EPR signal, but a significant quantity is observed in the VLF signal after treatment. Thus, a total of 3 EPR-observable manganese per 400 chl are induced by heat treatment, and most of this appears in a form assigned to loosely bound manganese.

Irreversible inactivation with 1 mM NH_2OH induces changes similar to those observed with heat treatment. In this case, inactivation was accompanied by the appearance of approximately 1 Mn to the g = 2 signal, and 3 Mn to the VLF signal. On the other hand, treatment with 30 mM NH_3, 10 μM TPB^- or 0.3% H_2O_2 which alter, but do not irreversibly destroy O_2 evolution cause very little changes in the binding of Mn as observed by low temperature EPR.

For reasons that are not completely understood, we do not always observe the VLF signal after inactivation by alkaline Tris treatment. The amounts that are observed are quite variable and thus difficult to quantitate. The g = 2 EPR signal from $Mn^{+2}(H_2O)_6$ is also not observed at 10°K after

Table 1. Quantity of Manganese Observed as g=2 and VLF EPR Transitions for Chemically Treated Chloroplast Samples.

Sample	Mn^{+2} per 400 chl detected by EPR			
	$Mn^{+2}(H_2O)_6$ g=2	Mn^{+2} · P VLF	Total EPR Mn^{+2}	Total induced by treatment
Chloroplasts (6.3 Mn/400 chl)	0.14	0.61	0.75	-
" + heat	0.27	3.40	3.67	2.92
High Salt Chloroplasts (4.9 Mn/400 chl)	0.03	0.36	0.39	-
" + heat	0.53	2.65	3.18	2.79
Chloroplasts (6.6 Mn/400 chl)	0.0	1.5	1.5	-
" + 10 μM TPB^-	0.0	1.7	1.7	0.2
" + 0.3% H_2O_2	0.0	1.2	1.2	-0.3
" + 30 mM NH_3	0.0	1.7	1.7	0.2
" + 1 mM NH_2 OH	0.89	4.5	5.4	3.9

Tris-inactivation, so it is likely that the presence of Tris in some way alters our ability to observe low temperature EPR signals from manganese. Extensive washing of Tris inactivated membranes to remove the Tris causes the appearance of the VLF EPR signal, but at reduced levels.

It was previously found that adding 40 mM Ca^{+2} to chloroplasts that have been treated with Tris or hydroxylamine increased the amount of aqueous Mn^{+2} observed by EPR at room temperature [5], presumably due to the displacement of membrane-bound forms of manganese by Ca^{+2}. We find that addition of 40 mM Ca^{+2} before inactivation does not substantially increase the aqueous Mn^{+2} EPR signal induced by the treatment. The VLF signal observed after NH_2OH or heat inactivation is decreased by 15-20% by addition of Ca^{+2}. The VLF signal present in untreated membranes is unaffected by the presence of Ca^{+2}. In addition, we have observed that the presence of 1mM EDTA does not affect the VLF EPR signal amplitude of heat treated chloroplasts (figure 4). Therefore, it is apparent that the membrane bound forms of manganese present after heat or hydroxylamine inactivation are not efficiently displaced by Ca^{+2} or EDTA under the conditions of our experiments.

Figure 4. VLF and g=2 EPR signals observed for spinach chloroplasts before and after heat inactivation and in the presence and absence of 1 mM EDTA. EPR conditions are as in figure 1.

SPINACH CHLOROPLASTS

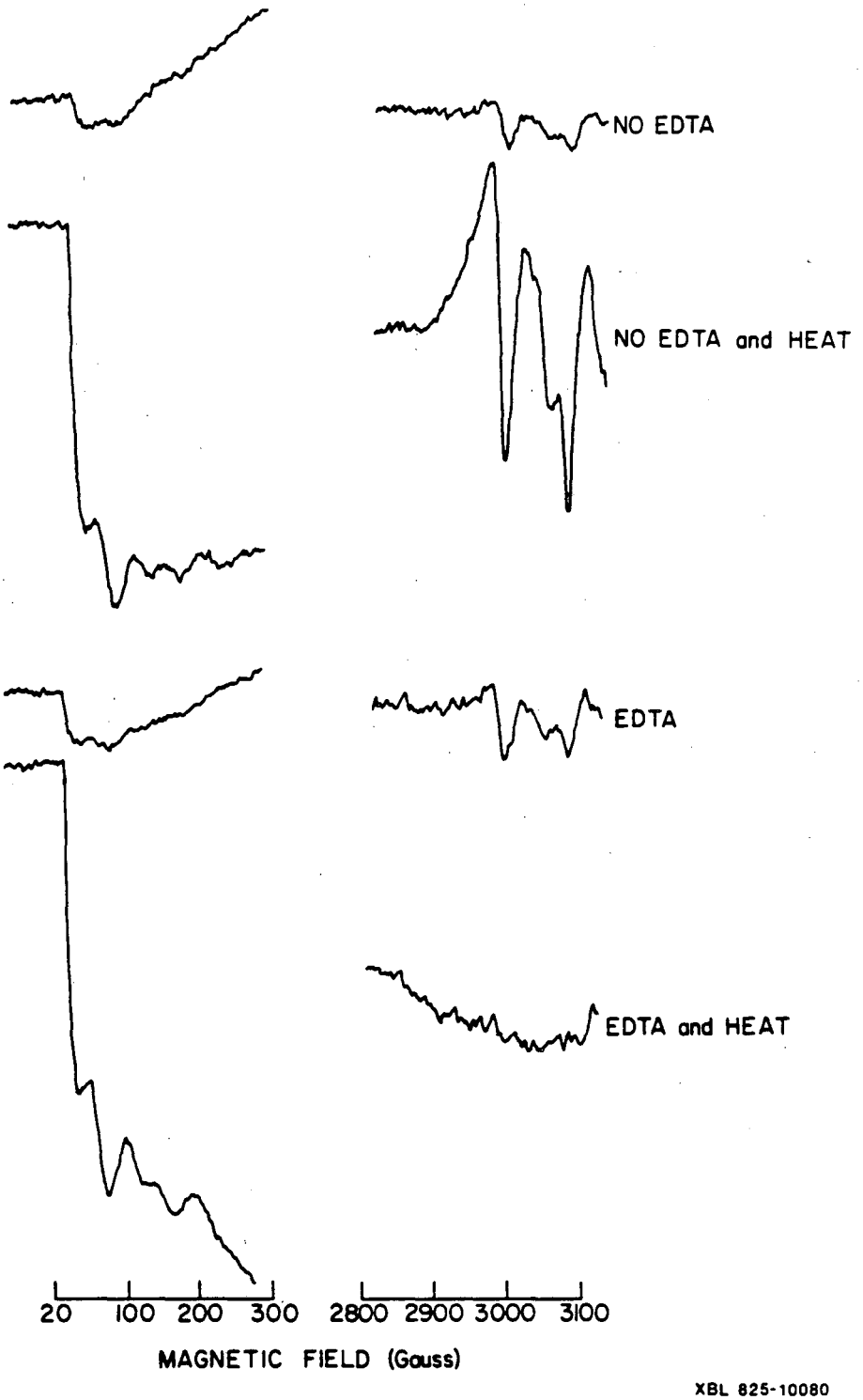

XBL 825-10080

IV. DISCUSSION

Inactivation of oxygen evolution in spinach chloroplast thylakoids by mild heating or NH_2OH treatment gives rise to a low temperature EPR signal observed at very low fields and assigned to Mn^{+2} weakly bound to the membrane. The observed signal is identical to one of two signals observed for Mn^{+2} weakly bound to bovine serum albumin, which has been assigned to carboxylate ligands of the protein [8]. This suggests that the signal observed in chloroplast membranes represents weak binding to surface protein components. In an earlier study of manganese binding to chloroplast membranes [2], approximately 70 Mn sites per 400 chl were observed with $K = 1.2 \times 10^{-4}$ M which is very similar to that observed for the weak binding to BSA. We have observed that this signal can also be observed in samples containing only manganese and high concentrations of Cl^-. It is thus likely that the signal species arises from manganese in a variety of environments or from one that is quite common.

In order to better understand the origin of this signal we have undertaken a series of computer simulations. The common techniques of simulation using perturbation treatments are not valid when used at low fields, because the hyperfine and spin-orbit contributions to the total spin Hamiltonian are not insignificant and cannot be considered perturbations of the high field basis states. Thus a computer program was written to simulate EPR spectra using an accurate but somewhat inefficient matrix diagonalization

method. The Hamiltonian matrix was constructed as

$$H = \beta_e H \cdot g_e \cdot S + \beta_n H \cdot g_n \cdot I + S \cdot A \cdot I + D(S_z^2 - 1/3S(S+1)) + E(S_x^2 - S_y^2) \quad (7)$$

which includes electron and nuclear Zeeman terms, the nuclear hyperfine interaction, and the spin-orbit zero-field splitting terms respectively [9]. A description of the EPR simulation method is presented in appendix B.

For reasonably chosen isotropic g-values and hyperfine couplings it was found that transitions in the low field region could be generated when the zero field splitting parameter D was approximately 0.17 cm^{-1} which would give a splitting between the $M_s = \pm 1/2$ and $M_s = \pm 3/2$ high field states approximately equal to the microwave energy. An example is shown in figure 5 which shows similarity with the general features of the VLF spectrum. A precise agreement of the hyperfine lines was not obtained, however, and it was not possible to test the inclusion of E or additional quartic terms as variables in the simulation due to the excessive amounts of computation required for these simulations. Nevertheless, it is apparent that signals of the nature observed can be expected from crystal-field induced zero-field splittings that may arise from distortion caused by manganese binding.

The quantities of manganese appearing in the VLF signal for the chloroplast samples support a recent proposal [5] that most of the manganese altered by inactivation remains

Figure 5. The VLF EPR signal observed in heat inactivated chloroplasts (bottom) and a computer simulation (top). Experimental conditions are described in figure 1. In the simulated spectrum, for each randomly chosen angle with respect to the z axis, the Hamiltonian matrix was diagonalized at 50 magnetic field values between 0 and 1000 G. The transition probabilities obtained at each observed resonance were convolved with an isotropic Gaussian linewidth of 25 G. The parameters used to construct the Hamiltonian were: $g_x=g_y=g_z = 2.0023$, $a_x=a_y=a_z = -0.010\ cm^{-1}$, $D = 0.165\ cm^{-1}$ and $E = 0.0\ cm^{-1}$.

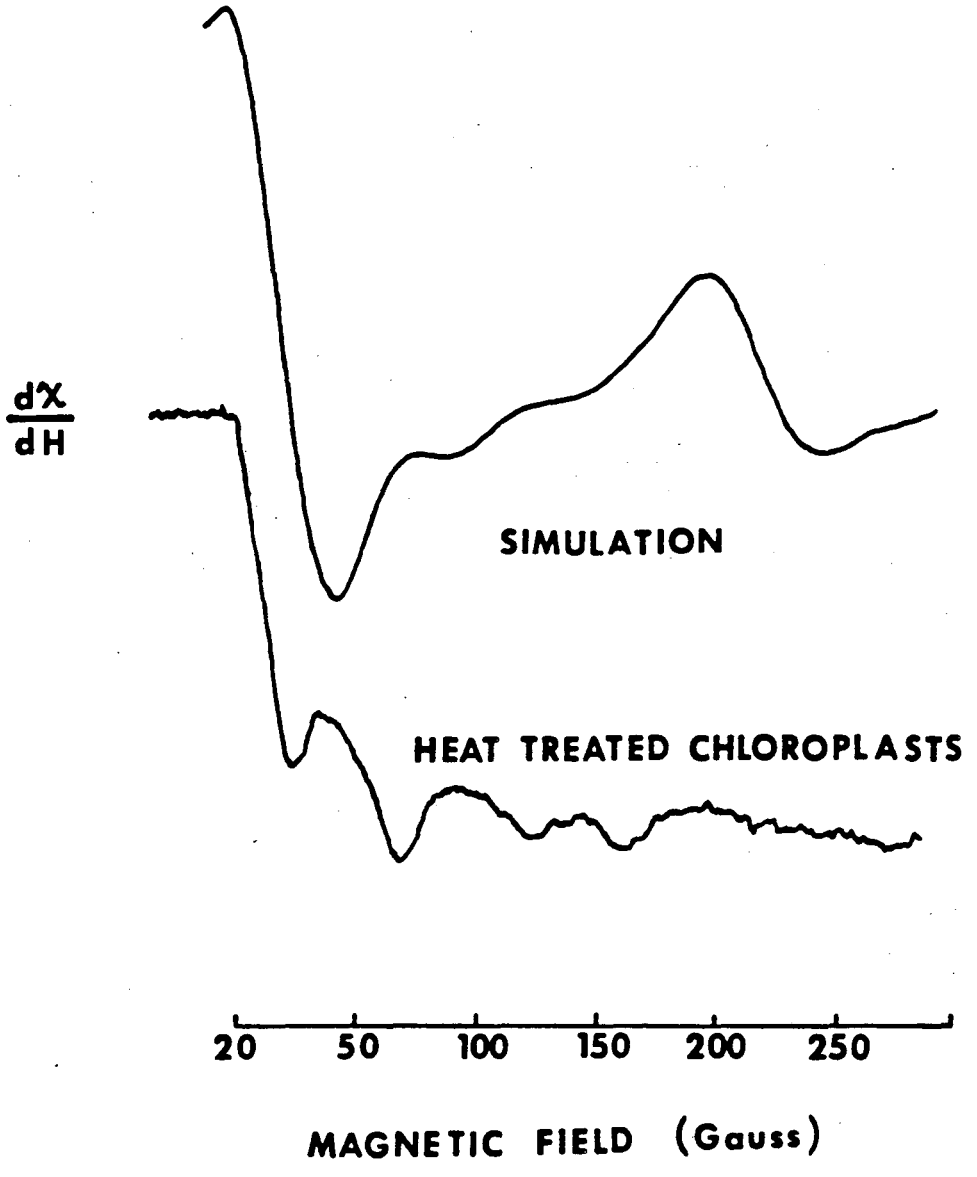
dχ/dH
SIMULATION
HEAT TREATED CHLOROPLASTS
20
50
100
150
200
250
MAGNETIC FIELD (Gauss)

weakly bound to the thylakoid membrane. Untreated membranes contain small amounts of manganese in the VLF signal, which probably arise from extraneous manganese binding. In each case, approximately 5 manganese/400 chl remain unobserved by EPR. Of this pool of 5 manganese, heat inactivation causes the appearance of 3 Mn into the g = 2 and VLF signals, while NH_2OH inactivation gives rise to the appearance of 4. This is consistent with the work by Yokum et al. [5] which showed that if weakly bound Mn is removed by washing in 40 mM Ca^{+2}, NH_2OH inactivation leaves only 1 Mn/400 chl tightly bound to the membrane, while Tris inactivation leaves approximately 2.

These results are summarized in figure 6 which presents a model for manganese binding to chloroplast thylakoids. Shown in this figure are three distinct sites of manganese binding. Mn_A sites denote manganese binding to unspecified surface protein components, and give rise to the VLF EPR signal. Some of these sites may be populated in active chloroplast preparations containing more than 5 Mn/400 chl. Approximately three Mn_B sites per PSII are also shown and appear distinct in that they are not observed by either of the low temperature EPR signals described. Inactivation of O_2 evolving capacity by treatment with mild heating, NH_2OH, or alkaline Tris releases these manganese from their native binding sites, where they are weakly rebound to surface proteins and become identical to the Mn_A species. The function of this fraction of manganese is unclear.

Figure 6. A model proposed for manganese binding to chloroplast thylakoid membranes.

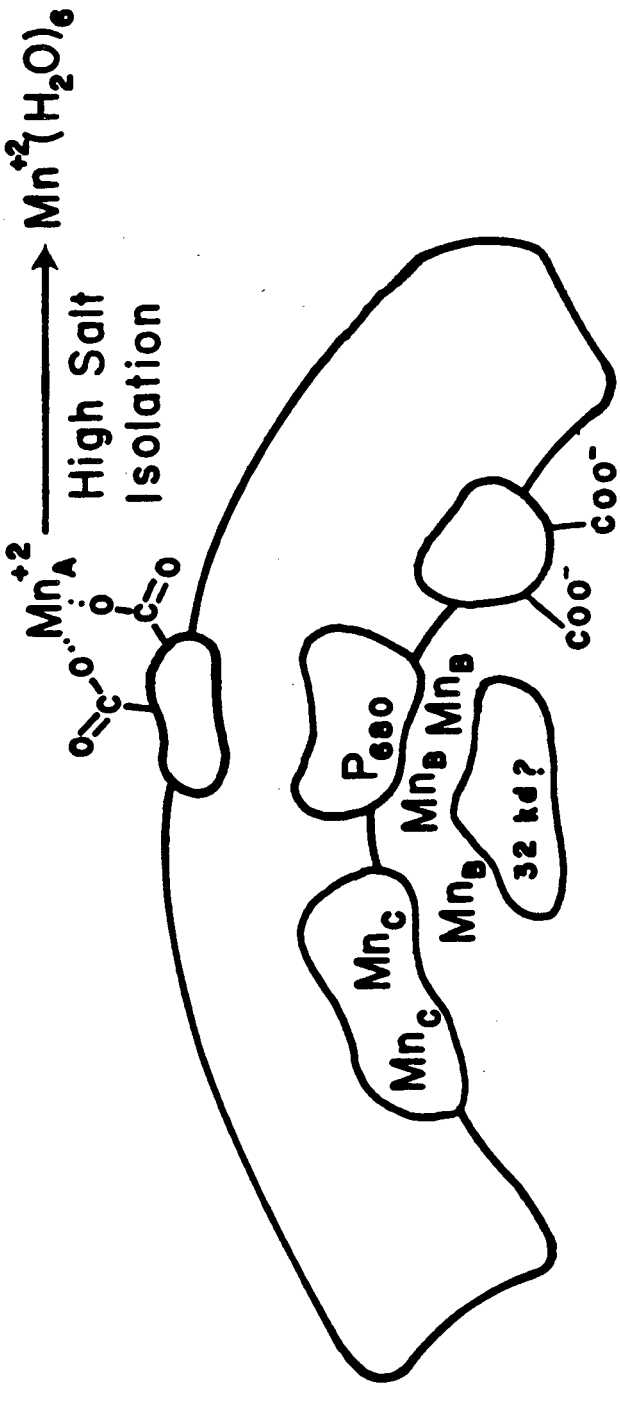
$Mn^{+2}(H_2O)_6$
High Salt
Isolation
Mn^{+2}_A
P_{680}
Mn_B Mn_B
Mn_B
32 kd?
Mn_C
Mn_C
COO⁻
COO⁻

Traditionally associated with oxygen evolution capacity because of its release upon inactivation, recent studies described in the previous chapter indicate that a portion of this pool is not required for reactivation of O_2 evolution. Thus, this fraction may represent manganese serving a structural role, possibly by stabilizing interactions of PSII protein components. There have been reports of an association of the specific release of a 32 Kd peptide by treatments that both inactivate O_2 evolution and remove chloroplast manganese [10].

As shown in figure 6 this manganese is released to the inside of the chloroplast thylakoid envelope where it may be trapped by slow diffusion [2]. This may not be necessary, however. Results on inside out chloroplast membranes [3] indicate that manganese is not trapped within Tris-washed vesicles, and other work [4] is consistent with rapid trans-membrane diffusion of free manganese. These studies make it difficult to explain why manganese release into solution from inactivated membranes is slow.

The presence of a bound form of manganese may provide such an explanation. It has been found that Tris inactivation of chloroplast membranes destroys most of the manganese binding sites that are present in untreated membranes [2]. This may reflect denaturation of damaged proteins on the membrane surface after alkaline Tris treatment, and if this process occurs slowly, manganese would be released from its weakly bound site over a period

of time.

Under the conditions of our experiments, we observe that the bound manganese of inactivated chloroplasts is not affected by added Ca^{+2} or EDTA. This may indicate that the sites are inaccessible to these agents. In a study of bound Mn in hydroxylamine treated chloroplasts by its effect on proton spin relaxation rates [11], Yocum et al. have observed bound manganese that is accessible by Chelex or EDTA only in the presence of an ionophore A23187. These results indicate that even though uncomplexed Mn^{+2} may freely diffuse across the membrane [3,4], most of the manganese present in the loosely bound form exists in binding sites on the inner surface of the thylakoids.

The third type of manganese site labeled Mn_C in figure 6 represents manganese unaccounted for by low temperature EPR upon inactivation. The quantities observed are in agreement with those observed to remain tightly bound to thylakoids after inactivation procedures. Inactivation by NH_2OH is unique in that it leaves only one Mn/400chl unaccounted for by EPR, while heat inactivation appears to leave 2 manganese firmly bound. Thus NH_2OH inactivation appears partially to remove manganese from the Mn_C sites as well as those from Mn_B.

REFERENCES

1. Radmer, R. and Cheniae, G. (1977) Primary Processes of Photosynthesis (Barber, J. ed.) Top. Photosynth. 2, 303-348.

2. Blankenship, R.E. and Sauer, K. (1974) Biochim. Biophys. Acta 357, 252-266.

3. Mansfield, R. and Barber, J. (1982) FEBS Lett. 140, 165-168.

4. Miller, M. and Cox, R.P. (1982) Photobiochem. Photobiophys. 4, 243-248.

5. Yocum, C.F., Yerkes, C.T. Blankenship, R.E., Sharp, R.R. and Babcock, G.T. (1981) Proc. Natl. Acad. Sci. 78(12), 7507-7511.

6. Velthuys, B.R. and Kok, B. (1978) Biochim. Biophys. Acta 502, 211-221.

7. Mildvan, A.S. and Cohn, M. (1963) Biochem. 2, 910-919.

8. Chasteen, N.D. and Francavilla, J. (1976) J. Phys. Chem. 80, 867-871.

9. Wertz, J.E. and Bolton, J.R. Electron Spin Resonance: Elementary Theory and Practical Applications (1972) McGraw-Hill, 258-312.

10. Henry, L.E.A., Lindberg Moller, B., Andersson, B. and Akerlund, H.-E. (1982) Carlsberg Res. Commun. 47, 187-198.

11. Robinson, H.H., Sharp, R.R. and Yocum, C.F. (1981) Biochim. Biophys. Acta 636, 144-152.

APPENDIX A

The following is a brief description of the use of the major VAX11/780 programs written for EXAFS data analysis. Four programs are discussed in the order in which they are normally used. For each program, a short description of its purpose is given, followed by an explaination of the parameters and/or commands required for operation of the program. Queries and commands generated by the computer for user response are shown in uppercase and underlined.

I. Program REFORM

The purpose of this program is to perform the necessary pre-processing of data as it arrives from SSRL. The file structures and formatting of the data are changed to make the data files compatable with the other programs. In addition, data are checked for some common errors, and are then normalized. Upon input to the program, the data are in the form of lists of incident, transmitted, and fluorescent intensity values as a function of monochromator angle. Upon output, one data file is generated for each data channel collected, and are in the form of normalized I_0/I, I_1/I_2, and F/I_0 ratios as a function of monochromator angle.

The required commands are:

INPUT FROM TAPE? (Y/N): Are input files arriving

directly from tape, or from disk? Default is no.

ENTER INITIAL INPUT FILE: The first file name to be input. These file names should be one or more (less than 6) characters followed by three or four numbers, and should not include the '.DAT' extension. Acceptable file names: A001, STUFF0023. Unacceptable names: A01, A001.DAT.

ENTER FINAL INPUT FILE : The last file name to be input. It should have the same character part as above. Files will then be processed successively in order of the file numbers.

OUTPUT TO TAPE? (Y/N): Should the output files be written to tape? If you answer both of the 'tape' questions yes at the same time, you will be in for a long wait.

ENTER INITIAL OUTPUT FILE: The name of the first file to be output. The name should consist of 5 (or fewer) characters followed by 4 numbers. Do not used the .DAT extension, as it will be automatically included.

POSITIONS OF I0,I1,I2 = 1, 2, 3 . ENTER IF DIFFERENT: These are the numbers of the HEX-SCALER inputs to the SSRL computer of the three ion chamber data channels. If, for example, the I_2 channel was not used, the appropriate response is 1,2,0.

ENTER FILE NAME (1 CHR, 4 #S), AND I2 GAIN FOR EACH TIME THE I2 GAIN WAS CHANGED. FILE NAMES MUST BE IN ORDER: If the I_2 channel was used, the data file does not contain its ion chamber gain, and this must be supplied manually. For example, the reply might appear as; A001,9,A032,10,A107,7.

NORMALIZATION SET - I0/I1, I1/I2, F/I0

TYPE N FOR UNNORMALIZED DATA, RETURN OTHERWISE: Just type return, unless you want the individual channels to be output instead of their ratios.

II. Program EXADD

This program is used for averaging EXAFS and edge data files. Each scan is weighted by the number of seconds spent collecting the data and by the incident intensity at the beginning of the scan. For each scan, the data are plotted over the summed data for comparison, and an option is given to not add the scan or to cut out a portion of the data before adding. Scan to scan shifts may be input manually, or automatically determined if reference data were collected using ion chambers I_1 and I_2. If this is desired, the program will look for a sharp peak in the reference channel and will shift the present scan so that it matches the peak position of the first scan used in the add.

The required parameters are:

HOW MANY DATA CHANNELS? (<50): For example, if two absorption and three fluorescence data channels were collected, the answer is 5.

DO YOU WANT SHIFTING OF DATA FILES? (Y/N): Input 'Y' if you want to shift scans before adding.

ARE SHIFTS MANUAL/AUTOMATIC (0/1): If you answer '0', you will be asked for the shift for each scan added. If you answer '1', the program will attempt to determine the shift from the reference data.

FOR REFERENCE FEATURE, ENTER XLOW,XHIGH: If automatic shifting is used, you must supply the region, in monochromator step numbers, in which the reference feature is expected to lie.

DO YOU WANT IN PROGRESS PLOTS? (Y/N): Answer 'Y' if it is desired to plot the scan over the averaged data for each added data file.

MONITOR WHICH CHANNEL NUMBER?: This is the channel that will be plotted. 1 is the primary absorption channel, 2 is the reference absorption channel if it was used, and the first fluorescence channel if not, etc.

ENTER XMIN,XMAX FOR PLOTS: The plotting region desired in monochromator motor step numbers.

ENTER GRAPHICS TERMINAL (4006,4010,4012,4014,4662): The Tektronix model number for the graphics device used.

FOR DERIV. CALCULATION, ENTER ORDER, AND NPTS/FIT : For automatic shifting of data, the reference peak position is determined from the zero-crossing of the first derivative. This is calculated using a sliding fit to a polynomial (usually quadratic) using 'NPTS/FIT' points. The values of the parameters should be determined beforehand so that the derivative is smooth, but undistorted.

The following are the same as for program REFORM.

INPUT FROM TAPE? (Y/N):

ENTER INITIAL INPUT FILE:

ENTER FINAL INPUT FILE :

OUTPUT TO TAPE? (Y/N):

ENTER INITIAL OUTPUT FILE:

FOR THE REFERENCE FEATURE, ENTER THE CORRECT VALUE OF CUEDGE: This is asked only for the first file. For that file, enter the number that CUEDGE would have to be so that the reference feature would have exactly the correct energy. This calibrates all of the added spectra.

III. Program EXAFS

This program is used for general data analysis, including plotting, stripping, normalization, background removal, and fourier transformation. The program uses the FFTLIB data analysis routines written by Alan Robertson, and the IGL graphics package PLOT10 by Tektronix.

Upon entering the program, it will first prompt you for a couple of things:

1. ENTER DATA DISK DIRECTORY-- It is asking for the disk directory containing your data. Unless you specify otherwise, when you read or write data this is the directory the program will go to. This allows many different users access to the program, and allows you the option of keeping all your data on a separate disk directory. If, for example, your directory is ABC, and the data is on subdirectory ABC.DEFG, then enter [ABC.DEFG] (The square bracketts are necessary.)

2. WHAT GRAPHICS TERMINAL ARE YOU USING?-- Enter the Tektronix terminal number, i.e. 4014.

The program will now become interactive, and ask for a command. There are 64 commands which do all of the manipulations required. You may enter commands individually, or in a string. To enter a command string, type as many commands as you wish, separated by commas , as long as they fit on a line.

The program has space to contain six data files of 2048 points each at any time. These are labeled A-F and can be used for temporary data storage. However, it is not a good idea to store files in array B since this array is used by the program in some cases.

GENERAL COMMANDS:

HELP - Use this command to obtain information about program use.

PROMPT - This command displays and allows change of the prompt mode. Many variables are needed to control such things as fit regions and order, window types, point numbers, etc. Whenever the program needs to use a parameter, it will in most cases ask you for values, or at least tell you what they are. If you know that all parameters are set correctly and get tired of answering the questions, you may change the prompt mode so that all parameters are used as is.

QUIT - Exits the program.

CREATE - This command allows you to create your own commands. If you create a command called STRIP,

which contains the commands 'RNEXA, H, N, Z, E, PLOTA, WNEXA', then you need only enter 'STRIP' to execute those commands. Any of the 64 commands may be used with the exception of CREATE and REPEAT. This will work at any later time (even if you have logged off and back on). Each created command contains its own copy of all analysis parameters, which have the values held when the command was last executed. Created commands may contain names of other created commands to 5 levels. This feature allows the program to become quite powerful, because virtually any analysis sequence can be individually tailored, and rapidly reconstructed with the use of a single command. There is no practical limit to the number of commands that may be created. A list of created commands often used by the author is presented at the end of the EXAFS program section.

HEADER - This command displays and allows change of the file header parameters such as NAME, CUEDGE, NPTS, XSTART, XSTOP, etc., for the data contained in array A.

PARAM - This command displays and allows change of all of the data analysis parameters. Note that this display is exactly that obtained in an older program, and some of the parameters are no longer used. If you are in prompt mode (default) when running this program, you may never need to use this command.

STORn - This command allows you to store all control parameters in n so that you may later restore them with the RECLn command. N may be from 1 to 5. This is useful for saving a particular analysis environment which you want to return to later. It also allows user created command files to communicate their parameters. Any user-created command has the ability to store or recall any of the five control blocks, and thus the command may change something without your knowing it, if you are not careful. It may be wise to hold N = 1, and N = 2 sacred, so that no created command stores into them.

RECLn - This commmand allows you to recall all analysis parameters from n. For more information, see STORn.

REPEAT - This command will repeat whatever command string you last entered. It will not work in a created command.

CHANGE - Replaces data with a line or deletes points. You will be asked for values whether you are in prompt mode or not.

VALUE - Gives the x value of the point number you specify.

POINT - Gives the point number closest (and not above) the x value you input.

ENERGY - Calculates the energy of the monochromator angle you specify.

ANGLE - Gives the angle of the energy you specify.

FILE MANAGEMENT COMMANDS

READ* - This command reads a data file from disk into the array '*'. '*' can be A-F. It will then ask for the file name. There are two options. You may use any file name at all on any disk directory by specifying the complete name. That is, if you type '[ABC.DEFG]HIJK.LMN;3' the program will read the third version of file HIJK.LMN which is on the subdirectory DEFG of the directory ABC. This can be cumbersome, so the program can also attempt to construct file names for you. If you enter a four digit number when it asks for the file name, it will try this. The disk directory it looks at is what you told it as you first entered the program. The file name used is EXAFS####.DAT where the #'s are those you gave for a file name. The letters EXAFS are default and can be changed by executing the command FNAME. It is thus suggested that you name your files this way (5 chrs followed by 4 numbers), as it makes it very easy to read and write them. For example, you might name angle space files by the date collected- JAN79,MAR75, etc. and name all other files by compound or element. After using command FNAME to set this, if you type 0176 in response to a file name request, it will get 'JAN790176.DAT' from

your directory.

WRITE* - This command writes a data file to disk from the array '*'. It will ask for a file name and this is handled just as for reading files.

RNEX* - Provided you have already used the READ* command once and specified the file name by a number, this command reads into array '*' the file which has a number one larger than this. For example, if the name 'FEB76' was set using command FNAME and then READA was executed, with 0056 as the response, the program reads into A the file FEB760056.DAT . Now when RNEXC is executed, it reads into C the file FEB760057.DAT without asking.

WNEX* - This command writes data files in just the way RNEX* reads them. Note that the file numbers written by WNEX* and read by RNEX* are completely separate. Continuing the above example, suppose WRITEC has been executed, with 0084 as the file name response. This is important as it is the only way the program knows what the next file should be. The program wrote the data from C to the disk file FEB760084.DAT. Now when WNEXA is later executed, it will write from A the disk file FEB760085.DAT. If RNEXA is the next command, data will be read into A from disk file FEB760058.DAT. If WNEXA had been next, it would have written A to disk file FEB760086.DAT.

SWAPXY - This command swaps arrays X and Y. For example, SWAPDA will swap arrays D and A.

COPYXY - This command copys array X to array Y. For example, COPYDA will copy array D to array A, overwriting whatever was in A.

FNAME - This command displays and allows change of FNAME. This is the 5 character string which is used to construct file names by the program. It is set by default at the beginning of the program to 'EXAFS', and can be changed to any string of 5 characters.

DISK - This command displays and allows change of DISK. This is the name of the disk directory the program uses to read and write data. When specifying the value of DISK it is neccessary to include bracketts: [JOEBLOW.DATA]

PLOTTING COMMANDS

PLOTX - This command plots array X. That is ,PLOTB will plot array B on the graphics terminal.

SETPL - This command displays and allows change of the plotting parameters. A menu is presented allowing changes that affect the plot type, the x and y range and size, labels, etc.

PLSAV - PLSAV is used to capure plots so they may be 'replayed' later. The command works like a switch. To turn on the capturing of plots, type PLSAV. It will ask for a 6 character name. Any plots that are

done while PLSAV is activated will be captured in the file with that name. To turn off the capturing of plots, enter PLSAV again.

REPLAY - Used to replay earlier captured plot files.

GIN - This command allows use of the cross-hairs on the 4014 and 4012 terminals to obtain x and y coordinates from the screen.

DATA ANALYSIS COMMANDS

FT - Replaces array A with its fourier transform if the data is in k-space, and with its inverse fourier transform if the file is in r-space.

DE - Corrects for 'twisting' of the data caused by transforming data that does not start at K=0.

PH - Corrects for a constant phase shift in the complex data array. The phase shift used in degrees is contained in PHAS58.

Note: DE and PH need only be used if one wants absolute phase information for the real and complex portions of the transform. If one is using only power spectra, these commands are not used. They should certainly not be used for a file that is to be transformed back into k-space without knowing their effects. A phase correction will cause admixture of the real and complex fourier transform, and a delay correction applied in r-space, will result in a shifted file when back-transformed.

A - Command 'A' replaces A(I) with -A(I).

B - Command 'B' replaces A(I) with (AMUL52) * A(I).

C - Command 'C' replaces A(I) with A(I) ** (IAPOW2).

D - Command 'D' replaces A(I) with A(I) ** (APOW53).

E - Command 'E' replaces A(I) with A(I) - B(I).

F - Command 'F' replaces A(I) with A(I) * B(I) (real and complex).

G - Command 'G' replaces A(I) with A(I) / B(I).

H - Command 'H' replaces A(I) with Ln A(I).

I - Command 'I' replaces A(I) with EXP A(I).

J - Command 'J' replaces A(I) with SQRT A(I).

K - Command 'K' replaces A(I) with A(I) + (AADD54) + (ALIN57)* (I-1)/(KRANGE - 1) (adds straight line to A(I)).

L - Command 'L' replaces A(I) with A(I) - (sum of A(I))/NUMPTS (subtracts avg.).

M - Command 'M' replaces A(I) with A(I) * SX(I) where, SX(I) = X(I) ** KXPOW3 if KXPOW3 < 100, and SX(I) = X(I) ** XPOW63 if KXPOW3 > or = 100.

N - Command 'N' converts A(I) from angle to energy space.

O - Command 'O' replaces X(I) (x-axis of A(I)) with X(I) - ZERK55 (shifts x-axis of A(I)).

P - Command 'P' converts A(I) from energy to k space.

Q - Command 'Q' converts A(I) from a non-linear x-y array to a linear array. The interpolation can be linear or a fit of order 1-9. The number of output points is contained in LINP12 and the fit region in WINL60.

R - Command 'R' applies a complex high and low cut off on A(I). It zeros the complex points A(1) to A(LCUT16) and A(ICUT17) to A(NPTS).

S - Command 'S' replaces B(I) with a smoothed A(I). A sliding fit of order 1-9 is done on A(I). The number of points in the fit is as critical as the fit order. Both values are contained in LPOL15. Order = mod (LPOL15,10) and # points fit = LPOL15/10.

T - Command 'T' replaces real part of A(I) with the power spectrum and replaces complex part of A(I) with the phase.

U - Command 'U' replaces A(I) with its complex conjugate.

V - Command 'V' creates a McMaster's background in B(I). You are asked what metal you are working with so that the program can create the appropriate theoretical background function. You are also asked for the edge energy (stored in ZERK55) so that proper normalization is done at this point

W - Command 'W' replaces A(I) with A(I) * (a gaussian window) width of window = SIGM51. That is , if a window is used in k space, then SIGM51 is the r-space broadening.

X - Command 'X' replaces A(I) with A(I) * (an exponential window) width of window = EXLWG2. That is, if a window is used in k space, then EXLWG2 is the r-space broadening.

Y - Command 'Y' does not exist.

Z - Command 'Z' replaces B(I) with a fit to all or some of A(I). ABS(NPOL19) = fit order. If NPOL19 < 0 then the Ln of the x axis is also taken. If NFIT13 > 0 then the fit is from point 1 to NFIT13. If NFIT13 < 0 then the fit is from point ABS(NFIT13) to NPTS. If NFIT13 = 0 then the fit is from point 1 to NPTS. AMUL52 is set to 1/B(ZERK55) and AADD54 is set to -B(ZERK55) so that after execution of command Z, command E will do a background strip, command K will subtract zero point values, and command B will do a post edge normalization automatically.

AA - Command 'AA' creates an x-y array from any file.

BB - Command 'BB' reduces NPTS by truncation. This is specified by the value of LENGH9.

CC - Command 'CC' reduces NPTS in A(I) by throwing out evenly spaced points in the file (reduces point density). This is specified by the value of LENGH9.

DD - Command 'DD' increases NPTS in A(I) to 2048 by adding zeros to the end of the file.

EE - Command 'EE' replaces A(I) with A(I) * F(I) where F(I) = 1. between WINL60 and WINR61, and F(I) = 0 otherwise

FF - Command 'FF' throws away points at beginning of the file. # pts is contained in LEFT21.

GG - Command 'GG' is not used at this time.

HH - Command 'HH' replaces B(I) with the derivitive of A(I). This does a sliding fit just as in command 'S', and

then takes the analytical derivitive of the fit for each point.

II - Command 'II' is not used at this time.

JJ - Command 'JJ' is not used at this time.

KK - Command 'KK' replaces A(I) with A(I) * F(I) where F(I) is a window function. KHAM22 controls type of window, and HKAI56 controls window shape If KHAM22 < 0 and the file is complex, command R is done first, (complex filter cut) and the window is applied from WINL60 to WINR61. If IABS(KHAM22) = 0 or 1 then a Kaiser window is applied, HKAI56 = 1. to 9. controlling the amount of windowing. If IABS(KHAM22) > 0 then a general hamming window is done. That is, if KHAM22 = 1515, then the window is applied to the first 15% of the data, the last 15% of the data, leaving the middle 70% untouched. HKAI56 controls the amount of windowing. HKAI56 = .0 to .5 under nearly all cases. Some standard windows are :

Kaiser - KHAM22=0 , HKAI56 = 1. to 4.

Hanning - KHAM22=5050, HKAI56 = .5

Hamming - KHAM22=5050, HKAI56 = .46

( ) - Command ' ' (blank) does nothing.

(**) - When no match to any of the above commands is found, the program tries to open and execute the command file of that name (see command 'CREATE').

The following is a list of the commands created

by the author that are considered useful for EXAFS analysis. In parenthesis are the commands used to create these special sequences.

ADDAB - Adds array B to A, leaving the result in A. (A, E, A,)

FULLPL - Plots array A full scale using default parameters (PLOTA)

SAMEPL - Overplots B on the same Y scale as the last plot. (PLOTB)

PMPL - Plots array A with the Y scale as + and - the largest value in the data file. (PLOTA)

SAMPLA - Overplot of A with the same Y scale as the last plot. (PLOTA)

SPLA06 - Overplot of A with the same Y scale as the last plot, and with and X scale of 0.0 to 6.0. (PLOTA)

STRIP - Does a general pre-edge background subtraction. (FULLPL, Z, SAMEPL, E)

NORM - Does a general post-edge normalization. (FULLPL, Z, SAMEPL, PROM, B, PROM)

BCK - Does a McMasters post-edge normalization and a low order background removal. (V, G, FULLPL, GIN, Z, SAMEPL, E)

ESSS - Linearizes an energy-space data file, and performs a triply smoothed background removal. (PROM, Q, PROM, FF, COPYAF, S, SWAPAB, PROM, S, SWAPAB, S, COPYFA, FULLPL, SAMEPL, E, PROM) CAUTION: Uses array F.

KSSS - Accepts an energy-space file, converts to k space, and performs a triply smoothed background removal. (O, P, FULLPL, Q, FF, COPYAF, S, SWAPAB, PROM, S, SWAPAB, S, COPYFA, PMPL, SAMEPL, E, PROM) CAUTION: Uses array F.

EBC - Accepts an energy-space file, converts to k space, linearizes, applies apodization windows and plots the fourier transform. (O, P, PMPL, Q, POINT, FF, PMPL, KK, M, PMPL, DD, FT, T, PLOTA, GIN, GIN, GIN)

KBC - Same as above, but accepts a k-space file. (POINT, FF, PMPL, KK, M, PMPL, DD, FT, T, PLOTA, GIN, GIN, GIN)

ETEST - Takes an energy-space file, and performs a trial background removal, followed by a plot of its fourier transform. (ESSS, PLOTA, EBC) CAUTION: Uses array F.

KTEST - Same as above, but does the background removal in k-space. (KSSS, PLOTA, KBC) CAUTION: Uses array F.

SFT - Standard fourier transform sequence of a k-space file. (PMPL, KK, M, SAMPLA, DD, FT, T, PLOTA, GIN, GIN)

ISOLAT - Accepts a linear k-space file, performs a fourier isolation, and transforms back into k-space leaving the fourier-filtered data in array A. (M, PMPL, COPYAF, DD, FT, T, PLOTA, GIN, GIN, COPYFA, DD, FT, KK, COPYAE, T, SPLA06, COPYEA, FT, SWAPAF, FULLPL, SWAPAF, POINT, BB, SAMPLA) CAUTION: Uses arrays E

and F.

III. PROGRAM EXFIT

This program accepts a k-space data file and performs single- and multi-shell fitting using stored values of the EXAFS phase and amplitude functions. The data should be weighted by the appropriate value of k before execution of the program.

The required parameters are:

WHAT GRAPHICS DEVICE ARE YOU USING? : The Tektronix device number.

ENTER DATA FILE NAME :The name of the file to be fit.

The program then displays menus for the additional parameters:

1) TITLE = PLOT TITLE GOES HERE

2) ABSORBING ATOM = MN

3) POWER OF K TO WEIGHT FIT = 3.000000

4) FIT STARTS AT K = 4.000000

5) FIT STOPS AT K = 13.00000

6) # OF ATOMIC SHELLS = 1

ENTER # TO CHANGE, RETURN TO CONTINUE : Select from above the number of the parameter to be changed.

FOR SHELL # 1 BACKSCATTER ATOM = O

ENTER IF DIFFERENT: Enter element for this backscattering shell.

	START	STEP	LOWER	UPPER
1) R =	2.00000	0.00500	1.50000	4.00000
2) N =	2.00000	0.05000	0.00000	5.00000
3) SIG =	-0.00500	0.00050	-0.05000	0.00000
4) DEO =	0.00000	0.20000	-20.00000	20.00000

ENTER # TO CHANGE, RETURN TO CONTINUE :Select from above the parameters to be changed. Shown are: R the distance, N the amplitude, SIG the Debye-Waller parameter, and DEO the correction in eV to the value of E_o. Each has associated with it a starting value, an estimated step size, and the upper and lower bounds.

You are then asked for the minimization commands. The commands commonly used are:

FIX nn - Fixes the nn^{th} parameter in the above list.

REST - Restores all fixed parameters.

SIMP - Initiates a simplex minimization algorithm.

MIGR - Initiates a migrad minimization algorithm.

MINI - Initiates a simplex, followed by a migrad minimization.

SEEK - Initiates a Monte-Carlo parameter search.

EXIT - Must be the last command in the list.

The fit is now performed, the results displayed on the screen, and the data and fit are plotted. If desired, the program will return to the start without changing any of the parameters so that additional fitting can be continued.

APPENDIX B

This appendix describes the method used for simulation of Mn^{+2} EPR powder spectra using matriz diagonalization techniques. For high spin Mn^{+2} ($S = 5/2$), the spin Hamiltonian is,

$$H = \beta_e H \cdot g_e \cdot S + \beta_n H \cdot g_n \cdot I + S \cdot A \cdot I + \qquad (1)$$

$$hI \cdot Q \cdot I + \Sigma B_k^q \hat{O}_k^q$$

in which the terms are, respectively, the electron and nuclear Zeeman interaction, the nuclear hyperfine term, the nuclear quadrapolar interaction (for $I>1/2$), and a series of field-independent fine structure terms shown as a sum of Orbach operators [1]. Depending on the symmetry of the ligand field, d^5 ions may require fine structure terms with $k = 2$ and 4, and these are usually written [1] using the spectroscopic parameters D, E, a, and f as,

$$\Sigma B_k^q \hat{O}_k^q = (D/3)\hat{O}_2^0 + (E)\hat{O}_2^2 + \qquad (2)$$
$$(a/120)(\hat{O}_4^0 + 5\hat{O}_4^4) + (a/180)(\hat{O}_4^0 + 20(2)^{1/2}\hat{O}_4^3) +$$
$$(f/180)\hat{O}_4^0)$$

in which $\hat{O}_2^0 = 3S_z^2 - S(S+1)$, $\hat{O}_2^2 = (1/2)(S_+^2 + S_-^2)$, and the quartic terms, $\hat{O}_4^n$, are described by similar, but more

complicated functions of the spin operators.

In cases in which the electronic Zeeman interaction is much larger than the zero-field terms, an isotropic signal at g' = 2 is observed. Often, D and E are comparable to or larger than $g\beta_e H$, and as a result, the spectral features are strongly dependent on the ligand symmetry [2]. For axial symmetry, in which E = 0, spectra are observed that are strongly anisotropic, and resonances may be observed at $g'_x = g'_y = 6$ and $g'_z = 2$, 6, and 10. For a completely rhombic ligand field, in which E/D = 1/3 [3], EPR spectra may exhibit a symmetric line at g' = 4.3.

The interpretation of EPR powder spectra in terms of the parameters D, E, a, and f can be difficult without the use of simulations. Methods have been used employing third-order perturbation theory, including the terms involving D and E, for the simulation of S = 5/2 spin systems [2], but these methods are accurate for only a limited range of parameters. We have used a more exact but inefficient method that is somewhat similar to that described by Oosterhuis [4], employing a field-swept matrix diagonalization method. A recent application of eigen-field perturbation theory has been reported [5], and may be of greater general use in that it is more efficient and quite accurate. This is especially true for calculations of Mn^{+2} which require the diagonalization of a 36x36 matrix.

The simulation program EPR proceeds by choosing a set of Euler angles θ and ϕ with respect to the z-axis of the high

field spin axis system. The Hamiltonian matrix is constructed from equation 1 using $H_x = H \sin\theta \cos\phi$, $H_y = H \sin\theta \sin\phi$, and $H_z = H \cos\theta$ as the components of the applied magnetic field along the principal magnetic axes. Terms in the Hamiltonian containing S_z contribute real diagonal elements to the matrix, and terms involving S_x and S_y contribute real and imaginary off-diagonal elements, respectively. For each angle, the matrix is set up at a number of field values across the spectrum, and each matrix is diagonalized. This is performed using the IMSL routines EHOUSH to first reduce the matrix to tri-diagonal form, and EQRT2S to diagonalize the reduced matrix.

Each pair of energy levels is examined as a function of magnetic field and resonance conditions are identified. If the field spacing is chosen finely enough, the energy levels vary quite smoothly. Thus the exact resonance field is determined using a quadratic approximation to the energy levels in the region of resonance. The Hamiltonian matrix is diagonalized again at the exact field of each resonance found, and IMSL routine EHBCKH is used to back-transform the matrix to give the eigen-vectors. The relative transition probabilities, $|\langle\psi_i|S_x|\psi_f\rangle|^2$, are then calculated from the eigen-vectors after normalization. The derivative of a Gaussian line with an amplitude proportional to this probability and an anisotropic line-width, $\Gamma = \Gamma_x \sin\theta \cos\phi + \Gamma_y \sin\theta \sin\phi + \Gamma_z \cos\theta$, is then centered on the resonance field, and added to a spectral array.

At this point, the spectral features corresponding to one angle have been calculated. This process is repeated at other angles, either by stepping through them in a regular fashion, or by randomly selecting them. The latter method has the advantage that the spectral features corresponding to all angles grow in at the same rate. The simulation may then be halted after the spectrum converges, preventing under- or over-sampling of angles.

After entering the program, the parameter values are displayed so that changes can be made before execution. The parameters are:

1)gx

2)gy

3)gz

(The x, y, and z components of the g tensor)

4)AX

5)AY

6)AZ

(The x, y, and z components of the anisotropic hyperfine coupling. Values are in units of cm^{-1}.)

7)D

8)E

(The quadratic fine-structure constants describing the zero-field splitting. Values are in units of cm^{-1}.)

9)THETA

10)PHI

(The Euler angles used for single angle calculations.)

11)HMIN

12)HMAX

(The magnetic field limits of the simulated spectrum in Gauss.)

13)FIELD INCREMENT

(The spacing in Gauss between fields used for diagonalization.)

14)MICROWAVE FREQUENCY

(In units of GHz.)

15)APRIME

(The value of a in the quartic terms of equation 2 in units of cm^{-1}.)

16)PPAR

17)PPERP

(Parallel and perpendicular components of the axial nuclear quadrapolar coupling in cm^{-1}.)

18)LINEWIDTH(X)

19)LINEWIDTH(Y)

20)LINEWIDTH(Z)

(The x, y, and z components of the anisotropic line-width in Gauss.)

21)NTHETA

22)NPHI

(The number of angles used within the spherical region specified by #23.)

23)NSPHERE

(Selects the spherical region in which angles are selected.

For NSPHERE = 1, calculation is done for a single angle, for NSPHERE = 2, THETA and PHI range from 0 to 90°. This is the normally used value, but other ranges are available for selection. If NSPHERE < 0, then angles are selected randomly.)

24)NOUT

(Controls the output. If NOUT = 0, a list of the resonances only are output. If NOUT = 1, the spectral array only is output. If NOUT = 2, both are output.)

25)IRANK

(The rank of the Hamiltonian matrix used. For S=5/2, I=5/2, IRANK = 36.)

26)ILEVEL1

27)ILEVEL2

(The energy levels used for finding resonances. They are usually set to 1 and IRANK. If, for example, it is desired to use only the lowest 12 energy levels, they may be set to 1 and 12.)

28)NANG

(The number of angles the calculation completes before writing intermediate results)

29)J

(The exchange interaction in cm^{-1} if it is included in the Hamiltonian.)

30)F

(The parameter f in the quartic coupling term of equation 2.)

REFERENCES

1. Abragan, A. and Bleaney, B. (1970) Electron Paramagnetic Resonance of Transition Ions, Oxford Univ. Press, London/New York.

2. Aasa, R. (1970) J. Chem. Phys. 52(8), 3919-3930.

3. Blumberg, W.E. (1967) Magnetic Resonance in Biological Systems (Ehrenberg, A., Malmstrom, B.G. and Vanngard, T., Eds.) Pergamon, London.

4. Oosterhuis, T. (1974) Structure and Bonding, Springer-Verlag, New York/Heidelberg/Berlin, 20, 59-99.

5. Scullane, M.I., White, L.K. and Chasteen, N.D. (1982) J. Mag. Res. 47, 383-397.

This report was done with support from the Department of Energy. Any conclusions or opinions expressed in this report represent solely those of the author(s) and not necessarily those of The Regents of the University of California, the Lawrence Berkeley Laboratory or the Department of Energy.

Reference to a company or product name does not imply approval or recommendation of the product by the University of California or the U.S. Department of Energy to the exclusion of others that may be suitable.

TECHNICAL INFORMATION DEPARTMENT
LAWRENCE BERKELEY LABORATORY
UNIVERSITY OF CALIFORNIA
BERKELEY, CALIFORNIA 94720